Faculteit Wetenschappen

Departement Fysica

Three-dimensional characterisation of nanomaterials: from model-like systems to real nanostructures

Driedimensionale karakterisering van nanomaterialen: van model systemen tot realistische nanostructuren

Proefschrift voorgelegd tot het behalen van de graad van

Doctor in Wetenschappen: Fysica

aan de Universiteit Antwerpen, te verdedigen door

Thaís Milagres de Oliveira

Promotor: Prof. Dr. S. Bals

Antwerpen

2020

Members of the jury

Chairman

Prof. Dr. Milorad Milosevic, University of Antwerp, Belgium

Promotor

Prof. Dr. Sara Bals, University of Antwerp, Belgium

Members

Prof. Dr. Paul Scheunders, University of Antwerp, Belgium

Dr. Wiebke Albrecht, University of Antwerp, Belgium

Prof. Dr. Johan Hofkens, Catholic University of Leuven, Belgium

Prof. Dr. Kees Joost Batenburg, University of Leiden, The Netherlands

Contact Information

Electron Microscopy for Materials Science
University of Antwerp

Thaís Milagres de Oliveira

EMAT – Electron Microscopy for Materials Science

University of Antwerp – Department of Physics

Groenenborgerlaan 171, B-2020 Antwerpen

Belgium

Thais.MilagresdeOliveira@uantwerpen.be

Table of Contents

List of abbreviations

0D	Zero-dimensional
1D	One-dimensional
2D	Two-dimensional
3D	Three-dimensional
ADF	Annular dark field
BDP	Bonding dimer plasmon
BF	Bright field
BP (plasmonic)	Bulk plasmon
BP (tomography)	Back-projection
CCD	Charged coupled device
CMOS	Complementary metal-oxide-semiconductor
CNN	Convolutional neural network
CTAB	Cetyltrimethylammonium bromide
CTAC	Cetyltrimethylammonium chloride
CTP	Charge transfer plasmon
DQE	Detective quantum efficiency
EDX	Energy dispersive x-rays
EELS	Electron energy loss spectroscopy
EWR	Exit wave reconstruction
FCC	Face centred cubic
FEG	Field emission gun
FFT	Fast Fourier transform
FWHM	Full width at half maximum
FIB	Focused ion beam
GPA	Geometric phase analysis
HAADF	High-angle annular dark field

HRTEM	High-resolution transmission electron microscopy
IWFR	Iterative wave function reconstruction
LAADF	Low-angle annular dark field
LEDs	Light-emitting diodes
LSNP	Light spatial noise portrait
LSP	Localized surface plasmon
LSPR	Localized surface plasmon resonance
MAADF	Middle-angle annular dark field
MAL	Maximum likelihood
NIR	Near infrared
PAM	Parabola method
PI-B-PEO	Poly(isoprene)-*block*-poly(ethylene oxide)
PI-DETA	Poly(isoprene)-diethylenetriamine
SBDP	Screened bonding dimer plasmon
SERS	Surface enhanced Raman spectroscopy
SIRT	Simultaneous iterative reconstruction technique
SP	Surface plasmon
STEM	Scanning transmission electron microscopy
TEM	Transmission electron microscopy
THF	Tetrahydrofuran
TIE	Transport intensity equation
TSP	Transverse surface plasmon
UHV	Ultra high-vacuum
UV	Ultraviolet
VIS	Visible
WBP	Weighted back-projection

Preface

Nanomaterials have attracted enormous attention during the last decades due to their unique physical properties (e.g. optical, thermal, electronic and catalytic properties). This is of importance for an increasing range of applications of nanomaterials, where the characterisation techniques are vital to understand the relationship between the morphology, size, composition or crystallinity and the physical properties. Recent advances in (scanning) transmission electron microscopy ((S)TEM) have enabled a comprehensive characterisation of the chemical composition, size and crystallinity of nanomaterials, from the nanoscale to the atomic level. Nevertheless, images obtained with (S)TEM only correspond to a two-dimensional (2D) projection of a three-dimensional (3D) object, hindering the quantification and interpretation of the material's shape. To unravel the structure-properties relationship, electron tomography is required. Electron tomography has become an important technique to investigate nanomaterials, but only relatively simple structures (e.g., model-like materials like monocrystalline nanospheres and nanorods) can be investigated in a routinely manner. In this thesis, more advanced 3D (S)TEM characterisation techniques were employed for a thorough characterisation of complex structures or beam sensitive nanomaterials. In the following paragraphs, I present an overview of my thesis.

The **first chapter** of this thesis presents a basic introduction to nanotechnology and the recent advances in this field. Next, a brief overview of the relevant physical properties of metallic nanoparticles and metal halide perovskite nanostructures with respective applications are given. Finally, the need for advanced characterisation techniques for complex nanomaterials is discussed.

Chapter 2 proceeds with the description of the electron tomography for the 3D characterisation of nanomaterials. The basis as well as the different imaging modes of electron tomography are explored, followed by an introduction to atomic resolution electron tomography and the 3D characterisation of nanomaterials under *in-situ* conditions.

The other chapters in my thesis will be devoted to the application of advanced electron tomography techniques for a thorough characterisation of complex nanostructures. I divided my thesis in two parts: "Electron tomography of metallic nanoparticles containing structural defects" and "Electron tomography of beam sensitive nanomaterials".

In the first part, three chapters are dedicated to the use of advanced electron tomography techniques to retrieve the 3D of structure of nanoparticles with defects. In **Chapter 3** nanotriangles and nanorods are treated by an oxidative etching procedure that may create defects. The resulting nanoparticles are further used as seeds in the synthesis process of larger nanostructures, which is why

a characterisation of the defect structure is important. In this manner, I aim to understand the relationship between the crystallinity of the seeds and the morphology of the final products. In **Chapter 4,** nanosecond laser pulses are used to introduce defects in spherical nanoparticles. The influence of the chemical environment during pulsed laser irradiation on the formation of defects is investigated. Atomic resolution electron tomography enabled the characterisation of hollow nanostructures, which are formed at specific irradiation conditions. The use of *in-situ* tomography experiments in combination with spectroscopic techniques furthermore revealed the contents inside the cavities of hollow nanoparticles as well as the dynamical behaviour upon increasing temperature conditions. **Chapter 5** focuses on the 3D characterisation of nanorods, welded together through laser irradiation. I will correlate the type of defect with the welding geometry and the plasmonic properties. Hereby, electron tomography, at the nano- and atomic scale, is applied. Simultaneously, the plasmonic properties are investigated using spectroscopic techniques.

The second part of this thesis focuses on the characterisation of beam sensitive nanomaterials. **Chapter 6** addresses the challenges related to the 3D investigation of soft-hard nano-assemblies. Alternative techniques are used to retrieve the 3D volume, while maintaining the structure as close as possible to its original state. In **Chapter 7**, an advanced methodology for the 3D characterisation of beam sensitive nanomaterials at the atomic level is tested and applied to metal halide perovskites.

Finally, **Chapter 8** presents the general conclusions of this thesis as well as an outlook for the future characterisation of complex nanomaterials.

Chapter 1. Introduction to metallic nanoparticles

1.1 Advances on nanoscience and nanotechnology

Nanoscience is a multidisciplinary field, including Physics, Chemistry, Materials Science and Biology[1–3], that studies phenomena and manipulation of materials at the scale of nanometres. The suffix 'nano' represents a billionth of a physical quantity. Therefore, one nanometre is equal to one billionth of a metre. Materials are often classified as nanomaterials when at least one of its three dimensions is in the nanometre size range, resulting in zero-dimensional (0D) nano-objects (e.g. quantum dots and nanoparticles), one-dimensional (1D) nanomaterials (e.g. nanotubes and nano-wires) and 2D nanomaterials (e.g. thin films). In Figure 1.1, a length scale is presented, where the size of a gold nanoparticle is compared to macro- and microscopic structures. Due to such small physical dimensions and an increased surface-to-volume ratio, the physical behaviour of nanomaterials is different from the bulk structures and can even be governed by the laws of quantum mechanics[1–5] (for nanomaterials with sizes of only a few nanometres known as quantum dots). Therefore, new physical properties[1] were observed, which are intrinsically correlated with the morphology, size, composition and crystallinity of nano-objects[4–9]. For this reason, nanomaterials have shown an increased interest during the last decades and have been used in a diverse range of applications, such as coatings[10–12], skincare products[13], batteries[14,15], data storage[16,17], cancer treatment[18–21] and nanosensors[22,23].

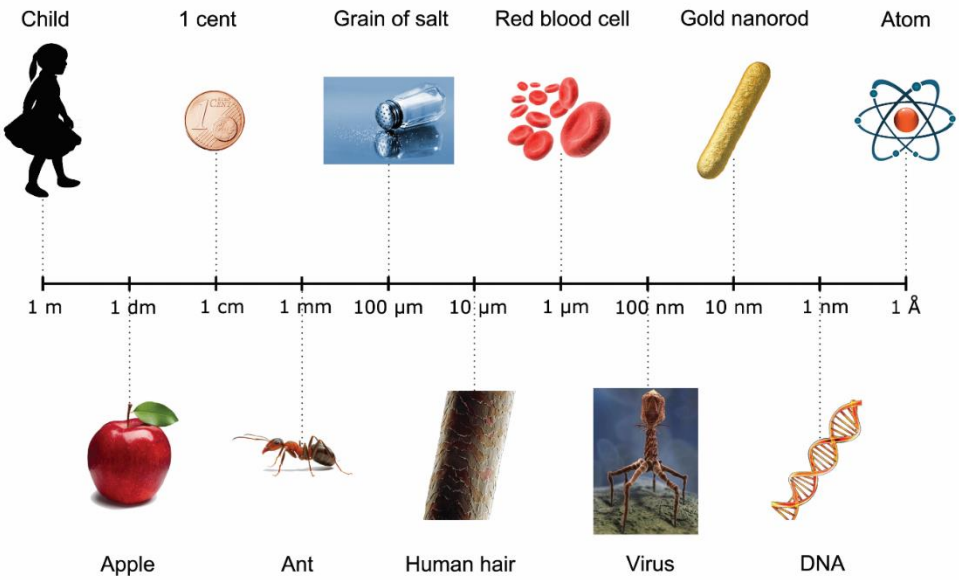

Figure 1.1 – Length scale comparing the size of nanoparticles with macroscopic and microscopic structures.

More interestingly, nanoparticles have been used since the ancient times in the preparation of red-coloured glasses. The first occurrence dates to the fourth century for a Roman opaque glass cup, the Lycurgus cup, as shown in Figure 1.2. Such cup yields a green colour when illuminated from the outside (Figure 1.2.a), whereas an internal illumination results in a ruby red colour (Figure 1.2.b). This variation of colours can be attributed to plasmonic properties of small alloys of silver and gold nanoparticles (ratio of silver to gold equals to 70:30)[24,25]. The production of the dichroic glass of the Lycurgus Cup still remains unclear, however evidences suggest that the heating process of a rare glass coloured with gold and silver might have induced the formation of alloyed nanoparticles[26].

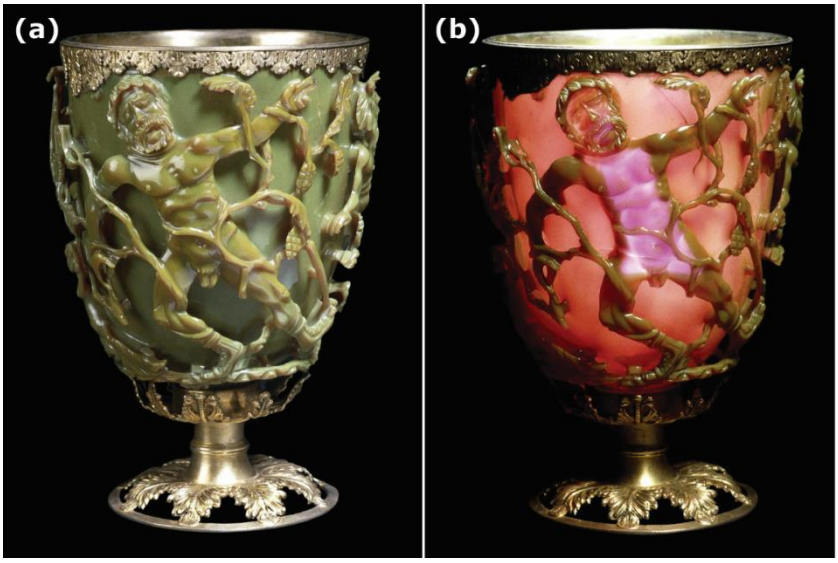

Figure 1.2 – The Lycurgus cup illuminated from the (a) outside and the (b) inside (image from the British Museum free image service[27]).

Nanomaterials can be produced with a diverse set of protocols that can be divided in two categories: the top-down and bottom-up approaches, as illustrated in Figure 1.3. The first starts from objects at the macroscale and by the removal of the excess of material, a nanostructure is created. Examples of nanofabrication using this approach consists of electron-beam lithography, focused ion beam (FIB) milling and block-copolymer lithography[3,28]. The second approach involves assembling of chemical components into the desired nanostructure and is commonly used for the fabrication of nanoparticles[28]. This synthesis approach allows the production of nanomaterials with very specific sizes, shapes and compositions, where the properties can be tuned by modifying one or more of the mentioned parameters[28].

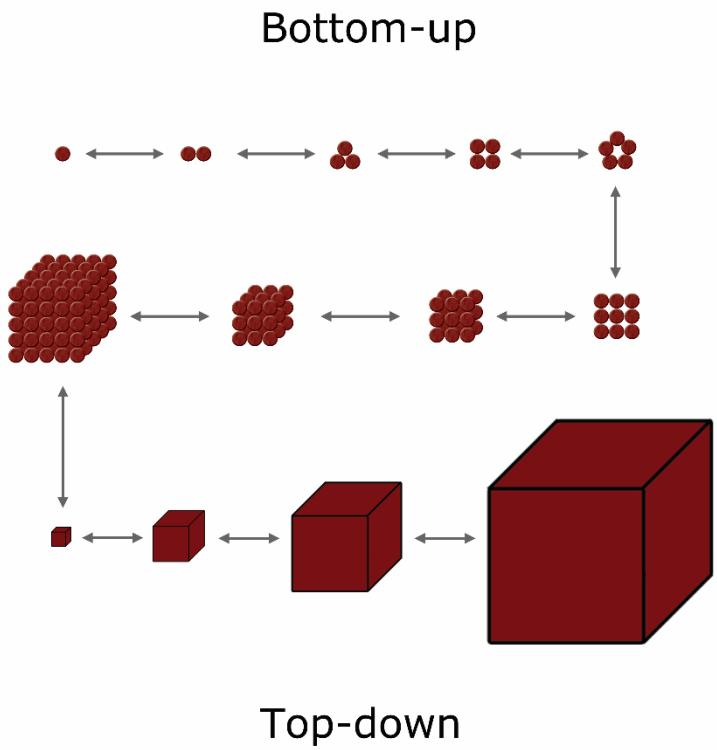

Figure 1.3 – Scheme of the principal routes for the synthesis of nanomaterials: the bottom-up and the top-down approaches. A sphere represents one atom. By assembling atoms together, larger structures can be formed, using bottom-up approaches. The first cube shown in the lowest row represents a nano-object, with size of a few nanometres, while the largest correspond to an object with dimensions in the microscale. In the top-down approach, material from an object of hundreds of nanometres (large cube at the lowest row) is removed, until a smaller structure of a few atoms in size is obtained. Figure adapted from [28].

Alternatively, new routes for the synthesis of nanomaterials have been developed for high monodispersity yield in shape and size [29,30]. For nanoparticles, the seed-mediated growth technique is one of the most reliable technique that enables the control over the chemical composition, shape, size and crystallinity during synthesis[30]. This technique consists of two steps, the synthesis of the nanoseeds and subsequent growth of the desired particle by controlling the metal precursors, reducing agents and shape-directing agents[30,31]. During the past years, the growth conditions have been meticulously optimized to increase the monodispersity yield in shape and size of overgrown structures[29,30]. However, little progress has been achieved for the optimization of the seeds and the protocols for their synthesis remain almost identical to the original version[32]. Recently, studies focusing on the optimization of the shape, size and crystallinity of the seeds has been carried out[32]. To control the size and crystallinity of the seeds, an oxidative etching approach is applied to mono-crystalline gold nanorods and mono-twinned gold nanotriangles (Chapter 3). As a result, the

monodispersity yield increased considerably. Moreover, the crystalline dispersity of the seeds enabled a synthesis protocol with improved shape and size dispersity of the final products, due to the close relationship of the crystallinity of the seeds with the final shape and size of the overgrown products[33–35]. Besides, different routines for the generation of seeds with specific type and quantity of defects have also been developed, where nanoseeds with specific crystallinity are obtained upon ultrafast laser pulses treatment of spherical nanoparticles (Chapter 4).

1.2 Physical properties and applications of metallic nanoparticles

Aspects that play an important role in the properties of nanomaterials are their size and shape. For example, nanoparticles display different plasmonic properties for different sizes as well as for different shapes (section 1.3.1). This section will focus on the qualitative description of the most relevant properties of metallic nanoparticles, with emphasis given to gold nanoparticle, which is one of the main subjects of this thesis.

1.2.1 Thermal stability

The study of the thermal stability of nanoparticles allows a better comprehension of the morphology of this type of structure by associating how the excess of free energy influences the formation of preferential facets, as it will be discussed in this section. Moreover, such study ultimately enables the enhancement of protocols for nanomaterials synthesis. The key parameter for the thermal stability of nanostructures is their small dimensions, as the surface/volume ratio increases for decreasing sizes[1,5,36]. For spherical objects with radius r, the total number of atoms N scales with volume, while the fraction of atoms in the surface is proportional to the surface area divided by the volume of the object. In this manner, surface atoms of a nanoparticle of 2 nm constitutes approximately 60% of the total atoms[36]. Surface atoms have fewer direct neighbours than the bulk atoms. Therefore, these atoms possess a lower coordination number and display unsaturated or dangling bonds, adding extra energy to the system when compared with the bulk atoms[5]. Besides, the atoms at the edges and corners have even lower coordination number.

The surface energy associated with the different surface facets (hkl) in the nanoparticle is described by the Gibbs free energy per area[36]. The increase of the total energy due to the increase of the number of surface atoms is not thermodynamically favourable during the synthesis of nanoparticles. Thus, the formation of preferential surface facets that minimizes the exposure of dangling bonds is promoted. Consequently, the final equilibrium morphology corresponds to the configuration with the less energetic surface facets and is predicted by the use of the so-called Wulff constructions[5,36]. Moreover, the functionalization of nanoparticles enables the interaction of the

surface atoms with free bonds with the functional groups, which modifies the total energy of the system and results in the formation of nanomaterials with preferential morphologies[5]. Besides, different morphologies can also be obtained during synthesis through modifications of the equilibrium conditions of the nanostructures in suspension, modifications of reactants, changes of solvent and/or temperature of the system.

More interestingly, the equilibrium position of surface atoms are also affected by surface effects. Since those atoms have dangling bonds, the net force is different from bulk atoms. Thus, the interatomic separation of surface atoms can be smaller when compared with bulk atoms for very small nanoparticles, known as surface relaxation[36,37]. Additionally, a decrease in the melting point of nanoparticles has been observed as a consequence of surface effects (increase in the number of surface atoms and consequently increase of the surface energy), when compared with the bulk materials with the same composition[1,36].

1.2.2 Optical properties

This section focuses on the description of the optical response of nanomaterials to external excitation. This knowledge is essential for a better comprehension of metallic nanomaterials performance in different applications and eventually allows the optimization of the design of existing applications. Upon interaction with external electromagnetic field, the oscillation of the conductive electrons generates a polarization state of the metal. The dielectric displacement $\vec{D}(\vec{r},\omega)$ due to the total polarization of the material (from the bound and free electrons) is given by[38–40]

$$\vec{D}(\vec{r},\omega) = \varepsilon(\omega)\vec{E}(\vec{r},\omega) \tag{1.1}$$

where $\varepsilon(\omega)$ is the dielectric constant of the metal. For metals, $\varepsilon(\omega)$ is a complex quantity and is given by $\varepsilon = \varepsilon' + i\varepsilon''$, with the real and imaginary parts described by the Lorentz model for an harmonic oscillator as[38–44]

$$\varepsilon' = 1 + \frac{\omega_p^2(\omega_0^2 - \omega^2)}{(\omega_0^2 - \omega^2)^2 + \gamma^2\omega^2} \tag{1.2}$$

and

$$\varepsilon'' = \frac{\omega_p^2\gamma\omega}{(\omega_0^2 - \omega^2)^2 + \gamma^2\omega^2} \tag{1.3}$$

where γ is the damping factor, ω_0 is the natural frequency of the oscillator and ω_p is the natural frequency of oscillation of the cloud of free electrons known as plasma frequency, defined as[38–42,44]

$$\omega_p^2 = \frac{Ne^2}{m\varepsilon_0} \tag{1.4}$$

with m equals to the mass of the electron, N is the free electron density and ε_0 is the permittivity of vacuum. A common approximation of the Lorentz model for the determination of the dielectric constant ε is the Drude model, which is valid for conductors that have free electrons. In this model, it is assumed an absence of a restoring force of the harmonic oscillator, due to presence of free negative charge carriers. In this manner, ω_0 is zero in equations (1.2) and (1.3)[41]. For gold nanostructures, the Drude model offers a limited perspective, as it only takes into account the free electrons (intraband transitions) and dismisses the contributions of bound electrons (interband transitions). Thus, to apply the Drude model to gold nanostructures, a correction factor that takes into account the interband transition in gold is incorporated to the model (known as Drude-Lorentz model) [45–47].

The collective oscillation of the conduction electrons is generated by the incident field within a thin layer of the metal close to the surface. For small nanoparticles of gold with spherical shape the maximum absorbance is located in the visible region of the electromagnetic spectrum (for a radius of 19 nm, the absorption wavelength was found to be 522 nm)[48]. The thickness of an object that the incident electromagnetic wave is able to interact is characterized by the skin depth δ parameter, where for metals δ is very small (few tens of nanometres for gold). Such coherent oscillation is known as a plasmon, which can be categorized in bulk plasmons (BP), surface plasmons (SP) and localized surface plasmons (LSP). Moreover, this coherent oscillation of the conductive electrons is responsible to generate a polarization state of the metal.

For nanoparticles, with dimensions much smaller than the wavelength of the visible light and in the range of the skin depth δ, the electron cloud of the complete particle is polarized. The electron cloud is displaced in the opposite direction of the polarization of the incident light to cancel the generated electric field inside the metal. A restoring force is then created due to the Coulomb interaction between the negatively charged free electron cloud and the positively charged lattice, resulting in the displacement of the electron cloud to the opposite side of the induced dipole, as illustrated in Figure 1.4 for a spherical nanoparticle. Moreover, for metallic objects with dimensions in the nanoscale, the LSP dominates and is characterized by localized surface plasmon resonance (LSPR) frequency that is dependent on the dielectric constant of the material, the dielectric constant of the surrounding medium, the size and shape of the metal. Finally, the coherent oscillation is damped by electron-electron and electron-phonon interactions and will therefore extinguish once the source of external irradiation is inactive.

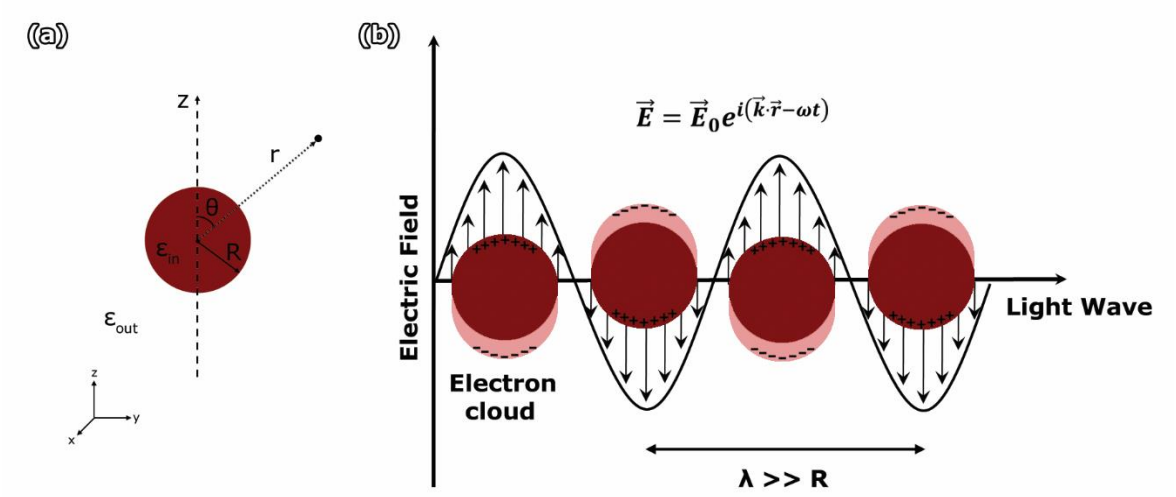

Figure 1.4 – (a) Representation of the metallic sphere. The coordinate system used is indicated in the bottom left of the image. (b) Oscillation of the electron cloud upon interaction with external field for a wavelength greater than the radius of the sphere. For the present symmetry, the oscillation of the electron cloud can be treated as an oscillating dipole.

For metals, the dielectric constant is a complex function. The imaginary part of the dielectric constant is responsible for the damping of the LSP mode and arises due to the energy absorption by the metallic object, which is ultimately converted in other forms of energy, as heat[36,41,49]. This effect will be explored in more details in section 1.2.3.

As mentioned, the size of the nanoparticle plays an important role in LSP modes[28,36,41]. For gold particles much smaller than the mean free path of the free electrons, the LSPR frequency experiences a slight blue-shift, compared to larger ones, and eventually vanishes for decreasing radius[36,50]. However, for particles with increasing radius (larger than the skin depth δ), a red-shift of the LSPR frequency is observed for increasing radius of the nanoparticles, as well as a broadening of the plasmon energy peak[28,40,41]. Alternatively, the morphology of the nanoparticle is also of vital importance for the plasmonic modes excited by the incident electromagnetic irradiation. For nanoparticles with anisotropic shapes and/or with the presence of sharp corners, different field distribution of their plasmon mode are observed as well as the resonant frequency shift[28,36,41,51]. For instance, rod shaped nanoparticles display two separated LSP bands associated with their width (transverse plasmon bands) and length (longitudinal plasmon bands)[52–55], as illustrated in Figure 1.5.

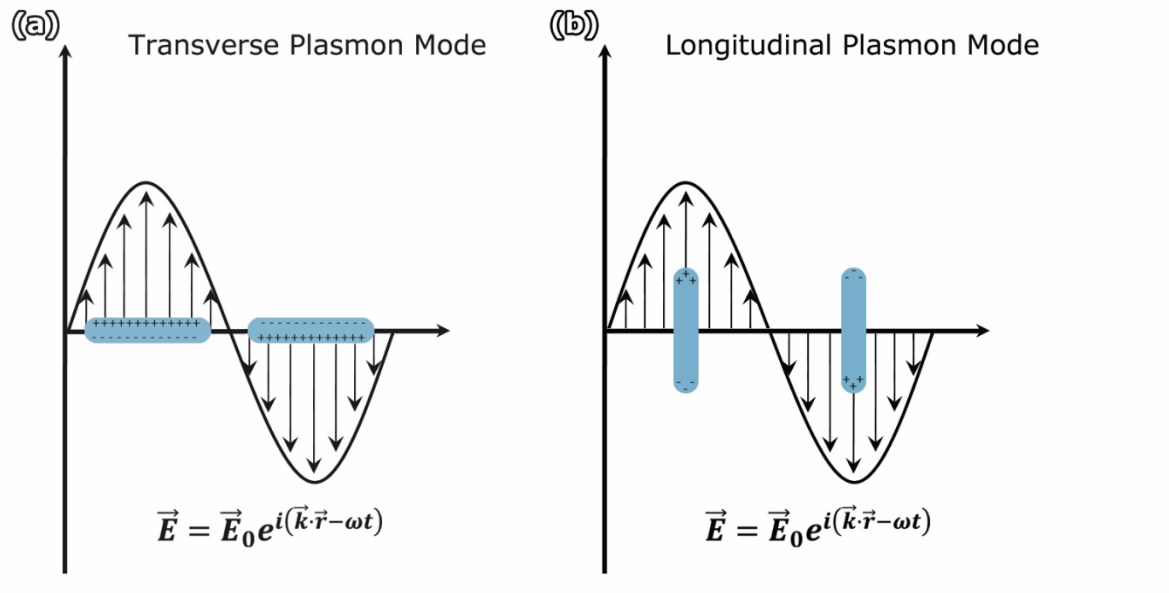

Figure 1.5 – (a) The Transverse Plasmon Mode associated with the width of the nanorod and (b) the Longitudinal Plasmon Mode associated with its length.

More interestingly, when metallic nanoparticles are placed closely together, coupling between the individual induced electric field of each particle occurs, resulting in a stronger field enhancement in comparison to single nanoparticles, also known as the generation of hot spots[56–58]. Such field enhancement for self-assemblies of nanoparticles is observed when the distance d between the particles is sufficiently small ($d < R$ for spherical nanoparticles, where R is the radius of the nanoparticle)[36,41,59]. For a qualitative analysis, consider two nanospheres aligned along the x-axis. The resultant plasmonic modes of such system is a result of the hybridization of the plasmonic modes of each nanoparticle. For a transverse excitation (perpendicular to the x-axis), the plasmon frequency of the two neighbouring spherical nanoparticles slightly blue-shifts because of the weak interaction between the individual fields, while for a longitudinal excitation (along the x-axis), a stronger interaction takes place resulting in a stronger red-shift of the plasmon frequency[28,36]. For instance, the magnitude of the module squared of the local electromagnetic field between the metallic nanoparticles in self-assembly is enhanced by several orders of magnitude when compared with a single nanoparticle[57,58,60]. Due to the field enhancement generated by the optical coupling of different modes, self-assemblies of metallic nanoparticles have shown increasing applications in sensors field[61,62].

1.2.3 Photothermal properties

A rising interest in metallic nanoparticles is associated with their ability to act as a nanoscale heat source under light irradiation. As discussed in the previous section, the imaginary part of the

dielectric constant is connected with the energy absorption of metallic nanoparticles from the incident electromagnetic wave. This absorbed energy can be converted into heat, which is most efficient when the frequency of the incident wave is equal to the plasmon resonant frequency[63]. The ability of a nanoparticle to convert the energy to heat is described by its photothermal properties. For gold nanospheres with sizes below 60 nm, the frequency is in the visible region of the spectrum[36].

For simplicity, we first analyse the effect of an ultrashort laser excitation on a gold spherical nanoparticle, with a few femtoseconds of pulse duration. Part of the energy from the incident wave is absorbed by the free electron cloud of the nanoparticle, where the energy absorption process will depend on the wavelength of the incident electromagnetic wave. The energy absorption process happens in a time interval between a few tens to a few hundreds of femtoseconds[36,64–67].The exact value for the absorption time depends on several factors, such as size of nanoparticle and the incident energy of the laser[36]. Moreover, the higher the proportion of the excited free electrons the faster the energy redistribution by electron-electron collisions[36]. Subsequently, the absorbed energy is transferred by electron-phonon scattering (duration of 1-10 picoseconds[36,67]) to the atomic lattice of the metal. As a result, a quantized lattice vibration, known as phonons, is observed, which in turn will modify the periodic potential experienced by the electrons, resulting in a modification of its wavefunction. Finally, the heat is released to the surrounding medium resulting in the cooling down of the nanoparticle through phonon-phonon collisions (time duration greater than 100 picoseconds[8,67]). The cooling dynamics in this process and the final temperature of the nanoparticle are affected by the properties of the surrounding medium, the geometry of the nanoparticle and by the density of nanoparticles in solution[36] (a high concentration of nanoparticles in solution results in a faster heating of the solvent, influencing the temperature transfer rate). Moreover, surrounding mediums with high thermal conductivity results in a faster relaxation process of the nanoparticles[36]. More importantly, the temperature reached by the nanoparticle will dictate if it will go through a shape transformation[68]. In summary, the described process will be completed upon the irradiation of a laser pulse of duration of only a few femtoseconds. Additionally, for increasing pulse duration and continuous laser excitation, the described events starts to overlap, as the nanoparticle absorbs energy from the incident wave for longer periods of time, which can eventually result in the fragmentation of the nanoparticles[68–71].

As a consequence of the described photothermal effect, metal nanoparticles can reshape and alloy upon laser excitation which has been exploited to tune the size, shape and chemical composition of colloidal metallic nanoparticles. Examples are the reduction in size of metallic nanoparticles for catalytic applications[72–74]; the controlled reshaping of gold nanorods with high monodispersity and

resulting in nanorods with ultranarrow LSP bands[68,70,75–77]; and the creation of self-assemblies of gold nanorods, resulting in nanosystems with new hybridized plasmon modes[78,79].

The main parameters that influences the interaction between incident wave and nanoparticles are the laser wavelength, fluence, pulse width, repetition rate and the properties of the surrounding medium. For instance, the laser fluence characterizes the radiant energy delivered to a surface per unit of area and can be used to tune the temperature that the nanoparticle is heated to[63], where the created heat is the highest when the nanoparticles are irradiated at their plasmon resonance. For example, gold nanorods were shown to undergo intermediate shape transitions up to complete deformation to a more spherical shape and even fragmentation upon increasing laser fluence[68–71]. Furthermore, it was found that heating is more efficient when using femtosecond pulses compared to nanosecond pulses, as for the latter, heat absorption and dissipation to the surroundings happens simultaneously[63,70,76]. As a consequence, more uncontrolled melting, fragmentation and the formation of particles with unusual shapes have been observed for nanosecond pulsed laser[70,76,80]. Next to the pulse width, the repetition rate plays an important role as well. High repetition rates may lead to heat accumulation preventing the cooling down of the nanoparticle between two consecutive pulses[63]. Additionally, the presence of coatings can significantly influence the nanoparticles' stability upon laser pulses illumination. Recent studies revealed that rigid coatings such as silica can drastically increase the photothermal stability of gold nanorods[68,71]. For example, cetyltrimethylammonium bromide (CTAB) was shown to act as a thermal barrier above the critical micelle concentration leading to nonhomogeneous reshaping of gold nanorods whereas uniform reshaping was observed for femtosecond laser pulses around the critical micelle concentration[75].

1.2.4 Applications

One of the most popular usages of gold nanoparticles is in the field of biomedicine, for image diagnosis and cancer therapy treatments due to their unique plasmonic properties[18,20,21,36]. To enable the use of nanoparticles in the field of biomedicine, a few requirements exist: the nanoparticles cannot be detected by the immune system, the nano-systems needs to recognize the target cells and it has to be properly eliminated from the body after completing the objective. Moreover, the toxicity of the nanoparticles to the living tissue needs to be taken into account[81–83]. All of this can be accomplished by modifying the surface, shape and size of gold nanoparticles[81,82].

More specifically, the cancer treatment can be achieved through several approaches and among them the hyperthermal treatment and targeted drug delivery[21,84]. In the former case, the nanoparticles are stimulated with an external electromagnetic field at the plasmon resonance frequency after attachment with targeted cells, resulting in temperature increase of the nanoparticles,

as illustrated in Figure 1.6. As the cells are very sensitive to increasing temperature and die above 42°C[18,20,21,36], if sufficient accumulation of nanoparticles is present at the target cancer cell, the death of those cells will be induced by photothermal stimulation of the metallic nanoparticles. However, this technique is restricted only to cancer cells that are localized close to the surface of the body, as tissues and organs can absorb most of the energy from the laser before reaching the nanoparticles attached to deeper cancer cells[36].

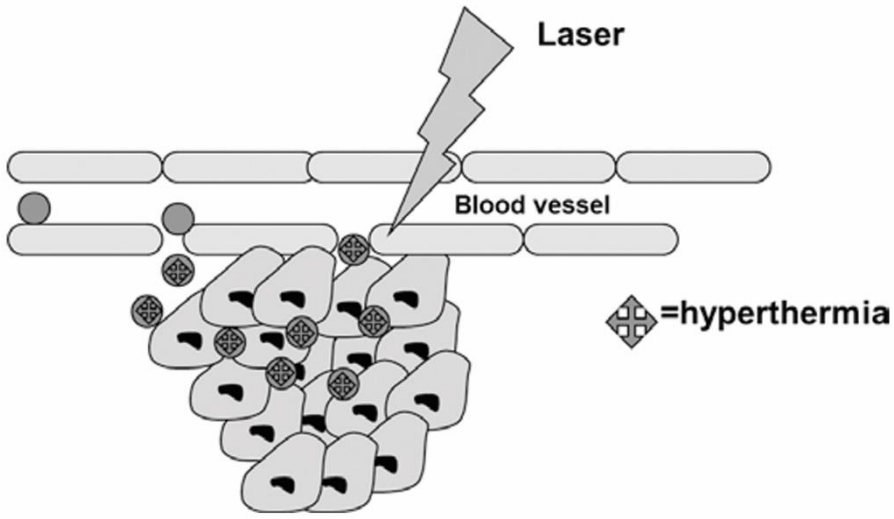

Figure 1.6 – Treatment of cancer cells by hyperthermia using gold nanoparticles. Functionalized nanoparticles with specific binding for the cancer cells are injected in the body. Laser illumination of the particles induces the production of heat that is sufficient to induce death of the surrounding cells. Figure adapted from [36].

Another very promising field of application of gold nanoparticles is in data storage. Here, gold nanorods with different aspect-ratio are deposited in a layer with a disk shape, with arbitrary orientations[16,17]. Femtosecond laser pulses irradiation promote the shape transformation into spheres for the nanorods with the same orientation as the polarization of the laser[68,75,79]. Moreover, the frequency of the incident laser will correspond to the LSPR frequency of nanorods with specific aspect-ratio. In this manner, the information can be stored through the use of different excitation wavelengths, corresponding to the LSPR frequency of specific nanorods and resulting the in shape transformation of those. Just a few example of the capabilities of nanomaterials in the development of new technologies were mentioned in the present section to illustrate their potential in innovative solutions.

Last but not least, the use of plasmonic nanoparticles have attracted a lot of attention in the past decades in the field of Raman spectroscopy [41,49,56,57,77,85–88]. To determine the vibrational modes of

molecules and obtain their structure fingerprint, Raman spectroscopy is largely applied. However, the signal obtained for this spectroscopic technique is very low[86]. To enhance the detection of Raman signals, the molecules under investigation are placed near the surface of plasmonic nanoparticles[86,89]. The interaction of the Raman effect with the plasmonic properties leads to a great enhancement of the Raman intensity[86]. By characterizing the resonant plasmon modes of functionalized metallic nanostructures, a red-shift of the resonant modes is observed due to the increase of the refractive index of the surrounding region of the nanoparticle[89]. This measured shift is later on used to identify the molecule and to obtain further information regarding their structure. The use of plasmonic nanoparticles as antennas for Raman spectroscopy of molecules is known as surface enhanced Raman spectroscopy (SERS) [41,49,56,57,77,85–88]. Besides, the use of nanoparticle assemblies is largely explored in this area, due to the further field enhancement associated with the creation of hot spots[57,86,88].

1.3 Physical properties and applications of metal halide perovskite nanoparticles

During the past years, increasing attention has been given to metal halide perovskite due to their potential application in photovoltaics and optoelectronics[90–95]. In this section, the main physical properties of metal halide perovskite nanostructures are briefly discussed, followed by a description of different applications. Due to the sensitivity of this materials to the electron beam[96], advanced electron microscopy techniques for the characterisation of the atomic structure will be discussed in Chapter 7.

1.3.1 Crystal structure

By definition, a perovskite crystal corresponds to compounds that have ABX_3 stoichiometry (Figure 1.7). For inorganic metal halide perovskites, the symbol A represents a monovalent inorganic metal cation (Cs^+ or Rb^+), the symbol B denotes a bivalent metal cation (e.g., Pb^{2+}, Sn^{2+}, Ge^{2+}, Cu^{2+}, Eu^{2+} and Ni^{2+}) and the symbol X designates one or mixed halide anions (Cl^-, Br^- and I^-).

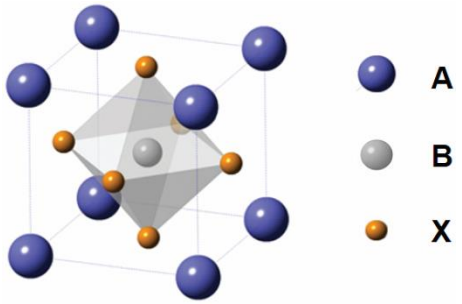

Figure 1.7 – Typical ABX_3 perovskite crystal structure. Figure extracted from [95].

The stability of perovskite structures are predicted by the Goldschmidt tolerance factor, which takes into account the effective ionic radii of the A, B, C ions[90–93]. In general, the metal halide perovskite structure have a tendency to be in a orthorhombic or tetragonal phase at room temperature, whereas the cubic phase is more likely for increasing temperature conditions[90–93]. During synthesis, the structure of metal halide perovskite nanoparticles can be either in a bulk shape or in a nanostructure format, such as nanoplateles, nanosheets, nanowires and quantum dots[90].

Perovskite structures are mostly held by ionic bonding[90,93]. As a consequence of their predominant ionic lattice and band structure, perovskite structures have shown a high defect tolerance[90–93].Defect tolerance is defined as the ability to retain the electronic properties of the structure even in the presence of defects. The introduction of defects in the crystal lattice promotes ionization levels within the material bandgap[97], which results in the trapping of charge carriers[92,97]. In this manner, non-radiative processes that convert electronic energy into thermal energy are not predominant, maintaining the optoelectronic properties similar to defect free structures[90–92]. More interestingly, the ionic property of the lattice protects the charge carriers from trapping and scattering[93]. Besides, interstitial and antisite defects, which form deep trap states, are almost absent since the ions in the lattice are energetically difficult to misplace[93]. Due to such high tolerance, perovskite structures might exhibit a high semiconductor performance, even at a large concentration of defects[90]. However, in some cases, defects can have an impact on the optoelectronic properties of metal halide perovskites[92,97]. For instance, recent studies have shown that the presence of Bi impurities in lead halide perovskites lead to a reduced electroluminescence yield and reduced charge carrier lifetimes[98].

1.3.2 Optoelectronic properties

Metal halide perovskite nanoparticles have shown high optical emission and absorption[90–92], due to their unique density of states configuration[90,92]. For instance, it has been shown that the optical emission and absorption wavelengths of $CsPbX_3$ can be tuned over the complete visible spectrum by changing the chemical element at the position X ($\lambda_{emission} = 410\ nm\ for\ X = Cl,\ \lambda_{emission} = 512\ nm\ for\ X = Br, \lambda_{emission} = 685\ nm\ for\ X = I$) or by using a mixture of halide elements[90,91,99]. Moreover, a dependency of the emission and absorption wavelengths were find for varying sizes due to quantum confinement effects[91,99]. Alternatively, the emission wavelength can also be tuned by selecting specific dopants to the structure of dopants[90]. For instance, doping $CsPbCl_3$ nanocubes with lanthanide atoms resulted in the shift of the emission wavelength from $\lambda_{emission} = 400\ nm$ to $\lambda_{emission} = 1000\ nm$[90,100]. Besides, metal halide perovskites display a high monochromaticity, as a

narrower full width at half maximum (FWHM) of the emission spectra (12-42 nm[90,99]) has been observed, in comparison to traditional quantum dots (CdSe, CdS and PbS)[91].

Metal halide perovskites also exhibits a high photoluminescence quantum yield, higher than 90% for organic-inorganic hybrid and all-inorganic structures[91]. Such high yield can be attributed to the large specific surface area of the nanostructures and the large exciton binding energy mechanisms[91]. Excitons corresponds to a bound state of an electron-hole pair state due to Coulomb attraction, where the exciton binding energy is the force between the electron-hole pair. Theoretical studies[91] have shown that exciton binding energy of $CsPbBr_3$ and $CsPbCl_3$ are greater than the thermal energy at room temperature. As a result, $CsPbBr_3$ and $CsPbCl_3$ structures are optically more favourable[91]. Moreover, defect tolerance and the high monochromaticity also contributes for a high photoluminescence quantum yield[91].

1.3.3 Applications

Because of the adjustable band gap, narrow linewidth of the energy spectrum, photoluminescence effect and the broad absorption range, metal halide perovskite nanocrystals have been shown potential applications in different fields[90–95]. For instance, light-emitting diodes (LEDs) have been coated with perovskite nanoparticles. The narrow linewidth of the emitted peak of perovskite nanocrystals is responsible for the observed high colour purity[91]. For this reason, perovskite nanocrystals are widely used in the backlight source of display devices with high colour saturation[91].

Additionally, the observed high carrier mobility, long carrier diffusion length, high optical absorption, high photoluminescence quantum yield and excellent defect tolerance of metal halide perovskites open new possibilities in the fields of solar cells[91–93,101] and photodetectors[91,102].

To further improve the performance of metal halide perovskites and eventually enable the optimization of synthesis protocols and the design of new applications, a thorough characterization of the structure is required. For instance, the characterization through electron microscopy combined with optical measurements enables researchers to verify the synthesized products and consequently assist in the enhancement of synthesis protocols. Moreover, the use of more advanced techniques of electron microscopy (e.g., electron tomography at the atomic level) combined with optoelectronic characterization methodologies allows researchers to establish connections between the crystallinity of metal halide perovskites with their physical properties, enabling a better comprehension on the defect tolerance for example.

1.4 The need of advanced electron tomography for the 3D characterisation of real nanomaterials

Because images obtained with (S)TEM only correspond to a 2D projection of a 3D object, the interpretation of the morphology based on those images can be misleading, as illustrated in Figure 1.8. However, the 3D information about the structure and shape is important to understand their physical properties (optical properties and catalytic activity, e.g.)[103,104]. The morphology of nanomaterials can be investigated by electron tomography, a technique capable of retrieving the 3D structure of an object from different 2D projection images[103,105,106]. Differently from the medical computerized axial tomography (CAT-scan imaging) where the x-ray source and the detector rotate around the patient, the object under investigation is tilted inside the electron microscope. Next, the so-called tilt series can be combined by using a mathematical algorithm and the 3D structure can be recovered. Besides the characterisation of the morphology and 3D structure of nanomaterials, electron tomography, in combination with spectroscopic techniques[107–109], enables one to characterise the 3D chemical distribution. Other possibilities involve the use of multimodal tomography[110] to investigate the presence of defects at the nanoscale. Moreover, the 3D atomic structure can be revealed by using high-resolution STEM images combined with some prior information about the object under investigation (position of the atoms, sparsity of the reconstruction, shape of the structure or the shape of the atoms) as input for the 3D reconstruction[111–113].

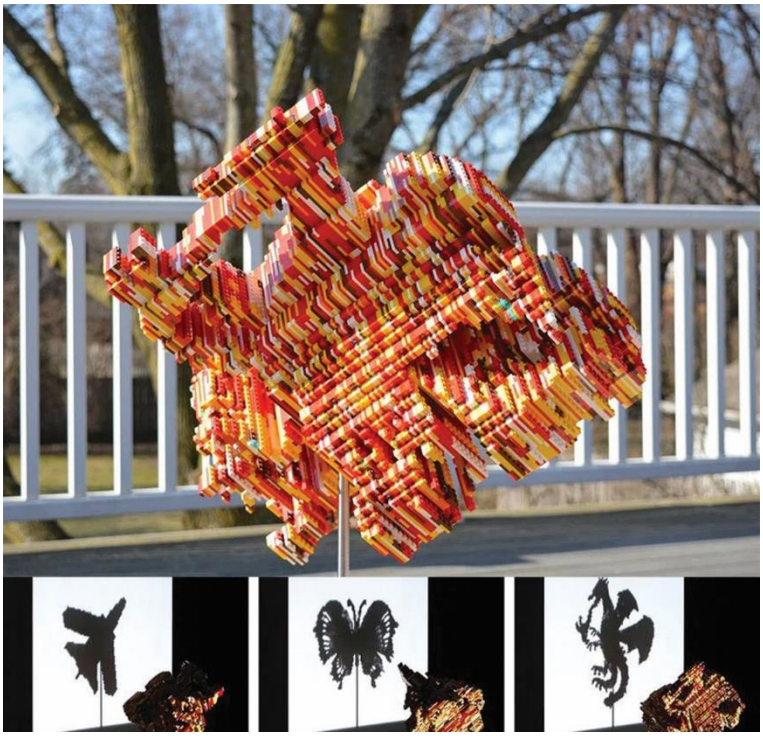

Figure 1.8 – Lego shadow sculpture by John Muntean[114]. By illuminating the sculpture along different orientations different shadow images could be created, such as airplane, butterfly and dragon, although the sculpture does not possess the shape of any of the shadows in particular.

Because techniques based on electron tomography were initially developed for the characterisation of simpler structures (e.g., model-like materials like mono-crystalline nanospheres and nanorods), the 3D investigation of more complex materials is not straightforward. For example, the recovery of the 3D atomic structure of very beam sensitive structures is still very challenging, as the atomic lattice is modified during electron beam illumination[115]. This is also a valid concern during the characterisation of nanostructures that contain a soft compound such as self-assemblies of nanoparticles encapsulated by a polymer shell. Additionally, structural modifications related to the drying process when drop casting the colloidal solution on a TEM grid may occur. This effect has been observed for clusters encapsulated with a soft shell and will hinder a quantitative interpretation. For complex nanostructures that contain defects, a 3D characterisation is also far from straightforward, especially at the atomic scale. Indeed, atomic resolution tomography is often based on the use of prior information [111–113], which may not be available for such complex structures. Finally, although electron tomography, at the nano or atomic level, provides very useful knowledge, it is restrained to room temperature and ultrahigh vacuum conditions inside the electron microscope. As most of nanomaterials will be used at specific conditions (e.g. temperature, pressure and chemical environment), it is essential to mimic those conditions during TEM investigations. Thus, new

approaches to investigate complex materials are required to overcome the limitations of model-like structures. During my PhD research, advanced techniques for electron tomography at the nanoscale and at the atomic scale were employed for the characterisation of defects in metallic nanoparticles as well as the investigation of beam sensitive nanostructures, such as metal halide perovskite nanostructures and soft-hard composites. The aim of the present thesis is to establish a better connection between the structure and the physical properties of different nanostructures and eventually contribute in the optimization of synthesis protocols and in the design of new and existing applications.

Chapter 2. Foundations of electron tomography and associated techniques

2.1 Introduction to electron microscopy

A thorough understanding of the physical properties of nanomaterials strongly depends on an accurate characterisation of the particle size, morphology, chemical composition and atomic structure[4–9]. Such knowledge is crucial for the optimization of the synthesis process to deliver products with desired properties[116] and may even guide the design of new applications. However, nanomaterials are not visible to the naked eye or conventional light microscopes, because of a lack of spatial resolution. Indeed, the resolution of a light microscopes is approximately 0.22 μm for the best available objective lenses[117].

In 1927, Davisson and Germer showed that electrons emitted from a heated filament and accelerated trough a potential difference of 50 V produced images of the diffraction pattern of a metallic object, confirming the duality behaviour of electron as proposed by de Broglie[118]. In this case, the electron wavelength was $\lambda_{electron}$ = 0.17 nm, which is comparable with the lattice parameters of crystalline objects. Around the same time, Ernst Ruska and Max Knoll started working in the development of a cathode-ray oscillograph[119]. For the next years, they worked in the development of magnetic lenses to focus the electron beam emitted from the cathode-ray. This work resulted in the development of a new instrument, the transmission electron microscope, capable of producing images of metallic arrangements with magnifications of 14.4x at that time. By accelerating the electrons through a potential difference of 75 kV, a resolution of 0.22 nm was expected. However, this resolution was not achieved due to the insufficient magnification to observe such small features and the presence of aberrations from the electromagnetic lenses. Besides, the first commercial electron microscope was produced by E. Ruska at Siemens in 1938. Followed by the progress with the TEM, Manfred von Ardenne, also at Siemens, developed the first STEM in 1938 by adding scanning coils to the instrument[118]. After the development of a of ultra-high vacuum (UHV) and the field-emission gun (FEG), the first dedicated STEM was constructed by Albert Victor Crewe and co-workers in 1970, equipped with an annular-dark field (ADF) detector[118,120,121]. Such instrument enabled the acquisition of chemical and morphological information simultaneously at high-resolution. Further progress in the development of the lenses, the detectors, the electron sources and the high-tension supplies enabled the visualization of objects (biological and crystalline materials) at the atomic scale with both TEM and STEM. Nowadays, after the invention of aberration correctors achieved in 1998[122], (S)TEM instruments are capable to achieve a resolution limit of 0.05 nm at an accelerating voltage of 300 kV[123].

2.2 Electron tomography

Although electron microscopy is a very powerful technique for the characterisation of nanostructures, it only provides 2D projected information of a 3D object. Clearly, the interpretation of the morphology of nanomaterials based on a single projection image might be misleading, as shown in Chapter 1. More specifically, the HAADF-STEM image of the gold nanoparticle in Figure 2.1.a might suggest a morphology corresponding to a nanostar. However, the actual morphology obtained by electron tomography corresponds to a truncated nanocube (Figure 2.1.b). The 3D information of the morphology of nanomaterials is vital to understand their physical properties (optical/photothermal properties and catalytic activity, e.g.), as highlighted in Chapter 1. Such 3D information can be obtained by electron tomography. This technique is capable of retrieving the morphology as well as the inner structure of an object from different 2D projection images using a mathematical algorithm.

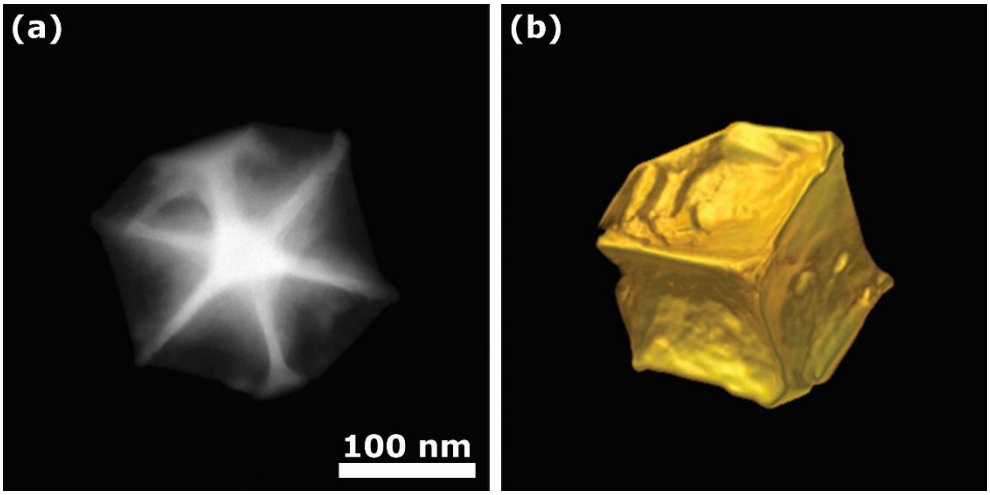

Figure 2.1 – (a) HAADF-STEM image of a gold nanoparticle. This 2D image suggests that the morphology corresponds to a nanostar. (b) Real morphology of the same nanoparticle shown in (a), obtained by electron tomography. It is clear that the morphology corresponds to a truncated nanocube. Image courtesy Prof. Dr. Thomas Altantzis.

2.2.1 Basic theory of electron tomography

In 1917, Radon developed a mathematical theory that relates how an object can be constructed from a series of projections[124]. More specifically, this theory states that a projection $p_\theta(r)$ of an object $f(x, y)$ in real space D, along a direction that is inclined with respect to the reference axis (x, y) by an angle θ, can be described by the Radon transform R (Figure 2.2). This transform is defined as the sampling of the object by line integrals through all possible lines L

$$p_\theta(r) = Rf = \int_L f(x,y)ds \tag{2.1}$$

where ds is the unit of length of L. Alternatively, the object $f(x,y)$ can be retrieved by applying the inverse Radon transform of a series of different projections $p_\theta(r)$. This concept constitutes the basic principle of a tomographic reconstruction. Due to the definition of the Radon transform, it is expected that the intensity of the projection images is a monotonic function of a physical quantity to be reconstructed. This is known as the projection requirement of tomography.

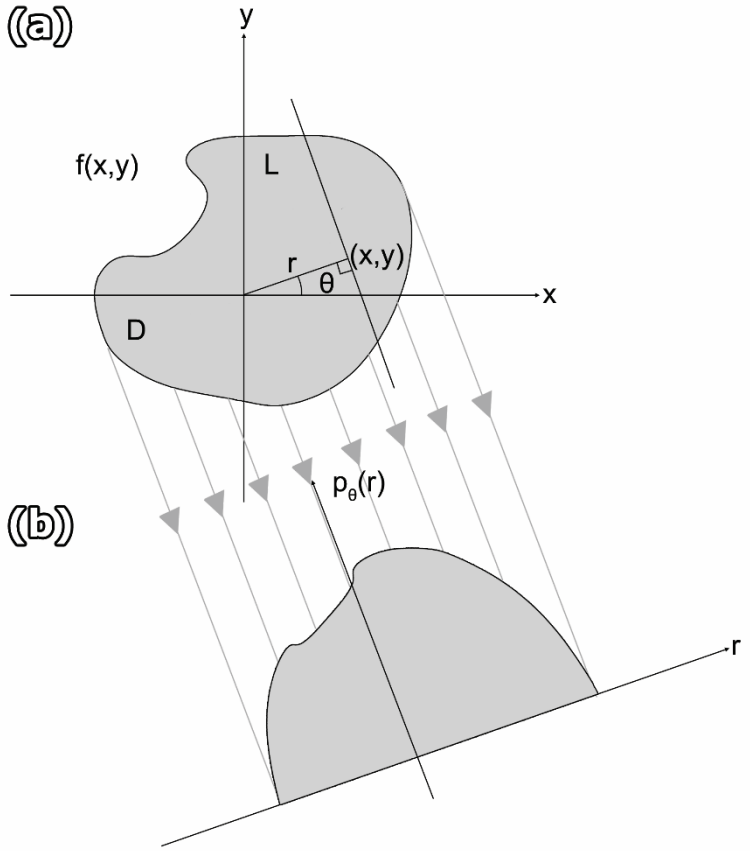

Figure 2.2 – (a) Object $f(x,y)$ represented in real space D. The projection $p_\theta(r)$ of such object can be obtained through the sampling of the object by solving line integrals of all possible lines L (b). The orientation of the projection of the function $f(x,y)$ is represented by the grey lines with arrows. By combining all the possible projections along different angles θ, the object $f(x,y)$ can be fully recovered.

The Radon operator R transforms the coordinate system of the object, in real space, to the Radon space (l,θ), where l is the direction perpendicular to the transform direction (projection direction) and equals to $l = r\cos\theta$, z is parallel to the transform direction ($z = r\sin\theta$) and θ is the projection angle (Figure 2.3.a). For a simpler mathematically description, it is convenient to use polar

coordinates (r, ϕ) instead of the Cartesian coordinates for the representation in real space. The polar coordinates are defined as $r = \sqrt{x^2 + y^2}$ and $\phi = \tan^{-1}(y/x)$.

Figure 2.3 shows that a projection of the complete object in Radon space corresponds to a line with a sinusoidal shape. Therefore, the projections in Radon space is commonly named a sinogram. The complete sampling of the object is finally achieved by recording projections along all possible projections angles, as it is shown for the Shepp-Logan phantom in Figure 2.3.b, in real and Radon space, respectively.

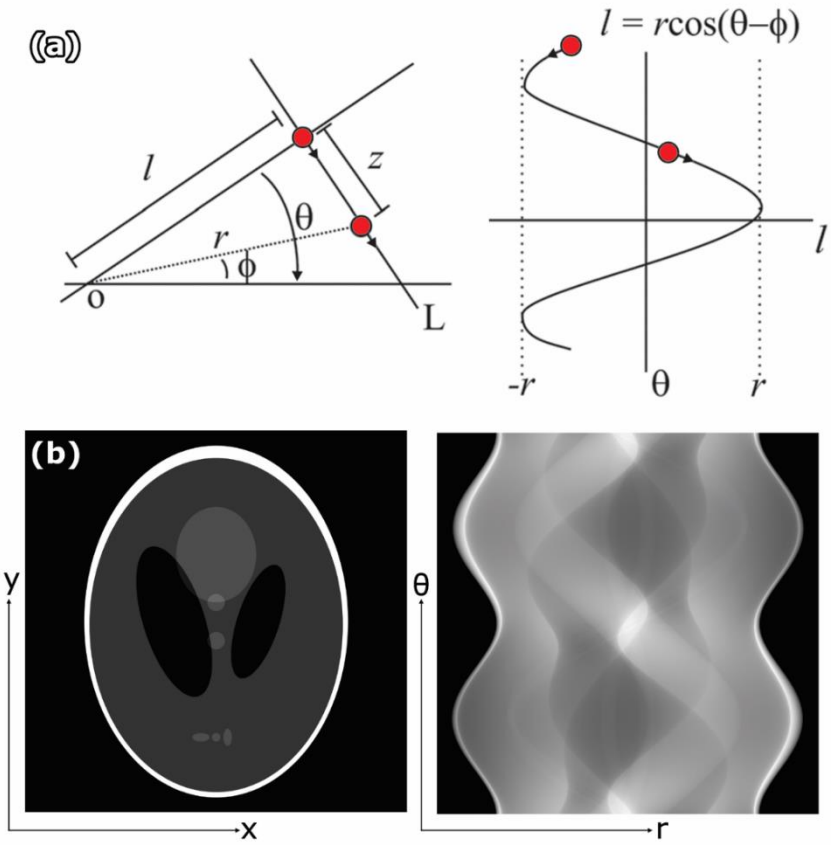

Figure 2.3 – Geometrical relationship between polar (r, ϕ) and Radon (l, θ) space. (a) The trajectory of the red circle on the right panel corresponds to the dislocation of the red circle of the left panel (Figure adapted from [125]). (b) Illustration of the same principle in (a) for the Shepp-Logan phantom[126].

2.2.2 Fourier slice theorem

Several methods for the recovery of the object $f(x, y)$ from its projections $p_\theta(r)$ based on the inverse Radon transform are available. The simplest technique is based on the Fourier slice theorem: a 1D projection of a 2D object at a given angle θ corresponds to a line in the Fourier representation of the same object, which goes through the origin with the same angle θ. When multiple projections $p_\theta(r)$ are available, multiple lines in a wide range of angles are present in Fourier space. The object

can be recovered by applying an inverse Fourier transform to the superposition of all projections in Fourier space. To prove this, the 2D Fourier transform of the object $f(x, y)$ is defined as

$$F(u, v) = \int_{-\infty}^{+\infty} \int_{-\infty}^{+\infty} f(x, y) e^{-2\pi i(ux+vy)} dx\, dy. \tag{2.2}$$

A slice of the object $P_\theta(u, v)$, in Fourier space, for a projection at $\theta = 0$ is then defined as

$$P_\theta(u, 0) = \int_{-\infty}^{+\infty} \int_{-\infty}^{+\infty} f(x, y)\, e^{-2\pi iux} dx\, dy$$

$$P_\theta(u, 0) = \int_{-\infty}^{+\infty} \left[\int_{-\infty}^{+\infty} f(x, y) dy \right] e^{-2\pi iux} dx \tag{2.3}$$

$$P_\theta(u, 0) = \int_{-\infty}^{+\infty} p_\theta(x) e^{-2\pi iux} dx$$

which corresponds to the Fourier transform of the projection $p_\theta(x)$, concluding the proof. Here, (u, v) is the coordinate system in the Fourier domain. The same analysis can be extrapolated for 2D imaging and the recovery of the 3D volume.

However, any combination of projections will result in an uneven sampling of the recovered object, where low frequencies are oversampled in comparison to higher frequencies, as illustrated in Figure 2.4. Such oversampling at low frequencies is responsible for the blurring effect on the recovered object, which will be discussed in more details in section 2.4.1.

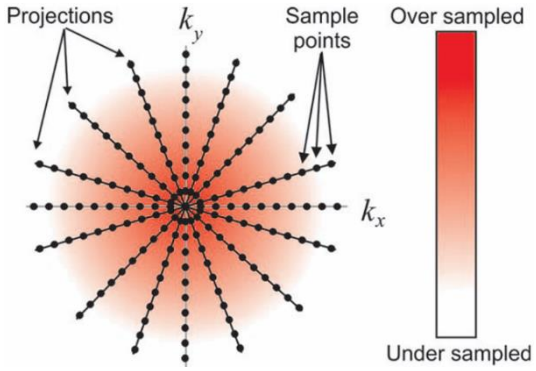

Figure 2.4 – Sampling density of the combination of projections in Fourier space. Regions in darker red correspond to oversampled areas. Figure extracted from [125].

2.3 Imaging modes for electron tomography

There are several imaging modes available in the electron microscope, as the optical system can be rearranged into different configurations setups and dedicated detectors can be used. In theory, all modes could be applied for electron tomography, as long as the projection requirement is fulfilled (section 2.2.1). This requirement states that the intensity in a projection image should be a monotonic function of a given physical property of the object under investigation, integrated along its thickness along the projection direction[103].

2.3.1 Bright Field TEM imaging

In bright field TEM mode, a parallel electron beam interacts with the specimen. The technique consists of the detection of only the non-scattered wave from the specimen. This mode can be achieved by inserting the objective aperture in the back focal plane of the objective lens and selecting only the direct beam of the diffraction pattern. In this manner, only the non-scattered electron wave that propagates through the TEM column will reach the detection medium. Images recorded under this condition typically display a bright intensity for regions where the electron beam does not scatter. By increasing the thickness of the specimen, the density of transmitted electrons decreases, resulting in the presence of darker grey levels in BF images.

BF-TEM is often used in electron tomography for biological investigations, where the specimen consists of mostly amorphous structures containing low mass chemical elements in majority (weakly scattering object) and, consequently, diffraction contrast is practically absent from the images. Therefore, the intensity of the image will be dominated by the mass-thickness contrast. However, in the material science field, the specimens under investigation are mainly crystalline objects and thus, diffraction contrast will be present and the projection requirement will no longer be valid.

2.3.2 Phase contrast (HRTEM) imaging

Phase contrast is responsible for the interference fringes in high-resolution TEM (HRTEM) images, which are produced when the electron beam is diffracted by the specimen along different crystallographic orientations. The nomenclature given to this image mode stems for the interference pattern formed in the image plane, resulting from the interaction of the scattered waves. This type of images contains information regarding the position of the atoms in the crystal lattice and are sensitive to many parameters, such as the crystal orientation of the specimen with respect to the incident electron beam, thickness of the specimen, thermal instabilities of the specimen and the presence of aberrations in the electromagnetic lenses. Due to this complexity, the quantification of the position of

the atomic columns is mostly far from straightforward and requires comparison with HRTEM image simulations. Besides, only intensities of the emitted electrons by the specimen are recorded and, consequently, the phase of the wave is lost. Because of the modification of the emitted wave from the specimen by the aberrations of the electromagnetic lenses in addition to the loss of the phase information, more advanced techniques are employed for the quantification and analysis of HRTEM images, such as exit wave reconstruction (EWR). This technique enables the deconvolution of the information from the specimen and the parameters of the microscope, enabling a direct interpretation and the recovery of the full emitted wave from the specimen (amplitude and phase). More details and the use for electron tomography will be given in Chapter 7. Moreover, aberration correctors are capable to further decrease the presence of the main aberrations by a factor of 10^3, greatly improving the resolution and interpretation of phase contrast images.

2.3.3 STEM imaging

Differently from the TEM mode, a focused electron beam interacts with the specimen in STEM mode. The image is obtained after the beam is scanned across the region of interest. To record scattered electrons with different angular directions, dedicated detectors can be used, as illustrated in Figure 2.5. Typical values of the acceptance angles of each type of detector are: (a) 50-190 mrad for high-angle annular dark field (HAADF) detectors, (b) 10-50 mrad for ADF detectors and (c) 0-10 mrad for BF detectors[127]. Because the HAADF detector only records electrons scattered at large angles, the diffraction contrast is mostly eliminated and mainly the incoherent elastic scattered electrons are recorded. Thus, a contrast variation is observed for different specimen thicknesses, as well as by changing its chemical composition (due to Coulomb interaction, heavier atoms scatters the electron at higher angles when compared with lighter atoms). In summary, the mass-thickness contrast dominates in the image formation process of HAADF-STEM images. The acceptance angles of the detector can be modified by changing the camera length (distance from the specimen to the projected image) of the microscope and/or by using another detector with smaller radius and, therefore, smaller acceptance angles. For detectors with smaller acceptance angles or by the use of larger camera lengths, contrast variation due to diffraction scattering events is visible. In addition, non-scattered electrons can be recorded in STEM mode with a BF detector.

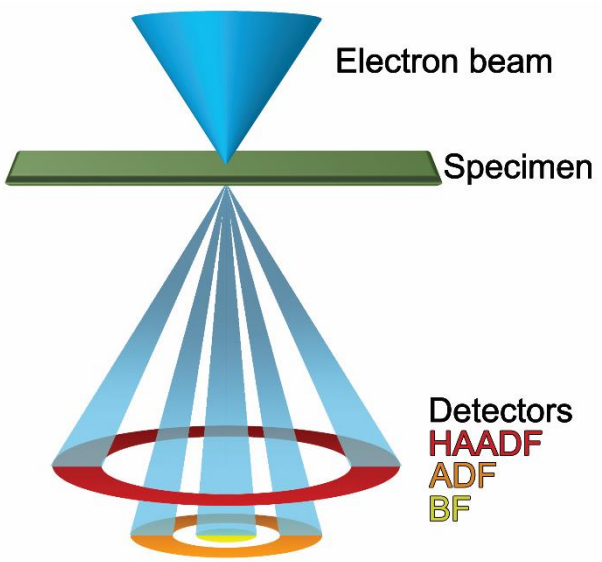

Figure 2.5 – Scheme illustrating the electron scattering by the specimen and detection geometry. A focused electron beam scans across the region of interest in the specimen and the transmitted electrons with different scattering angles can be recorded using different detectors.

For sufficiently thin specimens, HAADF-STEM imaging provides an approximately linear relationship between the image intensity and the mass/thickness of the specimen (for thicker specimens this statement is no longer valid due to absorption effects from multiple scattering events)[128]. For gold, the optimal thickness limit is approximately 20 nm. Nevertheless, gold nanoparticles with sizes larger than 20 nm can still be investigated with electron tomography. However, for thickness much larger than this limit (few hundreds of nanometres) the deviation from the linear behaviour of the intensity is more evident. Consequently, artefacts in the reconstruction of very large gold nanoparticles might arise, due to the violation of the projection requirement[103]. Because of the linearity of the image intensity with the information contained in the scattered electrons, HAADF-STEM imaging is the most preferred image mode for the characterisation of the morphology of crystalline objects by electron tomography. Additionally, images in the middle-angle annular dark field (MAADF), low-angle annular dark field (LAADF) and BF-STEM images can be used for electron tomography, although the quantification of the reconstructed 3D volume is not completely accurate[110] (Chapter 3).

2.3.4 Energy dispersive x-ray (EDX) spectroscopy

Typically, the information of the chemical composition of specimens can be obtained from HAADF-STEM imaging, when the difference of the atomic masses of the chemical species are sufficiently large to be visualized on a single image. However, when the chemical elements have very similar atomic masses, spectroscopic methods are required to properly characterize the chemical

nature of the specimen. Such information can therefore be retrieved from the combination of energy dispersive x-ray spectroscopy and electron microscopy[107,109,129]. To retrieve the chemical information of the investigated specimen, STEM is often used. To record the x-ray signal emitted after inelastic scattering events, semiconductor based detectors are employed. Upon interaction between the emitted x-rays and the detector, electron-hole pairs are created and, subsequently, translated by the detector as charge pulses. As the x-ray energies are well above 1 keV, several electron-hole pairs are generated and the quantity is directly proportional to the energy of the detected x-ray. Conventionally, microscopes are equipped with one silicon-drift detector and the collection efficiency is very poor, where only 1% of all x-rays are detected. To overcome this limitation, a Super-X detector can be used. The detector consists of four detectors as illustrated in Figure 2.6.a[130]. One of the main advantages of this setup is the possibility of an efficient acquisition of spectral maps, where each pixel from the region of interest will have an energy spectrum assigned to it (Figure 2.6.b). This spectrum can be fitted along the complete region of interest, resulting in a 2D chemical map of the region of interest, as illustrated in Figure 2.6.c for an iron-cobalt nanodumbbell. Moreover, to obtain results with statistical relevance, several scans over the region of interest are required to enable a higher signal-to-noise ratio.

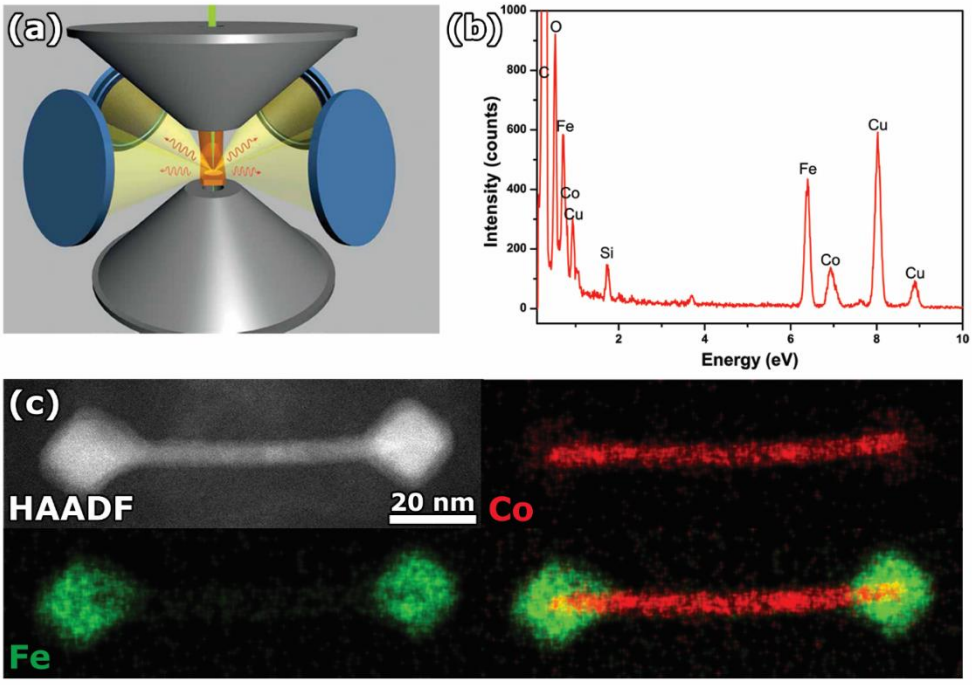

Figure 2.6 – (a) Design of the Super-X detector (blue) for the detection of x-rays emitted by the specimen (orange). (b) Typical spectrum obtained by EDX spectroscopy of an iron/cobalt nanodumbbell. (c) HAADF-STEM image and 2D chemical maps (iron, cobalt and the superposition of both) of the same nanodumbbells investigated in (b).

To quantify the chemical composition of the spectral map of a given element present in the specimen, different methods for the quantification of the energy spectrum can be applied, such as the Cliff-Lorimer ratio technique[120,131,132] and the ζ-factor[133]. Recent studies in our laboratory have demonstrated that a technique based on the combination of the ζ-factor methodology with 3D characterisation of nanomaterials provides more accurate quantification of spectral maps in comparison to the Cliff-Lorimer ratio[134].

The EDX spectroscopic technique can be extended to three-dimensions, since the x-ray detection is proportional to the volume of the chemical element in the specimen and therefore the projection requirement is fulfilled[135]. Typically, EDX maps are only acquired for a few projections, due to the long exposure time needed for an acquisition of a spectral map and, in this manner, prevent structural modifications from radiation damage. Generally, a tomographic series based on the HAADF-STEM mode is acquired over the full tilt range and combined with the spectroscopic data during the tomographic reconstruction[107,109].

2.3.5 Electron energy loss spectroscopy (EELS)

Because the energy resolution obtained with EDX detectors is very limited and due to the presence of a high signal-to-noise ratio, alternative methods are required to analyse scattered electrons with smaller energy losses. Therefore, the energy loss of the inelastic scattered electrons by the specimen associated with core excitation can be directly measured by electron energy loss spectroscopy (EELS). Prior to reaching the final detectors, the electrons are first dispersed by a magnetic prism (Figure 2.7.a). Electrons with lower energies than the primary beam move slower through the magnetic field and are bent upwards, resulting in the dispersion of electrons with different energy losses. A slit is placed after the magnetic prism and only the electrons with a specific energy range will be recorded. Subsequently, the energy dispersion is magnified by post prism electromagnetic lenses. Differently from EDX spectroscopy, the detector used in EELS is a serial detector. Thus, the spectrum acquisition over the region of interest consists of a single acquisition. Similar to EDX spectroscopy, the energy spectrum formed at the dispersion plane is acquired pixel-by-pixel over the region of interest (Figure 2.7.b) and can be fitted to the same region, yielding a 2D chemical map of the specimen for core loss events, or the magnitude of the electric field distribution of the induced plasmon modes at the specimen. Moreover, the information regarding the non-scattered electrons through the specimen are contained in the zero loss peak, which is of great importance for the proper alignment of the EELS system and determination of the energy spread of the electron beam (which corresponds to the full width at high maximum- FWHM of the zero loss peak).

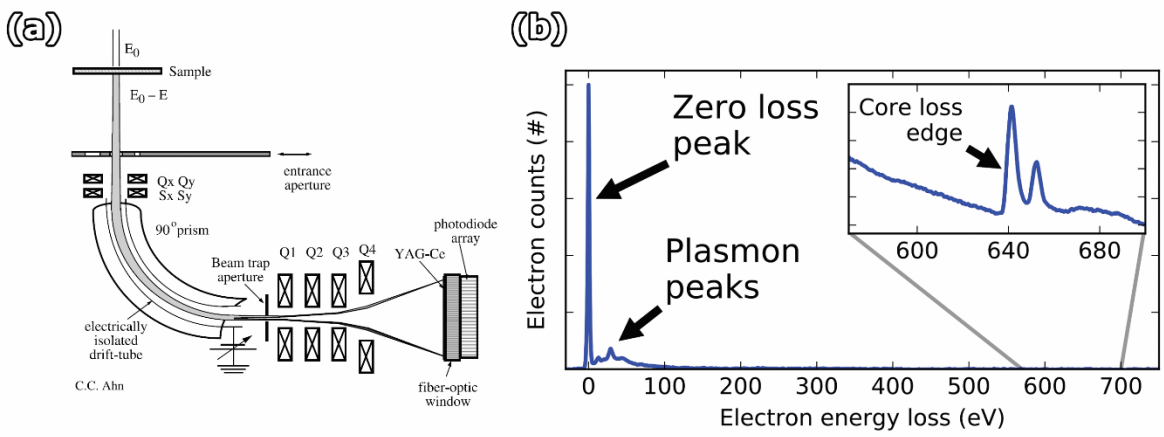

Figure 2.7 – (a) Setup of an energy loss electron spectrometer (Figure adapted from [136]). (b) Typical energy loss spectrum showing typical features, such as the zero loss peak corresponding to transmitted electrons through the specimen, the plasmon frequency and the chemical fingerprint of the material in the core loss edge. Image extracted from [137].

Since this methodology is very sensitive to small energy variation of the electrons, it is vital that the energy spread of the electrons from the gun system of the microscope is minimal. Thus, monochromators are largely employed for spectroscopic analysis based on EELS, as they can improve the energy resolution from 1 eV to 0.1 eV, for microscopes equipped with FEG's. The monochromator often consists of a Wien filter (for ThermoFisher microscopes), where electric and magnetic fields are created that induce competing forces on the passing electron beam. These fields are calibrated in a way that only electrons with a specific velocity will not be deflected. At the end of the monochromator, an aperture is placed to block the deflected electrons with different velocities.

EELS tomography is largely employed for the 3D characterisation of nanomaterials, since it allows the investigation of the chemical nature and the oxidation states of different specimens[108,138]. Again, the projection requirement for tomography is fulfilled[108,138], as the detection of electrons with a specific energy loss is proportional to the volume of a given chemical element. Although the projection requirement for a single projection of a plasmon map is fulfilled, the implementation of a tomographic experiment for the recovery of the 3D electric field distribution ($\left|\vec{E}_z\right|^2$) associated with a given plasmon mode is not straightforward. This stems to the fact that the coordinate system of the electric field is not rotated simultaneously with the coordinate system of the nanoparticle during the acquisition of a tomographic series[139–141].

2.4 Electron tomography in practice

2.4.1 Image acquisition and processing

Conventionally, a series of different projection images is acquired by discretely tilting the specimen inside the instrument, as illustrated in Figure 2.8. Due to the design of the instrument, the holder with the specimen can only rotate until a maximum angle θ to avoid a collision with the polepieces of the objective lens, as shown in Figure 2.9a. Moreover, the TEM holder, on which the grid containing the specimen is mounted, can also induce a shadowing effect as illustrated in Figure 2.9.b, reducing the number of projections that can be recorded even further.

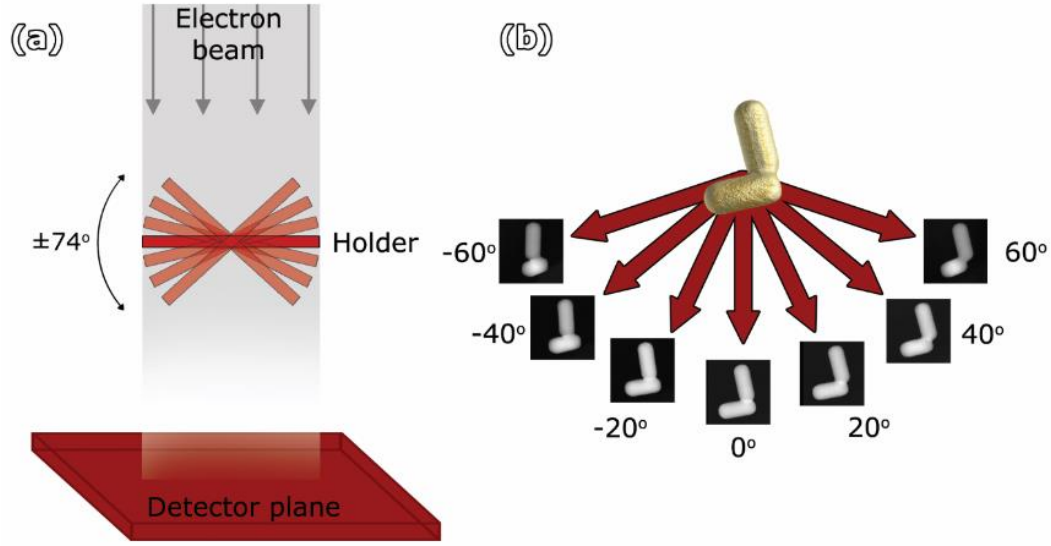

Figure 2.8 – (a) Geometry of the acquisition of series of projection images inside the microscope (single tilt acquisition scheme) and (b) obtained projection images of gold nanorods.

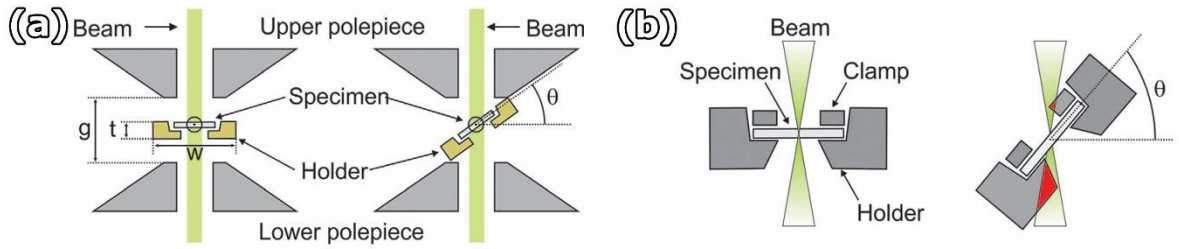

Figure 2.9 – (a) Geometry of the rotation angle limit of the holder in between the polepieces of the objective lens. (b) Geometry of the shadowing effect of the electron beam by the holder. Image adapted from [125].

The Fourier slice theorem showed that the resolution of the reconstruction is intrinsically connected to the number of projections available, as well as the angle range of the tomographic series.

Thus, the limitations on the angle range will impact the quality of the reconstructed object, introducing the so-called missing wedge artefacts (Figure 2.10). When in real space, the object will display elongations along the direction of the missing projections, as illustrated at the top row of Figure 2.10. A Fourier representation of the object revealed an incomplete sampling of the object, as illustrated in the bottom row of Figure 2.10. In order to minimize this effect, dedicated tomography holders with smaller dimensions have been developed, allowing a large tilt range for the acquisition (approximately from -76° to +76° depending on the exact electron microscope. Other possibilities involve the acquisition of a dual axis tomography series, to further minimize the presence of the missing wedge artefacts[142,143]. However, the reconstruction of such series is far from straightforward. Additionally, the use of a dedicated holder for pillar structures enables the acquisition of a tomographic series with a full tilt angle range (from -90° to +90°)[144].

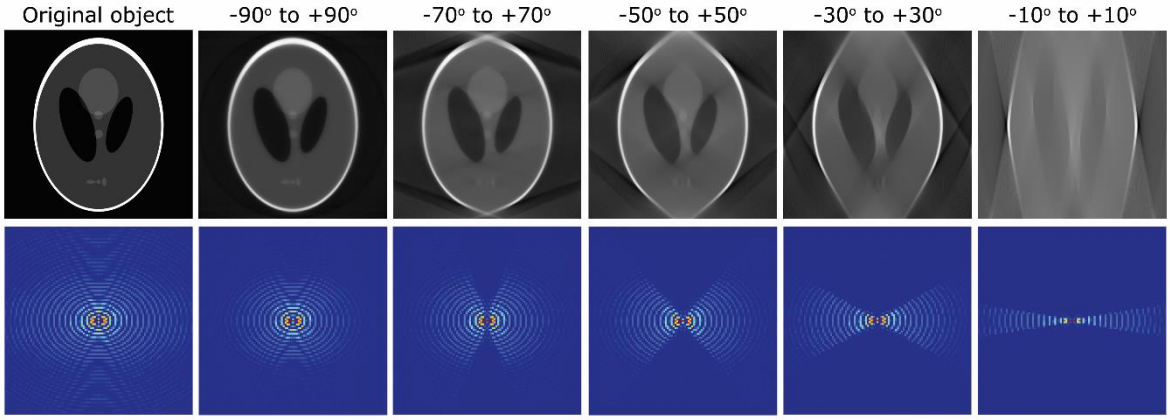

Figure 2.10 – Missing wedge artefact observed for different ranges of tilt angles of the Shepp-Logan phantom object, in real and Fourier space. The tilt step between each projection is 1°. For an enhanced visibility, the fast Fourier transform (FFT) is displayed for each case, where the missing wedge can clearly be seen.

Besides the tilt range, the tilt step between every projection is another key parameter of the resolution of the reconstructed object. For instance, Figure 2.11 shows reconstructions obtained with the same tilt range (from -90° to +90°) with different tilt steps. More specifically, undersampling starts at higher frequencies for smaller steps (e.g. 3° step) until it fills the complete frequency domain (10° step). Larger tilt steps result in a larger blurring of the reconstructed object in real space, hampering the visualization and quantification of small features in the reconstructed object. Analysis in the Fourier domain revealed the presence of undersampling for increasing tilt step. Conventionally, electron tomography series are acquired with a tilt step of 1-2°, as most of the information can still be recovered[145].

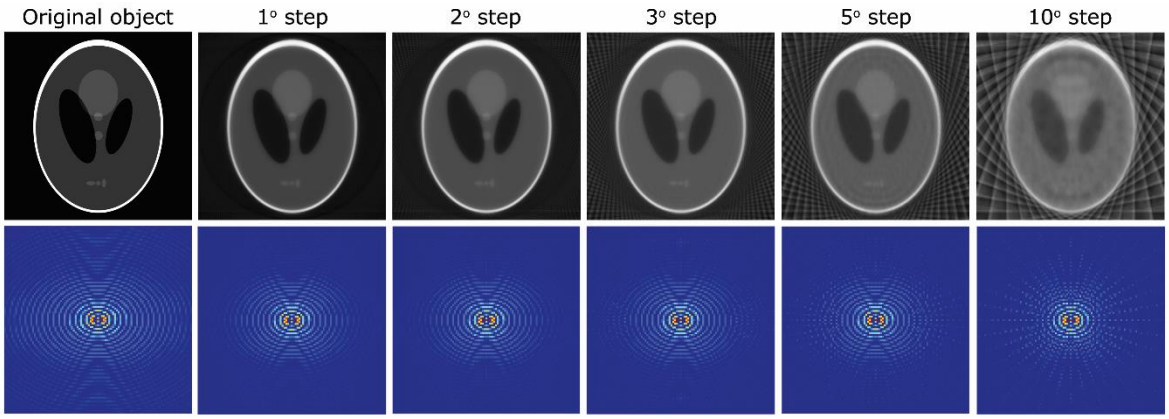

Figure 2.11 – Illustration of artefacts generated by undersampling when the tilt step increment is increased and the total number of projections is decreased. The tilt range was fixed for all cases, starting at -90° up to +90°. For increasing tilt step, an undersampling was observed in Fourier space.

Different acquisition schemes for electron tomography are available. The conventional methodology corresponds to a single image acquisition in HAADF-STEM mode for each projection angle (as described in the beginning of this section), with a typical dwell time in the range of 3 to 6 μs (frame acquisition of approximately 4 to 8s). The dwell time is defined at the period of time where the electron beam is stationary on the scan position[146]. The multiplication of the dwell time by the total number of pixels in the image results in the total time the specimen was irradiated by the electron beam. However, the frame time is often larger than the total time the specimen was illuminated, due to the synchronization effects of the electron beam[146].

Additionally, multiple frames can be acquired for each projection, where the acquisition time for each frame can be further reduced (as low as 1s, with dwell time of 0.4 μs). The alignment of all frames for a single projection followed by image summation allows the minimization of blurring effects in the image caused by a constant drift of the specimen during STEM investigations, which is critical for atomic resolution investigations.

A different approach for the acquisition of a tomographic series consists in the image recording of the object under investigation while the holder is continuously rotated[147], where hundreds of frames are acquired during the process. The rotation speed of the goniometer is chosen to ensure a good ratio between speed and image quality[147]. The total acquisition time for a tomographic series can be reduced from typically 1 hour to 6 minutes, when comparing conventional to fast acquisition schemes[147]. Typically, the acquisition time required for each frame in the tomographic series is relatively low (1s per frame). As a consequence of the reduced acquisition time, more tomographic series can be recorded in the period of 1 hour when using the fast acquisition scheme. Therefore, the

fast approach enables the acquisition of tomographic series of nanomaterials with higher throughput than conventional acquisition techniques.

One of the challenges of the acquisition of fast tomographic series consists in the tracking (x- and y-direction of the stage) and re-focusing (z-direction of the stage) of the nanoparticle during the acquisition, since a displacement of the particle always take place in the x-, y- and z-direction of the stage after tilting the goniometer. Differently from the conventional acquisition of a tomographic series in which the stage is manually re-centred in all directions prior to the acquisition of a new projection image, this process occurs simultaneously with the image acquisition in the fast tomography approach. For this reason, frames containing motion-blurring effects are often present in the tomographic series. However, those images containing the aforementioned artefacts only represents a fraction of the total number of projection images (50 images from a total of 360 frames)[147] and their removal from the series prior to the tomographic reconstruction does not affect the quality of the final result[147].

The next step to retrieve the 3D structure of the specimen under investigation is the image alignment. As already mentioned, during the acquisition of a tomographic series, the region of interest might be shifted by several nanometres after tilting the holder. Since the precision of modern goniometers is in the range of tens of nanometres, a residual shift between consecutive images in a tomographic series will always be present. By a manual re-centring of the stage or by using an automatic software for a series acquisition, the object can be brought to the field of view. Still, a residual shift of a few nanometres will be present between two projection images. Thus, to obtain an accurate 3D representation of the specimen, it is vital that the series of projection images is aligned and, if possible, with subpixel precision. Often a cross-correlation function is applied to measure the degree of similarity between two consecutive images, resulting in the determination of the shift difference between each image.

Next, the tilt axis needs to be adjusted in a specific manner prior to the tomographic reconstruction. To find the optimal tilt axis of the tomography series, a procedure involving the reconstruction of three slices along the object (at the top, middle and bottom) is applied, revealing the presence of arc artefacts on the reconstructed slices, as illustrated in Figure 2.12. For a misalignment of the position of the tilt axis, an arc is observed in all slices, pointing to the same direction (Figure 2.12.b). For a rotation of the tilt axis, only slices above and below the central slice show the presence of arc artefacts, pointing in opposite directions (Figure 2.12.c). Conventionally, the arc artefacts can be minimized during the data processing step by manually modifying the position

and inclination of the tilt axis. Finally, the series of aligned images can be used as input for the tomographic reconstruction.

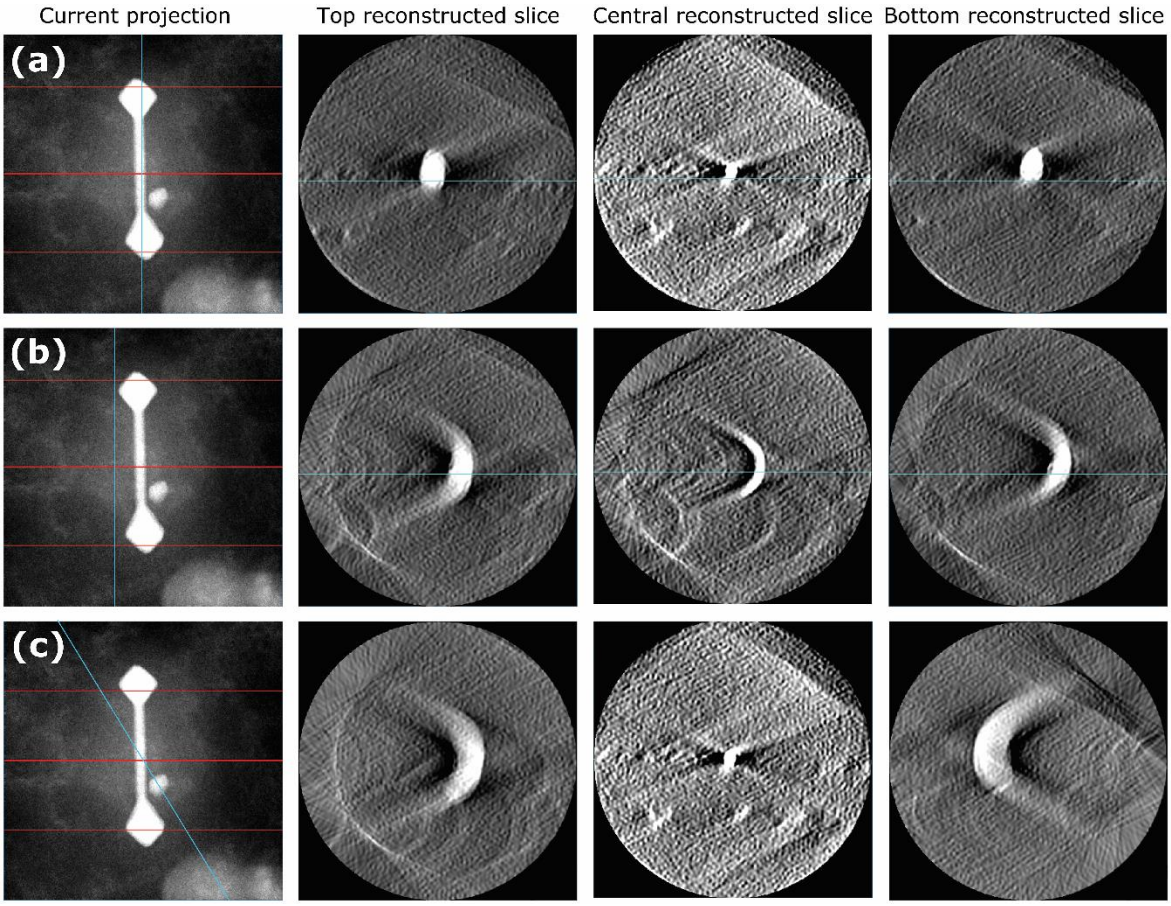

Figure 2.12 – Alignment of the tit axis of a tomographic series. The blue lines on the projection images represent the tilt axis, whereas the red lines indicate the location of the reconstructed slices. In (a), no artefacts are observed in the reconstructed slices due to the correct alignment of the tilt axis. In (b), a shift of the tilt axis results in the creation of arc artefacts in all reconstruction slices, always pointing to the same direction. In (c), an incorrect rotation of the tilt axis results in the formation of arc artefacts predominantly on the furthest slices from the central slice. In this case, the arc possesses an opposite direction for slices above the central slice in comparison to slices below than the central slice.

2.4.2 Reconstruction methods

Following the discussion of section 2.2.2: Fourier slice theorem, the tomographic reconstruction can also be performed in real space. A commonly used technique is the direct back-projection (BP) with a working principle similar to the Fourier slice theorem, but performed in real space. Again, the same limitation on the unevenness of the sampling is observed. The blurring caused by the uneven

sampling can be minimized by applying weighting filters, which will interpolate the missing sample points in the Fourier domain. This modified technique is known as weight back-projection (WBP) and it is largely employed for medical CAT reconstructions, where a set of projection images over all projection angles is available.

For cases where a large number of projection angles is not available, WBP yields reconstructions with poor quality due to insufficient sampling. To overcome such limitation, iterative methods are employed. A commonly used technique is the simultaneous iterative reconstruction technique (SIRT), which consists on the refinement of the reconstruction at each iteration by solving the minimization problem $\hat{x} = \ argmin_x \|A\boldsymbol{x} - \boldsymbol{b}\|_2^2$ ($\boldsymbol{x}$ is the vector that represents the reconstructed object, A is the projector operator and $\boldsymbol{b}$ is the vector that represents the projection images). The first iteration is obtained by applying the back projection method. Subsequently, images based on the first reconstructed volume are generated at the same projection angles and compared with the input images for the reconstruction. The relative error, or residual, between the input and the generated projection image is computed simultaneously for each tilt angle and applied to generate a new reconstructed volume. This procedure is repeated until convergence for the minimization of the residual is reached, as illustrated in Figure 2.13.

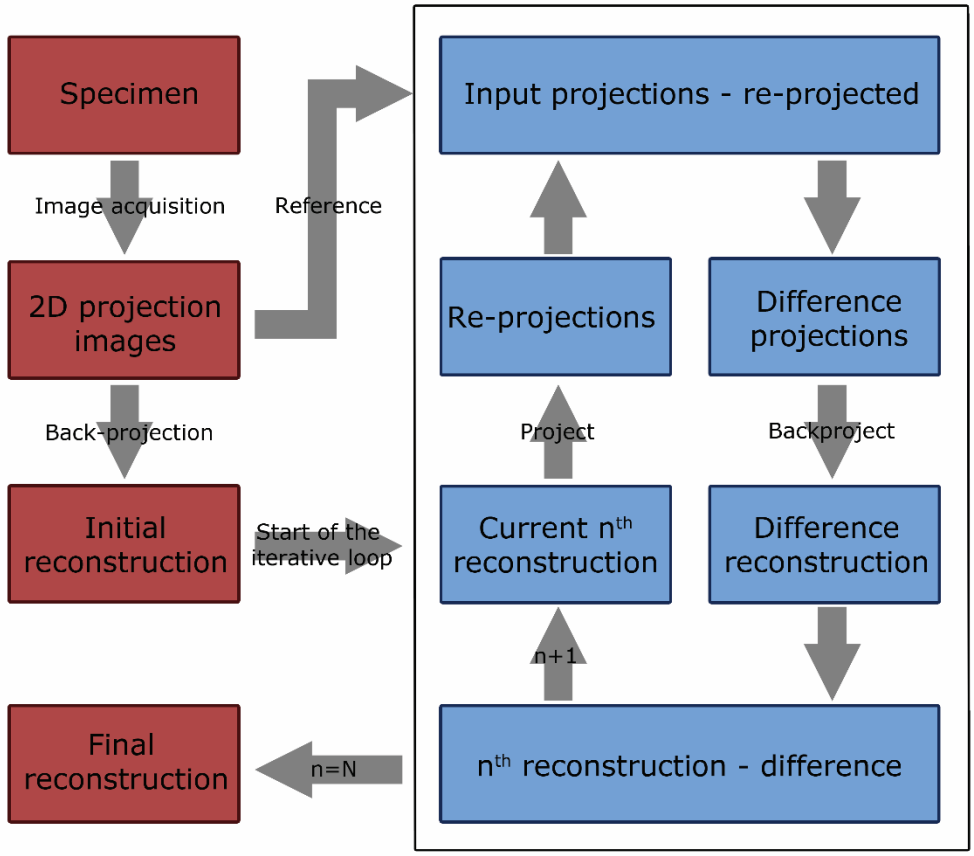

Figure 2.13 – Flowchart illustrating the iterative process (blue boxes) of the SIRT reconstruction technique.

2.4.3 3D visualization

The interpretation of the 3D reconstruction is crucial for the proper characterisation of the investigated object and it can be achieved by different means of visualization. The simplest approach is to display slices through the 3D reconstruction, as shown in Figure 2.14.a. This method reveals the distribution of intensities within the reconstruction, allowing the characterisation of not only the surface of the object, but also of its internal structure. Alternatively, the 3D morphology can be visualized through a 3D rendering based techniques that consists of the conversion of the data into visual display by the addition of texture, depth, perspective, lightning and shadowing effects. For instance, a surface rendering can be created for the visualization of the object using the isosurface method, which involves the selection of a threshold intensity and the generation of a polygon based on the chosen threshold (Figure 2.14.b). This method allows the simultaneous visualization of regions with different grey level distribution that are higher than the threshold value. Additionally, for the visualization of the complete 3D object, volume rendering based on the summation of every voxel (3D pixel) at arbitrary angles can also be applied (Figure 2.14.c).

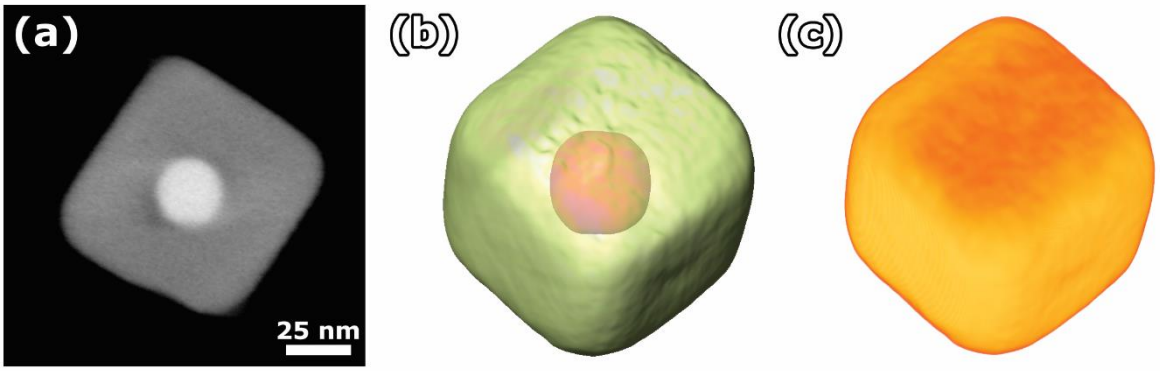

Figure 2.14 – (a) Visualization of a slice through the 3D reconstruction of a gold and silver core shell structure obtained in HAADF-STEM mode. The variation of grey levels indicates the variation of the chemical composition of the object. (b) Surface renderings of the same object, where the red surface correspond to the threshold value was applied to the brighter region in the centre of (a) and the green to the lighter grey value. (c) 3D volume rending of the same object.

2.5 Advanced 3D characterisation of nanoparticles by electron tomography

2.5.1 Electron tomography at the atomic level

Electron tomography became a powerful tool to investigate the morphology, the 3D structure and the composition of a broad range of materials at the nanometre level. However, further progress is required. For example, during my PhD research, the atomic structure of metallic nanoparticles containing defects was investigated, where the use of atomic scale tomography is fundamental.

One example of investigation of the characterisation of the atomic structure in 3D was based on two HAADF-STEM images acquired from a 3 nm silver nanoparticle embedded in an aluminium matrix along different zone axes. Using statistical parameter estimation theory, the number of atoms in each atomic column was retrieved. Afterwards, discrete tomography was used to combine the counting results into a 3D reconstruction with atomic resolution[111]. It was hereby assumed that the symmetry of the atomic lattice is known and that all atom positions are fixed on a grid. This technique allows the characterization of nanostructures that might be sensitive towards the electron beam, since the number of HAADF-STEM images required for the recovery of the 3D atomic structure of the object under investigation can be very small (2 images). In this manner, structural modification of the nanomaterial due to the interaction with the electron beam can be minimized. However, this technique assumes that the position of the atoms are fixed in the atom grid, preventing a further characterization of possible strain or defects present in the crystal lattice of the object under investigation.

Alternatively, Goris *et al*[148] proposed a methodology capable of retrieving the atomic positions based on a limited number of high-resolution HAADF-STEM images along main crystallographic zone axis. The 3D atomic structure was recovered from a compressive sensing reconstruction technique, where the sparsity of the object was assumed (only voxels containing an atom will be non-zero and the remaining corresponds to empty space). In order to minimize the missing wedge artefacts from the very limited number of projections, prior knowledge of the shape of the object is obtained from an electron tomography experiment at the nanoscale and subsequently incorporated during the 3D reconstruction. The use of this technique is also beneficial to nanostructures that are sensitive towards the electron beam, as the number of projection images with atomic resolution required to provide the 3D atomic structure is again very small. Moreover, due to the absence of assumptions of the position of the atoms during the tomographic reconstruction, this technique enabled the investigation of the presence of strain in the atomic lattice by extending Geometrical Phase Analysis (GPA) to 3D. Still, an acquisition of a full tomographic series at lower magnifications is required to provide the prior information of the morphology of the object under investigation. For extremely beam sensitive nanostructures, this step can be challenging. However, the use of more advanced acquisition schemes for electron tomography can be beneficial for the determination of the required prior information, such as fast tomography[147] and TEM tomography[149]. Another challenge for the use of this technique consists in the characterization of polycrystalline nanostructures, where it might not be possible to perform the acquisition of a STEM image where all regions of the object under investigation is orientated along zone axis.

Another methodology has been proposed where the use of the prior information of the shape is not required[113]. In this study, the 3D atomic structure of gold nanodecahedron was obtained from a continuous tilt series of high-resolution images in combination with the assumption that the atomic potential could be modelled with 3D Gaussian spheres[113]. As a result, the coordinates of each atom of the object were directly retrieved together with the 3D atomic structure, allowing the determination of the 3D displacement maps for strain analysis. In this technique, no assumption are made in regard to the crystal lattice of the object under investigation, at the expense of computational costs and complexity.

Additionally, for nanomaterials that contain unknown defects, the determination of prior information is not always straightforward. Therefore, the state-of-art techniques for electron tomography at the atomic level cannot be applied in a routinely manner for the characterization of nanomaterials containing unknown structural defects. Recently, a new methodology has been developed at EMAT, where the optimization of the acquisition in combination with the improvements of image processing and alignment made possible to obtain the atomic structure of nanomaterials

using SIRT without the use of any prior knowledge about the structure of the material[150]. This technique will be discussed in deeper details in Chapter 4 and Appendix A.

2.5.2 In-situ electron tomography

Although advanced (S)TEM techniques provide valuable information in 2D and 3D of nanomaterials, it only represents their static behaviour, where the investigations are carried out at the conventional conditions in a TEM (room-temperature and high-vacuum). For instance, chemical reactions at the surface of nanoparticles, phase transformations at high or even varying pressure/temperature and nucleation/growth events are of great importance for the engineering of nanomaterials for various applications and cannot be addressed by using (S)TEM techniques at fixed environmental conditions[151]. Therefore, the characterisation of nanomaterials under realistic conditions that resemble their true environment is of great importance. Recent advances in the TEM holders' technologies during the past decade enabled the 2D characterisation of nanomaterials in real time under real conditions stimuli, such as the presence of gaseous, liquid, thermal or electrical environment[151,152].

Expanding such investigations to 3D is a real challenge and recently this has been an important topic at EMAT. Recent examples of insights on the 3D dynamical behaviour of nanomaterials obtained with state-of-the-art techniques for *in-situ* (S)TEM are: (a) investigation of the shape transformation in 3D of anisotropic nanoparticles induced by increasing temperature environments[153,154]; (b) the understanding of 3D elemental diffusion of individual anisotropic gold-palladium core-shell nanostructures upon increasing temperature, enabled by the use of advanced *in-situ* heating holders in combination with advanced electron tomography techniques[155]; and (c) evolution of surface facets in platinum nanoparticles upon flow of selected gases (H_2 and O_2) enabled by the use of gas cell holders in combination with advanced techniques of electron tomography at the atomic level[150], corresponding to the first step towards to the comprehension of the relationship between the morphology and catalytic activity of nanoparticles.

It is clear that *in-situ* characterisation of nanomaterials is essential to overcome the barriers of the characterisation of model-like settings and make the transition to realistic conditions. Therefore, during my PhD research I characterized the dynamics of nanoparticles upon increasing temperature environment in 3D. For this purpose, a dedicated tomography *in-situ* heating tomography holder from DENSsolutions, equipped with a Micro-Electro-Mechanical Systems (MEMS) chips, was employed (Figure 2.15). To control the temperature that the system achieves, an external computer in combination with a heating unit is employed, as illustrated in Figure 2.15. The MEMS chip contains regions with an electron transparent thin layer of Silicon Nitride, where the specimen is drop-

casted (Figure 2.15.c). Often, to avoid effects of charge accumulation, a thin layer of carbon (3-10 nm) is deposited on the bottom of the chip. Due to the geometry of the holder, a tilt range of ±80^{o} can be reached.

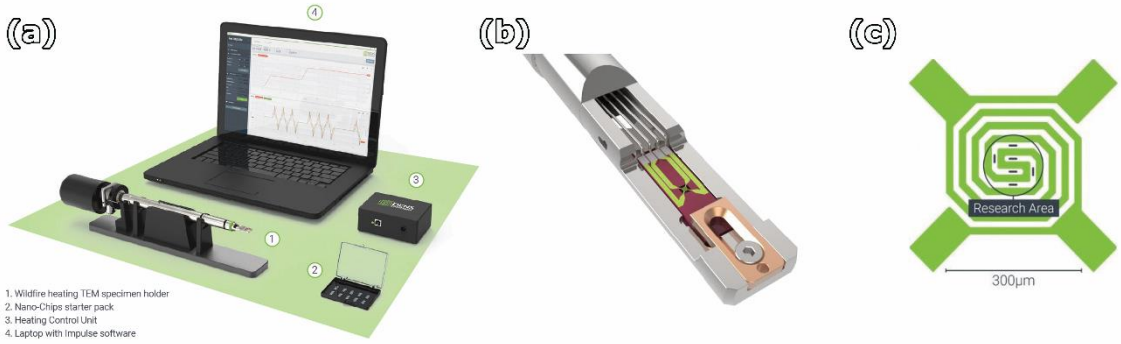

Figure 2.15 – (a) Complete package of the Wildfire *in-situ* tomography heating holder from DENSsolutions, containing a dedicated computer with devoted software for the heat control, heat control unit, holder and MEMs chips. (b)Detailed view of the tip of the holder, revealing the geometry of the MEMS chip. In (c) a scheme of the distribution of the contacts in green is shown. The dark lines inside the research area corresponds to the windows coated with a silicon nitride think layer, where the specimen is deposited. Figure adapted from [156,157].

2.6 Electron tomography strategies employed in the present thesis

Different approaches for electron tomography will be applied to a variety of complex nanostructures in the following chapters. More specifically, electron tomography based on different STEM signals will be used for the characterization of the morphology, inner structure and defects of different nanoparticles. The 3D structure of beam sensitive nanomaterials will be retrieved from a combination of low dose TEM imaging and electron tomography. Moreover, electron tomography experiments will be performed at increasing temperature conditions in one of the following chapters, to reveal the dynamical behaviour of the structure. Finally, two different approaches for electron tomography at the atomic level will be explored for a thorough 3D characterization of nanomaterials. More specifically, an approach based on the HAADF-STEM signal combined with optimized acquisition conditions and dedicated image processing will be used to retrieve the atomic structure of different nanoparticles, while another approach based on phase contrast images at low dose conditions will be experimentally implemented for the 3D characterization of beam sensitive nanomaterials.

Part 1

Electron tomography of metallic nanoparticles containing structural defects

Chapter 3. Understanding the effect of seed size and crystal defects on gold nanoparticle seeded growth by using advanced TEM

3.1 Introduction of seed-mediated growth

New synthesis protocols have been developed in the past decades to enable a better control over synthesis of nanomaterials leading to a high monodispersity yield in size, shape and crystallinity[29,30,158–161]. One of the main aspects related to the bottom-up growth of nanomaterials, is the nucleation step. This process can be either homogeneous or heterogeneous, where the first corresponds to a self-assembly of ions, atoms or molecules in solution into small crystals that are capable of spontaneous growth in an unstable liquid phase[162–164]. This is the principle behind procedures referred to as one-step growth of nanomaterials. Unfortunately, the synthesis of large gold nanoparticles (> 50 nm) using the one step growth results in a high polydispersity in size and shape, due to the overlap of nucleation and growth mechanisms[29,159]. Thus, protocols that enable better control over the size and shape of nanomaterials are required. Such control during synthesis can be achieved by using the seed-mediated growth technique, a heterogeneous process that is one of the most reliable methodologies to control the shape, size and crystallinity of the overgrown structure with a high monodispersity yield[29,30,158–161]. The seed mediated synthesis process is divided in three steps: (a) nucleation from atoms formed by reduction of metal salts; (b) the evolution of the nuclei into seeds; and (c) subsequent growth of larger structures in a supersaturated medium containing metal precursors, reducing agents and shape-directing reagents[29–31,165,166] (Figure 3.1). The advantage of this method is that during the growth of the final products, the final shape of the overgrown structures can be modulated by including shape-directing additives to the supersaturated solution, as they typically inhibit crystal growth on certain facets through selective adsorption of the metal precursors, e.g. [29,165–167].

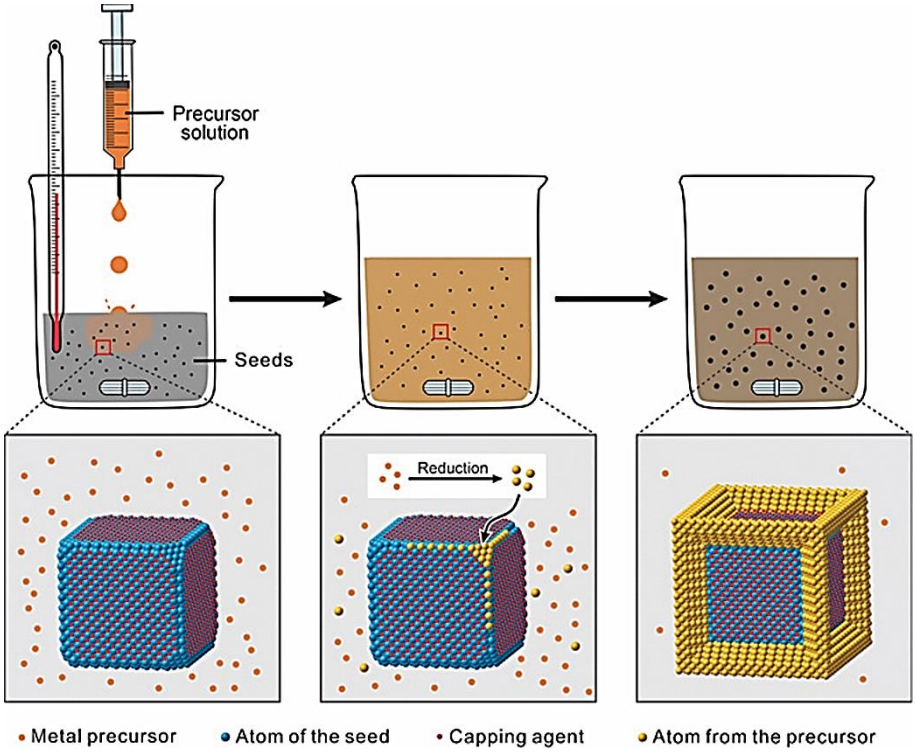

Figure 3.1 – General strategy used for the seed-mediated growth of colloidal metal nanocrystals. A precursor solution is injected into a vessel containing a mixture of seeds, reductant, capping agent, and colloidal stabilizer. The metal precursor is reduced (or decomposed) to form zerovalent atoms, which then heterogeneously nucleate on the surface of the seeds. Continued growth of the seeds, through one of the many possible pathways, results in the formation of well-defined nanocrystals. Figure extracted from [29].

The ability to control the morphological properties of the overgrown products with a high monodispersity is directly associated with the use of different types of seeds and by the meticulously manipulation of the growth conditions[29–31,158–161]. More specifically, it has been shown that the shape and crystallinity of the final nanoparticles are influenced by the crystallinity of the seeds[29,30,33–35,167–169]. For example, the use of single crystalline seeds leads to the growth of octahedral, orthogonal rods, cubes, rectangular bars, or cuboctahedra nanoparticles; seeds that contain a single twin boundary resulted in the formation of bipyramids; and, finally seeds with multiple twin boundaries lead to the synthesis of decahedra, icosahedra and penta-twinned nanorods/nanowires (Figure 3.2)[29,165,170].

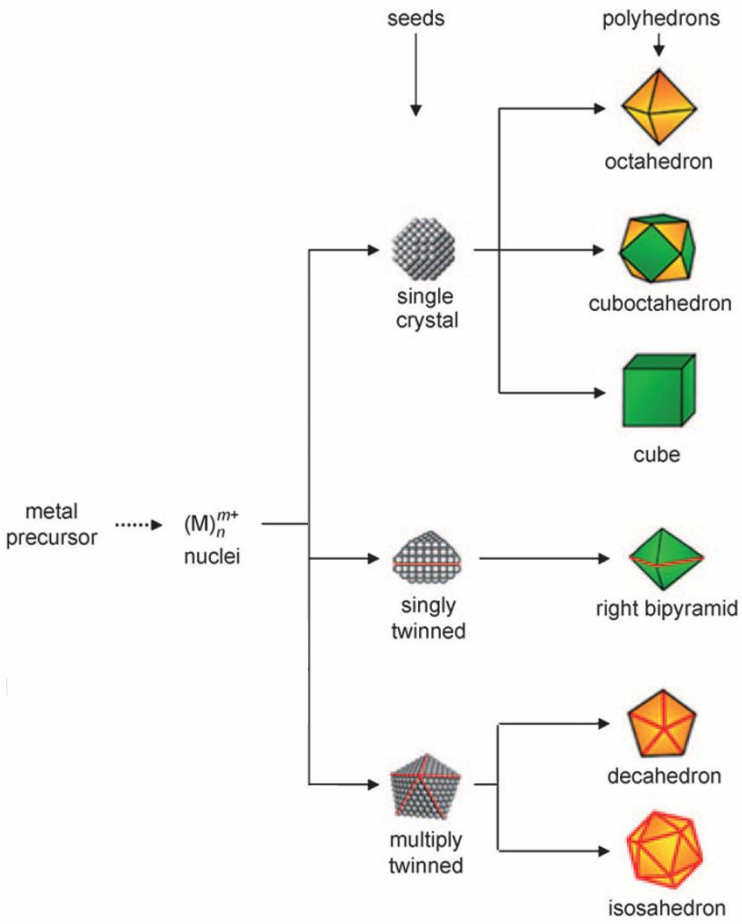

Figure 3.2 – Reaction pathways that lead to face-centred-cubic (fcc) metal nanocrystals having different shapes. First, a metal precursor is reduced or decomposed to form the nuclei. Once the nuclei have grown past a certain size, they become seeds with a single-crystal, mono-twinned, or multiply twinned structure. The green and orange colours represent the {100} and {111} facets, respectively. Twin planes are delineated in the drawing with red lines. Figure adapted from [165]

During the past two decades, growth conditions of gold nanoparticles have been meticulously optimized, but the protocols for the original seed preparation remained unaltered[165]. Because of the intrinsic relationship between the shape of the final product and the crystallinity of the seeds, new approaches focusing on the optimization of the seeds are of great interest. Recently, a new protocol based on a top-down oxidative etching approach of nanorods (mono-crystalline) and nanotriangles (mono-twinned) was developed to produce spherical seeds with a better control on the quantity of defects in the crystal structure[32]. The motivation behind this chapter is to understand how the size of the seeds and the presence of structural defects in the seeds could further influence growth into certain shapes. In this manner, we aim to contribute to a rational improvement of synthesis protocols for gold nanoparticles[32].

3.2 From nanorods and nanotriangles to spherical seeds by oxidative etching

Oxidative etching procedures can lead to atomic subtraction[166,170,171]. Here, this approach was used to produce seeds from single crystalline gold nanorods (average length of 59 ± 5 nm and average diameter of 25 ± 2 nm) and mono-twinned gold nanotriangles (average edge length of 59 ± 3 nm). The monodispersed spherical seeds were obtained from nanorods and nanotriangles by using Au(III) as oxidizing agent. Upon centrifugation, nanotriangles and nanorods were suspended in 4 L of an aqueous solution of 25 mM cetyltrimethylammonium chloride (CTAC) and 10 mM NaBr. The concentration in Au(0) (estimated using the absorbance at 400 nm) was set at 0.2 mM[172]. Subsequently, an amount of 0.05 M Au(III) solution was added under vigorous stirring (final Au(0):Au(III) molar ratio of 4:1). The reaction was then gently stirred at 30°C until oxidation was completed (absorbance at 400 nm decreased by ca. 50%)[172]. Finally, the mixture was centrifuged (1h at increasing rpm as the number of oxidation cycles increases, from 8000 to 13000 rpm), the supernatant was discarded and the precipitate re-dispersed in 25 mM CTAC solution. The entire process was repeated several times until the desired size was achieved. More precisely, four and seven oxidation cycles resulted in spherical gold seeds with diameters of 20 and 12 nm, respectively (Figure 3.3). An additional centrifugation step (2h at 2000 rpm for 20 nm seeds; 6000 rpm for 12 nm seeds) was performed to remove large particles that were not sufficiently etched. The final concentration of nanoparticles was fixed to 1.02×10^{17} nanoparticles per litre. A higher dispersity in size was observed for 12 nm seeds (seven cycles) in comparison to seeds with sizes of 20 nm (four cycles). The different nano-systems in this study are summarized in Table 3-1.

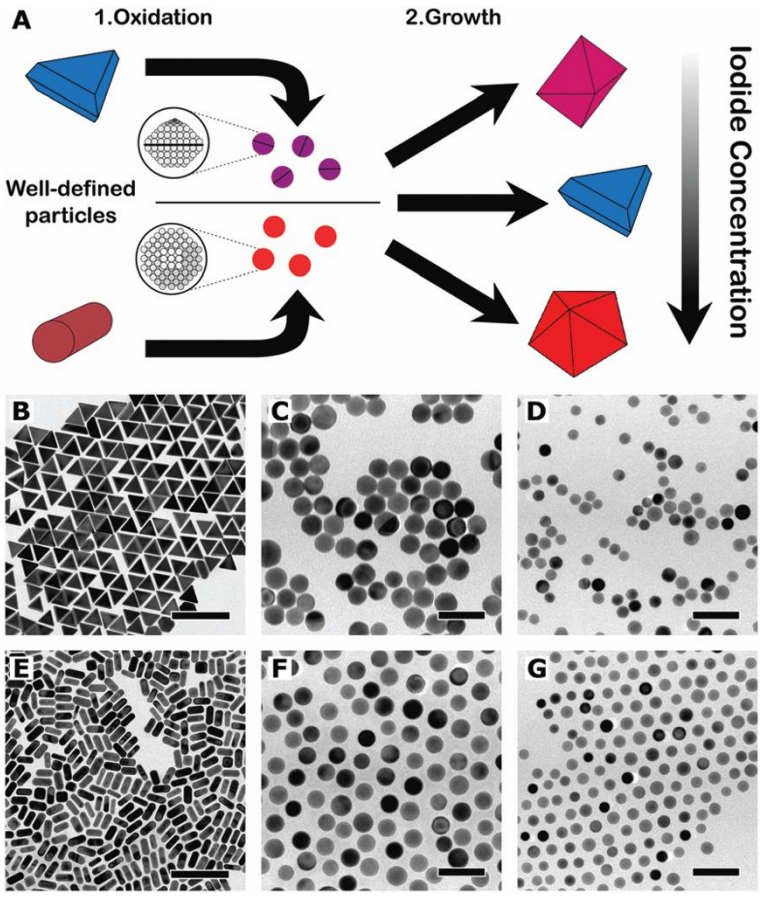

Figure 3.3 – (a) Schematic representation of the experimental procedure: an oxidative etch approach is applied to single crystalline nanorods and mono-twinned nanotriangles, resulting in the formation of spherical seeds without and with structural defects, respectively. The shape of the final product is linked with the crystallinity of the seeds. (b)-(d) TEM images of the starting nanotriangles (b) and nanorods (e). The obtained seeds after the iterative oxidation etching for four cycles (20 nm) from the nanotriangles (c) and nanorods (f), as well as, for seven cycles (12 nm) from nanotriangles (d) and nanorods (g). Figure extracted from [32].

Shape prior to the oxidation etch	Size of the nanoparticle (nm)	Number of oxidative etching cycles	Size of the seed (nm)	Nomenclature
Nanorod	Length: 59 ± 5	7	12 ± 1	12NR
Nanorod	Diameter: 25 ± 2	4	20 ± 1	20NR
Nanotriangle	Edge length:	7	12 ± 2	12NT
Nanotriangle	59 ± 3	4	20 ± 1	20NT

Table 3-1 – Table summarizing the nomenclature of the systems under investigation in this chapter.

3.3 Characterisation of seed size and crystal structure

To investigate the presence of structural defects, aberration-corrected HAADF-STEM imaging was performed using an aberration corrected 'cubed' ThermoFisher Titan microscope, operated at 300 kV. Figure 3.4 displays an example of a 12 nm seed originated from nanorods (12NR) and nanotriangles (12NT), respectively. High-resolution HAADF-STEM imaging of 13 particles revealed that all seeds originated from nanorods (12NR and 20NR) are single crystalline, whereas the seeds originated from nanotriangles (12NT and 20NT) showed the presence of twin planes.

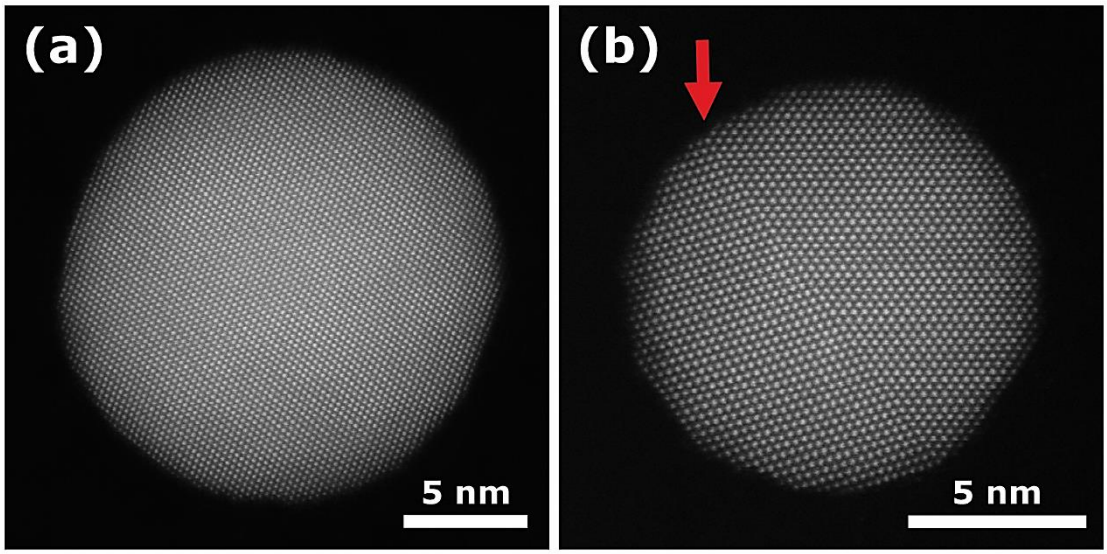

Figure 3.4 – High-resolution HAADF-STEM image of 12 nm seeds originated from (a) nanorods (12NR) and (b) nanotriangles (12NT).

The investigation of defects from high-resolution images requires orientation of the nanoparticle into a main crystallographic zone axis. Since this process is very time consuming, this technique is not suitable to obtain a statistically relevant distribution of the defect yield for each system, which is necessary to understand the connection between the presence of defects in the seeds and the final overgrown structure. BF-TEM images at lower magnifications show the presence of diffraction contrast, from which the presence of defects can be evaluated in principle. However, an intense contrast variation was observed in Figure 3.3.b-g, hampering a quantification of the defect yield. To overcome this limitation, ADF-STEM image was employed. By varying the camera length of the microscope, the contrast variation due to diffraction effects can be tuned, as demonstrated in Figure 3.5.

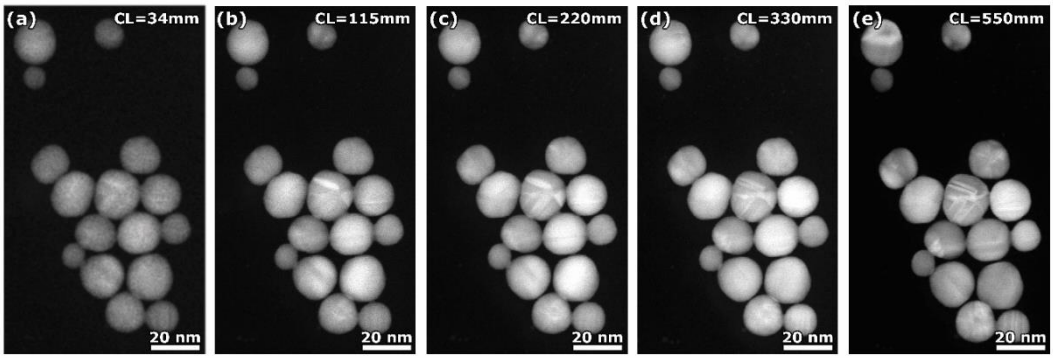

Figure 3.5 – STEM images of polycrystalline gold nanoparticles acquired using an HAADF detector, with varying camera lengths. An increase of the camera length results in a decrease in the scattering angle of the emitted electrons, enabling an optimized visualization of features associated with diffraction contrast. The specimen used for this image does not correspond to any of the nanomaterials mentioned in this chapter. The choice of nanomaterials for this image is merely to illustrate the presence of diffraction contrast for increasing camera length.

Although the diffraction contrast is very clear, a single projection image might not be sufficient to count the total number of particles containing defects, since the appearance of diffraction contrast is correlated with the crystallographic orientation of the nanoparticles with respect to the electron beam. For cases where the defect boundary plane is oriented parallel to the support film, the visualization of the defect is no longer possible (Figure 3.6.a,c). To enable the visualization of the diffraction contrast associated with the defect for the aforementioned condition, a rotation of 45^{o} of the specimen stage can be applied, revealing the desired feature (Figure 3.6.b,d). Therefore, a tilt series of ADF-STEM images were acquired over an angular range from -50^{o} to +50^{o} for the statistical analysis of the defect yield. Besides, the angular range of 100^{o} enables the rotation of the crystal lattice along at least on the main zone axes (e.g., [110] and [100]) of gold nanostructures, which can enhance the visualization of diffraction contrast due to the channelling effect[173]. The association of such contrast variation with the presence of defects is evaluated by the analysis of consecutive images, where a consistent variation of the contrast variation in nanoparticles along consecutive images is expected (e.g., the rotation of the defect line will be similar to the rotation of the specimen), as illustrated in Figure 3.7.

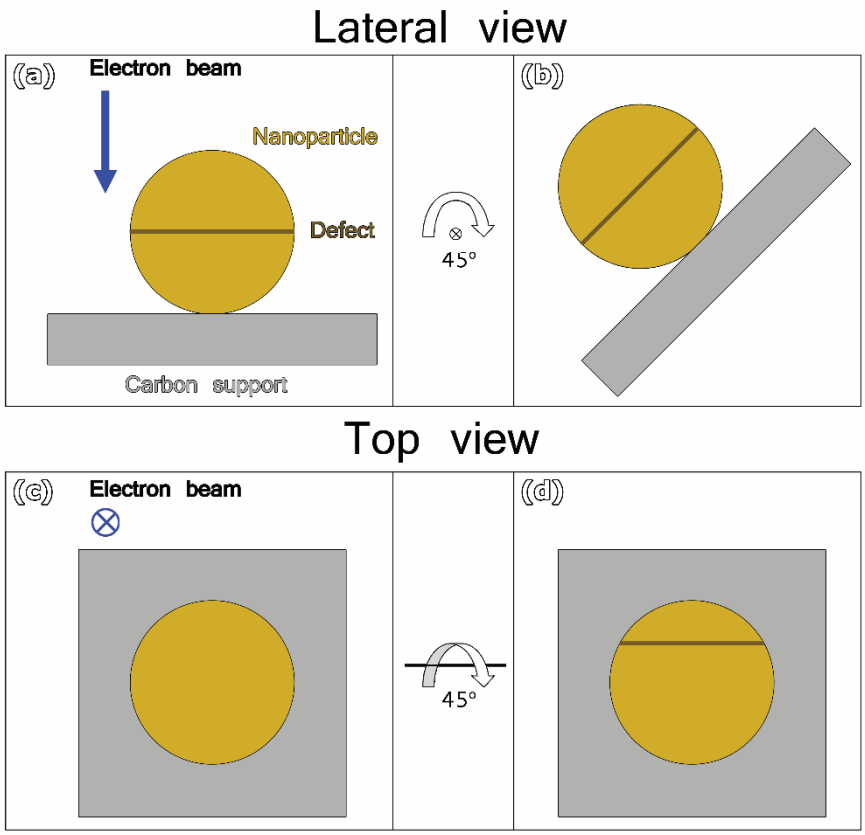

Figure 3.6 – Scheme for the visualization of the defect (brown line) at 0° and after rotation of the stage of 45° shown with lateral and top view perspectives. For cases where the nanoparticle is oriented with the defect boundary plane perpendicular to the electron beam, the visualization of the defect is not possible with ADF-STEM imaging (a), (c). The visualization of defect becomes evident after a rotation of 45° degrees is applied (b), (d).

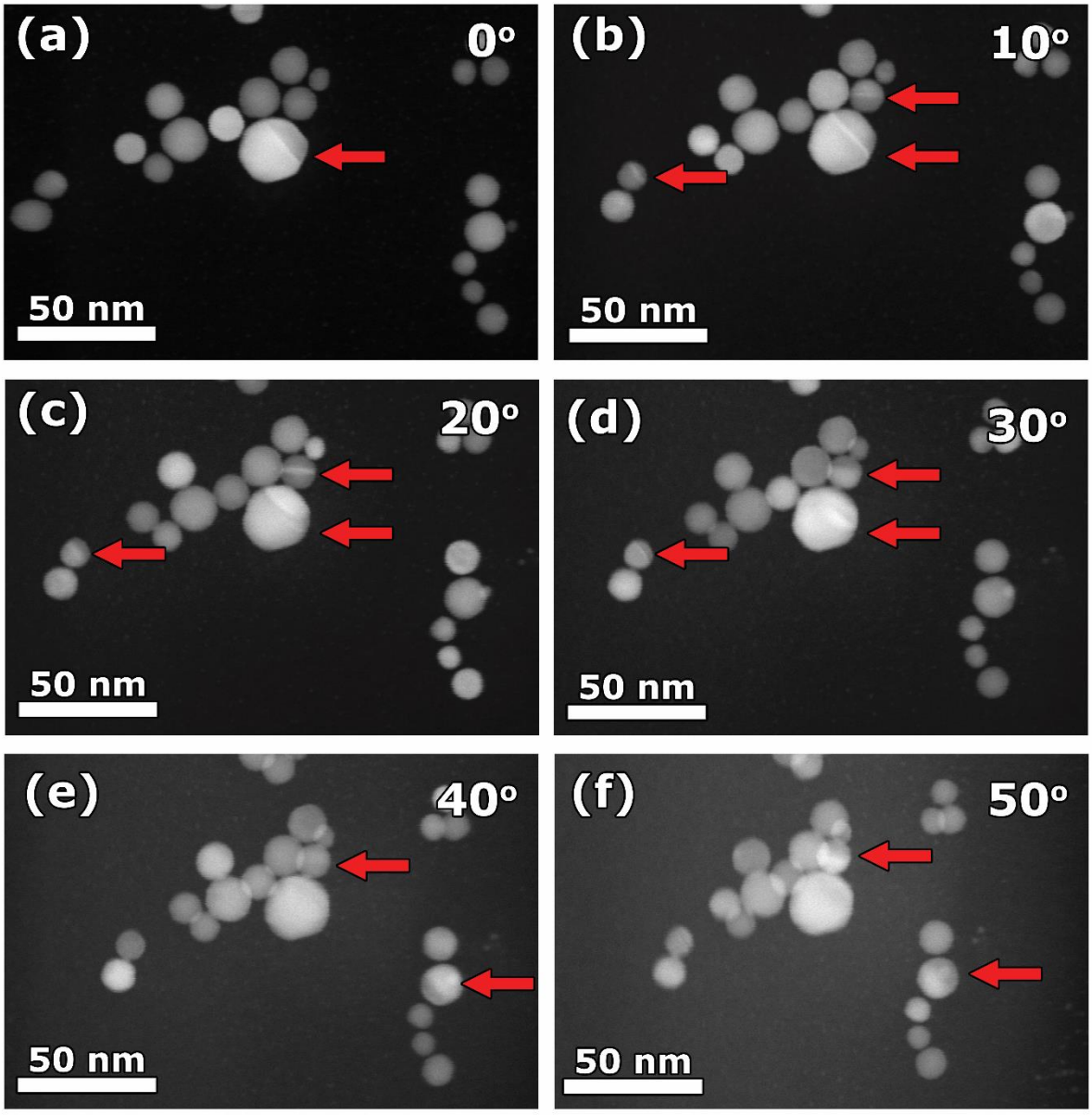

Figure 3.7 – ADF-STEM images of 12NT seeds for different tilt angles. A contrast variation in some nanoparticles is observed for different tilt angles. The red arrows indicate the nanoparticles with diffraction contrast due to the presence of a structural defect.

The error associated with such statistical analysis was very small (around 1%), as it has been observed in recent studies[32]. The statistical analysis of the defect yield proposed here was compared with statistical analysis of 2D TEM images of core-shell nanostructures overgrown from the same nanospheres investigated in this chapter, as shown in Table 3-2. The morphology of the overgrown structure is directly connected with the crystallinity of the seeds, as it will be demonstrated in section 3.4. Therefore, a comparison of the percentage of defect yield and the percentage of the number of particles with the same morphology shown in Table 3-2 revealed that only a difference of 1% was

observed for 20NT nanoseeds. For all the other cases, the statistical analysis presented a good match. Since the error bar is relatively small, structural defects in nanoparticles can be reliably identified through the analysis of tilt series of ADF-STEM images.

Nanoseeds	Single-crystalline:mono-twinned (%) ADF-STEM images	Single-crystalline:mono-twinned (%) Core-shell structures
12NT	71:29	71:29
12NR	99:1	99:1
20NT	49:51	48:52
20NR	99:1	99:1

Table 3-2: Crystal structure characterisation of the four nanoseeds, comparing results obtained for the nanoseeds before (ADF-STEM) and after (TEM) overgrown of core-shell nanostructures. For each sample, at least 300 nanoparticles were measured. Table adapted from [32].

Several tilt series ranging from -50° to +50° and tilt increment of 5° were acquired for each seeds type using a ThermoFisher Tecnai G2 microscope operated at 200 kV with a camera length of 490 mm. A typical example of ADF-STEM image for each system at 0° is shown in Figure 3.8. The red arrows indicate the features associated with structural defects.

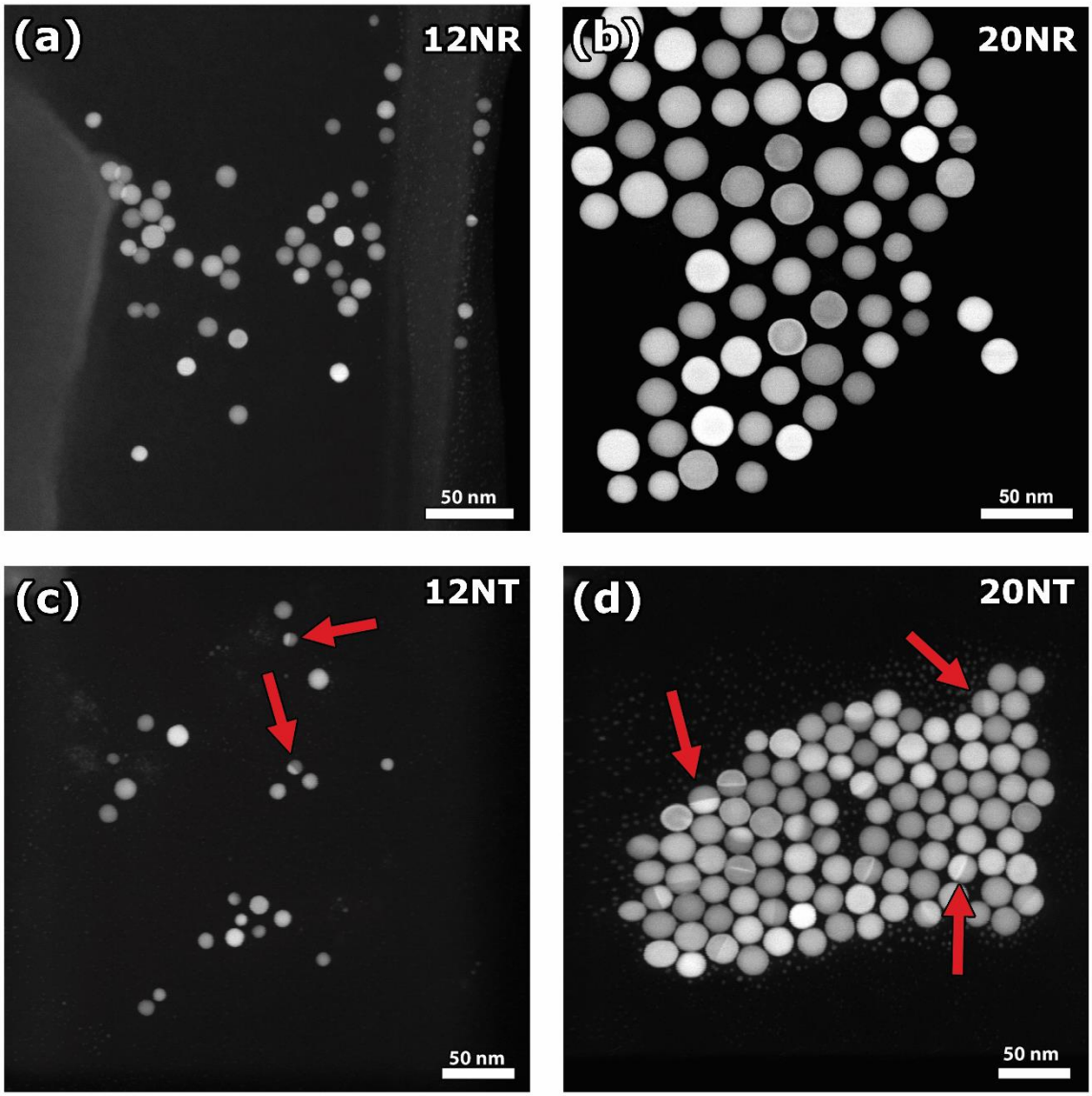

Figure 3.8 – ADF-STEM images of spherical seeds from (a), (b) nanorods and (c), (d) nanotriangles, with sizes of 12 and 20 nm, respectively. The red arrows in (c) and (d) indicates the contrast variation due to the presence of defects.

The resulting statistical distribution of the defect yield for each system is presented in Figure 3.9. Because the nanorods from which the 12NR and 20NR seeds originated were single crystalline, it is not surprising that also the majority of the resulting seeds after oxidative etching after four and seven cycles were single crystalline (99% of the total). For seeds originated from nanotriangles after four cycles (20NT), 51% of the nanoparticles showed the presence of defects. However, for the smaller seeds obtained from nanotriangles after seven cycles (12NT), the percentage of mono-twinned seeds was found to be equal to 29%. This finding confirms that oxidative etching process can be used to remove twin-defects from the gold particles, as previously reported for silver nanoparticles[32,166,171].

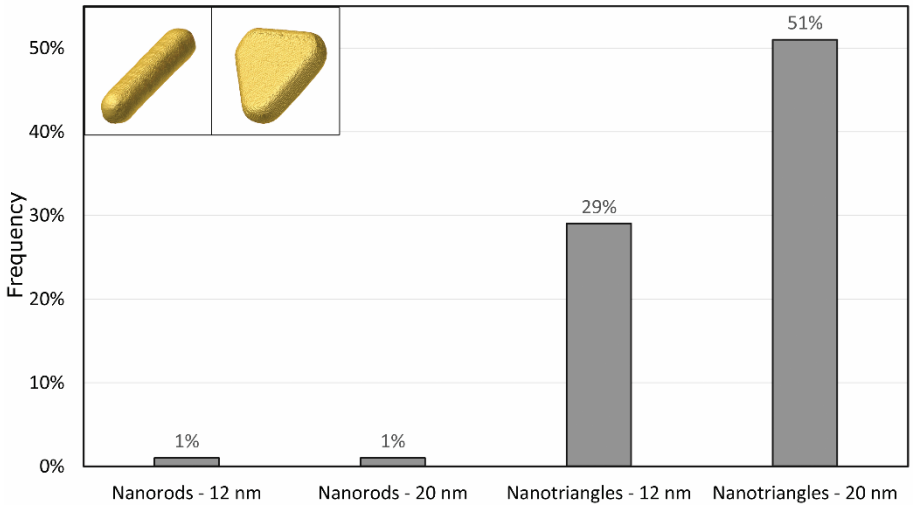

Figure 3.9 – Statistical distribution of the total number of defects present in the crystal structure of the four types of spherical seeds based on a 2D analysis. Insets on top left represent a 3D reconstruction of a typical nanorod and a typical nanotriangle, respectively. Nanotriangle: image courtesy from Dr. Eva Bladt[174].

3.4 Characterisation of overgrown structures

To investigate how the crystallinity of the seeds affects the shape of the final product, first a core-shell structure of silver and gold was synthesized. The main advantage of using silver instead of gold for the overgrowth is the possibility to visualize the seed and the overgrown structure in HAADF-STEM mode simultaneously. Electron tomography was applied to the silver overgrown structures based on 12NR and 20NT seeds. In this manner, we can understand the relationship between the shape of the final structure and the crystallinity of the seeds. For the mono-crystalline seeds (12NR), a cubic shape of the final core-shell structure was retrieved (Figure 3.10.a), whereas a trigonal bipyramid shape was obtained for mono-twinned seeds (20NT) (Figure 3.10.b).

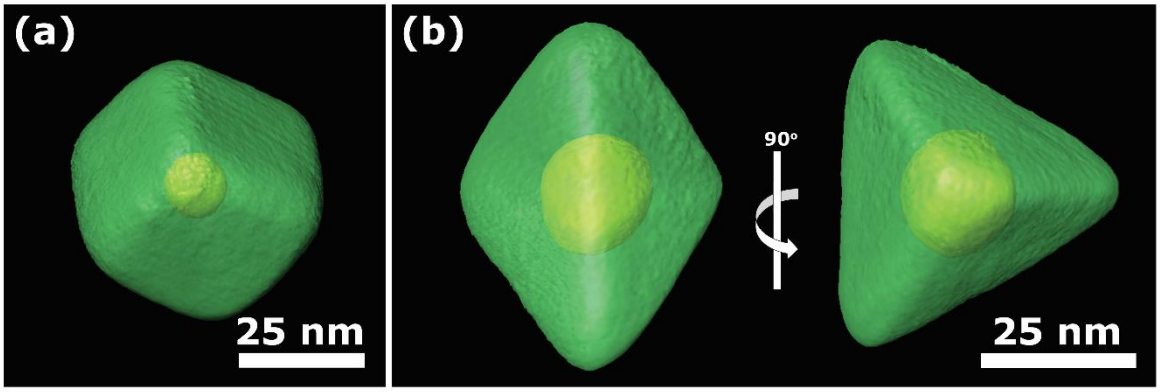

Figure 3.10 – Isosurfaces of the 3D reconstruction volume of silver overgrown structures from (a) mono-crystalline seeds (originally nanorods) and (b) mono-twinned seeds (originally nanotriangles). Here, a cube and a trigonal bipyramid were retrieved, respectively. The region in yellow represents the spherical gold nanoseeds and the green the silver overgrown structure.

Because HAADF-STEM detectors only collect the scattered electrons at high-angles, the information about the presence of defects is lost in the projection images. Consequently, it is no longer possible to retrieve the 3D spatial distribution of defects from tomographic reconstructions. However, by selecting scattered electrons with smaller angle range (e.g., using an ADF detector), the presence of defects becomes clear as illustrated in Figure 3.8.

Images acquired with the ADF detectors are, generally, in the MAADF regime (inner/out collection angles of 26/95 mrad[110]). In this manner, the detector collects both coherent and incoherent scattered electrons. However, by further decreasing the collection angles, mostly coherent scattered electrons, in the low-angle regime, are collected by the ADF detector. This signal is known as LAADF STEM and contains a substantial signal fraction associated with diffraction contrast. Because the LAADF signal is mostly coherent, the projection requirement is no longer fulfilled, resulting in a reconstructed object with higher inaccuracy of the estimation of the total volume, in comparison to conventional methods based on the HAADF signal[110]. Nevertheless, the LAADF images can still be used as input for tomographic reconstructions for qualitative analysis. To evaluate how the variation of intensities in the reconstructed slices corresponds to features associated with diffraction contrast or artefacts from the violation of the projection requirement, comparison with the projection images obtained experimentally are essential. In this manner, the intensity variation can be properly addressed to the eventual presence of diffraction contrast. To obtain qualitative information regarding the complete structure under investigation, HAADF-STEM images are obtained simultaneously and reconstructed independently. Such combination is the core principle of the multimodal tomography methodology, which allows the recovery of the morphology and the 3D

distribution of defects from the HAADF and LAADF signals respectively. For a proper visualization of the distribution of the defect in 3D, a segmentation of the defects in the LAADF-STEM reconstruction is performed and superimposed with the volume rendering of the HAADF-STEM reconstruction.

A ThermoFisher Osiris microscope operated at 200 kV was used to acquire the dataset. The camera length of the microscope was adjusted to guarantee the acquisition of images in the high-angle and low-angle scattering regime (detector inner/outer collection angles of 115/157 mrad for HAADF-STEM detector and 13/26 mrad for LAADF-STEM detector). Figure 3.11 shows HAADF- and LAADF-STEM images for a few projection angles of the trigonal bipyramid structure grown from the 20NT seed, where the presence of the diffraction contrast associated with the defect is clearly visible (Figure 3.11.b,d,f) . The diffraction contrast present in the LAADF-STEM images reveals that the defect extend from the gold seed to the silver shell. Inspection of the tilt series of LAADF-STEM images of a cubic core shell structure originated from the 20NR seed revealed the absence of diffraction contrast. Indeed, 99% of the 20NR seeds were single crystalline and the formation of defects is not expected during the growth of the silver shell.

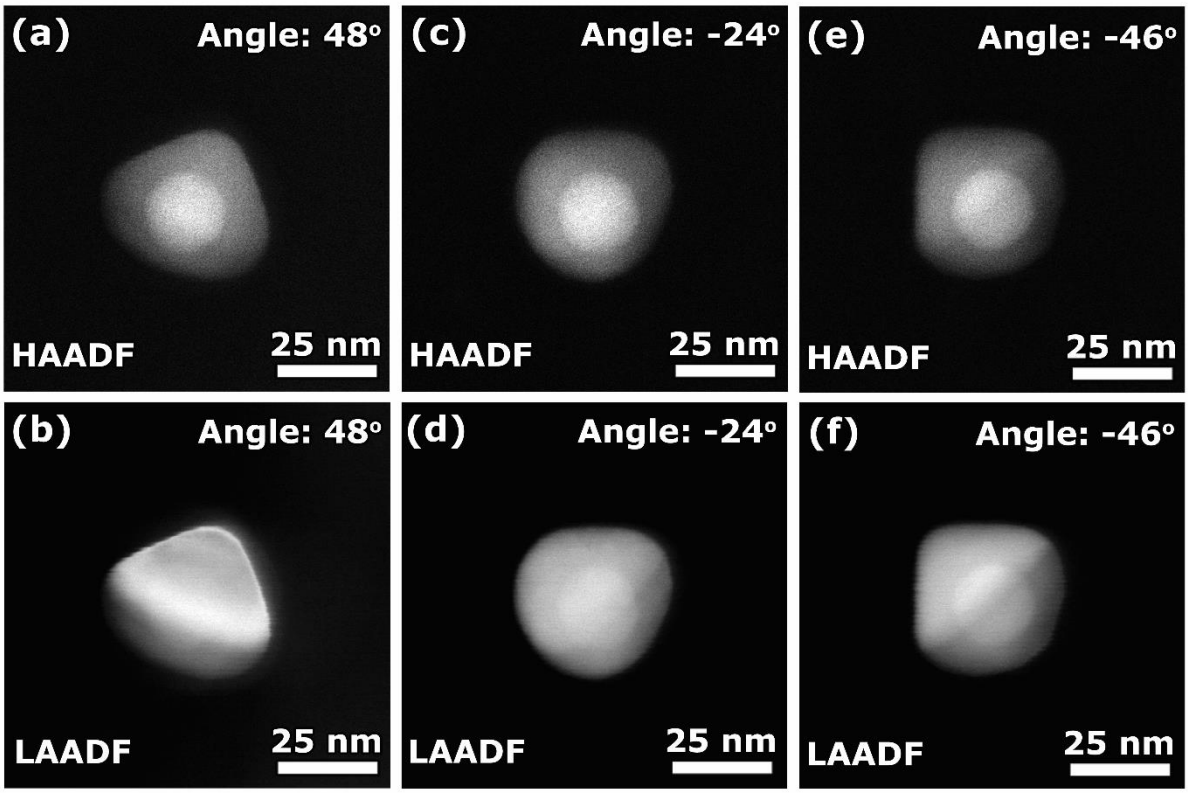

Figure 3.11 – HAADF- and LAADF-STEM images of an overgrown core shell structure of gold and silver at different tilt angles. Intensity variation in the LAADF-STEM images (b),(d) and (f) are attributed to the presence of structural defects.

The reconstruction of the 3D volume based on the HAADF and LAADF signal was performed using the Astra Toolbox for MATLAB[175] for both core shell structures overgrown from the 20NT and 20NR seeds. The inspection of the reconstructed slices along the cubic core shell structure confirmed the single crystallinity nature of the object and intensity variation due to diffraction contrast was not found (Figure 3.12.b). However, hints of contrast variation were found by inspection of the reconstructed slices from core-shell structure originated from the 20NT seeds (trigonal bipyramid), as indicated by the red arrow in Figure 3.12.d. A simultaneous analysis of the reconstructed slices (Figure 3.12.d) and the projection LAADF-STEM images (Figure 3.11.b,d,f) confirmed that the presence of structural defects (twin boundaries) in the nanoseeds extends over the overgrown silver shell during the growth process, as it has been proposed in literature[32–35,88,167]. It is interesting to note that some artefacts are present in HAADF reconstructed slices (Figure 3.12.a,c). More specifically, cupping artefacts were observed, where the interior of the reconstructed particle is underestimated[128]. This type of artefact is caused by the non-linear damping of intensities in STEM images[128,176,177]. The presence of cupping artefacts in the LAADF-STEM reconstructed volume imposes limitations to the identifications of the features associated with defects. The analysis of the slices through the retrieved 3D volume only suggested the location of certain defects, which was subsequently confirmed by a simultaneous inspection of the LAADF-STEM tomographic series.

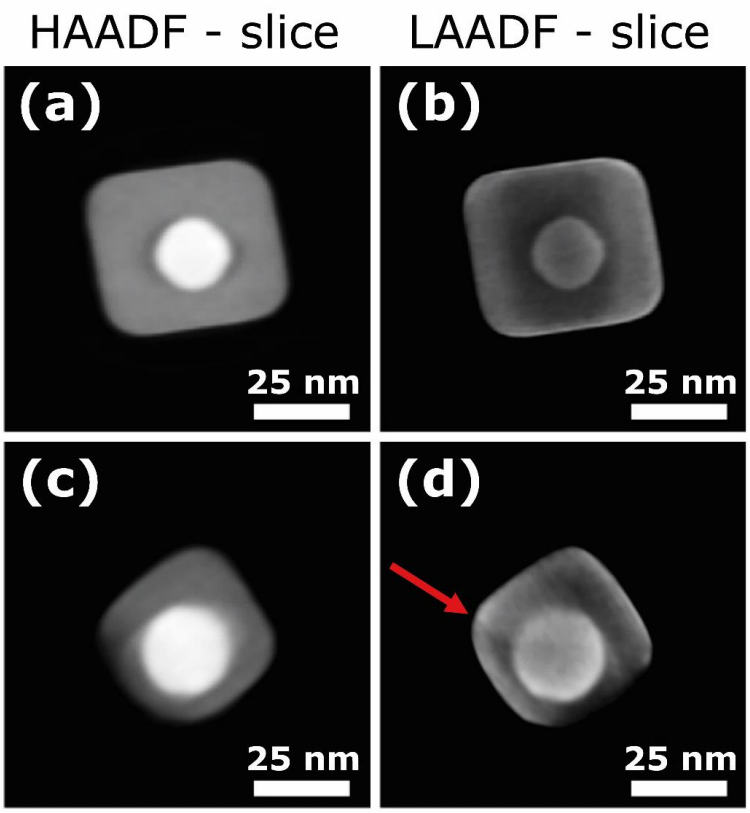

Figure 3.12 – Slices through the 3D reconstructed volume of the (a)-(b) cubic and (c)-(d) trigonal bipyramid core-shell structure. (a), (c) correspond to slices through the 3D reconstructed volumes based on the HAADF-STEM images and (b), (d) represent the slices through the volume reconstructed from the LAADF-STEM images. In (d), a red arrow indicates a slight variation of contrast in the 3D reconstruction due to the presence of the defect.

To visualize the defect in 3D, a manual segmentation step was performed in the 3D reconstructed volume obtained from LAADF-STEM signal along the line indicated by the red arrow in Figure 3.12.d. Figure 3.13 shows a superposition of the 3D volume obtained from the HAADF signal, where the purple plane through the object represents the 3D defect. Our findings revealed that, indeed, the defect extends over the seed and are present in the crystal lattice of the silver shell.

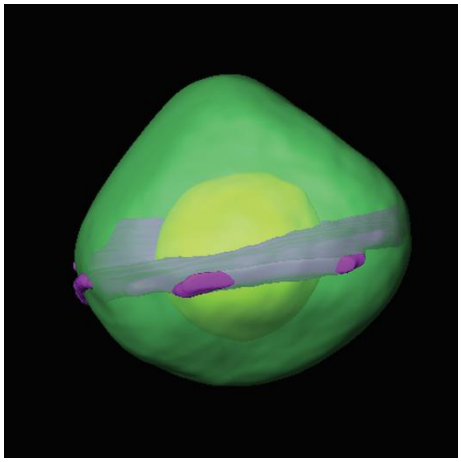

Figure 3.13 – Superposition of the segmented defect (purple) and the 3D volume. The segmentation of the defect was obtained from the ADF-STEM signal. Isosurfaces in yellow (gold seed) and green (silver shell) of the reconstructed object were obtained from the reconstruction based on the HAADF-STEM signal.

Next, gold nanoparticles were grown starting from the four types of seeds (12NR, 12NT, 20NR, 20NT). The growth procedure applied to the seeds used CTAC as surfactant, ascorbic acid as reducing agent and iodide ions as shape-inducing agent. It has been reported in literature that the use of iodide ions promotes the growth of nanoparticles with defined shapes[88,178–183] because of the strong adsorption of iodide at the surface of seeds in comparison to other ion types (e.g., chloride and bromide)[179]. The shape control is associated with preferential reduction of gold ions onto the {111} surfaces[183]. Moreover, it is known that iodide ions not only stabilize preferential facets during the growth mechanism, but it is also responsible for decreasing the rate of gold ions reduction[183]. Therefore, the use of iodide can potentially induce the formation of twin boundaries defects during the growth process[88,183]. Additionally, growth of gold nanoparticles in the absence of iodide ions results in the formation of products with undefined shapes.

3.4.1 Analysis of overgrown gold products originated from 20 nm seeds

The analysis of the shape dispersity of the final products through TEM imaging revealed that the concentration of iodide has no significant influence on the final shape of the overgrown product when starting from 20NT seeds, where nanotriangles were found in approximately 64-70% of the total products for a varying concentration of iodide (50 μM-100 μM). The remaining shapes obtained upon growth of 20NT seeds corresponded mainly to nanooctahedra by-products. Moreover, the growth of penta-twinned products was not observed, unless for iodide concentrations higher than 500 μM[32]. Analysis of the growth process starting from 20NR seeds showed that 99% of the by-products were nanooctahedra for iodide concentration of 50 μM. By increasing the concentration of iodide to 75 μM,

a fraction of 30% of nanotriangles were obtained during the growth, while the remaining corresponded to nanooctahedra. The total of nanotriangles increases to 44%, for concentration of 100 μM. To obtain a majority of overgrown nanotriangles starting 20NR seeds, an iodide concentration of 500 μM was required[32]. Therefore, a relationship between the final shape and the iodide concentration was observed when starting from 20NR seeds. These results are summarized in Table 3-3 and Figure 3.14.

Nanooctahedra : nanotriangles : nanodecahedra

Seed type	Crystal structure of defects Mono-twinned : mono-crystalline (%)	$[I^-]$ = 50 μM	$[I^-]$ = 75 μM	$[I^-]$ = 100 μM
20NT	51:49	26:64:9	20:64:9	11:70:5
20NR	1:99	99:1:0	59:30:0	42:44:0
12NT	29:71	13:66:10	7:63:15	4:54:29
12NR	1:99	27:41:0	3:59:5	3:49:9

Table 3-3 – Influence of the crystal structure of seeded in the overgrown particles based on the analysis of 2D images. For each sample, at least 250 nanoparticles were counted. Three main shapes were observed: nanooctahedra, nanotriangles and nanodecahedra. The total number of nanoparticles differs from 100 because the shape could not be identified for a small fraction of particles. Table extracted from [32].

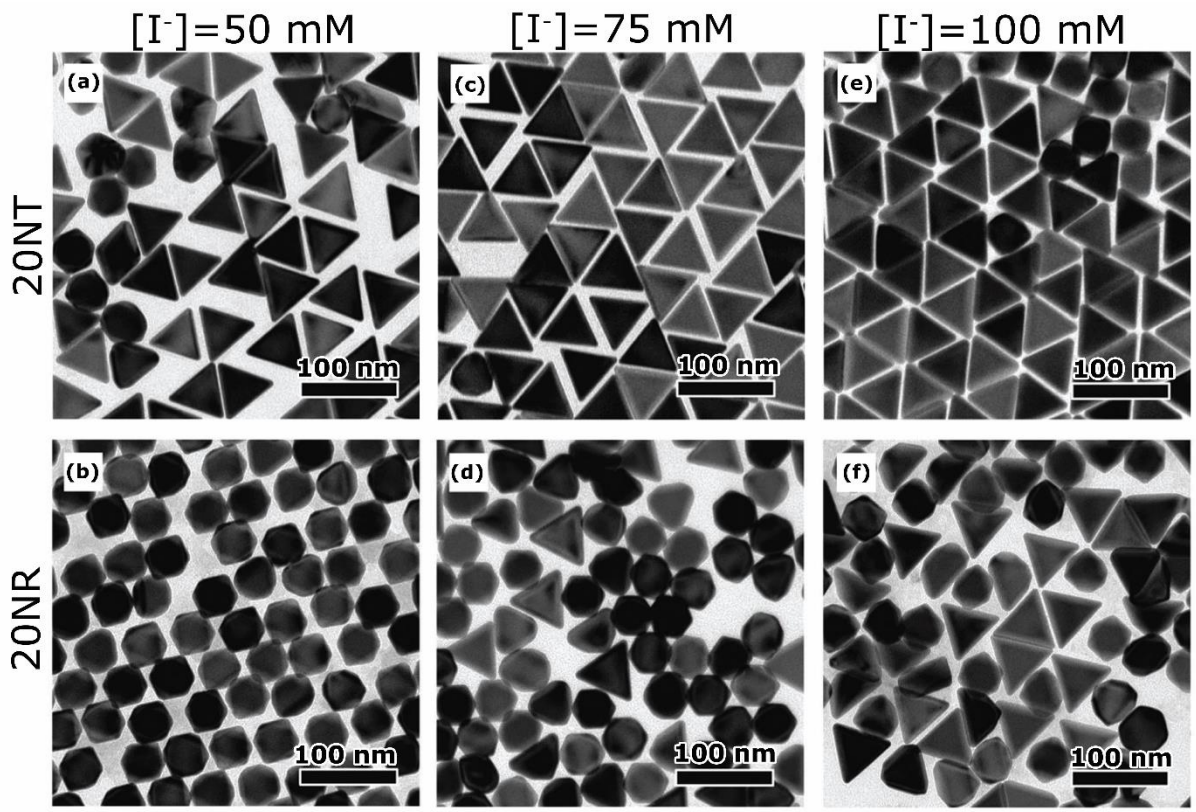

Figure 3.14 – TEM analysis of 20NT (left) and 20NR (right) grown with different iodide concentrations: 50 mM (a) and (b), 75 mM (c) and (d), 100 mM (e) and (f). Figure extracted from [32].

3.4.2 Analysis of overgrown gold products originated from 12 nm seeds

A similar analysis was performed using 12NT seeds and revealed that only 13% of nanooctahedra (mono-crystalline) were formed (iodine concentration of 50 μM), even though the statistics obtained in section 3.3 shows that 71% of the total seeds were mono-crystalline. Surprisingly, for 12NR seeds at the same iodide concentration, mostly nanotriangles were formed (41% of the total). Differently from the 20 nm seeds (20NR and 20NT), the formation of penta-twinned by-products (nanodecahedra) were obtained by slightly increasing the iodide concentration (up to 100 μM). Thus, for smaller seeds, the crystal structure can evolve during the growth, resulting in the formation of both mono-twinned and penta-twinned structures, at lower iodide concentrations.

3.5 Conclusions

In this chapter, we investigated the production of gold seeds by oxidative etching of nanorods and nanotriangles. More specifically, we characterized the presence of defects in the seeds in a statistical manner. The use of alternative techniques for the characterisation of the defects, such as ADF-STEM imaging and multimode tomography were hereby essential. More precisely, the

combination of the acquisition of a tilt image series and the use of ADF signal enabled us to obtain a statistical relevant distribution of the defect yield of each type of seeds (12NR, 12NT, 20NR and 20NT). Here, it was found that the defect yield of seeds was associated with the initial crystallinity of the nanoparticle prior to the oxidative etching and the number of oxidation cycles. The use of advanced techniques for electron microscopy allowed the confirmation of the preservation of the crystal structure of the seeds during the growth of the final products. Moreover, our findings demonstrated that the shape of the final product is connected with the crystallinity of the seeds and the chemical composition of the solution during growth. The obtained results are valuable for the optimization of synthesis approaches based on the seed-mediated growth technique.

3.6 Experimental methods

In this section, a summary of the different approaches for the characterization of nanomaterials based on advanced techniques for electron microscopy is provided. High resolution STEM imaging provided information regarding the atomic structure of the nanoseeds, as well as the crystallographic nature of the structural defects found. The analysis of a tilt series of ADF-STEM images was used to identify nanoparticles that contained structural defects with statistically relevant distribution. Electron tomography was employed for the structural determination of overgrown core-shell structure, allowing the association of the crystallinity of the nanoseeds and the morphology of the final product. The acquisition and analysis of a multimode tomographic series of core-shell nanostructures was employed for the verification of the extension of the structural defect of the nanoseed to the overgrown structure. Analysis of the reconstructed slices also hinted the extension of the defect to the overgrown structure. The combination of the used advanced approaches for electron microscopy enabled the optimization of the synthesis protocols for the seed-mediated growth.

3.7 Author contribution

The author of the present thesis, Thaís Milagres de Oliveira, performed the HAADF- and ADF-STEM image acquisition, the statistical analysis, the tomographic reconstructions and 3D segmentation. High-resolution HAADF-STEM imaging was acquired together with Prof. Dr. Thomas Altantzis. Synthesis of gold nanotriangles and nanorods, oxidation etch procedure, growth of silver and gold nanoparticles, as well as the characterisation of grown products based on gold were carried out by the research team of Prof. Dr. Luis M. Liz-Marzán from the BioNanoPlasmonics Laboratory at CIC biomaGUNE, Spain.

The author of the present thesis contributed to this study by providing a statistical analysis of the defect yield for different systems, by demonstrating how the crystallinity of the seeds are connected with the morphology of final overgrown structures and by demonstrating that the crystallinity of the seeds is maintained during the growth process.

Chapter 4. Electron microscopy for the 3D characterisation of gold nanocrystals after nanosecond laser irradiation

4.1 Interaction of gold nanoparticles with ultrafast laser pulses

Because of the strong LSPR effect of gold nanoparticles, external electromagnetic illumination has been extensively applied to such nanoparticles[8,57,63,76,87,184]. More specifically, the study of the dynamics of coherent light-matter interaction enabled the understanding of various phenomena occurring in the ultrashort time scale[185–188]. For instance, femtosecond laser pulses provided access to the dynamics of bond formation and breaking during chemical reactions[185,189] and, together with short pulsed and continuous-wave lasers, they have contributed to the development of novel spectroscopies for the exploration of light-matter interaction phenomena[185,190].

Interestingly, studies based on laser pulses have been crucial to reveal the fast electron dynamics responsible for LSPR excitation and relaxation[79,185]. More specifically, due to the extremely high power intensity of lasers (10^7–10^{12} W/cm^2), deformation and/or disintegration of the nanocrystals can be readily induced[68,70,72,74–76,80,185,191–197]. In addition, as discussed in Chapter 1, the pulse duration determines the evolution of the shape of the irradiated gold nanoparticles. For instance, femtosecond laser pulses deposit energy extremely fast to the crystal lattice, resulting in an almost adiabatic expansion of the nanoparticles, due to the electron-phonon coupling, with duration of a few picoseconds[185,192,193,198–202]. Therefore, the relaxation processes mainly occur once the laser pulse has terminated. Under these conditions, the temperature may easily exceed the melting point of the bulk material, triggering events of shape modification. In the case of nanosecond laser pulses, the amount of energy absorbed by the nanoparticle is even higher due to the longer pulse duration. However, due to the lower energy deposition rate, the energy is still transferred to the nanoparticle when its lattice is already excited or in a molten state[70], resulting in nanoparticle fragmentation or size reduction due to the excitation of acoustic phonon modes[70,185,194,196,201,203–205].

More specifically, nanosecond laser pulses has been applied for the creation of a new shape type for nanoparticles, denominated "ϕ-shaped"[68,70,79,203]. This type of nanoparticles was obtained by nanosecond laser pulses interaction with single crystalline gold nanorods. It has been reported that initial states of such shape transformation corresponds to the addition of point defects that could be associated with a local melting of the crystal lattice. This serves as the nuclei for the formation of twin boundaries and stacking faults[79,203]. At the same time, surface melting takes place, due to the higher instability of surface atoms. In a thermodynamically stable system, the direction of heat diffusion is from the surface to the centre of the object, differently from what has been observed in nanorods

illuminated by nanosecond laser pulses[203]. Experimental observations suggested that, upon nanosecond laser pulses, heat was uniformly distributed across the object (due to the electron-phonon coupling), whereas the cooling of the surface atoms was faster than the bulk atoms. This resulted in a temperature gradient, explaining the molten state in the interior of the nanoparticle that leads the formation of defects[203].

4.2 The use of nanosecond laser pulses to induce the formation of structural defects in gold nanoparticles

Recent studies have demonstrated the ability of introducing defects in gold seeds by using an oxidative etching approach[32], as discussed in Chapter 3. Using this methodology, the maximum defect yield achieved was 51% for spherical seeds with sizes of 20 nm obtained from the oxidative etching of gold nanotriangles. It has been demonstrated in Chapter 3 that the crystallinity of the seed is maintained during the growth process and the seed crystallinity is directly associated with the final shape of the overgrown structures. However, the use of nanoparticles obtained from the oxidative etching process as seeds during the seed-mediated growth can result in the presence of multiple shapes, as demonstrated earlier in section 3.3 of Chapter 3. Thus, if one aims the growth of nanoparticles with only one type of shape, an approach that is capable to introduce defects with a yield larger than 90% is of great importance.

Inspired by the ability to introduce defects in mono-crystalline structures through nanosecond laser pulses irradiation, another approach for the synthesis of seeds with a high defect yield has been developed. Here, spherical nanoparticles were synthesised to deliver mono-crystalline structures with different sizes (10 nm and 20 nm). Next, the obtained nanoparticles were irradiated with nanosecond laser pulses (pulse duration of 8 ns at a wavelength of 532 nm and pulse frequency of 10 Hz) in the presence of different chemical elements (only 100 mM of CTAC or combined with 100 μM Ag^+ or 75 μM I^-). Characterisation of the nanoparticles before and after ultrashort laser pulses irradiation using electron microscopy enabled the determination of the optimal conditions for the formation of specific structural defects, as well as the verification of the efficiency of the approach.

4.3 The effect of environmental conditions during laser irradiation on the crystal structure of nanoparticles

Here, we aimed at investigating the effect of silver ions (Ag^+) and iodide (I^-) on the morphology and internal structure of gold nanospheres irradiated with nanosecond pulsed laser (see Table 4-1). Such additives play an important role in the controlled synthesis of gold nanoparticles with different morphologies due to their ability to adsorb on the different gold facets. Thereby, Ag^+ and I^- can

determine the shape adopted by gold nanoparticles, giving rise to nanorods, nanostars or nanotriangles among others. Thus, we hypothesize their ability to adsorb on gold facets can also impact the nanoparticle interaction with nanosecond laser pulses and the heating-cooling dynamics.

Sample	Size (nm)	Irradiation Conditions	Experimental conditions
10 Control	10	No irradiation	100 mM CTAC
10 CTAC		0.2 J/cm^2 5 min	100mM CTAC
10Ag			100 mM CTAC + 100 µM Ag^+
10I			100 mM CTAC + 75 µM I^-
20 Control	20	No irradiation	100 mM CTAC
20CTAC		0.2 J/cm^2 5 min	100 mM CTAC
20Ag			100 mM CTAC + 100 µM Ag^+
20I			100 mM CTAC + 75 µM I^-

Table 4-1 – Summary of the experimental conditions used during laser irradiation of gold nanoparticles.

Preliminary analysis based on STEM images of the 20 nm nanoparticles irradiated in the presence of only CTAC (20CTAC) revealed that the size of nanoparticles decreased from 21 ± 1 nm to 16 ± 2 (Figure 4.1.a). However, for nanoparticles irradiated in the presence of CTAC and Ag^+ ions (20Ag) the presence of very small particles (<3 nm) was also found (red arrow in Figure 4.1.b). The presence of such small nanoparticles for 20Ag nanoparticles suggest the occurrence of particle fragmentation. Besides, the formation of irregular shapes was also found (Figure 4.1.b-c), corroborating the hypothesis of particle fragmentation events upon laser irradiation. . Moreover, spectroscopic investigations by EDX (Figure 4.1.c-f) revealed the formation of a silver shell on the gold nanoparticles, giving rise to bimetallic nanoparticles (gold and silver core-shell structure). The amount of silver estimated from the obtained EDX spectrum indicated that ca. 22.5% of the resulting core-shell structure was composed with silver. Since the melting point of silver is approximately 103 K lower than that of gold, the photo-reduction of silver induced by the laser might decrease the energy require to melt the nanoparticles. In this manner, it might be possible to explain the larger fraction of fragmented nanoparticles observed when silver ions were present during the irradiation process, as the present core-shell nanoparticles may have a lower melting temperature and be more easily fragmented.[85,206–208]. It is important to note that the addition of other adsorbing additives such as I^- did not lead to significant differences in nanoparticles fragmentation compared to those irradiated only in CTAC. This

might be caused by the incapability of I^- to get incorporated into the gold nanocrystals and to modify the nanoparticle melting point. Nevertheless, such hypothesis would require more investigations to be confirmed.

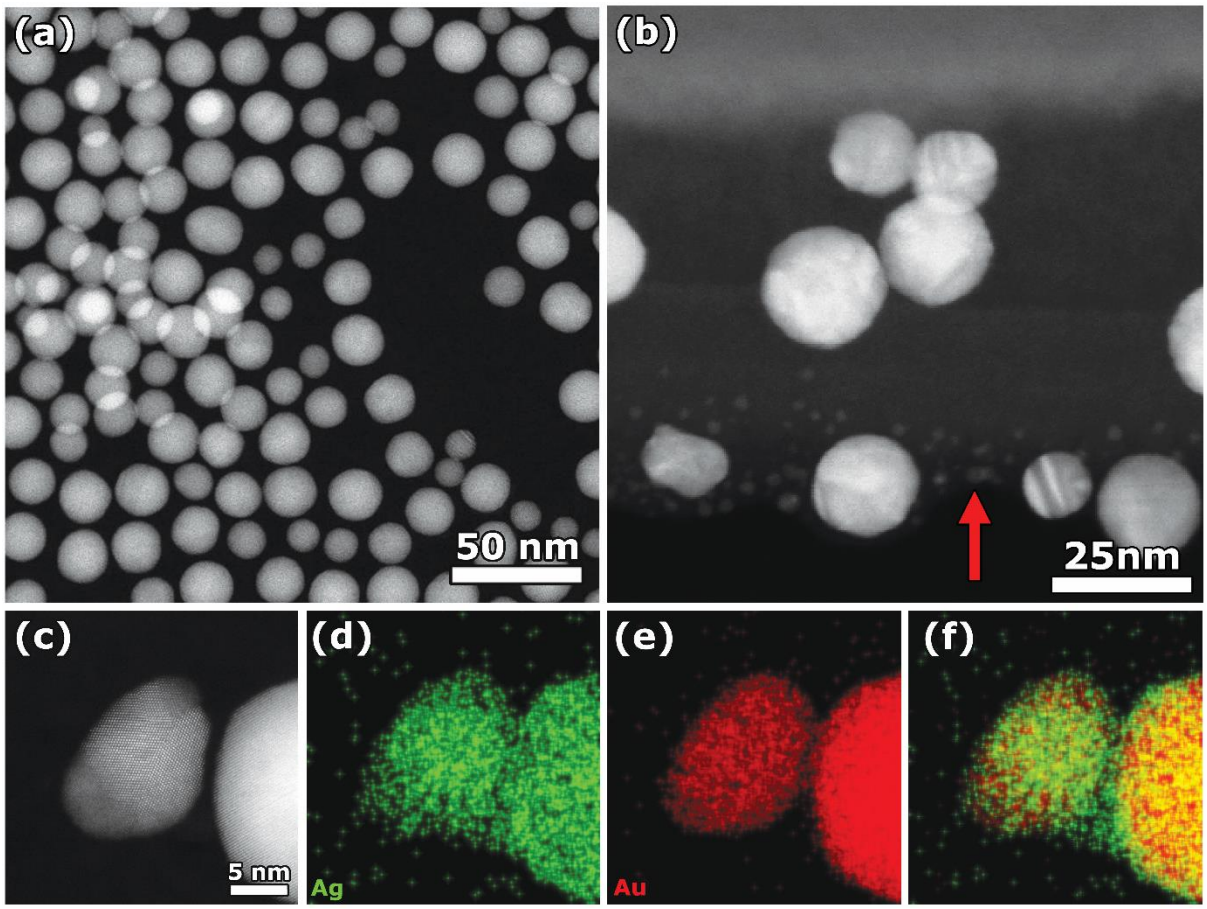

Figure 4.1 – HAADF-STEM images of 20 nm nanoparticles irradiated with nanosecond laser pulses in the presence of (a) CTAC and (b) CTAC + Ag^+. Nanoparticles smaller than 3 nm (red arrow) indicated that fragmentation events occurred during laser irradiation. Moreover, nanoparticles with anisotropic shapes were observed. (c) HAADF-STEM image of a nanoparticle with an irregular shape. (d)-(e) EDX spectroscopic confirmed the formation of gold and silver core-shell nanoparticles. In (f) a superposition of the gold and silver chemical maps distribution is shown.

Interestingly, the presence of I^- during the irradiation was found to impact the defects formation in the gold nanoparticles in a different manner compared to that of CTAC or CTAC and Ag^+, as revealed by high-resolution HAADF-STEM imaging (Figure 4.2). The analysis shown the presence of different types of defects, such as twin and grain boundaries, when the 20 nm nanoparticles were irradiated in the presence of CTAC or CTAC and Ag^+ (Figure 4.2). However, only twin boundaries were found when I^- was present. The absence of grain boundaries upon laser irradiation under such conditions might be explained by an enhanced diffusion of the gold atoms at the nanoparticle surface

induced by I^-, thereby helping to form twin boundaries as a way to reduce the strain created by grain boundaries[88,178–183]. However, further investigations are required to properly address this phenomenon. Additionally, high-resolution imaging of 10 nm nanoparticles revealed the presence of only twin boundaries (Figure 4.3).

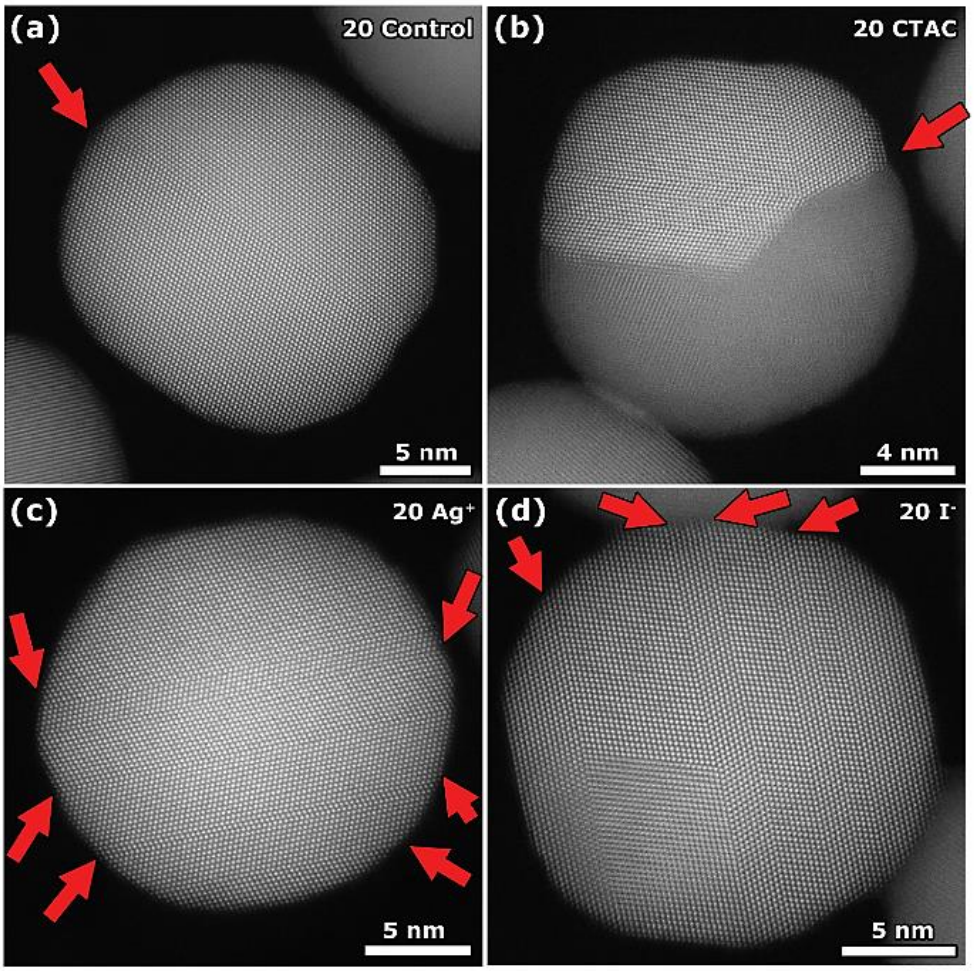

Figure 4.2 – High-resolution HAADF-STEM images of structural defects in 20 nm nanoparticles (a) before and (b)-(d) after irradiation with nanosecond laser pulses. The effect of the chemical species in solution during the laser irradiation on the defect type was investigated. For (b) 20 nm nanoparticles in the presence of 100 mM CTAC, multiple twin boundaries and grain boundaries were encountered. In presence of CTAC and Ag^+, (c) irregular shapes were found in addition to the previous mentioned case. For 20 nm nanoparticles irradiated by laser pulses in the presence of CTAC and I^-, multiple twin boundaries were observed (d).

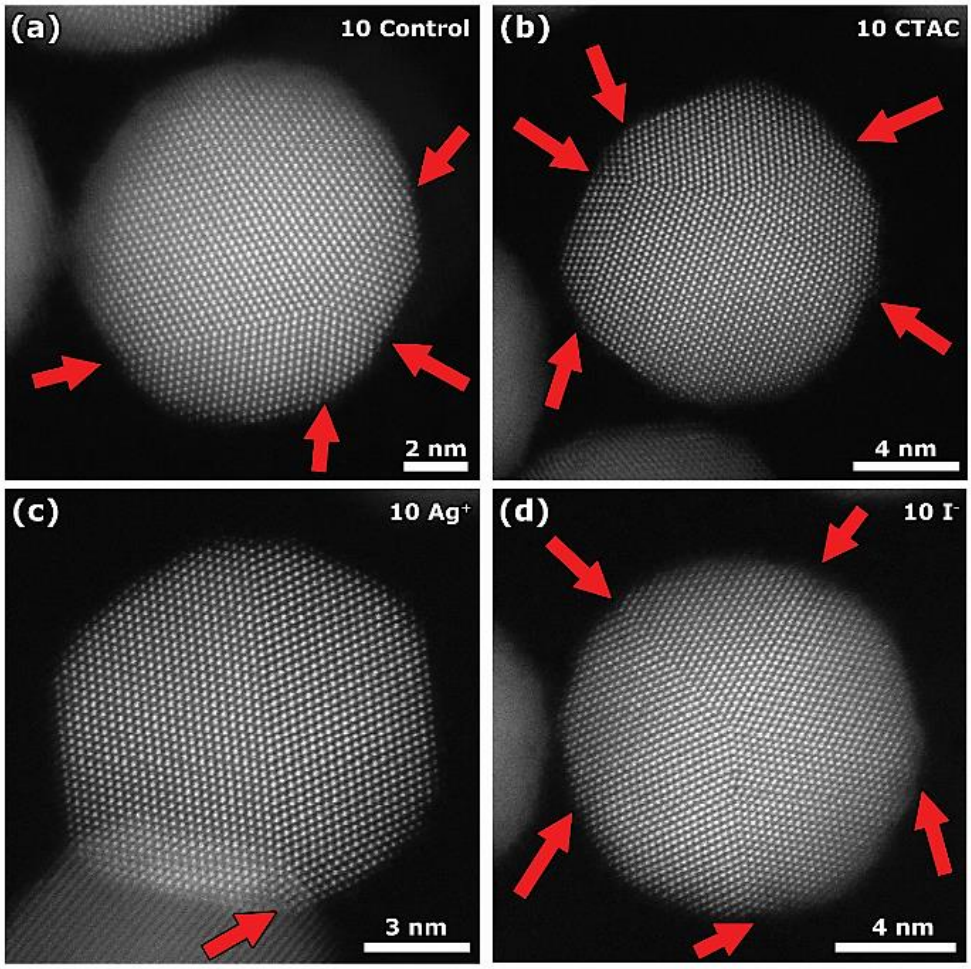

Figure 4.3 – High-resolution HAADF-STEM images of structural defects in 10 nm nanoparticles (a) before and (b)-(d) after irradiation with nanosecond laser pulses. The effect of the chemical species in solution during the laser irradiation on the defect type was investigated. For (b) 10 nm nanoparticles in the presence of 100 mM CTAC, multiple twin boundaries were observed. In presence of CTAC and Ag^+, low-index facets and twin boundaries were found (c). For 10 nm nanoparticles irradiated by laser pulses in the presence of CTAC and I^-, multiple twin boundaries were observed (d).

Finally, to determine the efficiency of defects introduction into the crystal lattice of gold nanoparticles by nanosecond laser pulses, a statistical comparison between the total number of defects before and after laser interaction is required. Therefore, the same approach used for the acquisition of a tilt series of images in ADF-STEM mode, as described in section 3.3 of Chapter 3, was used. The results on the statistical analysis are presented in Figure 4.4.

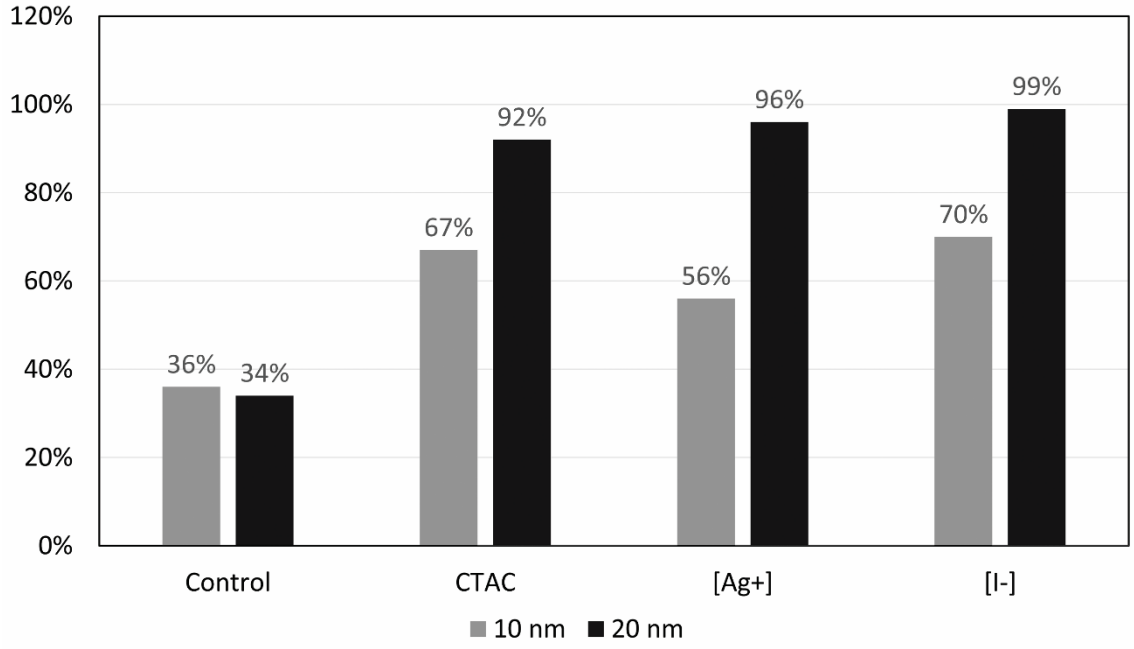

Figure 4.4 – Statistical distribution of the total number of defects present in the crystal lattice of spherical nanoparticles before and after laser irradiation, based on the analysis of 2D images. Three different cases were investigated, where the nanoparticles were irradiated by the laser pulses in the presence of: 100 mM of CTAC, 100 mM of CTAC and 100 µM of Ag^+, and 100 mM of CTAC and 75 µM of I^-. In general, a higher defect ratio for larger nanoparticles was observed.

The characterisation of the as synthesized 10 nm and 20 nm nanospheres (before laser irradiation) revealed that ca. 35% of the nanoparticles were initially twinned. However, their irradiation with nanosecond laser pulses significantly increased the number of defects. For example, analysis of 10 nm nanospheres showed that the proportion of defects was doubled after laser irradiation, independently of the chemical environments (see Table 4-1), although a slightly higher number of defects was observed in the presence of I^-. Moreover, the introduction of defects was found to occur more efficiently in the case of 20 nm nanospheres than in the 10 nm ones, i.e., 92-99% vs 56-70%. The lower yield of defect introduction observed in the case of the 10 nm nanoparticle might be related to the cooling dynamics of the nanoparticles, which depends on the surface-to-volume ratio among other parameters[185,209]. Due to the faster cooling of smaller nanoparticles, it might be possible that the temperature reached by 10 nm nanospheres during laser irradiation was smaller than in the case of the 20 nm nanospheres. If we assume the introduction of defects is favoured at high temperatures, that may explain why their introduction is less efficient for the smaller nanoparticles.

4.4 The use of nanosecond laser pulses to create hollow nanoparticles

Most interestingly, 20 nm nanoparticles displayed a variation of contrast upon nanosecond laser pulses in the presence of 100 mM CTAC or in combination with I^- ions, as indicated by the red arrows in Figure 4.5.

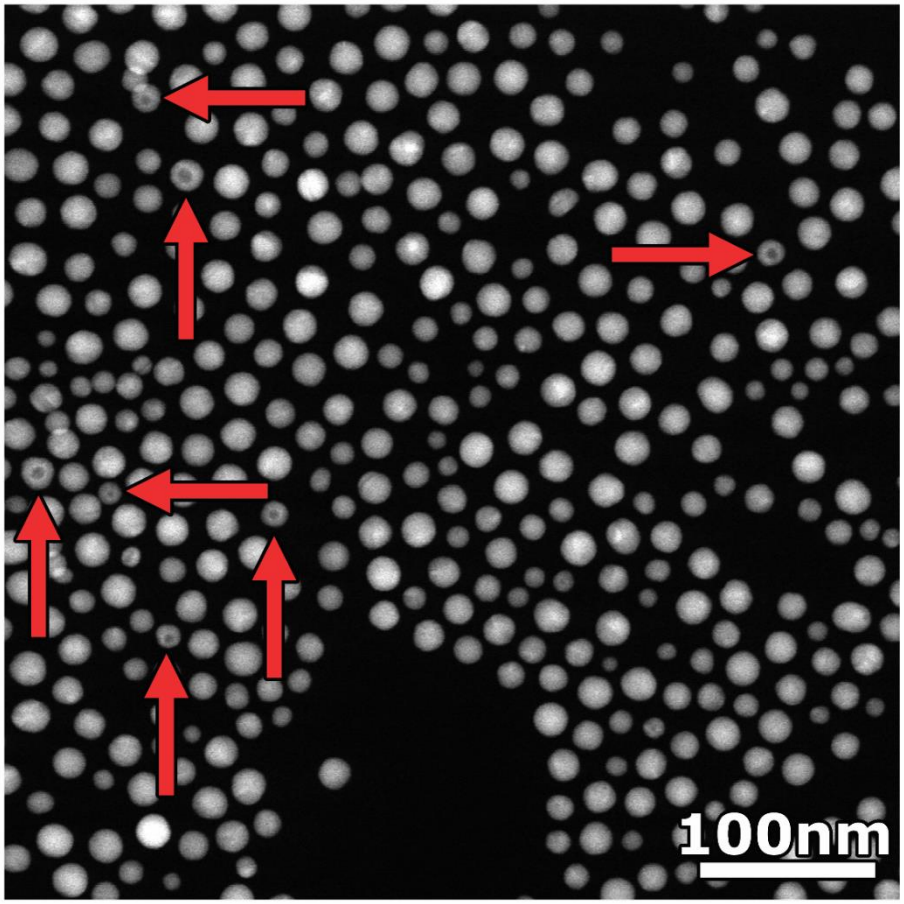

Figure 4.5 – HAADF-STEM image of 20 nm nanoparticles irradiated by nanosecond laser pulses in the presence of 100 mM CTAC. A variation of particle size is visible as well as the variation of contrast in some particles indicated by the red arrows.

Because the contrast in HAADF-STEM images depends on the chemical composition and the thickness of the object, the darker region in some nanoparticles in Figure 4.5 could correspond to different structures, such as core-shell nanostructures or hollow nanoparticles. The formation of a porous array inside the cavity is excluded prior to STEM analysis due to treatment approaches applied on the investigated nanoparticles. Previous studies have demonstrated that porous gold structures are fabricated using methods such as dealloying, self-assembly, templating and electrochemical anodization[210], which were not employed in the present discussion.

In order to determine the structure of such nanoparticles, spectroscopic techniques were applied. EDX mapping confirmed the presence of only gold, as indicated in Figure 4.6. Moreover, the spectral map with the chemical distribution of gold revealed a decrease in the intensity in the region corresponding to the darker contrast in the HAADF-STEM image, suggesting this structure corresponds to a hollow nanoparticle.

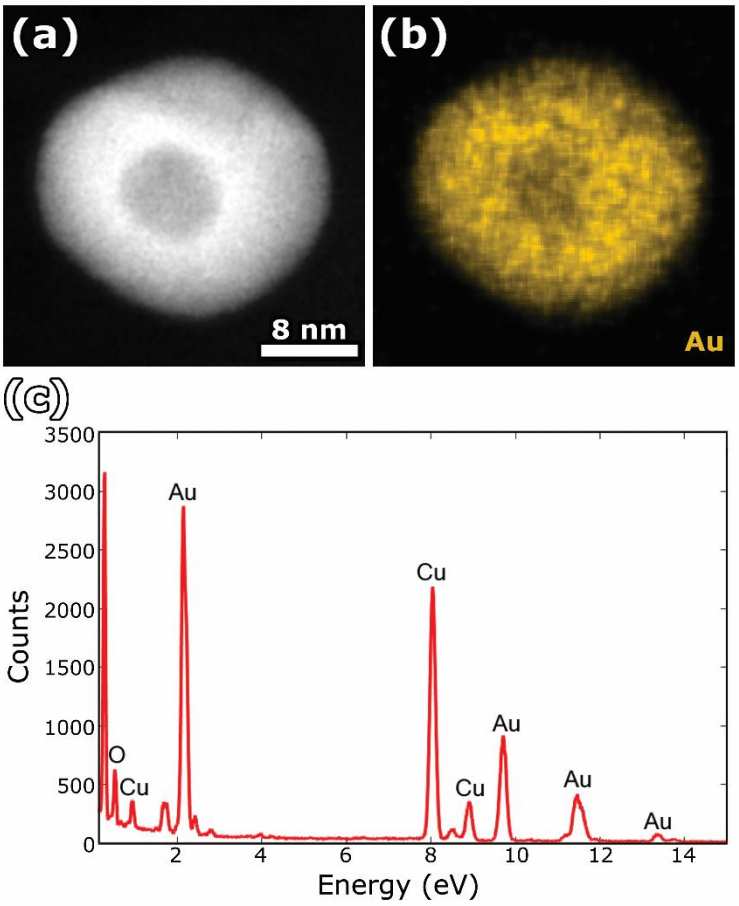

Figure 4.6 – (a) HAADF-STEM image of nanoparticle containing a cavity. (b) Chemical distribution of gold along the region of interest shown in (a). (c) Energy spectrum of the region of interest. The presence of copper is attributed to the TEM grid.

The formation of the observed hollow nanostructures for only larger particles (20 nm) might be linked with the higher temperature achieved by the nanoparticle when compared to smaller sizes, as well as the occurrence of expansion and material loss of the object during the laser irradiation[185]. The absence of cavities in nanoparticles irradiated by the laser pulses in the presence of Ag^{+} could be associated with the observed higher rate of particle fragmentation and explosion.

Moreover, the conditions for the formation of cavities were further investigated[185]. The aim of the study was to associate the formation of cavities with the pulse duration, the concentration of

surfactant (CTAC) and the size of the nanoparticles. Therefore, 20 nm nanoparticles were irradiated by nanosecond laser pulses with laser fluence of 0.1 J/cm^2 and the structures remained almost intact (Figure 4.7.a). By increasing the laser fluence to 0.2 J/cm^2, a size reduction from 21 ± 1 to 16 ± 2 nm was observed, as well as the formation of cavities in 17% of the nanoparticles. By further increasing the laser fluence to 0.3 J/cm^2, the absence of cavities and a notable size reduction to 13.5 ± 2 nm (Figure 4.7.b) were observed. This suggest that the range of the laser pulse fluences that induce the formation of hollow nanostructure is rather narrow[185]. The next parameter to be evaluated is the concentration of the surfactant. When the CTAC concentration was reduced to its corresponding critical micelle concentration (1.0 mM), two well-defined size populations of 6 ± 2 nm and 18 ± 3 nm were obtained upon irradiation of 20 nm gold nanoparticles with 0.2 J/cm^2 pulses (Figure 4.7.c), however cavities were not formed. Upon increasing the CTAC concentration to 25 and 100 mM (Figure 4.7.d), cavities were formed again. Therefore, these findings demonstrated that the surfactant concentration had a strong effect on the fragmentation process and cavity formation[185]. Nevertheless, the greatest impact on the nanocrystal morphology and cavity formation was found when varying the size of the irradiated gold nanoparticles. Whereas 10 nm gold nanoparticles (10 ± 1 nm) remained largely unaffected by the laser pulses (0.2 J/cm2), 40 nm gold nanoparticles evolved into a large number of fragmented nanostructures, some of them containing large cavities of up to 20 nm (Figure 4.7.e-f). In particular, irradiation of 40 nm gold nanoparticles at low surfactant concentrations (i.e., the optimal conditions to induce fragmentation) resulted in irregular nanostructures with large cavities, as reflected in the broadening of the extinction band and increased absorption in the near infrared range[185]. The effect of the particle size is likely related to two effects. First, bigger particles remain hot for longer periods of time because the heat release rate depends on the surface-to-volume ratio, which is proportional to 1/R[209]. Second, the mechanism behind cavity formation may involve stretching of the nanoparticle and/or material loss. Hence, larger gold nanoparticles are less affected by the leakage of atoms and better suited to re-assemble and also to support larger cavities, as observed experimentally.

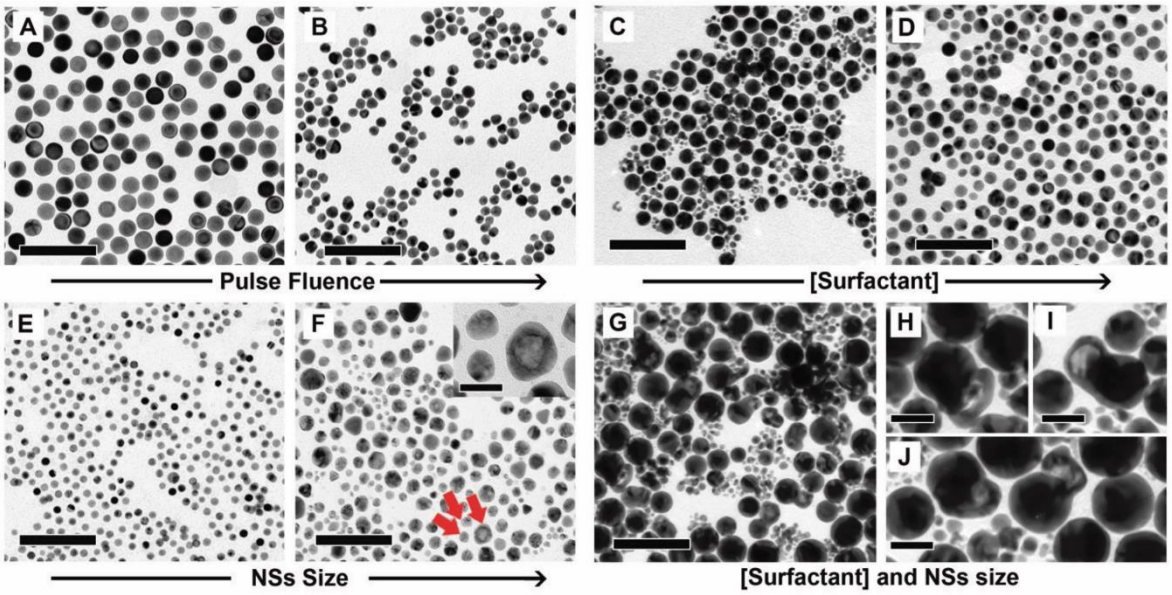

Figure 4.7 – TEM analysis, showing the effect of pulse fluence, surfactant concentration, and particle size on the formation of gold nanoparticles with cavities. (a)-(b) gold nanoparticles obtained after exposure of 20 nm gold nanoparticles in 25 mM CTAC to 0.1 J/cm2 (a) and 0.3 J/cm2 (b) laser pulses. (c)-(d) gold nanoparticles resulting from irradiation of 20 nm gold nanoparticles with 0.2 J/cm2 pulses in the presence of 1 mM (c) and 100 mM (d) CTAC. (e)-(f) Effect of irradiation with 0.2 J/cm2 pulses on 10 nm (e) and 40 nm (f) gold nanoparticles suspended in a 25 mM CTAC solution. Red arrows point to particles with holes, which are magnified in the inset. (g)-(j) Low and high magnification images of nanostructures produced upon irradiation of 40 nm gold nanoparticles in the presence of 1 mM CTAC. Black arrows below the images indicate the direction of magnitude increment. Scale bars: 100 nm (a)-(g) and 20 nm (f) inset, (h)-(j). Figure extracted from [185].

4.5 3D characterisation of the presence of cavities at the atomic level

To clarify the shape of the cavity in hollow nanoparticles and to evaluate a possible connection with the outer surface of the nanoparticle, electron tomography was applied to several nanoparticles containing holes. Figure 4.8 exemplifies a typical slice through the 3D volume and its isosurface rendering. The series were acquired over a tilt range from −72° to +72°, with tilt increment of 2 or 3°, with dwell time of 6 µs at the ThermoFisher Tecnai G2 microscope operated at 200 kV. As it can be seen from the 3D reconstruction, the cavity is enclosed. A statistical analysis revealed that 17% of the total of nanoparticles are hollow, with average size of 15.2 ± 4.7 nm. The average cavity size measured over 9 reconstructed volumes was 4.5 ± 2.0 nm, where the smallest distance from the edge of the cavity to the closest surface of the nanoparticle was, on average, 3.1 ± 1.4 nm. Therefore, our results indicated that the cavities were not always exactly in the centre of the nanoparticles.

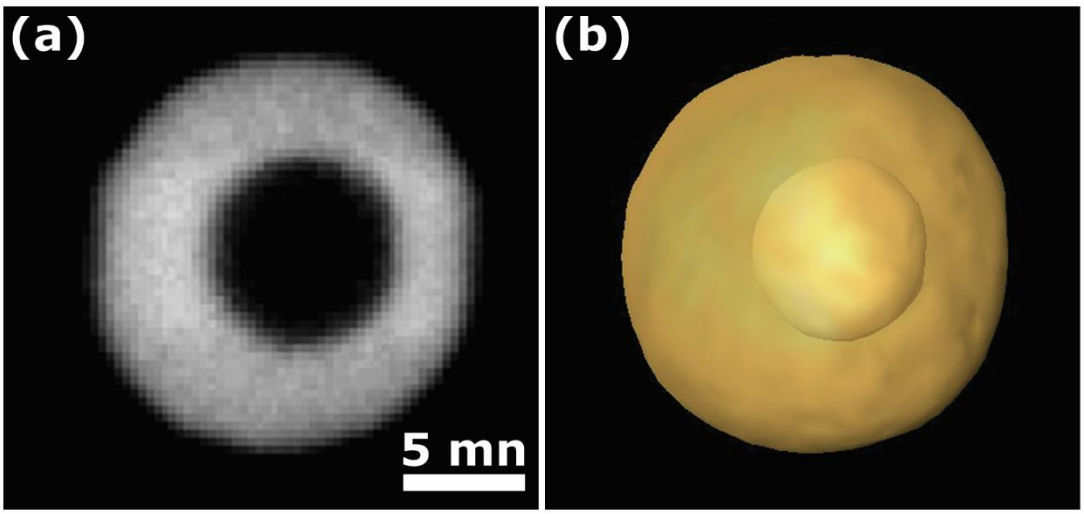

Figure 4.8 – 3D reconstruction by electron tomography of a hollow nanoparticle. (a) Slice through the 3D volume and (b) isosurface rendering of the reconstruction, confirming the absence of connection between the cavity and the external surface of the nanoparticle.

So far, the impact of pulsed laser pulses on metal nanoparticles has been mainly explored by ensemble measurements such as extinction spectroscopy or transient absorption spectroscopy[195,211,201,199]. For example, Fales and co-workers carefully examined the impact of nanosecond pulses of different fluences on spherical gold nanoparticles of different sizes by large-scale electron microscopy and extinction spectroscopy. Although single particle measurements revealed more insight into the deformation mechanism[71,212,213], these studies mainly looked at the size and shape of the laser-irradiated NPs. For instance, it was revealed that curvature driven surface diffusion leads to below melting point reshaping of gold nanorods and this process strongly depends on the aspect ratio of the nanorod[212]. However, to fully understand the impact of laser pulses on metal nanoparticles it is important to not only study their size and shape after laser irradiation, but to go further and characterize at the atomic structure. Since the atomic structure of metal nanoparticles strongly influences their mechanical and optical properties[7], the impact of laser pulses on these properties needs to be studied. Up to this point, no research has been reported that describes the influence of pulsed laser irradiation on the three dimensional crystal structure of metal nanoparticles.

As shown in Figure 4.8, conventional electron tomography is not capable to reveal the crystal nature of the defects and cavities of hollow nanoparticles. The use of high-resolution HAADF-STEM only provides partial information, as it only represents a 2D projection of a 3D object (Figure 4.9). Interestingly, high-resolution HAADF-STEM imaging suggested that in some cases, the twin boundaries also propagated through the cavities. For a thorough understanding of the atomic structure of hollow

nanoparticles and how defects are distributed, a full 3D characterisation of nanomaterials at the atomic level is required.

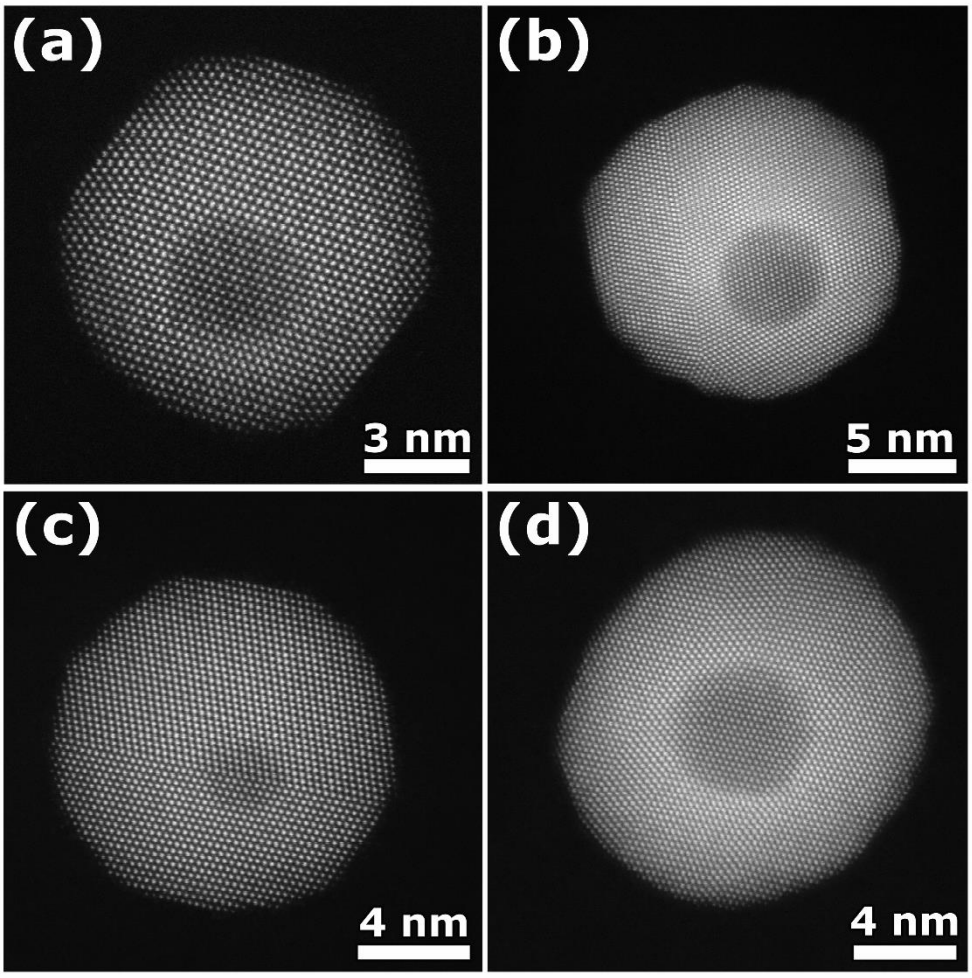

Figure 4.9 – High-resolution HAADF-STEM images of different hollow nanoparticles obtained upon nanosecond laser pulses in the presence of I^-. (c) and (d) suggested that twin boundaries propagated through the cavity region.

In the present study, hollow nanoparticles obtained upon laser interaction in the presence of I^- were investigated in 3D at the atomic level. This choice relies on the absence of grain boundaries in nanoparticles produced under this condition, as grain boundaries may complicate the 3D characterisation at the atomic scale. The unknown crystallographic nature of hollow nanoparticles prevents the use of any prior information commonly used in state-of-the-art techniques for electron tomography at the atomic level as mentioned in Chapter 2. Recently, a new methodology has been developed where the optimization of the acquisition in combination with the improvements of image processing and alignment enabled the 3D reconstruction of the atomic structure of nanomaterials using a conventional SIRT algorithm during which no prior knowledge about the structure of the

material is used[150]. This technique exploits a fast acquisition of multiple frames at every tilt angle, rather than one image acquisition at a longer exposure time. In this manner, we were able to minimize slight rotations and drift of the nanoparticles while imaging, which is a common problem when imaging in HAADF-STEM mode[150]. Scanning artefacts are corrected with the use of a convolution neural network (CNN) combined with rigid and non-rigid transformations, and finally, a phase correlation approach with subpixel accuracy is applied for the alignment of the tilt series. All the mentioned steps for image processing were developed by Dr. Ivan Lobato and are explained in more detail in Appendix A.

Figure 4.10 displays the volume rendering and slices through the 3D reconstruction of the hollow nanoparticles from Figure 4.9.a and Figure 4.9.c, respectively. For the acquisition of the atomic resolution tomography series, we recorded a time series for each projection with a fast acquisition scheme (dwell time of 0.4 µs) using an aberration-corrected 'cubed' ThermoFisher Titan 60-300 electron microscopes operated at 300 kV. The series were acquired within a tilt range from −72° to +72°, with tilt increment of 2°.

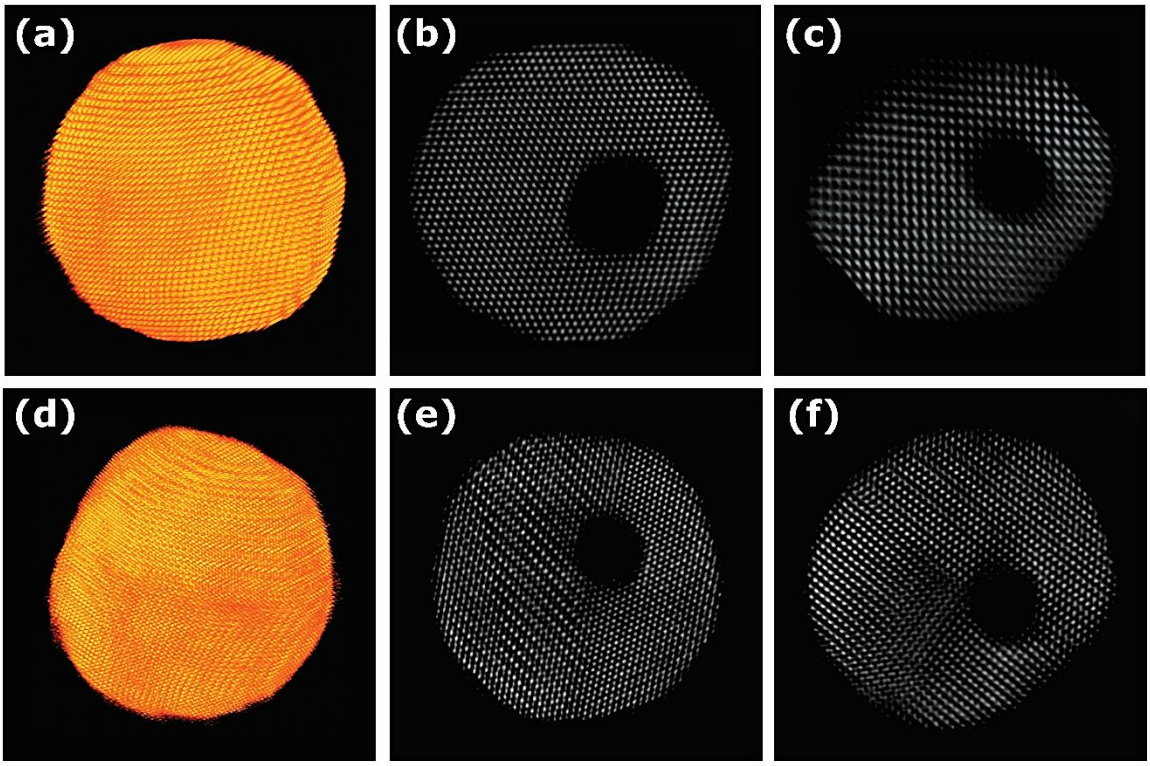

Figure 4.10 – (a) Volume rendering of the hollow nanoparticle shown in Figure 4.9.a. Slice through the 3D reconstruction oriented along the (b) [110] and (c) [100] zone axes. The same representations for the hollow nanoparticle shown in Figure 4.9.c are displayed in (d)-(f).

Analysis through slices along different crystallographic axes revealed the presence of facets at the cavities inner surface. Figure 4.11 shows the volume rendering of both reconstructions with a cut through the 3D reconstruction along the orientations shown in Figure 4.10.b and Figure 4.10.e. Indexation of each facet of the cavity was performed based on the Fourier transform of a reconstructed slice at the cut plane. In Figure 4.11.b, a twin plane is crossing the cavity at the middle. Because of this, the orientation of the facets in the blue region and the yellow region are not complementary.

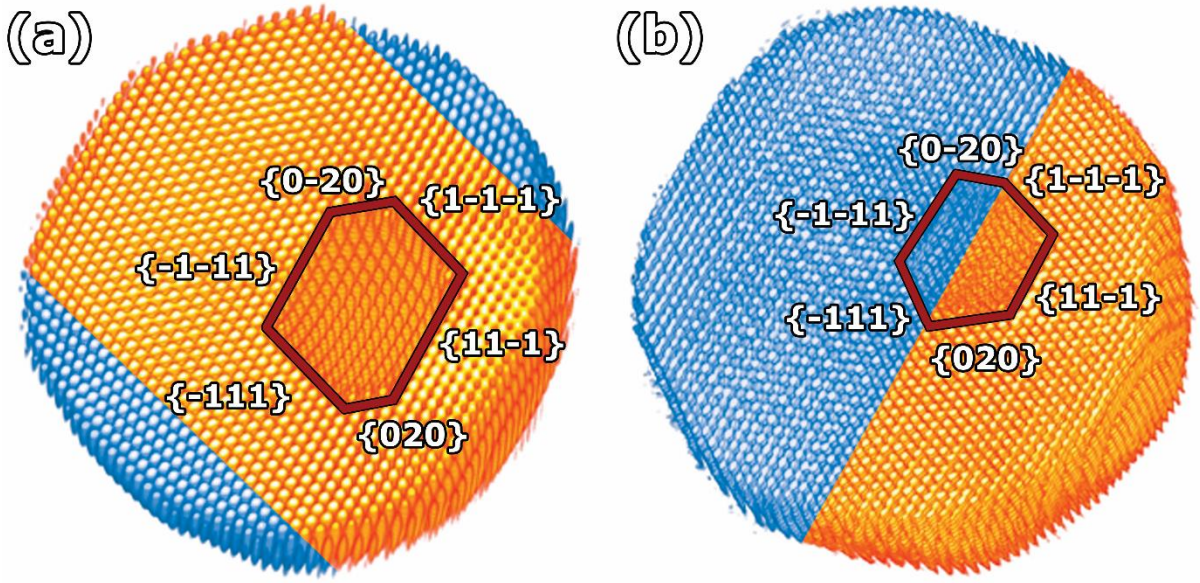

Figure 4.11 – Volume rendering of both reconstructions with a cut across the volume along the orientations shown in Figure 4.10.b and Figure 4.10.e, revealing the atomic arrangement at the region of the cavity in 3D. The red lines represent the facets at the surface of the cavity, which were indexed based on the Fourier transform of the slices shown in Figure 4.10.b and Figure 4.10.e, respectively. The blue regions represent a different crystallographic orientation, due to the presence of twin planes.

To further investigate if the presence of cavities was associated with the build-up of stress in the crystal structure, Geometric Phase Analysis (GPA) was applied to the 3D atomic structure of the hollow nanoparticles. This study is of interest, as the presence of strain in the crystal lattice of nanoparticles could alter their optical properties[214–216] (a change on the scattering cross section of the free electrons results in the modification of the dielectric constant and therefore in the refractive index of the material[40]), for instance. The used methodology quantifies the displacement and strain fields of crystalline arrangements, by means of image processing associated with Fourier filtering. As a result, the strain tensors ε_{ij}, with units of length, can be derived. Typically, such analysis is performed using 2D images, but here, the approach was applied in 3D[112,217]. Goris and co-worker have demonstrated that the analysis of lattice strain of a gold nanodecahedra based on projection images

lead to different conclusions than obtained from a 3D analysis[113], demonstrating the need to extend the GPA analysis to 3D.

The approach for the 3D characterisation of lattice strain was implemented in MATLAB based on the studies of Hytch et al[217] and Goris at al[112], where three reciprocal lattice non-collinear reflections were chosen from a region free of defects. The chosen reflections were used to calculate a mask to filter out the information associated with the other reflections. After applying the mask to the Fourier transform of the 3D reconstruction, an inverse of the resultant reconstruction was taken. Next, the phase and its gradient could be retrieved. From the gradient of the phase, the full 3D strain tensors ε_{xx}, ε_{yy} and ε_{zz} were extracted. In order to reduce the noise and to smooth the resulting displacement field images, a 3D Gaussian mask was used, yielding a spatial resolution of 0.7 nm[112,217]. For the visualization, only one slice along the 3D object was chosen. To determine the error bar of the strain fields, a gold nanosphere was simulated, where some atoms were deviated from the perfect position. The atoms were approximated by Gaussian spheres and projection images were generated using the Astra Toolbox[175]. The reconstruction was carried out using SIRT algorithm implemented in MATLAB. A reference region for the calculation of the strain fields was chosen in the middle of the crystal, where no deviations were present. The strain fields for both simulated and reconstructed volumes were performed in an identical manner as for the experimental data (Figure 4.12). By using the strain fields obtained from the simulated object as the ground truth, the error bars were determined and is equal to ±1.6%.

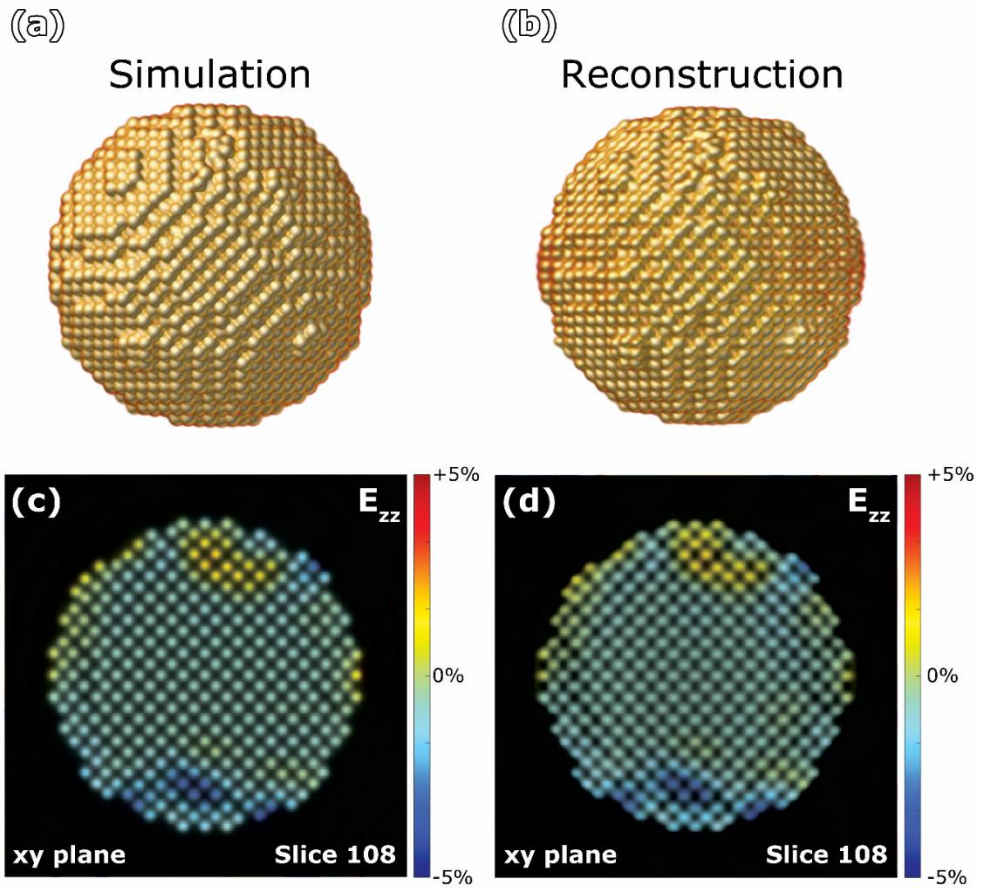

Figure 4.12 – Determination of the error bars for the strain fields based on 3D GPA. (a) Simulated object with a given relaxation to the system and (b) the reconstructed volume based on the projection images of the simulated object. Strain ε_{zz} map for specified orthoslice of the simulated (c) and reconstructed (d) volumes, overplayed with the atomic plane of the respective 3D objects. The calculated error of the strain fields corresponds to 1.6%.

Figure 4.13 displays a colour map of the atomic displacement (with respect to a reference region that is defect-free) for a single slice through the object, ranging from -3 to +3% from the perfect atomic positions. This figure was obtained from the superposition of the atomic structure with the calculated 3D strain tensors ε_{yy}. Our results revealed the presence of effects of surface relaxation are observed on the surface of the nanoparticle. More specifically, relaxation effects are observed on the left surface of the nanoparticle (red atoms), in agreement with the discussion presented in section 1.2.1. Besides, relaxation effects has also be found close to the vicinity to twin boundaries at the top and bottom of the nanoparticle. Due to the different crystallographic orientation, the blue regions indicated in Figure 4.11 are not shown in strain analysis. More interestingly, a small surface relaxation has also been observed at the surface of the cavity, at the rightmost facets ({11-1} and {1-1-1}).

Besides, the aforementioned facets are the closest to the nanoparticle surface. Such localization suggests a possible connection with the observed surface relaxation at the right side of the cavity.

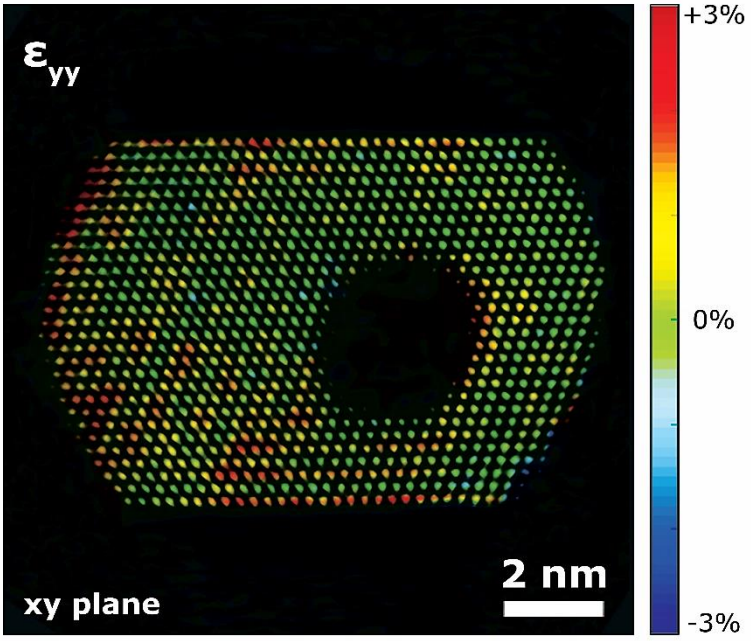

Figure 4.13 – Strain field ε_{yy} map through a slice of the 3D volume, obtained from 3D GPA. The region at the top and bottom of the nanoparticle correspondent to a different grain orientation was omitted from the strain analysis. Effects of surface relaxation are observed on the surface at the left side of the nanoparticle (red atoms), as well as close to the vicinity to twin boundaries at the top and bottom of the nanoparticle. A small surface relaxation has also been observed at the inner surface of the cavity, at the rightmost facets ({11-1} and {1-1-1}).

4.6 Determination of the composition in the cavity's interior

For the potential use of hollow nanoparticles in future applications, it is crucial to determine if the cavity is empty or e.g. filled with organic materials or water vapour. This can not be determined by the EDX map in Figure 4.6, since organic materials or water vapours are mainly composed of low mass chemical elements. Additionally, because electron tomography was performed in HAADF-STEM mode, the detection of organic compounds was impossible due to a lack of contrast.

The presence of organic elements inside the cavity was therefore investigated by EELS measurements. Hereby, an aberration corrected 'cubed' ThermoFisher Titan 60-300 operated at 120 kV was used. The exposure time for the EELS acquisition was 5 s. The analysis of the spectra was carried out in Digital Micrograph. To map the resulting signal, two window background (before and after the edge) were estimated as power laws in the following range: 277-325 eV for carbon, 395-444 eV for nitrogen and 532-580 eV for oxygen. Figure 4.14 shows the resulting maps for the oxygen, nitrogen,

and carbon distributions. Oxygen was mainly present at the surface of the particle, most likely due to partial oxidation of the surface ligands (Figure 4.14.b). Nitrogen was uniformly distributed over the entire scanned region (Figure 4.14.c), which is not surprising considering that the particle was lying on a silicon nitride support. The darker region in the upper right corner of Figure 4.14.d can be attributed to beam damage of the thin support (5 nm of thickness). The signals of both elements, oxygen and nitrogen, did not show any significant enhancement in the region of the cavity. However, a local increase of the carbon signal was clearly visible inside the cavity (Figure 4.14.d), indicating the presence of organic compounds, most likely surface ligands. Due to the chemical composition of such ligands (CTAC – $C_{19}H_{49}CIN$), an increase of oxygen levels inside the cavities is in principle not expected, while a very small fraction of nitrogen is present. Carbon could also be observed on the surface of the particle, due to the presence of CTAC. An especially high concentration of carbon was detected in between particles, due to the accumulation of CTAC molecules[185]. We therefore confirm the presence of organic contents inside the cavities. This knowledge is of importance for the understanding of the formation mechanism of the cavities in hollow nanoparticles, as will be shown in section 4.8.

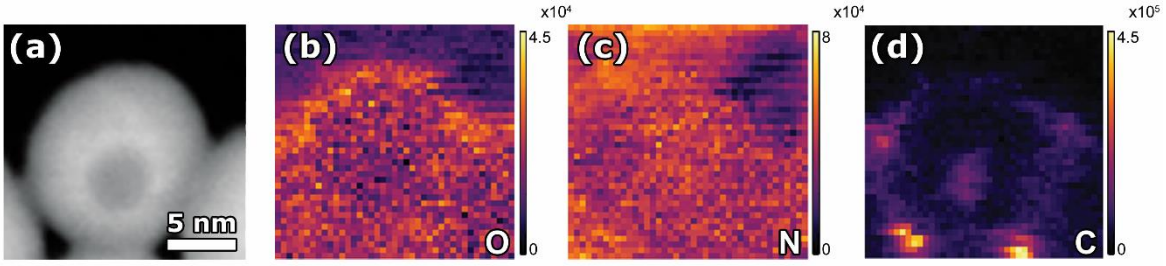

Figure 4.14 – (a) Scanned region for EELS measurements. (b)-(d) Elemental mapping of oxygen, nitrogen, and carbon in the scanned region, respectively. Figure extracted from [185].

4.7 3D investigation of the defect behaviour under in-situ heating environmental conditions

An interesting case where the dynamics of nanoparticles could be investigated under *in-situ* heating conditions is the evolution and response of the cavities in hollow nanostructures obtained after interaction with nanosecond laser pulses (section 4.4). The behaviour of the cavities in 56 hollow nanoparticles under increasing temperature conditions was first investigated in 2D. The system was heated to specific temperatures for 5 minutes. Then, the sample was quenched to room temperature and image acquisition was performed for different sets of particles. This process was repeated at room temperature and from 100 to 800 °C, with intervals of 100 °C, as indicated in Figure 4.15. Our results revealed that heating of the nanoparticles until 100°C presented no substantial change in the hollow nanoparticles. Starting from 200°C, some cavities disappeared, as indicated by the red arrows Figure

4.16. At 800°C, 9 cavities were totally eliminated from the hollow nanostructures. Figure 4.17 shows the different regions where hollow nanoparticles were investigated in *in-situ* conditions, at room temperature and at 800 °C. In summary, our results revealed that 55% of cavities were eliminated upon heating at 800°C.

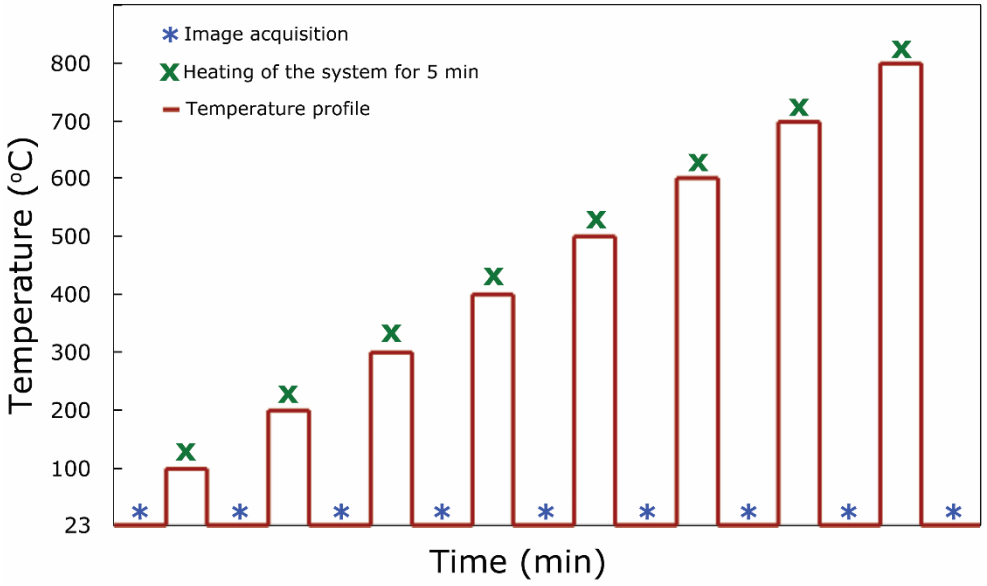

Figure 4.15 – Temperature evolution of the investigated system during *in-situ* heating tomography experiments. The red line (–) indicates the temperature profile during the experiment. The nanoparticles were heated to specific temperatures for five minutes (green x), followed by a quenching of the temperature, where image acquisition took place (blue *). The time axis is not in scale and is represented only in a qualitative manner.

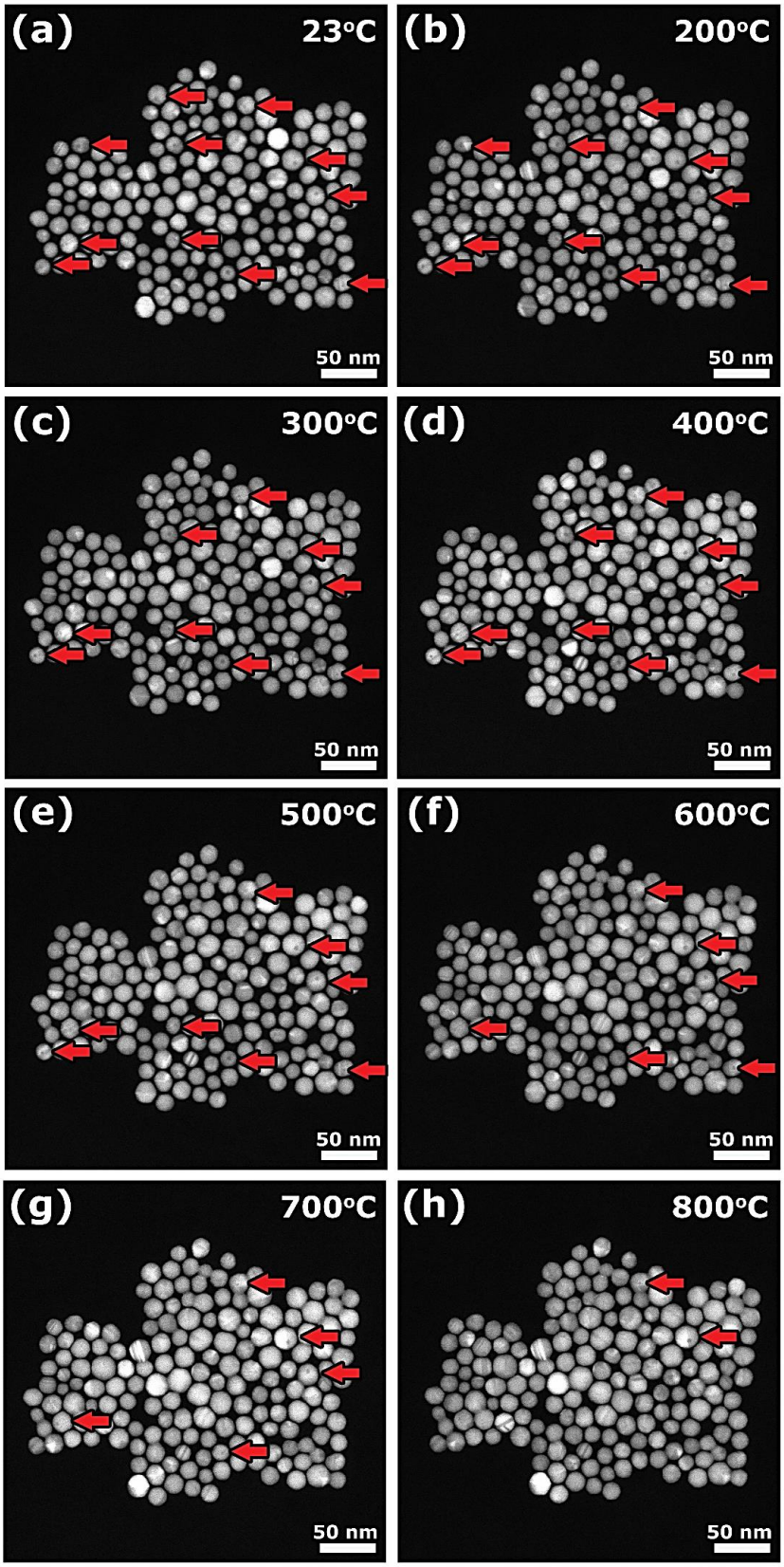

Figure 4.16 – HAADF-STEM images of hollow nanoparticles upon increasing temperature. At room temperature (a), 11 hollow nanoparticles were identified (red arrows). Heating at 100°C had no impact

on the presence of cavities. However, from 200°C, disappearance of cavities was observed. The total of hollow nanoparticles after heating at 800°C decreased to 2.

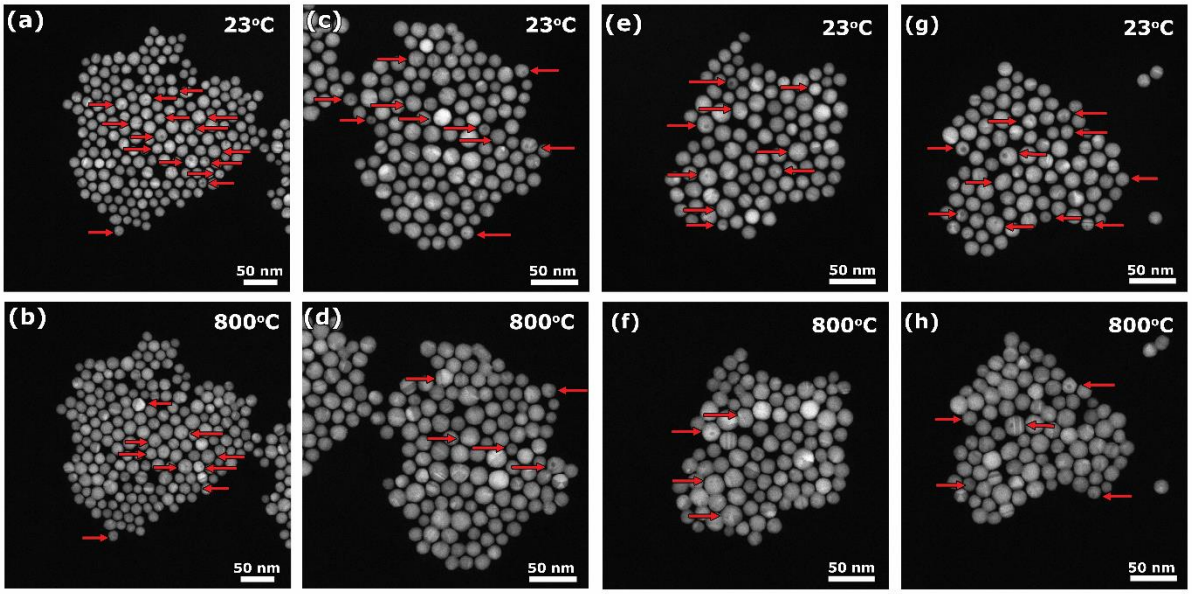

Figure 4.17 – HAADF-STEM images of hollow nanoparticles upon increasing temperature. At room temperature, 45 hollow nanoparticles were found. After heating the system up to 800°C, this number decreased to 23.

Additionally, the threshold temperature for the total elimination of cavities was further investigated. Figure 4.18 indicates the total number of cavities that were totally eliminated at a given temperature. However, no specific trend on the threshold temperature for such elimination could be derived from the obtained results. The observed variation on the threshold temperature could be associated with the asymmetry of the cavities and, more specifically, their non-eccentric location and the varying sizes of the cavities and nanoparticles (section 4.5). Therefore, we expect that cavities that are closer to the external surface of the hollow nanoparticle would have a greater tendency to migrate towards the closest external surface upon increasing temperature conditions.

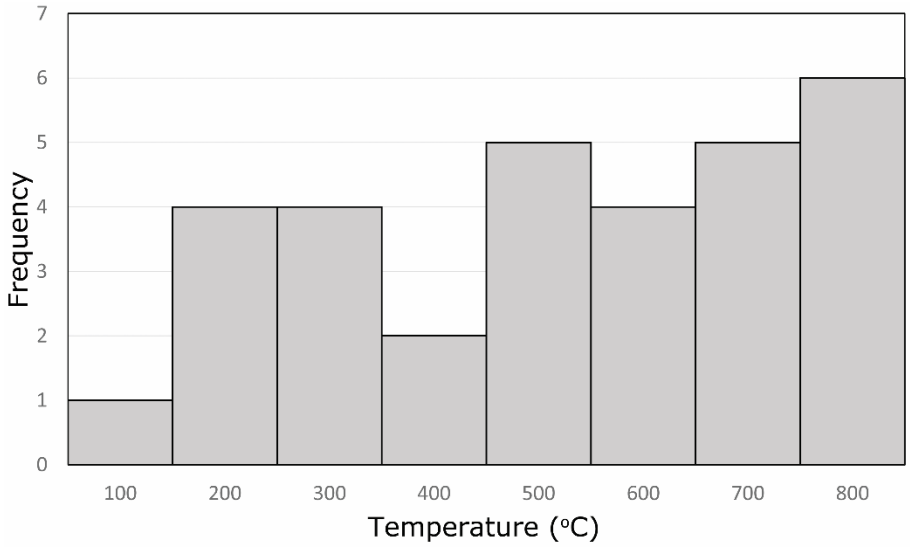

Figure 4.18 – Frequency distribution of the total elimination of the cavities from the nanoparticles for given temperatures, based on the analysis of 2D images of particles shown in Figure 4.16 and Figure 4.17. A total of 56 hollow nanoparticles were investigated in *in-situ* heating conditions, where 31 nanoparticles presented the disappearance of the cavities.

In some cases, 2D imaging of hollow nanostructures upon heating suggested a migration of the cavity inside the nanoparticles, as shown in Figure 4.19. For each case, the threshold temperature at which the cavity started to shift was unique: in the first case at 200°C and in the second, at 600°C. Moreover, a decrease of the image contrast in the region of the cavity upon heating, suggesting a volume decrease of the cavity (Figure 4.19.b and Figure 4.19.e), and eventually its total elimination (Figure 4.19.c and Figure 4.19.f) were observed for some cases. We expect that cavities that are closer to the external surface of the hollow nanoparticle would have a greater tendency to possibly migrate towards the closest external surface upon increasing temperature conditions. However, it is still unclear how the cavities disappear upon heating.

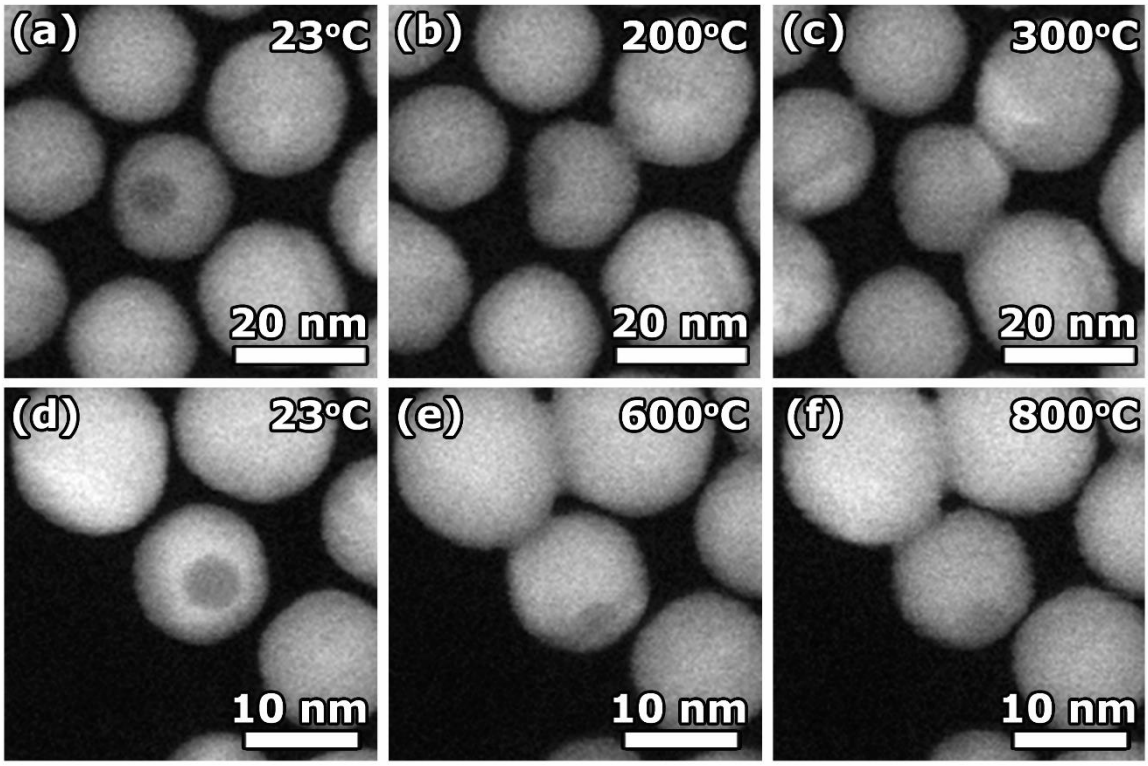

Figure 4.19 – HAADF-STEM imaging of two different sets of nanoparticles (a)-(c) and (d)-(f) upon increasing temperature conditions. Our findings suggest a possible movement of the cavities inside the nanoparticles, until they were totally eliminated. The temperature threshold for the possible cavity movement was not the same.

To address the mechanism behind the elimination of cavities upon increasing temperature conditions, different electron tomography series were acquired after heating of the nanoparticles for 5 minutes and quenching to room temperature (Figure 4.15) for 4 randomly selected hollow nanoparticles. In one case, the cavity remained unchanged upon increasing temperature conditions up to 800°C. For all the other cases, a migration of the cavity towards the closest external surface of the nanoparticle until its total elimination was observed. Figure 4.20 displays the volume rendering of the reconstructed nanoparticles for all investigated temperatures for two cases. More precisely, the temperatures at which the cavities reach the surface were found to be 300°C (top row of Figure 4.20), 500°C (middle row of Figure 4.20) and 400°C (bottom row of Figure 4.20), whereas the temperatures of the total elimination of the cavities corresponded to 700°C, 600°C 500°C, respectively. Additionally, the location and size of the cavities were further investigated for nanoparticles at room temperature for all the cases in 3D and are summarized in Table 4-2. Although the analysis of the location and size of cavities versus the temperature that the cavity is completely eliminated has not revealed a trend, nanoparticles that displayed the disappearance of the cavity showed an increasing behaviour of the

location of the cavity in regard to the external surface *versus* the temperature threshold for the cavity reaching the outer surface (Figure 4.21). One possible hypothesis is that cavities closer to the outer surface of the nanoparticle might show more surface relaxation effects, as discussed in section 4.5. The increase of the surface relaxation at the vicinity of the cavity could trig the mechanism behind the migration of the cavities towards the external surface of the nanoparticles. However, further investigations with relevant statistical analysis in 3D together with the combination of strain analysis in 3D with *in-situ* characterization will be required to confirm the stated hypothesis. Therefore, high throughput tomography[218,219] and electron tomography at the atomic scale combined with *in situ* experiments (Chapter 8) will be an important challenge for the future[218,219]. In summary, our 3D characterisation confirmed that the temperatures of the movement and elimination of cavities in hollow nanostructure were not fixed, as already suggested by 2D image characterisation. Our results indicated a possible connection of the cavity distance-to-surface with the temperature that the cavity reaches the external surface of the nanoparticle. Still, further investigations are required to confirm our observations.

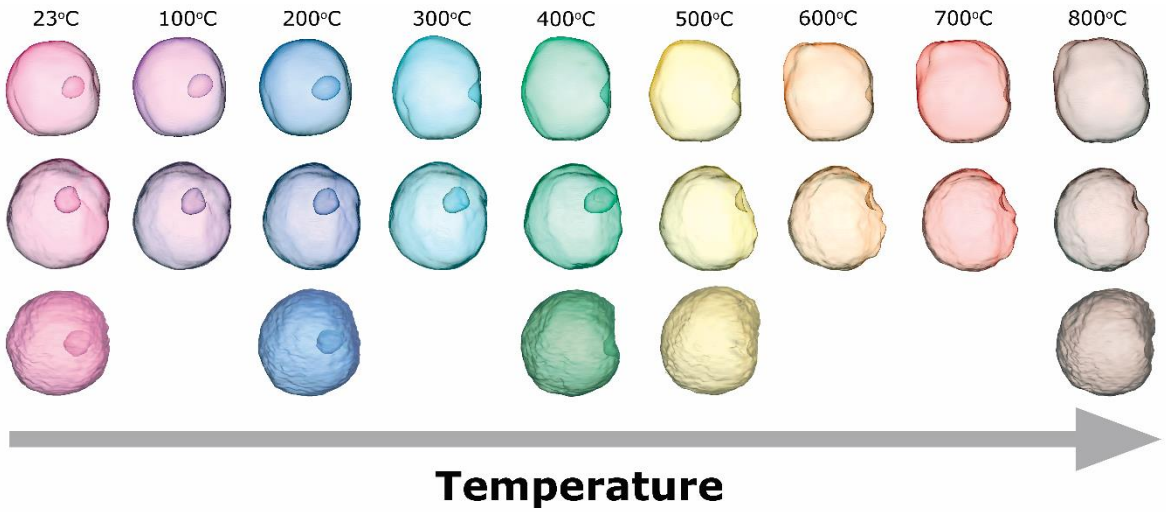

Figure 4.20 – Volume rendering of the 3D morphology of two different hollow gold nanoparticles during *in-situ* heating at the indicated temperature, for 5 min. For the nanoparticle 1 (top row), the cavity reached the outer surface of the nanoparticle at 300°C while for nanoparticle 2 (middle row), the temperature was 500°C and for nanoparticle 3 (bottom row), the temperature was 400°C.

System	Nanoparticle size (nm)	Cavity size (nm)	Distance of the cavity from the closest surface (nm)	Threshold temperature for cavity reaching the surface/total elimination (°C)	Was the cavity eliminated upon increasing temperature conditions?
1	16	6	3	-	No
2	13	4	1	300/700	Yes
3	24	6	4	500/600	Yes
4	13	3	2	400/500	Yes

Table 4-2 – Table summarizing the physical properties of hollow nanoparticles at room temperature obtained from the 3D reconstructions.

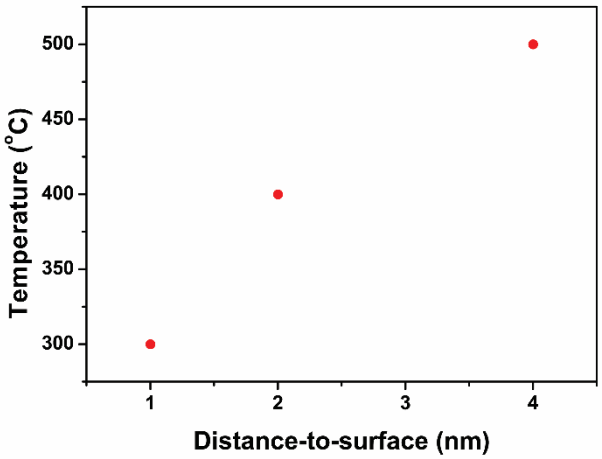

Figure 4.21 – Analysis of the cavity distance-to-surface and the threshold temperature for cavity reaching the external surface. Here, an increasing trend has been observed.

It is important to note that regions of the TEM grid that were not illuminated with the electron beam prior to heating of the system showed a segregation and formation of larger particles with irregular shapes at increasing temperature conditions (Figure 4.22). Besides, the presence of cavities were not observed for temperatures higher than 500°C. The formation of a carbon layer on top of the region of interest during the scanning of the beam is a well known mechanism[220,221]. Such layer can act as a shell for the nanoparticles under investigation during *in-situ* heating experiments, preventing their agglomeration into larger structures[222] and minimizing the effects of morphological deformations upon thermal heating[71]. Indeed, the characterization of nanostructures with a silica shell

at higher temperatures revealed the absence of clustering effects upon heating, even for non-illuminated particles[223]. To further determine how the formation of the carbon layer upon electron beam irradiation influences the dynamical behaviour of hollow nanoparticles, *ex-situ* heating experiments are required.

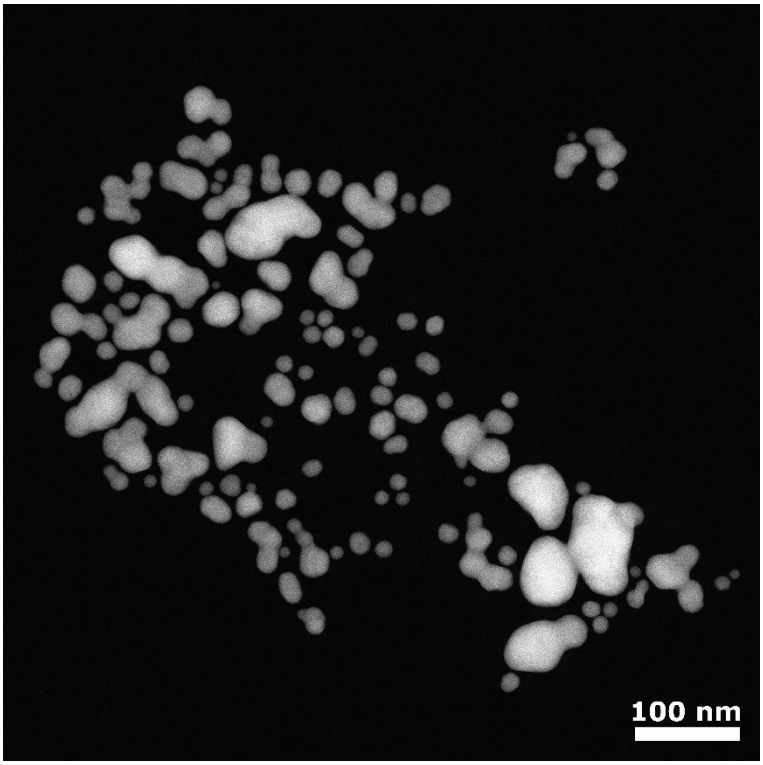

Figure 4.22 – HAADF-STEM image of gold nanospheres at 500°C that we not previously illuminated with the electron beam at room temperature. Agglomeration of nanoparticles and the formation of larger structures with irregular shapes were observed.

4.8 Formation mechanisms of cavities in hollow nanoparticles

To understand the nature and formation of the cavities, molecular dynamic simulations were carried out by the group of Prof. Dr. O. Peña-Rodrigues (Universidad Politécnica de Madrid). For this purpose, three different systems were investigated (Figure 4.23): (a) an empty cavity, (b) a cavity filled with argon and (c) a cavity filled with water. The precise composition of the content of the cavity is unknown, but EELS measurements indicate that the cavities contain organic material from the surfactant, water molecules from the medium, or a gas derived therefrom. Therefore, molecular dynamic simulations were performed for cavities filled with a liquid (water) and a gas (argon). Water is the most likely liquid candidate to exist in the cavity, whereas argon was chosen for the sake of simplicity, considering that noble gases are easier to represent in molecular dynamics simulations with a simple Lennard-Jones potential. The technical details of the simulation can be found in [185].

Moreover, the results concerning the dynamical behaviour of the cavities upon increasing temperature obtained from *in-situ* electron tomography are of great relevance during the evaluation of the findings obtained from simulations.

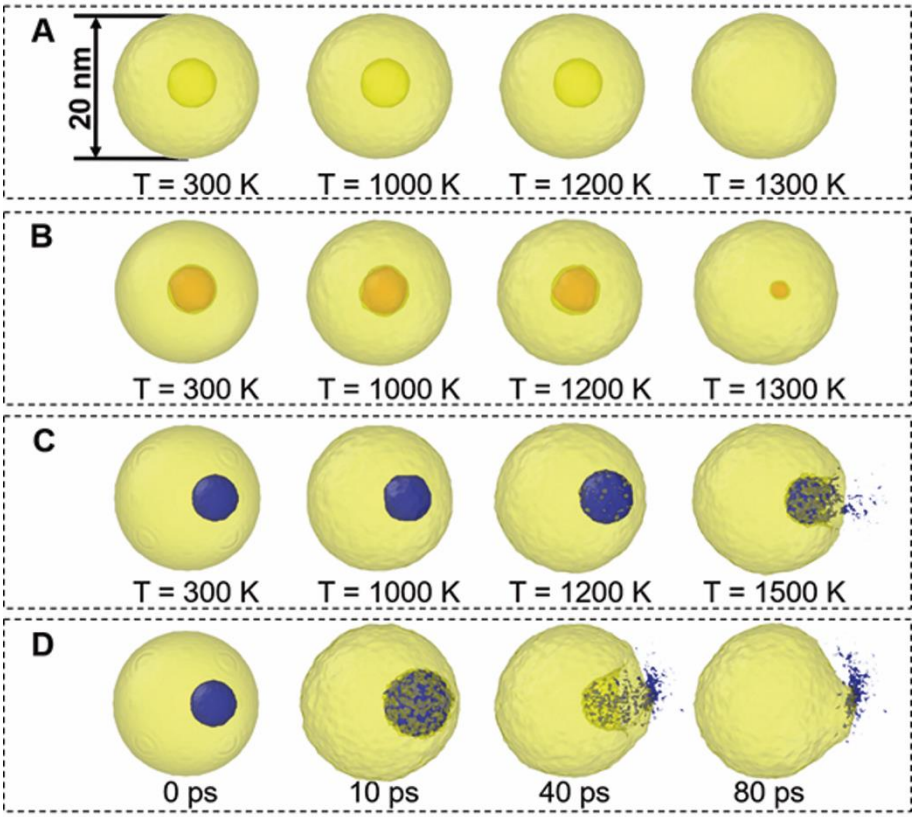

Figure 4.23 – Summary of molecular dynamics results. Snapshots of (a) hollow, (b) Argon-filled, and (c) water-filled gold spheres, as a function of temperature. (d) Snapshots of a water-filled gold sphere heated at 2000 K, as a function of time. The OVITO visualization software was used to generate the snapshots[224]. Figure extracted from [185].

For empty cavities or filled with argon, at temperatures of 1200 K and below, no changes were observed in the cavity size and position. However, for the second case, for temperatures of 1300 K and above, the cavity size was found to reduce until the particle collapsed into a solid sphere (Figure 4.23.b). For cavities filled with water, the movement towards the closest surface was observed for temperatures of 1200 K or above, until its contents were eliminated to the external environment, similar to our findings based on *in-situ* heating tomographic experiments (Figure 4.23c).

The water-filled cavity (Figure 4.23.c) moved towards the outer surface without size reduction and the displacement could already be observed at 1200 K (i.e., below the melting point of gold). It should be noted that water travels collectively inside the gold nanoparticle, and diffusion of individual molecules was not observed. This collective displacement generates a protrusion in the nanocrystal

at times prior to the release. Once the crack occurs, a massive release of water molecules is produced in all directions, followed by collapse of the nanocrystal surface. The gold nanoparticle thus heals the gap by closing on itself and producing a flat region with a small pore. The displacement and release of water from the nanocrystal is enhanced by a temperature increase (i.e., the outwards movement is faster at higher temperatures, Figure 4.23.d). The observed migration can be explained by the eccentric location of the cavity, which translates into asymmetric resistance to a sudden expansion of the inner sphere. This effect creates a net force in the direction of the thinner gold wall that displaces the cavity in the same direction[185].

The findings from *in-situ* heating tomography (section 4.7), EELS analysis (section 4.6) and the molecular dynamics simulation shed light on the formation mechanism of hollow nanostructures upon nanosecond laser pulses. The hypothesis formulated[185] based on all the mentioned results states that the transformation into hollow gold nanoparticles by nanosecond pulsed irradiation can be mediated by melting of the gold nanocrystal. Subsequent expansion and stretching of the resulting liquid droplets would result in formation of gaps and, at high enough energies, in an explosion, thereby releasing some fragments (Figure 4.24). Under rather specific conditions, such as those investigated in this study, the explosion can be counteracted and a small amount of water and organic matter (derived from surfactant molecules) would enter the gold nanoparticles through the gaps created during expansion, and remain trapped during the cooling process (recrystallization). In this manner, in addition to the small fragmented gold nanoparticles typically observed in nanosecond laser pulse experiments, some hollow gold nanoparticles would also be produced (Figure 4.24).

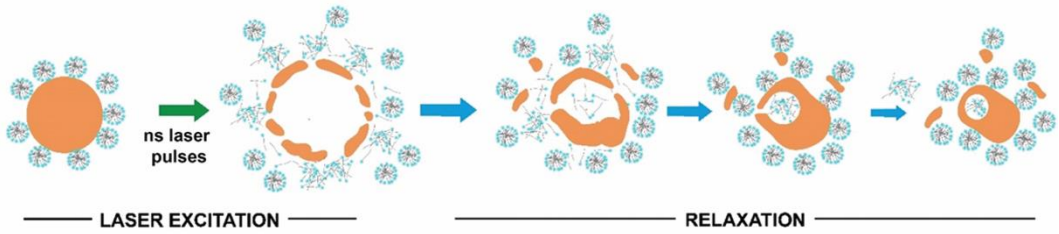

Figure 4.24 – Proposed mechanism for the fragmentation and formation of hollow gold nanoparticles by ns laser pulses. Excitation with ns pulses may lead to melting of the gold nanoparticles. The expansion and stretching of liquid droplets produce gaps and induce the release of fragments by explosion. During the cooling process under specific conditions, the explosion can be counteracted by the penetration of some water molecules and organic matter (derived from surfactant molecules) in the gold nanoparticles, thereby stabilizing the cavity. Figure extracted from [185].

4.9 Conclusions

Using electron microscopy, we have shown that defects are introduced in the crystal structure of gold nanospheres upon nanosecond laser pulses. Moreover, we could reveal that hollow structures were produced upon laser irradiation at specific conditions. Our atomic resolution reconstructions allowed a further characterisation of the morphological properties of the crystal lattice, such as the verification of the presence of lattice strain and facets. Moreover, 3D *in-situ* investigations, together with spectroscopic measurements and molecular dynamic simulations were of great relevance in the determination of the internal composition of cavities in hollow nanoparticles as well as in the comprehension of the formation mechanism of such cavities. The possibility of entrapping matter from the surrounding medium during thermal expansion of gold nanoparticles may be the first step toward the development of novel methods for the preparation of hollow nanostructures in high yield. The trapped matter can be subsequently released either by means of conventional heating or by irradiation with ultrashort laser pulses, with potential applications, for example, in controlled gas and liquid storage and delivery.

4.10 Experimental methods

In this section, a summary of the different approaches for the characterization of nanomaterials based on advanced techniques for electron microscopy is provided. High resolution STEM imaging delivered information regarding the atomic structure of the spherical nanoparticles before and after laser interaction, as well as the crystallographic nature of the structural defects found. The analysis of a tilt series of ADF-STEM images was used to identify nanoparticles that contained structural defects with statistically relevant distribution. Spectroscopic techniques such as EDX was used for the chemical composition determination of nanospheres irradiated in the presence of CTAC and Ag^{+} ions. Moreover, EDX measurements were used to shed light on the chemical composition of some nanospheres that showed a different contrast pattern in HAADF-STEM images. Electron tomography was employed for the structural determination of the latter structures, confirming the contrast pattern observed corresponded to the presence of cavities in those nanoparticles. Atomic resolution electron tomography was used to further investigate the crystalline structure of hollow nanoparticles and determine the presence of lattice strain associated with the existence of cavities, by applying 3D GPA method. Moreover, EELS measurements were used for the determination of the presence of compounds inside the cavities, while *in-situ* heating experiments in 2D and in 3D were performed to further investigate the dynamical behaviour of the cavities upon increasing temperature conditions. The combination of the advanced methods for electron

microscopy resulted in the determination of the formation mechanism of cavities in hollow nanoparticles.

4.11 Author contribution

Thaís Milagres de Oliveira performed the statistical analysis of defects and high-resolution HAADF-STEM imaging of the nanoparticles with different sizes before and after nanosecond laser pulses in collaboration with Prof. Dr. Thomas Altantzis. Thaís Milagres de Oliveira performed acquisition of the tomographic series, at low and high magnifications, the reconstruction of the low magnification series, the statistical analysis of the cavities, the optimization of the acquisition scheme for the atomic resolution tomographic series, the 3D GPA code implementation/application in MATLAB, all the analysis of all reconstructions on STEM imaging and EDX spectroscopy. Dr. Ivan Lobato developed the Convolutional Neural Network for the image processing of multiple frames. Both Dr. Ivan Lobato and Thaís Milagres de Oliveira performed the reconstruction of the atomic structure in 3D. Dr. Wiebke Albrecht performed the EELS spectrum acquisition and analysis. Thaís Milagres de Oliveira performed all the image acquisitions, all the reconstructions and all the analysis based on the 3D evolution of the cavities upon increasing temperature conditions. Synthesis of gold nanospheres, nanosecond laser pulses treatment and the TEM characterisation of the formation of hollow nanostructures by varying the laser fluence, the surfactant concentration and the particle size were carried out by the research team of Prof. Dr. Luis M. Liz-Marzán. Molecular dynamics simulations were carried out by the group of Prof. Dr. O. Peña-Rodrigues (Universidad Politécnica de Madrid).

The author of the present thesis contributed to this study by providing a statistical analysis of the defect type and defect yield for different systems, by investigating the atomic structure of hollow nanostructures in 2D and 3D and by investigating the dynamical behaviour of cavities under increasing temperature conditions in 2D and 3D.

Appendix A. Methodology for electron tomography at the atomic level without the assumption of prior knowledge of the material under investigation

Image restoration based on Convolutional Neural Network (CNN)

Conventional HAADF-STEM images always contain scanning artefacts mainly due to the instrument instabilities (acoustic, mechanic and electromagnetic interferences), scanning speed and drift of the specimen. Those artefacts can hamper the quantification of structural information, such as the atomic lattice arrangement. Besides, such prolonged illumination can result in radiation damage of the specimen, altering its atomic structure. Thus, in this approach, multiple frames of the specimen, with a fast scanning time, are acquired at each tilt angle, offering more reliable results of the specimens under investigation. However, the use of very fast scanning times (1s for an image of 2048 by 2048 pixels) can introduce extra scanning distortions in the range of kHz-MHz frequency[150]. Additionally, due to the very short acquisition time, the resultant signal-to-noise ratio in the images is very low. Recently, an image restoration based on a convolution neural network (CNN) with 12 layers was developed in our laboratory by Dr. Ivan Lobato[150] and applied in the present PhD research. With this approach, it is possible to minimize the effects of e.g. scanning distortions, jitter x/y, dead pixels, saturation, count and thermal noise. To train the CNN, several HAADF-STEM images with and without known distortions were simulated[150]. To illustrate this effect, Figure A.1 shows a single frame before (a) and after (b) image restoration. As a result, the signal-to-noise level is largely improved and the atomic resolution features are recovered after applying the image restoration approach.

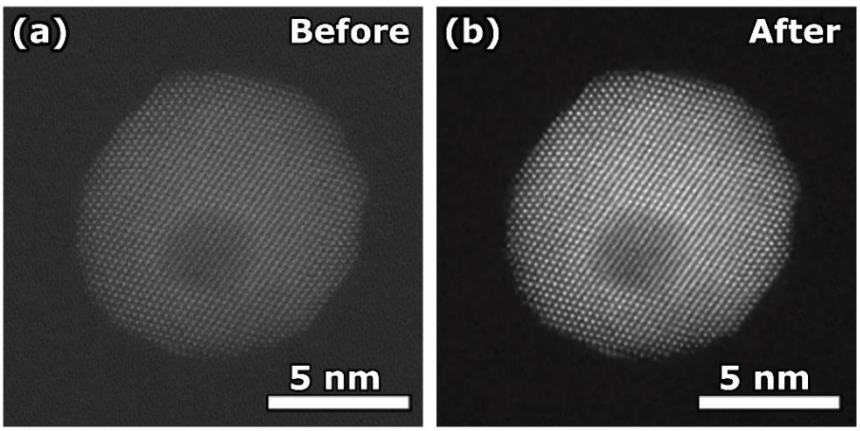

Figure A.1 – High Resolution HAADF-STEM frame (a) before and (b) after the image restoration through the Convolutional Neural Network.

Image registration

Another bottleneck for high-resolution STEM imaging is the specimen/stage drift, due to thermal and mechanical instabilities of the nanoparticle on the grid upon interaction with the electron beam, as well as the mechanical instabilities of the goniometer. Consequently, the recorded images display distortions that can degrade both the resolution of the features and the signal-to-noise ratio of the image. By acquiring a time series of images for each projection, it becomes possible to minimize this effect by a proper alignment of the images, followed by an averaging step that yields a single projection image. This can be achieved in two parts. First, a rigid transformation step based on affine operations is carried out, where the image displacement between frames and the shear effect of each image is corrected. Subsequently, a non-rigid transformation is applied to compensate the residual low frequency distortions from the CNN step. For this correction, an averaged image after rigid transformation is generated and used as the reference image. In an iterative process, each frame is compared with the averaged image and local corrections are applied. After a number of iterations (chose by the user), a new averaged image is generated based on the corrected frames, followed by another set of iterations. Figure A.2 illustrates the image quality improvement before and after image registration (rigid and non-rigid) of the averaged time series at a given projection. The development and implementation of image registration was carried out in MATLAB, by Dr. Ivan Lobato.

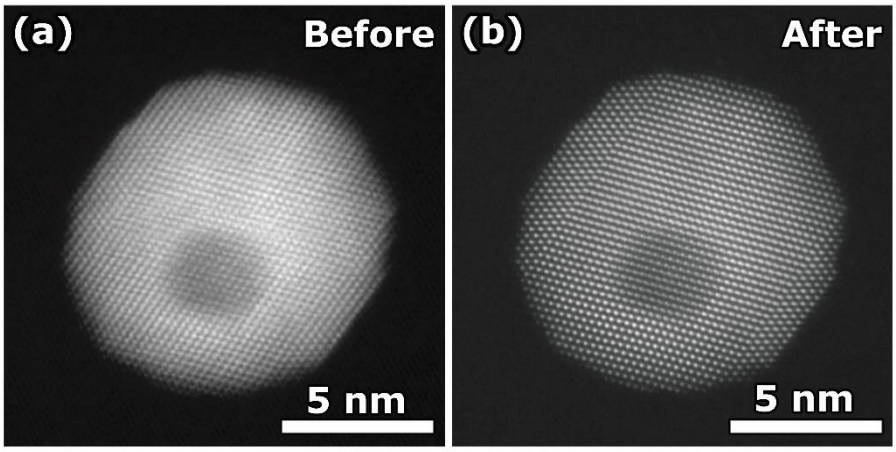

Figure A.2 – Averaged and restored frames for a single projection (a) before and (b) after drift compensation is applied.

Image alignment of the tomography series

Similarly to the conventional electron tomography for nanometre characterisation, it is vital that the projection images are aligned with respect to each other, as well as the tilt axis of the tomography series. In case of residual misalignments, the recovery of the complete atomic structure

in 3D cannot be achieved[113]. For the alignment of the tomography series, a modified phase correlation is used to estimate the offset between consecutive images with subpixel precision. To obtain such sub-pixel precision, the phase correlation between two consecutive images are convoluted with a 2D Gaussian sphere. One important aspect for a proper alignment is the presence of a carbon support and the deposition of organic species on top of the specimen during electron beam illumination[220,221]. The main sources of contamination are the specimen, the specimen holder, the diffusion pump and the grease from o-rings inside the microscope[221]. Consequently, the surrounding environment might not be the same for projections at different angle tilts. Thus, background subtraction and segmentation steps are applied before the alignment of the images to avoid any deviation on the calculations of the shift between consecutive images. For the determination of the shift and rotation of the tilt axis, slices along the object are reconstructed for different values of the shift and rotation. An incorrect shift and/or rotation of the tilt axis will result in a larger residue value of the reconstruction in comparison to the residue value of the correct alignment. The determination of the correct parameters correspond to the minimal residue value obtained for each reconstruction condition. The described alignment procedures were developed and implemented in MATLAB by Dr. Ivan Lobato.

3D reconstruction

The 3D reconstruction at atomic level is carried out using conventional SIRT algorithm, from Astra Toolbox, implemented in MATLAB using high performance GPU[175,225]. Additionally, constraints on the grey levels in real and reciprocal space are applied in the obtained 3D volume from a SIRT reconstruction[226,227]. Subsequently, a normalization step is carried out, using one projection image as reference. This is required because the filtering in Fourier space modifies the values of each voxel. To avoid the introduction of extra artefacts during the next reconstruction steps, it is important to rescale the voxels to the corresponding values of the tomographic series. The obtained 3D volume is used as the starting point for the next SIRT reconstruction and the described procedures are applied until convergence is reached. The aim of this approach is to ensure that the 3D reconstructed volume corresponds to the global minimum of the residue instead of a local minimum. This methodology was implemented in MATLAB by Dr. Ivan Lobato.

Chapter 5. 3D characterisation of gold nanorods welded by femtosecond laser pulse irradiation

5.1 The use of femtosecond laser pulses to control the distance tip-to-tip in dimers and trimers of nanorods

The use of ultrafast laser pulses is not restricted to the introduction of defects in the crystal lattice of nanomaterials (Chapter 4). The approach can also be used to weld the tips of the nearest nanorods[78,228]. For such structures, coupling of the electromagnetic field leads to additional hybridized plasmon modes and potentially strong field enhancements[229–236]. Moreover, it was found that the laser fluence is a key parameter. For laser fluences higher than 500 J/cm^2, it has been demonstrated that gold nanorods achieve the melting temperature for gold (1337 K)[78,228]. Due to the field enhancement present in the gap between the tips of the nanorods arranged in dimers and trimers, the tips of nanorods can melt at such high fluences[235]. Thus, femtosecond laser pulses can be used to enable a tip-to-tip welding process of gold nanorods [69,68,79,71]. Due to the presence of a conductive nanojunction between the nanorods, a new plasmon mode arises, associated with the charge flow between the nanorods, resulting from the hybridization of the longitudinal modes of the individual nanorods[231,233,229,236]. Because of these unique plasmonic properties, metallic welded nanorods are of great interest, with potential applications in molecular sensing to nanoscale wave-guiding[86,237–239].

The impact of femtosecond laser pulses on the welding of gold nanorods has been explored using 2D optical ensemble techniques such as the absorbance measurements by ultraviolet/visible/near-infrared (UV/VIS/NIR) spectroscopy, in combination with simulations[78,234,235]. Although TEM have also been used for characterisation of welded nanostructures, these studies mainly focused on determining the average aspect ratio of the nanorods and the 2D projected geometry of welded nanorods[234,235]. However, the presence of defects can e.g. lead to additional scattering of electrons[240], resulting in damping of the plasmon modes[7,241,44]. Unfortunately, it remains unclear what type of defects are introduced by the femtosecond laser pulses and how these defects relate to the welding geometry. In this study, we therefore analysed the 3D atomic structure of welded nanostructures with different welding geometries. Moreover, the energy and spatial distribution of plasmon modes, for individual systems with different welding geometries, using STEM-EELS. Finally, we investigate the influence of the presence of defects in the nanojunction on the plasmonic properties.

5.2 3D characterisation of the welded nanorods

First, single gold nanorods were investigated before and after femtosecond laser pulses by high resolution HAADF-STEM (Figure 5.1.a-b). For the specific excitation conditions used in the present study, individual gold nanorods did not show the presence of structural defects after laser pulse irradiation. This is likely depending on the frequency and/or the fluence of the laser used for the excitation. However, in the case of gold nanorods that are welded by laser pulses, grain boundaries (Figure 5.1.c-d) or dislocations (Figure 5.1.e-f) could be observed at the interfaces between gold nanorods. We therefore investigated the relation between welding geometry and defect type formation.

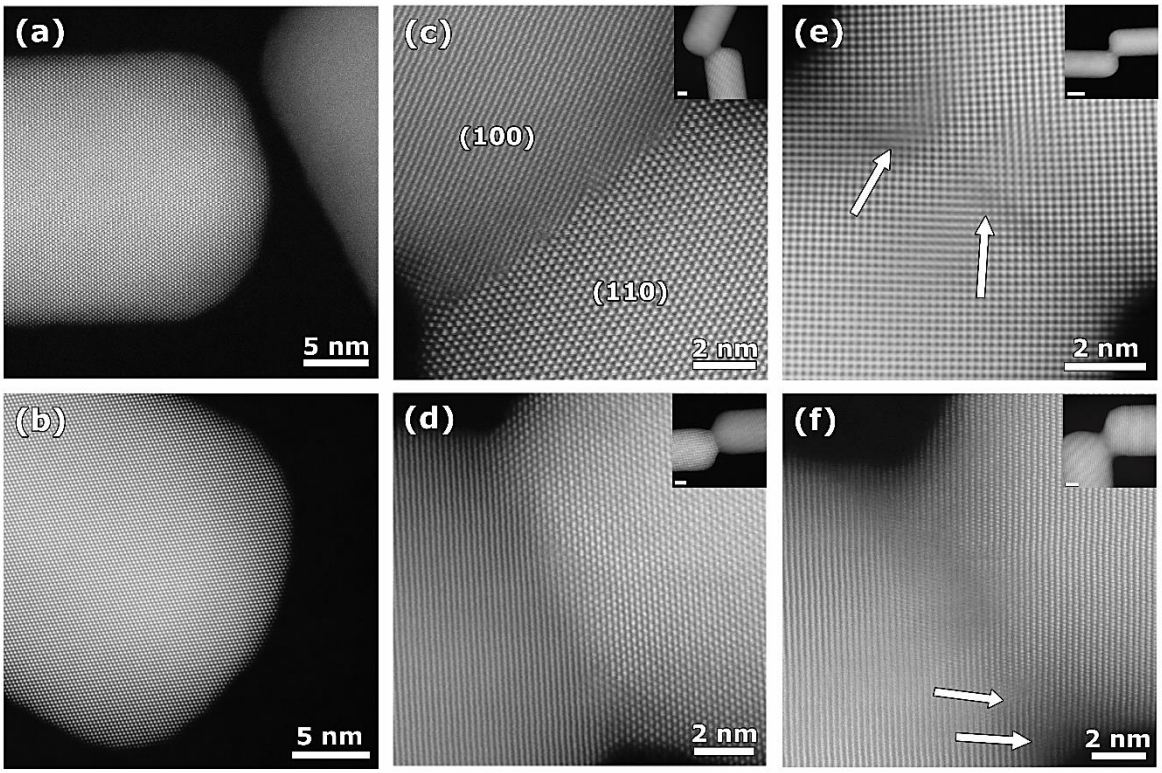

Figure 5.1 – High-resolution HAADF-STEM images of different welded gold nanorods showing the presence of different types of defects. The characterisation of single gold nanorods before (a) and after (b) irradiation with femtosecond laser pulses revealed the absence of defects. (c)-(d) Grain boundaries were often observed at the junction between welded gold nanorods. (e)-(f) Dislocations at the interface of welded nanorods. The insets at the top right show lower magnification HAADF-STEM images.

In order to investigate the geometries after welding in more detail, electron tomography was used. Examples of 3D visualizations of the reconstructed volumes for different welding geometries are displayed in Figure 5.2.a. From these results, the welding angles were determined in 3D and correlated

with the type of defect (grain boundary or dislocation). The welding angles were defined as the Euler angles α and β, with one of the gold nanorods oriented along the z-axis, as illustrated in Figure 5.2.b. However, this parameter can only be obtained from analysis of the 3D atomic structure. Statistical 3D analysis of 32 configurations revealed that α ranges from 61° to 179° and β from 0° to 42° (Figure 5.2.c-d). Studies have reported a similar distribution of α for nanorods dimers and trimers connected by molecular linkers before welding, albeit based on 2D images[78]. This comparison suggests that the gold nanorods maintain their initial orientation after welding under femtosecond laser pulses. Besides the welding angles, the epitaxy rotational relationship between both nanorods needs to be considered. For 10 out of these 32 welded gold nanorod pairs, we acquired 2D high-resolution HAADF-STEM images, with examples shown in Figure 5.1.c-f. We observed dislocations for geometries in which the crystallographic directions of the individual gold nanorods were close to perfect epitaxy. For all other welding geometries, grain boundaries were identified.

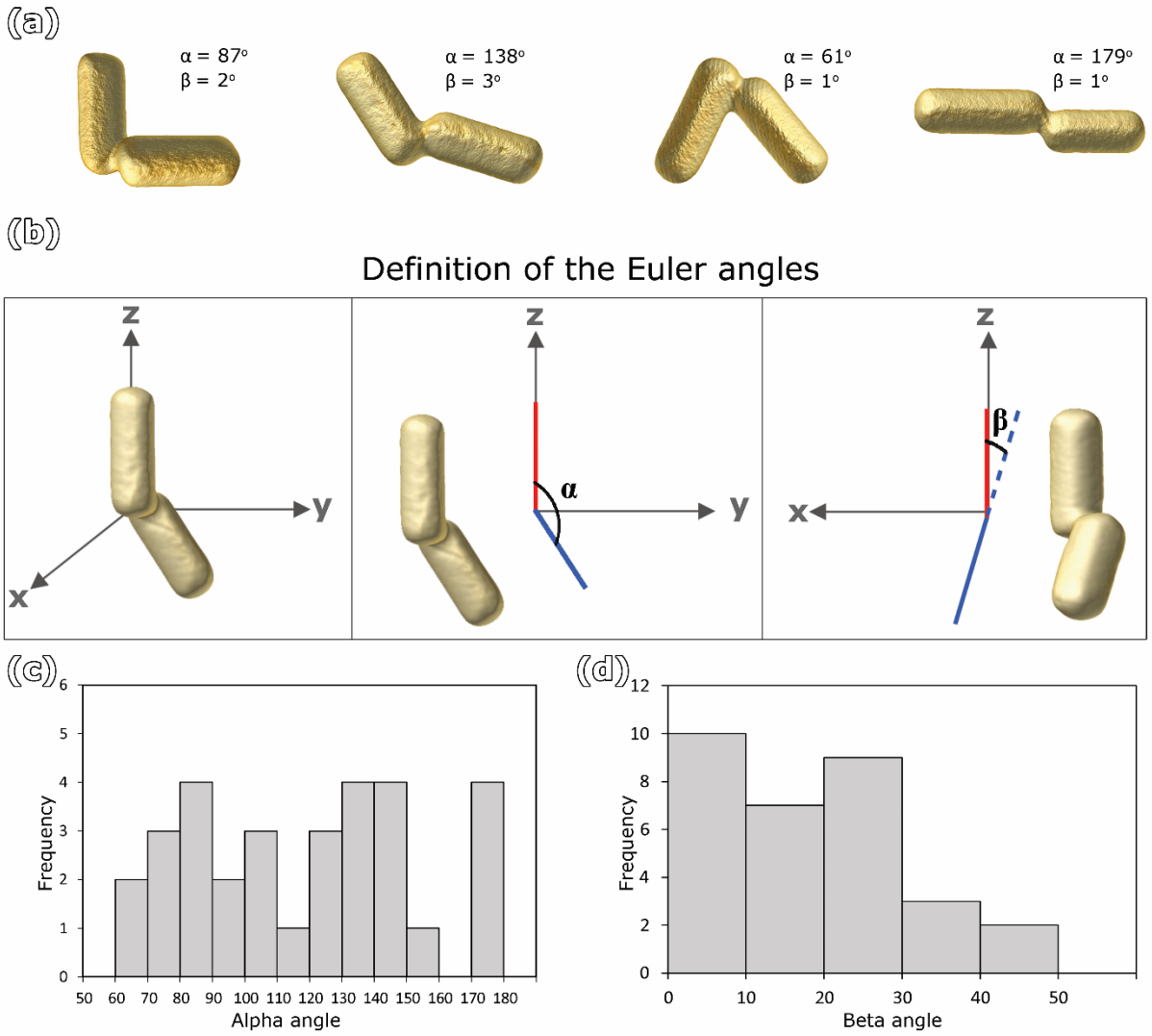

Figure 5.2 – (a) 3D morphology of different welding geometries determined by electron tomography with respective welding angles. (b) Definition of Euler angles: one gold nanorod is placed along the z-axis. α and β correspond to the angle of the other Au NR around the y and x axes, respectively. The measured welding angles of the different welded systems shown in (a) are indicated next to the 3D morphology. Statistical distribution of the welding angles (c) α and (d) β for 32 gold nanorods dimers with different configurations, based on the analysis of 3D data.

In order to visualize the distribution of defects in 3D, multimode tomography was employed, as described in the Chapter 3. Figure 5.3 shows a HAADF- and LAADF-STEM projection image of welded nanorods and respective slices through the 3D reconstructions. In both the projection image and a slice through the LAADF-STEM reconstruction, an intensity variation due to the presence of the defect is visible. More specifically, a bright line was observed at the interface between the two nanorods, as indicated by the white arrow in Figure 5.3.d. By performing a manual segmentation over such intensity variation, the visualization of the 3D distribution of the defect could be obtained (Figure 5.4). These

results revealed that the presence of planar defects that are always located at the interface between the nanorods in the welded system. However, it is still unclear the crystallographic nature of those defects in 3D.

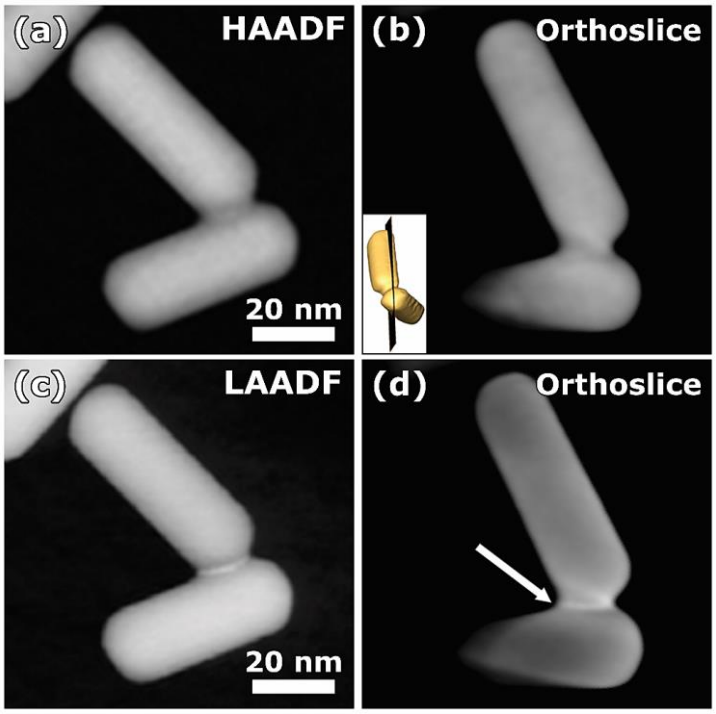

Figure 5.3 – (a) HAADF-STEM projection image with (b) respective slice through the 3D reconstruction. (c) LAADF-STEM projection image with (d) respective slice through the 3D reconstruction.

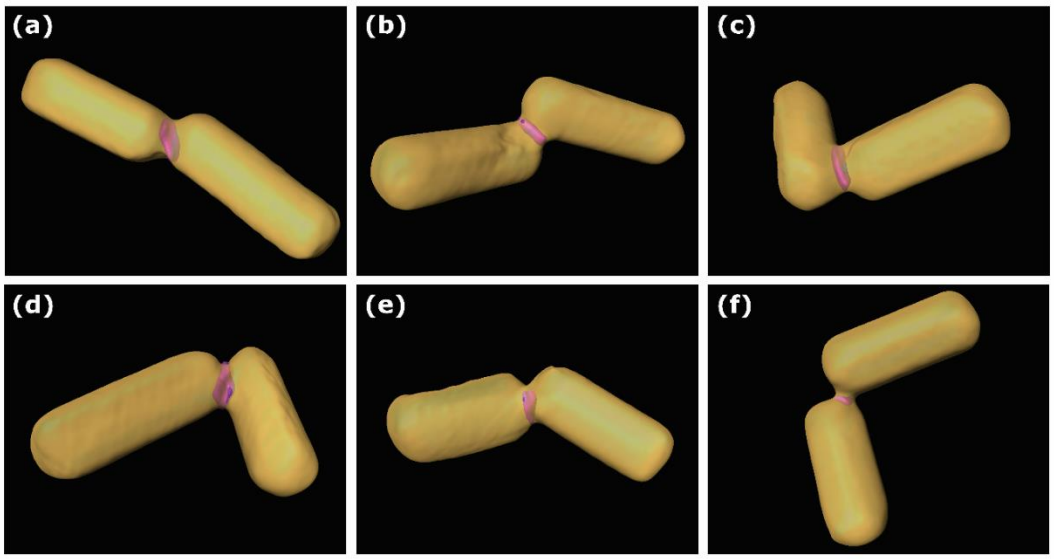

Figure 5.4 – 3D reconstructions of different welded geometries. The reconstructed morphology originates from HAADF-STEM images, whereas defect region is indicated in pink, based on manual segmentation of LAADF-STEM reconstruction.

5.3 3D investigation of the defect type at the atomic level

To visualise the crystallinity of defects at the nanojunction, electron tomography at the atomic level was performed. In the past, prior information about the investigated material was often used to achieve high resolution in 3D[111–113]. These methods are unfortunately no longer applicable for the 3D investigation of more complex nanostructures such as the welded gold nanorods in this study. Therefore, an approach, recently developed at EMAT, was applied here (Chapter 4 and Appendix A) using the same parameters and microscope described in Chapter 4.

The first system investigated by atomic resolution tomography corresponds to nanorods with welding angle α of 146°, as indicated in Figure 5.5. A 3D representation of the reconstructed volume and slices through it are shown in Figure 5.5.b,d-e respectively. It is clear that both nanorods did not share the same crystallographic orientation (Figure 5.5.b), and, therefore, a grain boundary was formed at the nanojunction (indicated by the white arrow). More specifically, the left gold nanorod is oriented along the [110] zone axis in Figure 5.5.d, whereas the right gold nanorod is oriented along the [110] zone axis in Figure 5.5.e. Measurements of both crystallographic orientations revealed a rotational deviation of 3° and a tilt deviation of 50° from the perfect epitaxy relation between the gold nanorods (as defined in Figure 5.6). By performing a manual segmentation, the grain boundary at the interface between both crystal lattices could be visualised (Figure 5.5.c). Another example (α = 131°) yielding similar results is provided in Figure 5.7. These examples suggest that grain boundaries are formed at the interface between the nanorods in case there is a large deviation from perfect epitaxy.

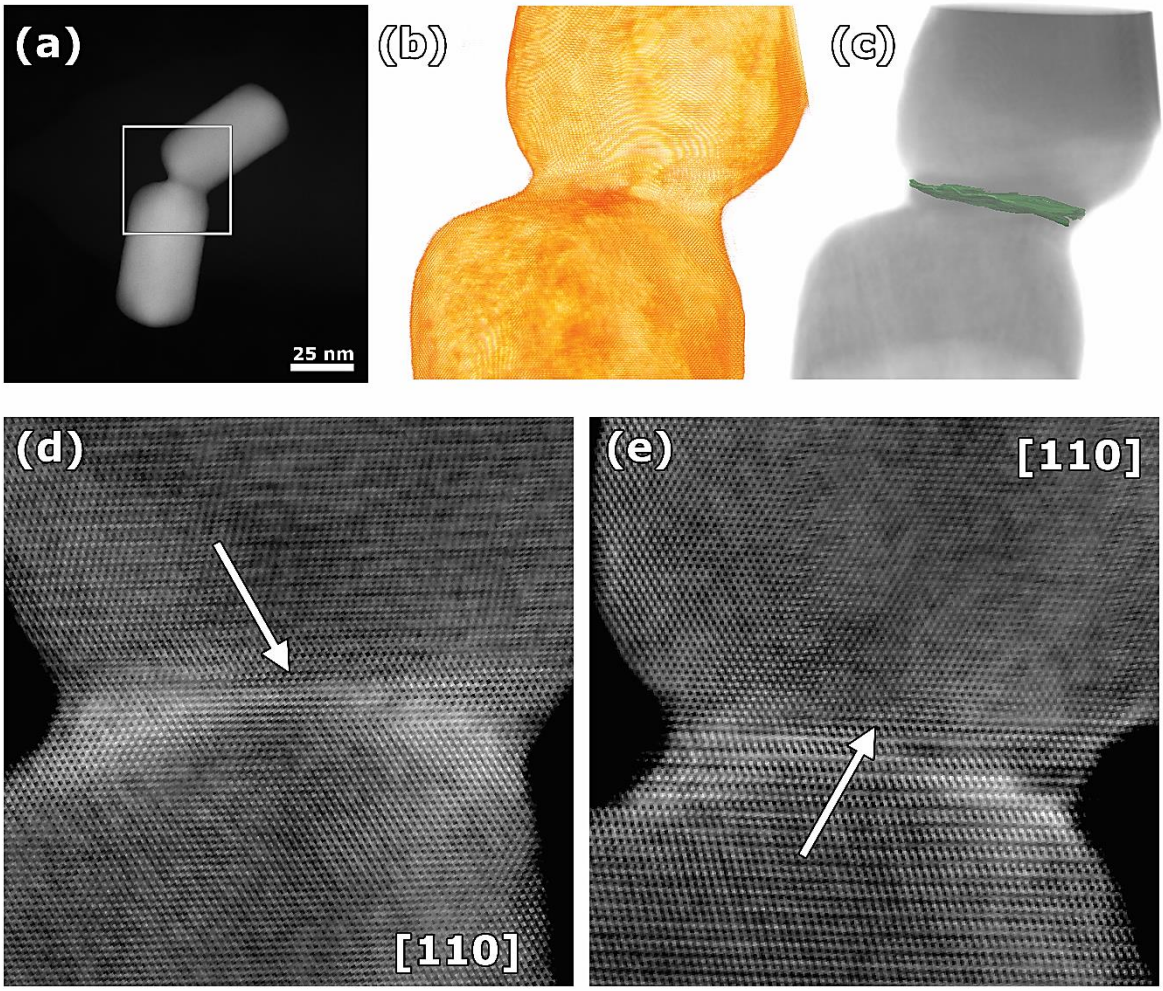

Figure 5.5 – (a) HAADF-STEM image of welded gold nanorods. The region inside the white box was studied by using atomic resolution electron tomography. (b) 3D visualization of the reconstructed volume. (c) Segmented grain boundary. (d)-(e) Slices across the 3D reconstruction along different orientations, revealing the presence of a grain boundary.

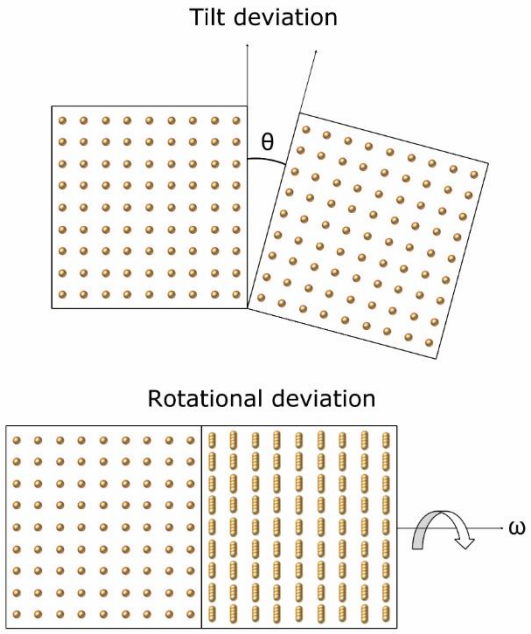

Figure 5.6 – Definition of tilt θ (top) and rotational ω (bottom) deviation from perfect epitaxy between two crystals.

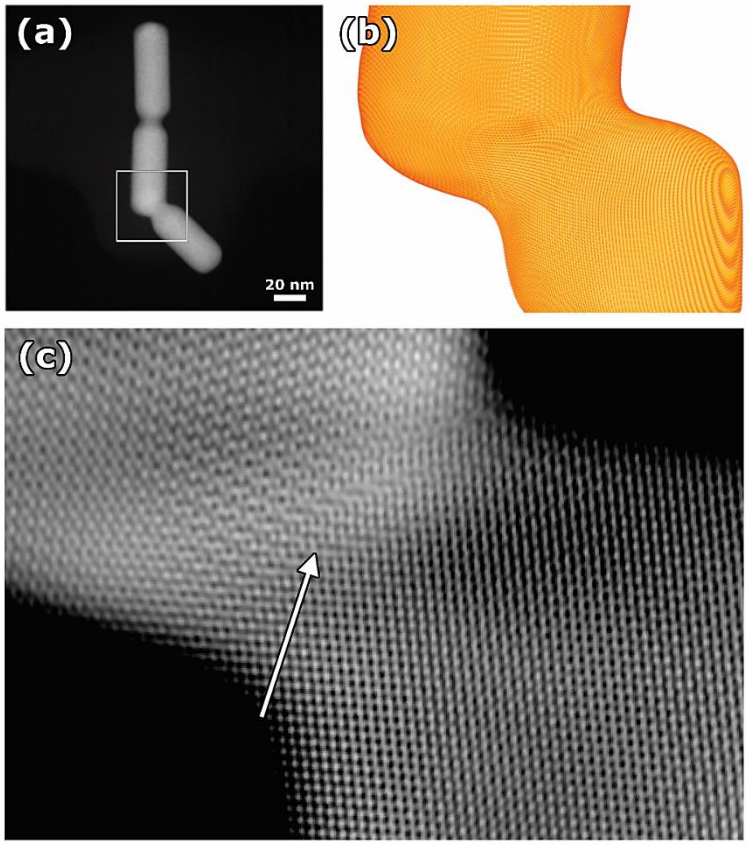

Figure 5.7 – (a) HAADF-STEM image of the investigated welded gold nanorods. The white box indicates the region used for the acquisition of tilt series by electron tomography. (b) 3D representation of the

reconstructed volume. (c) Higher magnification orthoslice, revealing the presence of a grain boundary, as indicated by the white arrows.

As mentioned in 5.2, a small crystallographic mismatch of the two nanorods before welding is expected to lead to dislocations at the interface. The representation of the 3D crystal lattice at the atomic level for such an example is presented in Figure 5.8, where a tilt of only 1.3° was measured between the crystallographic orientations of the welded nanorods. The overview image of the geometry and the volume rendering of the atomic structure at the nanojunction is displayed in Figure 5.8.a-b. Two dislocations at the interface of the welded nanorods are revealed, indicated by the white arrows in Figure 5.8.c. To determine the exact location of the defects in the crystal lattice, Fourier filtering was applied to all atomic planes of the crystal, as presented in Figure 5.9 for a given atomic plane. Additionally, the recovery of the 3D structure enabled the investigation of the extension of the defect in the third dimension, which was achieved through a precise 3D segmentation of the position of each dislocation, based on the Fourier filtering of selected atomic planes (Figure 5.9.b-c). Figure 5.8.d displays the segmented dislocation 1 at the nanojunction, which traverses the nanorod in a non-parallel path with respect to the atomic arrangement. For dislocation 2, with the segmentation shown in Figure 5.8.d, a more irregular pattern of the defect was observed.

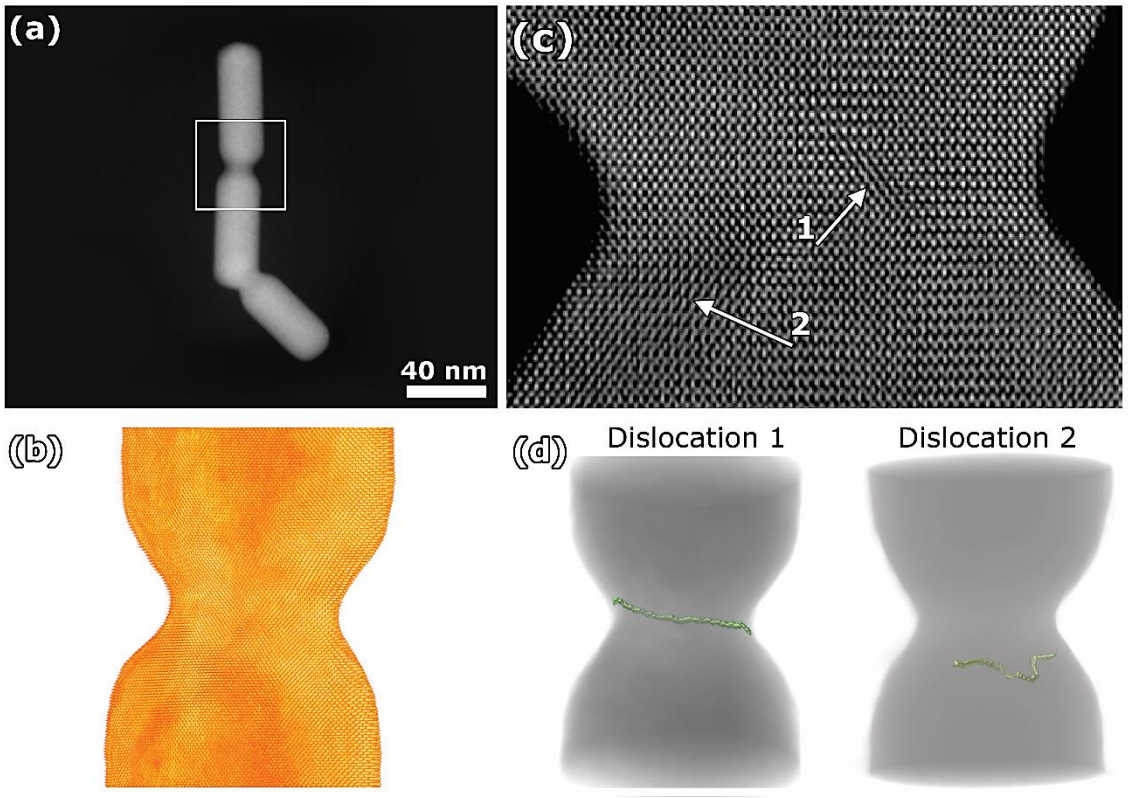

Figure 5.8 – (a) HAADF-STEM image of a trimer of welded gold nanorods. The region inside the white box was studied by high-resolution electron tomography. (b) Visualization of the 3D reconstructed

volume. (c) Orthoslice through the 3D reconstruction revealing the presence of two dislocations, as indicated by the white arrows. (d) Dislocation 1 was linear, whereas dislocation 2 presented an irregular pattern.

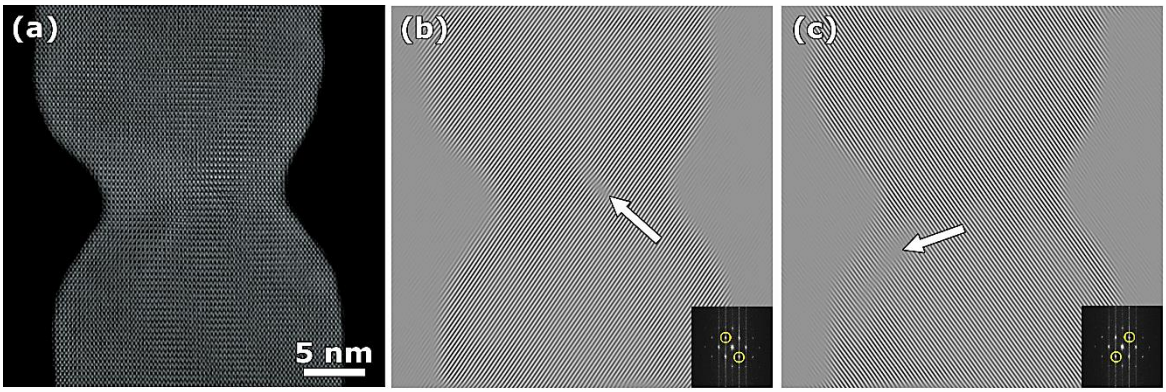

Figure 5.9 – (a) Slice through the 3D retrieved atomic structure. The Fourier filtering allowed the determination of the exact location of the dislocations, as indicated by the white arrows in (b) and (c). Insets display the spots used for the Fourier filtering.

5.4 Characterisation of the plasmonic properties of welded nanostructures

Next, the plasmonic properties of welded nanorods with different welding geometries were evaluated. We hereby analysed the spatial distribution of the plasmon modes for different welding geometries using monochromated STEM-EELS. Low-loss spectrum maps were acquired in a monochromated aberration-corrected 'cubed' ThermoFisher Titan 60-300 electron microscope operated at 120kV, with energy resolution of 175 meV.

The normalized spectra of different welded nanorods(Figure 5.10.b-d and Table 5-1) are shown in Figure 5.10.a. By selecting the energy range associated with each of the three peaks, three different field distributions could be detected, as shown in Figure 5.10.e-m. As mentioned earlier, when metallic nanoparticles are placed closely together, a collective behaviour arises from electromagnetic coupling of the LSP modes of each nanoparticle, giving rise to different plasmonic modes,[233], such as the so-called bonding dimer plasmon (BDP) mode[231,233,242]. Moreover, due to the presence of a conductive nanojunction between the nanorods after welding, a new plasmon mode arises, associated with the charge flow between the nanorods. This is the result of the hybridization of the longitudinal modes of the individual nanorods, known as the charge transfer plasmon (CTP) mode[229,231,233,236]. Additionally, it has been observed that the BDP resonant peak displays a blue-shift after welding, due to the decreased capacitive coupling of the nanorods and the interaction with the CTP mode. This is referred as the screened bonding dimer plasmon (SBDP)[229,232,233]. Moreover,

simulations of conductively connected nanorods revealed that a screened antibonding dimer mode (SADP) can also be observed as a bright mode[232]. Moreover, it has been shown that EELS measurements are capable to detect dark modes[243]. Therefore, the SBDP and SADP modes of welded nanorods can be characterized using EELS measurements.

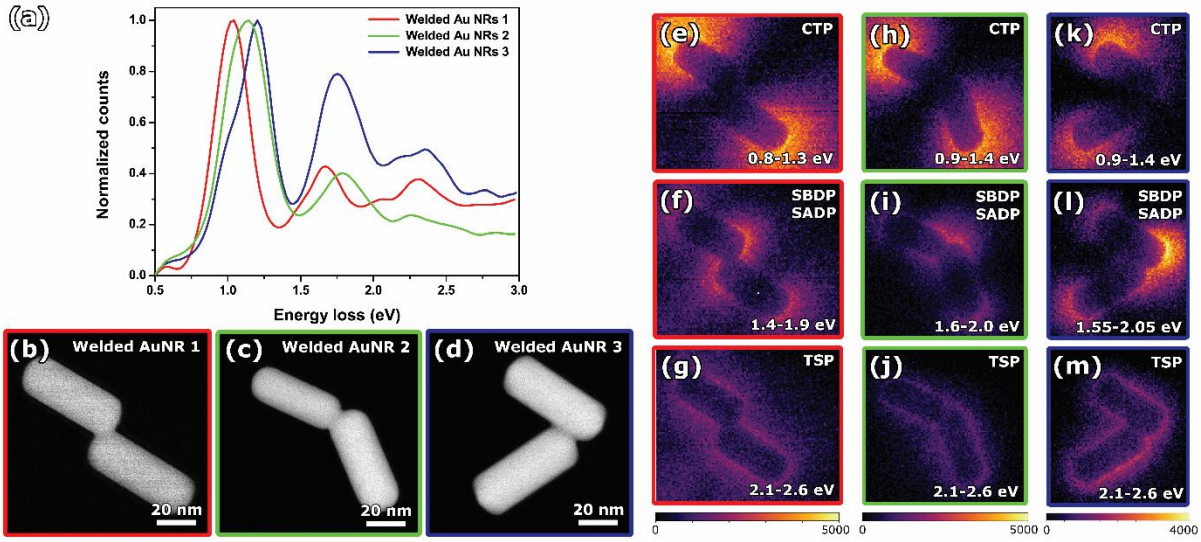

Figure 5.10 – (a) Normalized EELS spectra of three different welded NRs shown in (b)-(d). (e)-(m) Spatial distribution of the plasmon modes for the different welding geometries observed from the spectra. Three different plasmon modes were identified as the CTP, SBDP/SADP and TSP mode. The energy range of the plasmon maps is indicated in each map.

System	Length (nm)	Width (nm)	Aspect-Ratio
Welded Au NRs1 - NR1	55	22	2.50
Welded Au NRs1 - NR2	60	22	2.73
Welded Au NRs2 - NR1	46	19	2.42
Welded Au NRs2 - NR2	54	22	2.45
Welded Au NRs3 - NR3	58	23	2.52
Welded Au NRs3 - NR4	59	23.5	2.51

Table 5-1 – Table summarizing the dimensions of welded Au NRs shown in Figure 5.10.

From our EELS results, we were able to identify the different plasmon modes for various dimers according to their spectra and associate them to the obtained field distributions, based on previous knowledge reported in the literature[229–233,236,244] (Figure 5.10.b-d). The field concentration at

the non-welded tips (Figure 5.10.e,h,k) corresponds to the CTP mode, as this map is a result of the energy selection correspondent to the first peak. Besides, the energy range is in good agreement to the resonant energy of the CTP mode reported in literature[229–233,236,244]. The surrounding medium was different for areas at the top and the bottom of the region of interest due to the deposition of organic species during the acquisition of the EELS spectral data[220]. Therefore, the dielectric constant of the surrounding of the welded nanorods was slightly modified, causing a red-shift of the resonant energy peak for regions with a thicker layer of organic compounds[233,245]. The extend of deposition of organic compounds is strongly dependent on the type of solvent and ligands used in solution. To quantify the extent of the energy shift caused by the deposition of organic compounds, the spectrum from a selected region (Figure 5.11.b) was extracted. As a result, the spectrum for each mode could be separately obtained (Figure 5.11.a), differently to the spectrum shown in Figure 5.10.a, where the contribution of different plasmonic modes are displayed in the same curve. The present analysis revealed a clear red-shift of the CTP peak of the bottom non-welded tip (0.96 eV) in regard to the top non welded tip (1.08 eV) is clearly visible and equals to 0.12 eV.

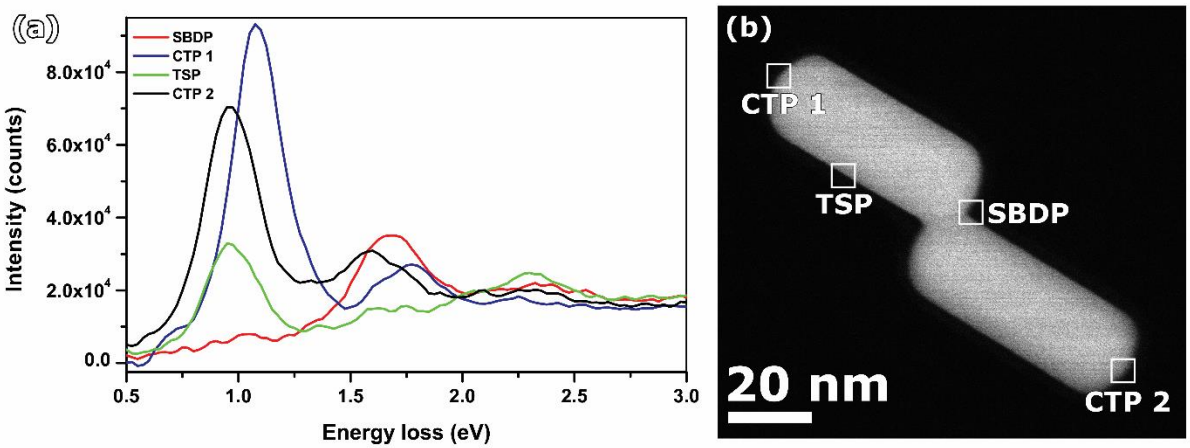

Figure 5.11 – (a) EELS spectra of the SBDP, CTP and TSP modes for the welded NRs shown in (b). (b) Example of selected regions for the extraction of energy loss spectra to fit the CTP, SBDP and TSP modes. A clear red-shift is observed in CTP 2 curve in comparison to CTP 1, due to the deposition of organic species.

The plasmon maps for the energy range correspondent to the second peak are shown in Figure 5.10.a and revealed a field concentration at welded and non-welded tips, indicating that both the SBDP and SADP modes were excited[246] (Figure 5.10.f,i,l). This observation is in agreement with previous results reported in literature[229,232,233]. Finally, the field distribution observed in Figure 5.10.g,j,m is associated with the transverse surface plasmon (TSP) mode.

Moreover, the SBDP/SADP mode exhibited a field concentration at the welded and non-welded tips of the nanorods pairs, indicating the contribution of both bonding and anti-bonding modes[246]. For the welded nanorods with the largest α angle (Figure 5.10.f), a rather uniform distribution was observed for all four tips[246]. The upper nanorod had a slightly smaller aspect ratio (2.50) than the lower one (2.73)[246]. The differences in aspect ratios suggest that the field distribution around the lower (upper) nanorod is connected to the bonding (anti-bonding) mode[232,246,247]. This observation is supported by optical measurements and simulations, where the bonding (anti-bonding) mode is governed by the longitudinal plasmon resonance of the higher (lower) aspect ratio nanorods for both connected and non-connected nanorods heterodimers[232,247]. Additionally, a slightly higher field concentration at the non-welded tip of the lower nanorod compared to the upper was observed, suggesting a stronger contribution of the SBDP mode[246]. Besides, for the configuration with the lowest α angle (Figure 5.10.l), the concentration of the field distribution was the highest not around the welded nanojunction, but rather at the welded tip of the upper nanorod[246]. This observation suggests that the SBDP mode extends over the nanojunction[246], as previously observed[232].

Next, the influence of the defect type (dislocation or grain boundary) on the CTP mode was investigated in more detail. Such experiments performed here by STEM-EELS, with energy resolution of 90 meV, are of great interest since they enabled us to directly link the optical properties with the structure of individual nanoparticles. For this purpose, two welded systems with almost identical welding geometry and different epitaxy relationships were selected (α = 180^o and β = 0^o), where in one case a grain boundary was present and in the other, a dislocation. For the present study, two welded gold nanorods were investigated for each defect type (Figure 5.12). Because higher magnifications are responsible for an increase of carbon build up during the scanning of the electron beam, the identification of the defect type was performed with ADF-STEM imaging. In this manner, we were able to minimize the effects of the deposition of organic species prior to the EELS measurements.

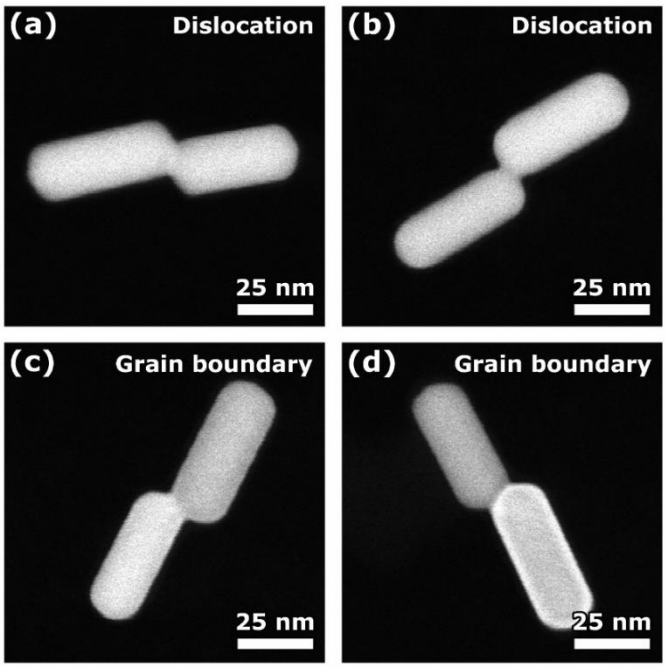

Figure 5.12 – ADF-STEM images of welded Au NRs with almost identical welding geometry containing (a)-(b) dislocations and (c)-(d) grain boundaries. The presence of diffraction contrast enabled us to identify the systems containing grain boundaries, at relatively low magnifications. This image mode prevents the deposition of organic species during the electron beam scanning prior to the spectroscopic data acquisition.

Analysis of the energy spectrum of the CTP mode for both cases revealed a difference smaller than an average of 20 meV for the resonant energy of the CTP mode. Since this value is smaller than the energy resolution of the measurement, it is most likely that the defect type has no substantial influence on the resonant energy of the CTP mode. The dimensions of the welded gold nanorods can be found in Table 5-2. In addition, to evaluate the broadening of the plasmon mode by the different types of defects and hence the damping induced by these defects, the linewidth of the CTP mode (Γ) was determined from fitting the measured CTP mode with a Lorentzian function[246]. To ensure that no carbon build-up artificially broadened the plasmon mode, the CTP mode was only extracted at the side of the welded system, which was closer to the beginning of the EELS scan. In addition, deconvolution of the EELS spectra was used. The obtained linewidth Γ for the two systems containing dislocations was equal to 229 meV in average, whereas for a grain boundary this value corresponded to 206 meV, for two different welded gold nanorods, as shown in Figure 5.13.b by the red and blue dots respectively. Although these results suggest that dislocations cause a slightly larger broadening compared to grain boundaries, the observed differences are smaller than the energy resolution. To compare the influence of defects on the plasmon damping with systems without defects, single

crystalline gold nanorods with similar aspect ratios as the welded systems were investigated under the same conditions. Such comparison is possible, since the CTP mode of welded gold nanorods mimics the longitudinal mode of a single nanorod larger in size[235]. Here, 9 gold nanorods with aspect ratios ranging from 3.7 to 6.3 were investigated (details can be found in the Table 5-2). In this manner, we could observed that he linewidth Γ increases for increasing energy of the resonant mode, as expected from literature[248]. This behaviour is illustrated in Figure 5.13 by the green dots. Moreover, the line linewidth Γ of the longitudinal mode of long gold nanorods at similar energies of the welded system was found to be smaller than 180 meV.

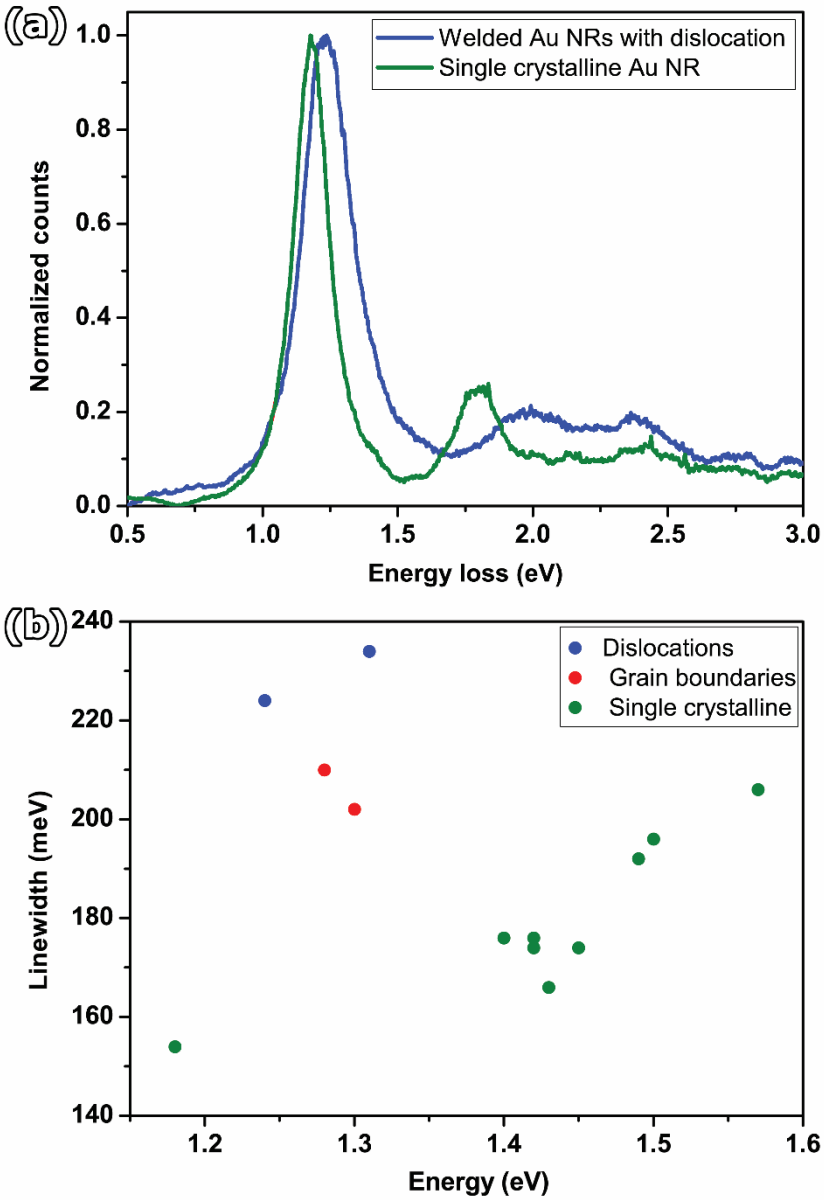

Figure 5.13– (a) EELS spectra of a welded gold nanorods with dislocations at the interface (blue) and a single crystalline gold nanorod (green), where their Lorentzian character is evident. (b) Linewidth of the CTP mode for welded gold nanorods containing dislocations (blue) and grain boundaries (red),

with almost identical welding geometry. In green, the experimental values of the linewidth observed for different single crystalline gold nanorods with similar aspect ratio of the welded systems, at varying resonant energies.

System	Length (nm)	Width (nm)	Linewidth Γ
Long AuNR_1	145	39	140
Long AuNR_2	145	34	116
Long AuNR_3	137	30.5	96
Long AuNR_4	145	31	100
Long AuNR_5	154	38	128
Long AuNR_6	135	20	64
Long AuNR_7	159	36.5	118
Long AuNR_8	145	31	100
Long AuNR_9	142	31	100
Welded AuNR_dis1_NR1	55	21	54
Welded AuNR_dis1_NR2	47	20	-
Welded AuNR_dis2_NR1	51.5	19.5	58
Welded AuNR_dis2_NR2	52	22	-
Welded AuNR_GB1_NR1	49	19	56
Welded AuNR_GB1_NR2	54	22	-
Welded AuNR_GB2_NR1	56	20.5	52
Welded AuNR_GB2_NR2	49.5	20	-

Table 5-2 – Table summarizing the dimensions of long gold nanorods (AuNR) and welded gold nanorods experimentally investigated. The linewidth Γ of welded nanorods is displayed only once, since the physical quantity was obtained for the complete welded system and not for individual nanorods.

Moreover, simulations based on Boundary Element Method (BEM)[249–251] using the full Maxwell's equations of long gold nanorods with same dimensions and volumes of the experimental

cases revealed the same trend (Figure 5.14)[246]. The simulated results also showed an increasing behaviour of the linewidth Γ for increasing energy, as observed experimentally. However, the linewidth Γ of the experimental results are broader than the values obtained by simulations, due to the limited energy resolution of the electron microscope and the additional damping from the interaction of surface electrons with the environment at the interface of the nanorods[252,253], which contains organic species (from the carbon support of the TEM grid, surface ligands and deposition of organic species).

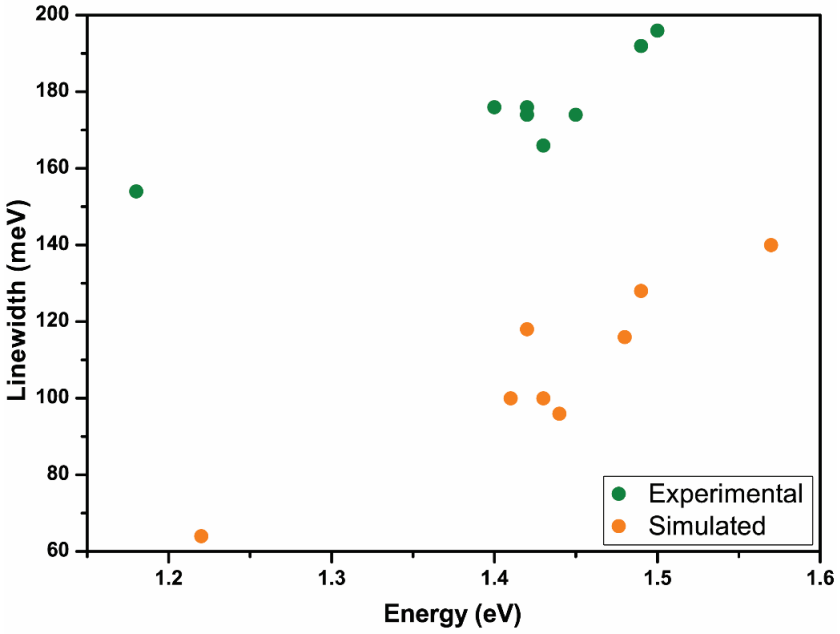

Figure 5.14 – Linewidth obtained from the determination of the FMHW of the CTP mode for long gold nanorods obtained experimentally (green) and from simulations (orange). The larger values observed in the experimental data arise from a combination of the limited energy resolution of the microscope and additional broadening due to the surface ligands, carbon support and the deposition of organic compounds upon interaction of the region of interest with the electron beam.

Additionally, simulations of welded gold nanorods were carried out. In this case, the geometry of the welded system was obtained from the 2D images and from tomographic results[246]. In both cases, the simulated results of welded gold nanorods showed smaller linewidth Γ when compared with the values obtained experimentally for the systems with similar geometry (Figure 5.15 and Table 5-2). The obtained linewidths Γ for the simulated welded nanorods are slightly smaller in comparison to single crystalline nanorods at the same resonant energy. This observation can be explained by the smaller radiation damping observed in nanoparticles with smaller volumes[254]. Moreover, the effect of the volume of the system in the broadening of the linewidth Γ is discarded, as the simulations were based on welded gold nanorods with the same geometry of the experimental cases. Besides, the

crystallinity of the welded gold nanorods were not taken into account during the simulations. Therefore, our findings suggest that the observed broadening of the linewidth Γ of the resonant mode observed for experimental welded gold nanorods is attributed to the presence of defects.

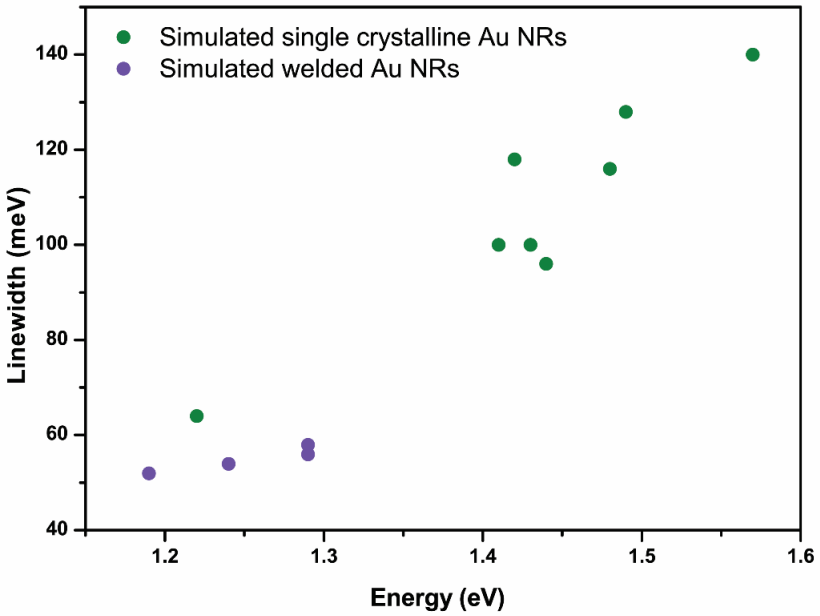

Figure 5.15 – Linewidth obtained from the determination of the FMHW of the CTP mode for long Au NRs (orange) and welded Au NRs (purple) obtained from simulations.

Our findings unambiguously indicated that the presence of defects in welded gold nanorods are responsible for a broadening of the CTP resonance, where the type of defect has not shown a direct influence. The presence of structural defects is responsible for changing locally the atomic potential of the object and, consequently, the dielectric constant of the material[89,255]. Besides, for polycrystalline structures where the grain size is smaller than the mean-free path of the cloud of free electrons, an increase of the collision rate of the free electrons with the boundary of the defect is expected[46,252,256]. Thus, an increase of the damping constant (characterized by the linewidth Γ) is observed for structures containing lattice defects, since the total damping term is the sum of the contribution from radiative (resonant scattering), non-radiative (absorption) processes and the coupling of plasmonic modes with electronic transitions in the matrix in which the nanoparticle is embedded [257–259]. For the non-radiative processes, contributions from the collision rate from electron-electron, electron-phonon and electron-defect scattering are the main parameters for metallic nanostructures[46]. Consequently, the intensity of the plasmon mode might be reduced due to the corresponding increase of the aforementioned damping process[252]. Recent studies of polycrystalline gold nanostructures lithographically fabricated confirmed the decrease of the plasmon linewidth Γ

after the annealing process, where the density of defects is smaller when compared to non-thermally treated structures[46,47,89,252,260].

The use of advanced techniques for electron microscopy enabled the identification of the defect type present at the interface of welded nanorods. Additionally, the use of such advanced techniques allowed a further correlation of the plasmonic properties of the investigated structures with the presence of structural defects. More interestingly, the characterization of the observed broadening effect of the plasmonic modes of welded nanostructures are of great importance for the design of new applications as well as the optimization of the existing ones in the field of Raman spectroscopy. One of the main consequences of the observed plasmonic broadening is the decrease of the associated of field enhancement (due to the decrease of the total energy of the polarized cloud of free electrons which is proportional to $\left|\vec{\boldsymbol{E}}\right|^2$)[28,45,89,261,262]. As discussed in section 1.2.4, the plasmonic properties of nanostructures are critical for the enhancement of the Raman intensity. Therefore, a decrease on the field enhancement is directly associated with a decrease in the SERS performance of plasmonic nanostructures.

5.5 Conclusions

In conclusion, our findings demonstrate the importance of the characterisation of complex welded metallic nanoparticles for a better understanding of the relationship between their fundamental physical properties and their morphology. The use of electron tomography at the atomic level was essential for the identification and visualization of the 3D distribution of defects present at the nanojunction of welded nanorods. This knowledge, combined with spectroscopic techniques, allowed the verification of a possible influence of the structural defects on the plasmonic properties of welded nanorods. Although it was not yet possible to determine how the defect type has an influence on the plasmonic properties, the present study revealed that the presence of structural defects are responsible for a further broadening of the plasmonic properties. This finding is of great relevance for the design of new applications and the optimization of the existing ones in the field of molecular sensing, where the additional broadening of the plasmonic properties due to defects can be a critical factor for the performance of the sensor.

5.6 Experimental methods

In this section, a summary of the different approaches for the characterization of nanomaterials based on advanced techniques for electron microscopy is provided. High resolution STEM imaging delivered information regarding the atomic structure of the welded nanorods before and after laser interaction, as well as the crystallographic nature of the structural defects found.

Electron tomography was employed for the determination of the welding angles for welded nanorods with different geometries. Multimode tomography was used for the determination of the 3D extension of the defect at the interface of the nanorods at the nanoscale. Atomic resolution electron tomography was used to further investigate the crystalline structure of welded nanorods and the crystallographic nature of the defects found. By combining the analysis of the welding angles with high resolution imaging and the results from the atomic resolution electron tomography, a link between the welding geometry and defect type that is formed upon laser interaction was established. Moreover, EELS measurements were used for the determination of the plasmonic modes excited by the electron beam. EELS measurements combined with ADF-STEM imaging of welded nanorods with almost identical welding geometry allowed the determination of the impact of the presence of structural defects (dislocations and grain boundaries) on the plasmonic properties of welded structures, as further confirmed by simulations.

5.7 Author contribution

Thaís Milagres de Oliveira performed all the image acquisition, reconstruction and analysis for this study. Dr. Wiebke Albrecht and Thaís Milagres de Oliveira acquired the EELS data for nanorods with different welding geometry. Dr. Wiebke Albrecht analysed the spectroscopic data. Dr. Armand Béché and Thaís Milagres de Oliveira acquired the EELS data for welded nanorods with the same geometry and different defect type. Dr. Wiebke Albrecht performed the analysis of this spectroscopic data and the BEM simulations. Synthesis of gold nanorods and femtosecond laser pulses treatment were carried out by the research team of Prof. Dr. Luis M. Liz-Marzán.

The author of the present thesis contributed to this study by providing a connection of the welding geometry with the type of defect that is formed at the nanojunction through the retrieve of 3D structure of welded nanorods at the nano/atomic level and by assisting in the analysis to determine the influence of the presence of defects on the plasmonic properties.

Part 2

Electron tomography of beam sensitive nanomaterials

Chapter 6. Optimization of electron tomography techniques for soft-hard matter self-assemblies

6.1 Applications of self-assemblies of nanoparticles

In the past decades, the interest in metallic nanoparticles has increased significantly due to their plasmonic properties. One of the most promising fields of their applications is in the photothermal treatment of tumour cells[18,21,84,263–266], as explained in Section 1.2.4. However, one of the main challenges for the implementation of plasmonic nanoparticles for *in-vivo* treatments relies on their cytotoxicity, which is associated with their size, shape, surface chemistry. More importantly, due to environmental variation of the *in-vivo* organisms, (e.g. environment pH or temperature changes[267]) oxidation processes might occur resulting in the release of ions in the living structure[268], as it is the case when using silver nanoparticles. In order to potentially enable the use of plasmonic nanoparticles in the biomedical field, coating strategies using polymers, di-, tri-block copolymers and silica shell have been developed[266,269–271].

The size of the nanostructure to be used in biomedical applications is mainly determined by the cell type[81,272–275]. Thus, it is of great importance to deliver synthesis protocols that allow an effective control and reproducibility over size of the nanostructures. Recently, a new methodology for the synthesis of clusters of metallic nanoparticles (gold and silver) has been proposed, where the size of the final nanostructure is tuned by the number of particles in self-assembly[268]. In this methodology, gold (19 ± 2 nm) and silver (42 ± 9 nm) nanoparticles were coated with citrate in aqueous solution, since the encapsulation of initially hydrophilic nanoparticles confers an extensive generality of the method (e.g., the encapsulation of anisotropic nanoparticles). The methodology for synthesis of the clusters is divide in three parts, as illustrated in Figure 6.1. First (i), a step of ligand exchange reaction with poly(isoprene)-diethylenetriamine (PI-DETA) performed by emulsifying an aqueous suspension of nanoparticles with a hexane solution of PI-DETA through vigorous magnetic stirring (Figure 6.1.b).The obtained colloids were dried and re-dispersed in tetrahydrofuran (THF). Next (ii), PI-DETA nanoparticles were encapsulated in aqueous media, inside a supramolecular system formed by the addition of poly(isoprene)-*block*-poly(ethylene oxide) (amphiphilic PI-*b*-PEO di-block-copolymer), triggering the formation of a supramolecular micellar system. The number of particles present in the micelle can be controlled by modifying the molar ratio between nanoparticles at PI-DETA and PI-*b*-PEO. Finally (iii), a seeded emulsion polymerization step was applied in the hydrophobic part of the system, resulting in the formation of a cross-linked polymer protective polystyrene shell. The cross-linked polystyrene shell confers the system high stability in biological environments and prevents

oxidation events[268]. The obtained colloidal suspension is then purified through centrifugation for the removal of empty supramolecular micelles and unreacted reagents. More details about the synthesis protocols used can be found in [[268]].

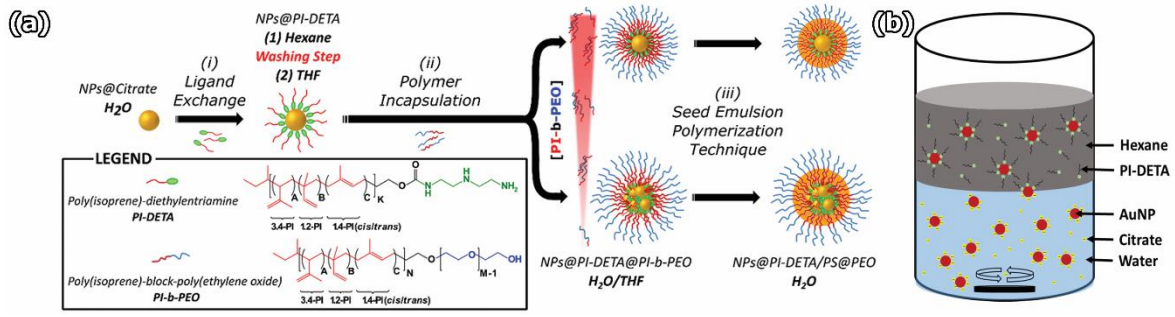

Figure 6.1 – (a) Schematic representation of the three step protocol for the encapsulation of clusters of hydrophilic metallic nanoparticles using (i) PI-DETA, (ii) PI-*b*-DETA di-block copolymer and (iii) seeded emulsion polymerization steps. The orange shell displayed in (iii) corresponds to the protective polystyrene shell. (b) Representation of the phase transfer of citrate-stabilized nanoparticles from water to hexane using PI-DETA. Figure adapted from [[268]].

The biocompatibility and biostability of the prepared nanostructures with the soft tissue was verified after incubation of the supramolecular micelles with mammalian cells in *in-vitro* conditions[268]. More importantly, the cross-linked polystyrene shell remained intact during the exposure to different mammalian cells[268], as observed from TEM imaging. These findings are of vital importance for biomedical applications, since the encapsulation method confers a protection against oxidation effects, minimizing the effects of toxicity from silver nanoparticles[276,277].

More importantly, the self-assembly nature of the plasmonic nanoparticles in such complex structures gives rise to a plasmon coupling, resulting in a red-shift of the plasmon mode[268]. The observed behaviour is mainly connected with two characteristics of the nanoparticle clusters: the total number of particles per cluster and the interparticle distance between neighbouring particles. For a better understanding and control of the synthesis design, a thorough characterisation of the self-assemblies is indispensable. For instance, a proper quantification on the number of particles and interparticle distance is essential to determine the optimum ratio between PI-DETA and PI-*b*-DETA during the synthesis and the resonant energy of the excited plasmon mode, respectively. Thus, here different methodologies for the 3D characterisation of self-assemblies of nanoparticles were employed for the determination of the number of particles per cluster and the interparticle distance between neighbouring nanoparticles.

6.2 The use of TEM tomography for reducing beam radiation damage

Due to the superposition that stems from a single 2D projection (Figure 6.2.a-b), it is impossible to determine the total number of particles per cluster and the interparticle distance between neighbouring particles. In order to recover the complete 3D morphology of this structure, electron tomography is applied. Here, series of 2D projections of clusters of gold nanoparticles were recorded over a tilt range from -72^{o} to +72^{o}, with steps of 2^{o}, using a dedicated tomography holder (Fischione tomography holder model 2020) at a ThermoFisher Tecnai G2 operated at 200 kV. Image alignment and series reconstruction (using the SIRT method) was carried out in MATLAB, using the Astra Toolbox[175](Figure 6.2.c-d).

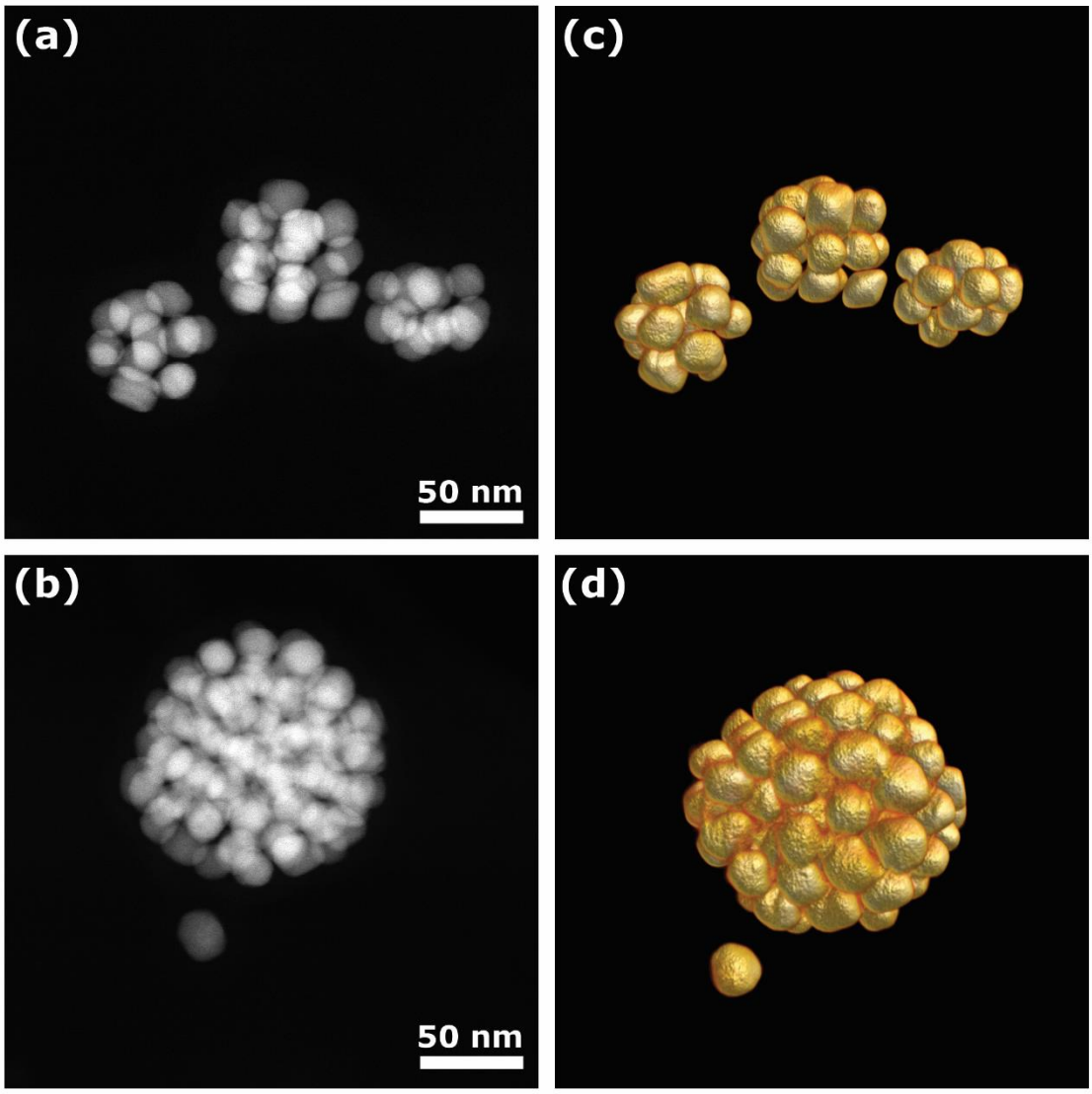

Figure 6.2 – (a), (b) HAADF-STEM imaging of clusters of gold nanoparticles. Due to the large number of particles in each cluster, the determination of the number of particles and the interparticle

distances are not straightforward. For the determination of such parameters, electron tomography is employed. (c), (d) shows the volume rendering of the same structures after 3D reconstruction.

The number of particles per cluster was determined by a 3D segmentation of the reconstructed volume. Since most of the particles were connected in the 3D reconstructions, the use of dedicated reconstruction algorithms for self-assemblies, previously developed at out laboratory[278] could not be successfully applied. Automatic segmentation techniques are also not applicable in a straightforward manner for the same reason. Therefore, manual segmentation was performed for 17 reconstructions. Figure 6.3 displays the frequency distribution (in %) of the number of particles per cluster for encapsulated gold nanoparticles. Our results revealed a relatively broad range distribution in the number of particles per cluster and, consequently, the total size of the self-assembly. The deviation from the perfect linearity can be attributed to the polydispersity of the size of the individual nanoparticles, as well as the variation of the shape of the clusters (in some cases, elongated clusters were found). Preliminary results based on 2D imaging also revealed a relatively broad range of the total size of the clusters, in accordance with our findings based on the 3D characterisation. Therefore, the synthesis method developed here has a potential drawback over the control on the number of particles per cluster and the overall size of the structure[268]. For biomedical applications, continuously density gradient centrifugation technique[279,280] can be applied to narrow down the size distribution of the supramolecular micelles. However, it can only be applied to volumes smaller than 500 μL.

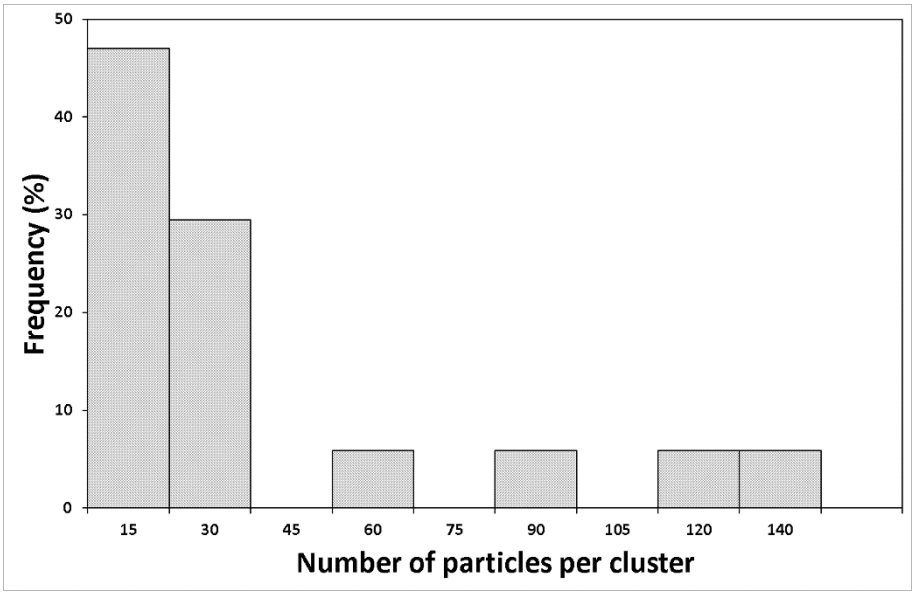

Figure 6.3 – Histogram for the frequency distribution (%) of the number of particles per cluster of encapsulated gold nanoparticles, where a broad range of total size distribution of the encapsulated clusters were found.

Unfortunately, HAADF-STEM images before and after the acquisition of the tomographic series revealed structural changes of the clusters (i.e. the change in the distance between neighbouring nanoparticles), as indicated by the red arrows in Figure 6.4. Moreover, image quantification confirmed the system shrunk during the acquisition of the series, which might explain the observed connection of the nanoparticles during the segmentation step. For the current example displayed in Figure 6.4, the shrinking corresponds to 5 nm in diameter. It should be noted that the quantification of the number of particles per cluster is not hampered by the shrinking effect. Still, for the determination of the interparticle distance, this method cannot be used. Adjustments of the gamma level in the HAADF-STEM images allowed the visualization of the organic structure of the polystyrene shell of the system before the acquisition of the tomographic series (blue arrows in Figure 6.4). However, the same structure is not visible after the acquisition of the series, indicating that electron beam damage took place during the image acquisition. Furthermore, the deposition of organic species during the scanning of the electron beam over the region of interest compromised the visualization of the polystyrene shell, hindering the determination of the stability of the shell after the acquisition of a full tomography series.

To minimize this effect, HAADF-STEM tomography based on a fast acquisition[147] scheme was applied. Within this methodology, a stack of images is obtained while the holder is continuously tilted inside the microscope. This enabled the acquisition of a tomographic series in a time scale of approximately five minutes. In general, the conventional acquisition scheme for a tomographic series might take from 25 to 40 minutes per series. One of the main advantages of the fast acquisition scheme is indeed the shorter time required to obtain a tomographic series, reducing the exposure of the specimen under investigation to the external radiation. Nevertheless, the acquisition of a fast tomographic series is less straightforward than the conventional methods, since during the rotation of the specimen stage and therefore the acquisition, one needs to track the object back into view and adjust the focus values manually. Due to this, some frames of fast tomographic series might contain additional artefacts (e.g., motion effects and blurring), requiring a post processing prior to the reconstruction or even their removal from the tomographic series for further reconstruction[223,281]. Still, a shrinking effect of the cluster of 3 nm and the degradation of the polystyrene shell were observed after the acquisition of a fast tomographic series of approximately 8 minutes (500 frames of 1s), as shown in Figure 6.5.

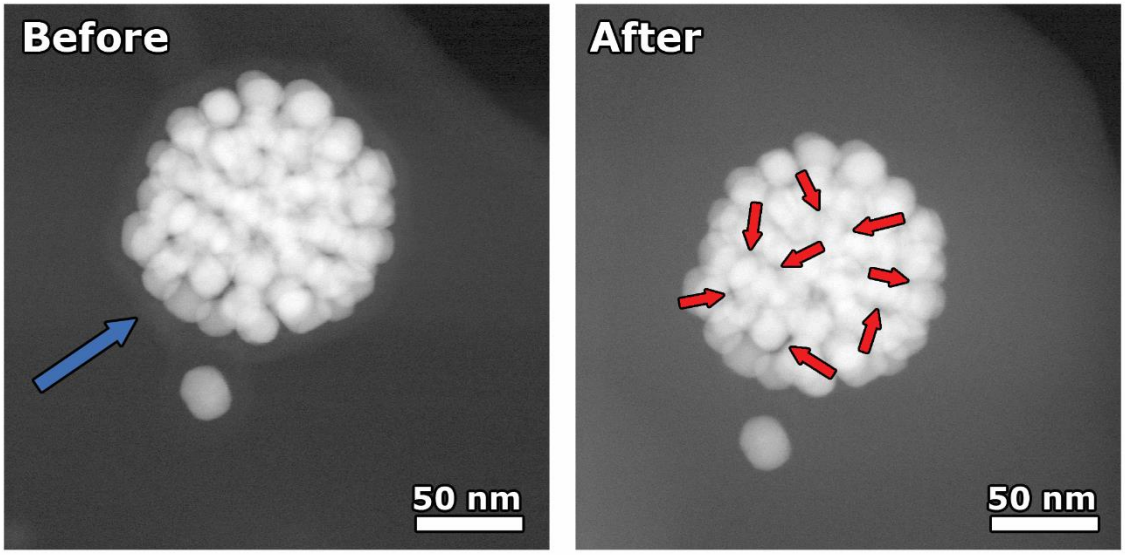

Figure 6.4 – HAADF-STEM images before and after the acquisition of a conventional tomographic series. A layer of organic material is clearly visible before the acquisition of the series (indicated by the blue arrow) and absent after the acquisition. Moreover, a shrink effect of 5 nm of the cluster was measured, where distances between particles showed clear modifications after the tomographic acquisition (red arrows).

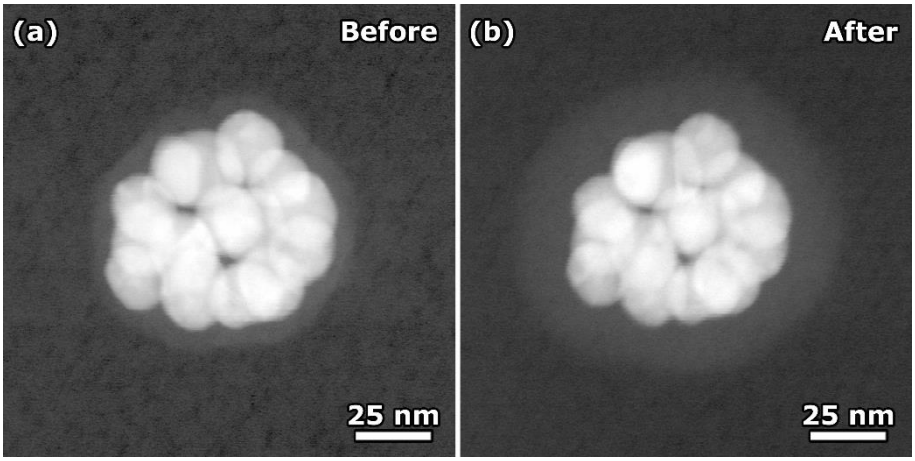

Figure 6.5 – HAADF-STEM images before and after the acquisition of a fast tomographic series. The layer of organic material is clearly visible before the acquisition of the series (a) and an dilation effect of the same layer is visible in panel (b). Moreover, it was observed the structure shrunk 3 nm. Image courtesy of Dr. Eva Bladt.

The STEM imaging conditions used for the investigation of clusters of metallic nanoparticles consisted of a beam current of 0.050 nA, a dwell time of 6.0 μs (time to scan a single pixel) and pixel size of 0.255 nm, using the conventional acquisition setup for a tomographic series acquisition. The total dose accumulated $Dose_{accum}$ can be determined by solving the following equation:

$$Dose_{accum} = \frac{beam\ current \times total\ acquisition\ time}{charge\ of\ electron \times scanned\ area}. \quad (6.1)$$

For the mentioned parameters, the total dose accumulated after the acquisition of a single image obtained with conventional methods corresponds to $Dose_{accum} = 2.88 \times 10^4 electrons/nm^2$. The dose rate $Dose_{rate}$is equivalent to the total dose accumulated divided by the total acquisition time and corresponds to $Dose_{rate} = 4.58 \times 10^3 electrons/(nm^2 \cdot s)$. For a fast acquisition scheme, the total accumulated dose $Dose_{accum}$ of a single image will be lower than in comparison to the conventional acquisition scheme, since the dwell time typically used is smaller (0.4 μs). Thus, the total dose accumulated per image is $Dose_{accum} = 1.92 \times 10^3 electrons/nm^2$ for a fast acquisition scheme and the dose rate is $Dose_{rate} = 4.58 \times 10^3 electrons/(nm^2 \cdot s)$. As discussed in section 2.4.1, the frame time is typically larger than the total time the specimen is illuminated by the electron beam, justifying the differences observed for the $Dose_{accum}$ and $Dose_{rate}$. The dose accumulated over the complete acquisition of a tomographic series corresponds to the multiplication of the $Dose_{accum}$ by the number of images in the tomographic series. For the fast approach, the dose accumulated over the complete series was $Dose_{fast} = 9.60 \times 10^5 electrons/nm^2$, three times smaller than for a conventional approach $Dose_{conventional} = 2.10 \times 10^6 electrons/nm^2$, while the dose rate remained the same for both cases. Indeed the critical parameters for the dose rate (current of the electron beam, number of pixels in the image and magnification) were kept the same for both acquisition schemes (50 pA, 1024x1024 pixels and 450.000x). Although the total dose accumulated for the complete tomography series using fast approaches was smaller, degradation effects were observed in the clusters. Our results indicate that the radiation damage is not associated with the total acquisition time of a series, but rather with the electron dose concentrated in the electron probe. It is clear that the main disadvantage of STEM over TEM imaging relies on the fact that the STEM probe focuses all the dose in a very small region of the specimen (probe size), whereas in TEM, the dose is spread over a large field of view. Consequently, the dose rate in TEM modes can be of orders of $10 - 1000\ electrons/(nm^2 \cdot s)$[115,282–284].

Therefore, to preserve the polystyrene shell of the supramolecular micelles, TEM imaging was used to perform the electron tomography series acquisition. Although the use of TEM images violates the projection requirement (as discussed in Chapter 2), recent studies have shown that the organic shells withstand the electron beam radiation when in TEM mode[149,269]. Tomographic series were acquired in TEM mode for clusters of both gold and silver nanoparticles at underfocused condition at the ThermoFisher Tecnai G20 and Osiris microscopes operated at 200 kV, which contributes for enhancement of visualization of the polystyrene shell (Figure 6.6). A quantitative comparison of the cluster before and after the acquisition of a tomographic series confirmed the absence of the shrinking

effect previously observed with HAADF-STEM imaging (Figure 6.6.a-b). However, further studies are still required for the precise determination of the critical dose in TEM mode where the micelles start to suffer from structural modifications, where tomographic series would be acquired for a vast range of dose values.

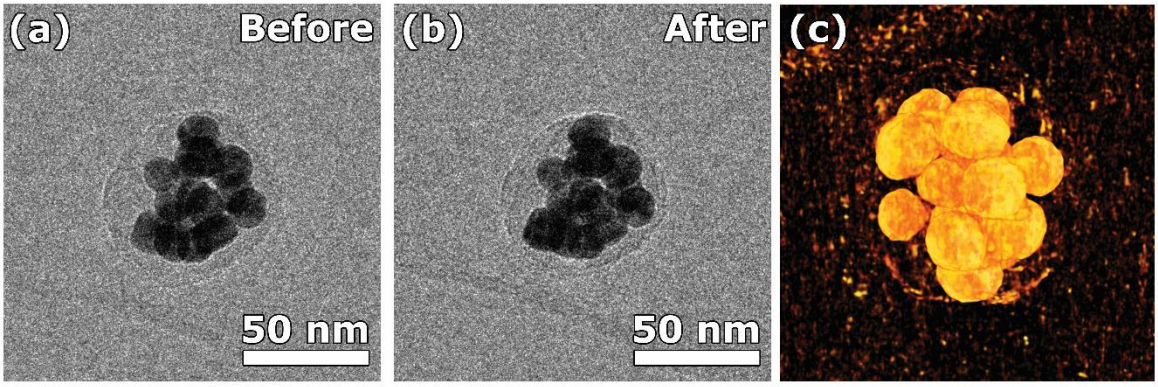

Figure 6.6 –TEM images (screen current of 0.106 nA, $Dose_{rate} = 850 \pm 425\ electrons/(nm^2 \cdot s)$ and acquisition time of 1s) of clusters of gold nanoparticles (a) before and (b) after the acquisition of a tomographic series, where the polystyrene shell is fully visible. (c) Reconstructed 3D structure of the cluster of nanoparticles. The $Dose_{rate}$ value was obtained from the sensor attached to the phosphorous screen of the microscope.

A simultaneous analysis of the slices from the 3D object and its volume rendering revealed the presence of a higher level of noise when compared with tomographic reconstructions based on HAADF-STEM imaging (Figure 6.6.c). This can be attributed to the image formation process behind TEM imaging, where low scattering materials are more visible in TEM mode than in HAADF-STEM mode. Due to the higher contrast of the background (carbon support layer - 3 nm) in TEM mode, these materials will also be recovered during the reconstruction. Additionally, the use of lower doses during TEM imaging ($\sim 850\ electrons/nm^2$), results in the presence of more counting noise in comparison to standard techniques in materials science (HAADF-STEM), contributing to the presence of a higher noise level in the reconstruction. Moreover, artefacts might also arise due to the violation of the projection requirement for tomography, hampering the quality of the reconstruction.

6.3 The influence of standard techniques for sample preparation and electron tomography

Analysis of slices through the 3D reconstructions in TEM mode revealed that neighbouring nanoparticles were still connected, although the shrinking effect of the polystyrene is no longer observed. Unfortunately, the quantification of the interparticle distance is still hampered by the

sample preparation techniques. Standard procedures consist of the natural evaporation of a droplet containing nanoparticles in suspension on top of the TEM grid. A diverse number of artefacts may arise from this type of sample deposition, such as the agglomeration of nanoparticles on the TEM grid[285] or a flattening effect of large self-assembly of nanoparticles[286], as illustrated in Figure 6.7.a-b. Investigations based on the comparison of TEM images (Figure 6.7.c-d) at low and high projection angles revealed the presence of a flattening effect of the polystyrene shell on the contact point with the carbon support film of the TEM grid, as indicated by the red arrow in Figure 6.7.d. This observation was later confirmed by the analysis of the 3D structure obtained from electron tomography experiments performed in TEM mode, where the retrieved structure was oriented along the same acquisition angles and further compared with the experimental images. For instance, Figure 6.7.e-f correspond to representations of a single slice through the 3D reconstructed volume, at orientations that reproduce the projection tilt of 0^{o} and $+74^{o}$, respectively. From Figure 6.7.g, it becomes clear that the nanoparticles closer to the carbon support layer are horizontally disposed, confirming that the present artefact generated by the drying process is responsible for displacing the nanoparticles in the self-assembly. The integrity of the polystyrene shell as well as the relative position of nanoparticles in the cluster was confirmed by further comparison of images before and after the acquisition of the tomographic series were performed.

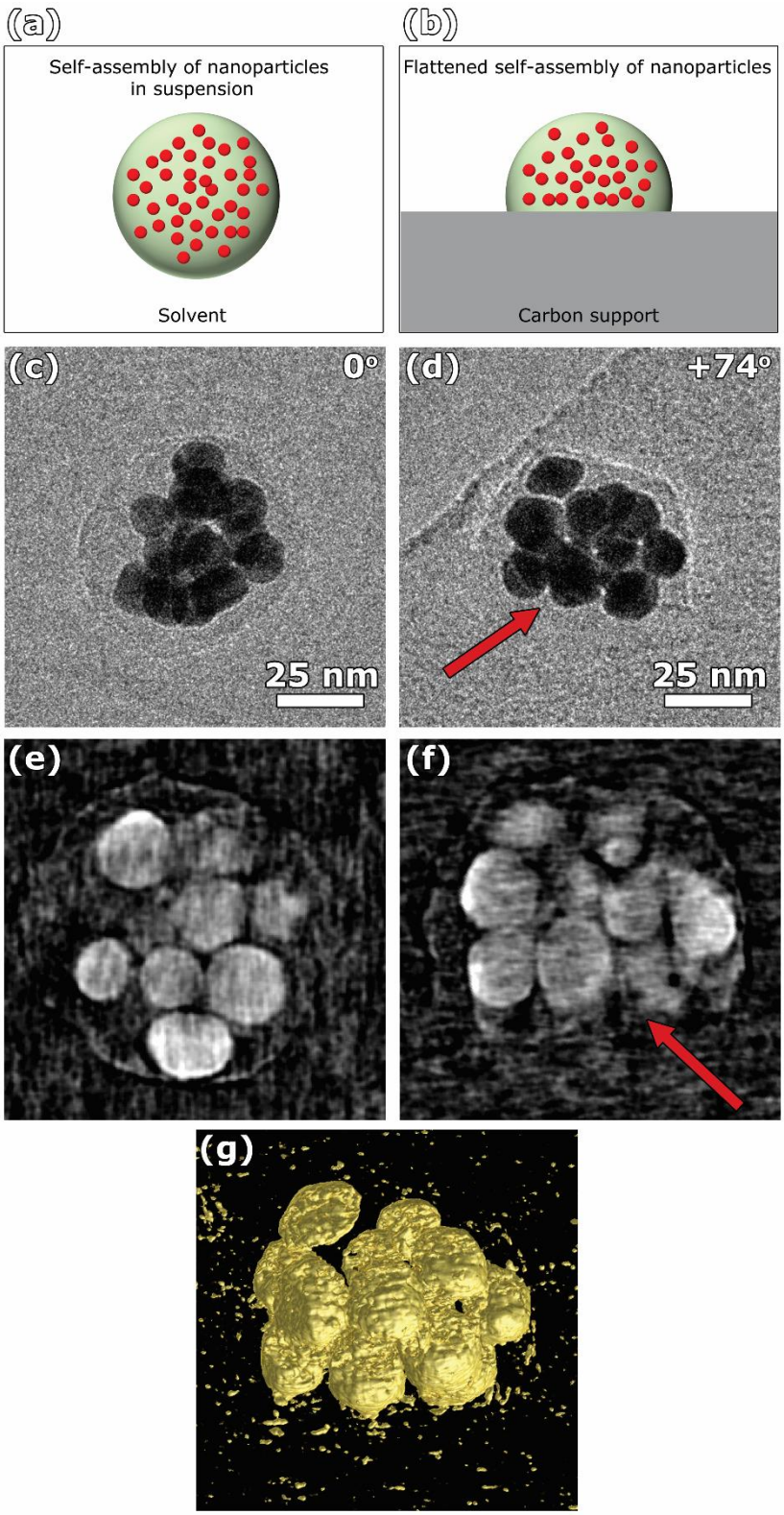

Figure 6.7 – (a) Representation of a self-assembly of nanoparticles (red spheres) encapsulated by a polymeric shell (green sphere) in suspension in a given solvent. (b) The same encapsulated self-assembly after transfer to a TEM grid and drying effect. The surface of the polymeric shell in contact with the supporting layer of the grid shows a flattening effect, which can result in the displacement of

individual nanoparticles in the self-assembly, hindering the quantification of the interparticle distances. (c) TEM image at lower doses ($\sim 850\ electrons/nm^2$) showing the top view of a cluster of gold nanoparticles on top of the carbon support film. In (d), the holder is tilted to angle of +74°, allowing an almost lateral view of the system. As indicated by the red arrow, we found indications of the flattening of the polystyrene shell, confirmed by the analysis of the projection images and the 3D structure obtained from electron tomography. (e)-(f) Orthoslices along orientations that represent the tilt of the holder shown on (c)-(d). (g) Volume rendering of the 3D reconstructed volume at the same orientation displayed in panel (f).

To fully understand their property-structure relationship, alternative methodologies are required for the sample preparation of encapsulated clusters of metallic nanoparticles. Still, there are very few studies published in literature that explain the observed flattening effect upon drying of self-assemblies of nanoparticles into a TEM grid[286]. However, it is likely that the surface tension between the solvent of the suspension containing the clusters and the carbon support layer is the main reason for the flattening[287].

6.4 The use of cryo-TEM tomography for soft hard matter assemblies

An ideal solution for the full characterisation in 3D of the supramolecular micelles would be the use of liquid cell TEM[288]. In this type of experiment, a solution containing the specimen in suspension is injected inside a dedicated holder loaded into the microscope. Unfortunately, the geometry of the holder does not allow high tilt angles and it is therefore impossible to record a tilt series of images to perform conventional electron tomography. An interesting alternative would be the use of cryogenic techniques to enable the visualization of the specimen in suspension in a frozen state. In the past, cryogenic techniques for electron microscopy was largely employed for the investigation of biological structures, to keep the structure of cells intact and avoid the introduction of artefacts from water evaporation[289–292]. In 2017, Jacques Dubochet, Joachim Frank and Richard Henderson were the laureates of the Nobel Prize in chemistry for developing cryo-electron microscopy for high-resolution structural determination of biomolecules in solution[293]. Alternatively, this technique has also been applied in the field of materials sciences[294–299], for the investigation of morphology evolution in macromolecular assembly, inorganic nucleation, growth and evolution of hybrid materials and even for atomic resolution investigations of lithium batteries, to avoid oxidation of lithium and electron beam radiation damage.

The vitrified state of the specimen in aqueous solution can be obtained through cryo-fixation, a method that involves the rapid cooling of the entire system to maintain its structure as close as

possible from its natural environment (details can be found in Appendix B). By applying this technique, we would be able to fully characterize the supramolecular micelles that are suspended in the vitreous ice layer, where the nanoparticles are not affect and displaced by the drying process from standard sample preparation techniques for TEM.

After cryo-fixation in liquid ethane or propane, the TEM grids are transferred to a specialized cryo grid box in liquid nitrogen. The grid box is store in liquid nitrogen until it is inserted in the Fischione model 2550 cryo-transfer tomography holder (Figure 6.8). The retractable tip of the holder is immersed in liquid nitrogen for the transfer of the TEM grid, to prevent crystallization of the ice layer. To avoid contact with air, the tip of the holder is retracted during insertion in the microscope. Moreover, the holder is equipped with a dewar that is filled with liquid nitrogen, to keep the tip at lower temperatures during insertion of the holder in the microscope. Because the vacuum inside the TEM column is very high, the crystallization of the ice layer is not stimulated. For imaging and acquisition of tomographic series, the microscope is operated in TEM mode at lower doses (dose rate below $850 \pm 425\ electrons/(nm^2 \cdot s)$, to avoid melting of the ice layer.

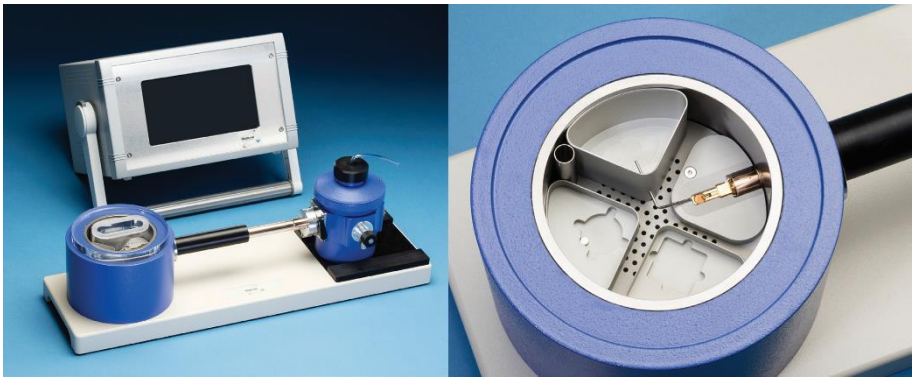

Figure 6.8 – Fischione model 2550 cryo-transfer tomography holder, with details on the recipient for liquid nitrogen to perform the grid transfer to the holder[300].

Cryo-TEM imaging of the supramolecular micelles after cryo-fixation revealed the absence of the vitreous layer in the holes of the carbon support layer. The clusters embedded on the vitreous ice were only found on top of the carbon layer (Figure 6.9.a). Due to the large thickness of the carbon layer (20 nm) and the vitreous ice layer, the image contrast of the background at high tilt angles prevented the visualization of the metallic nanoparticles (Figure 6.9.b). Consequently, it was not possible to acquire a tomographic series. For this reason, it was no longer possible to determine the interparticle distance using cryo-TEM imaging, as 2D imaging are very misleading. A possible limiting factor for the successful realization of this experiment could be associated with the large size of some

supramolecular micelles (larger than 200 nm), which prevented the formation of the vitreous ice in the gaps of the carbon support layer (with thickness of approximately 20 nm).

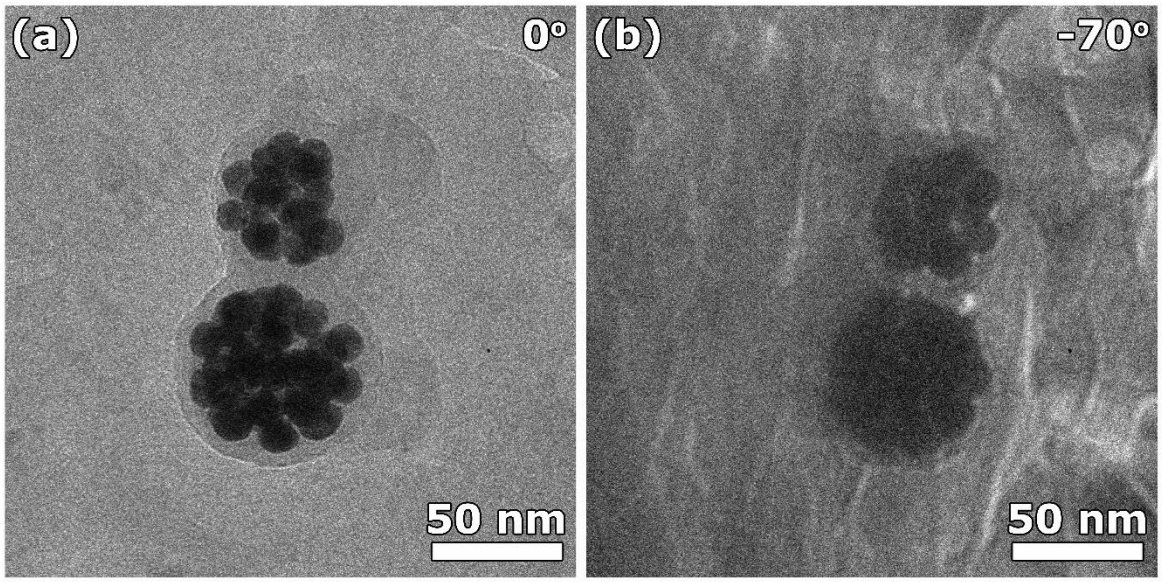

Figure 6.9 – TEM images under cryogenic conditions of a clusters of nanoparticles for a tilt angle of (a) 0° and (b) -70°. In the latter case, the thickness of the carbon support and ice layers prevented a clear visualization of the clusters of nanoparticles.

6.5 Freeze-drying technique for the investigation of clusters of nanoparticles

Since cryo-TEM imaging was not capable to provide a thorough 3D characterisation of the genuine structure of supramolecular micelles, alternative methods are required. Instead of visualizing the nanostructures under cryogenic conditions, an alternative would be the promotion of a controlled phase transition of the vitreous ice layer, from solid to gaseous state, where the liquid phase can be avoided. In this manner, we are able to prevent structural modifications of the morphology of the system due to the evaporation effects. This can be achieved by applying a so-called freeze-drying process, where the system is heated in a controlled manner under very low pressures after the cryo-fixation of the specimen on the grid. This procedure has been reported in the past for the investigation of cells and viruses[301,302] and it was demonstrated that the morphological structure of the objects under investigation is kept intact when applying this method. Based on the phase diagram of water, it sublimation from solid to gaseous state can be achieved by heating the object under medium vacuum (below 10 mbar). Recently, this methodology has been applied in the materials sciences field, for the investigation of spherical quasicrystals under spherical confinement[303,304]. Thus, the freeze-drying approach was applied in the current investigation for the determination of the interparticle distances.

The cryo-fixation of the grid containing the solution with nanoparticles in suspension is described in Appendix B. In order to heat the grid to room temperature, the Fischione model 2550 cryo-transfer tomography holder was inserted in a vacuum chamber, at pressure of $5 \times 10^5\ mbar$. The holder dewar with liquid nitrogen was kept full for 4-6h, for the thermal stabilization of the system at -90 ^{o}C. After this period, the liquid nitrogen was not refilled, resulting in its slow evaporation and a slightly temperature increase of the system over time. It was estimated a temperature increase rate of +2.6 ^{o}C. From our experiments, it was observed that the carbon support layer was destroyed upon fast temperature increase rates. After room temperature was reached, the grid was transferred to a conventional tomography holder (Fischione model 2020) and TEM imaging at lower doses ($Dose_{rate} \cong 850 \pm 425\ electrons/(nm^2 \cdot s)$ was applied for the acquisition of tomographic series of different clusters of silver and gold nanoparticles. By inspecting the projections images at low and high tilt angles (Figure 6.10.a-b), it becomes clear that the polystyrene shell is preserved for all tilt angles, indicating the absence of the flattening effect associated with the drying process. Analysis of the 3D reconstructed volume of those systems were performed in the same conditions as described in section 6.2 and Figure 6.6, confirming our observations (Figure 6.10.c-d).

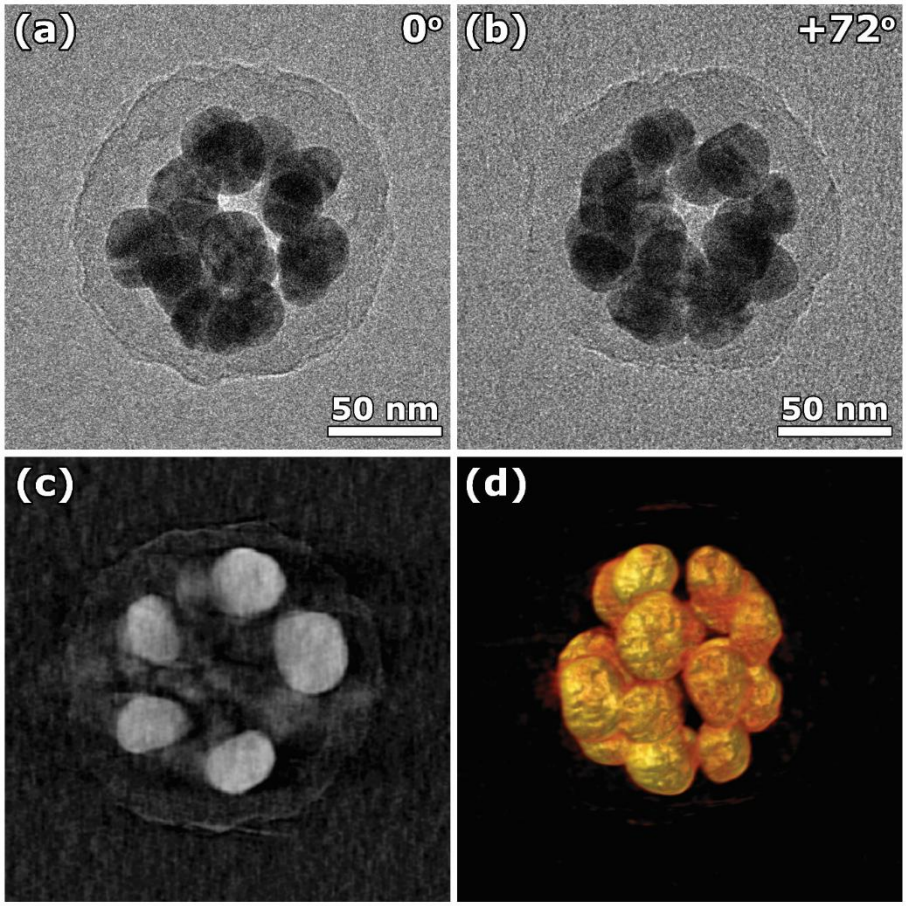

Figure 6.10 – TEM image ($Dose_{rate} \cong 850 \pm 425\ electrons/(nm^2 \cdot s)$) of silver nanoparticles encapsulated with a polystyrene shell at (a) 0° and (b) +72°. The polystyrene shell is fully visible at higher tilt angles, indicating the absence of the flattening effect due to the drying process. (c) Slice through the 3D reconstructed volume and (d) representation of the 3D structure through volume rendering.

The quantification of the interparticle distance between neighbouring particles became possible combining TEM tomography with freeze-drying approach for sample preparation, since we were able to retrieve of the structural morphology of the supramolecular micelles as close as possible to their native state. The other methodologies explored in this chapter (conventional HAADF-STEM tomography, fast HAADF-STEM tomography and cryo TEM tomography) were not optimal for such analysis. More specifically, the use of acquisition approaches in STEM mode was responsible to cause irreversible changes to the structure of the investigated micelles (polystyrene shell and the position of the nanoparticles), preventing the determination of the interparticle distances. Besides, the usage of cryogenic techniques for sample preparation has shown to be an important step to minimize the structure modification caused by wet drying processes. However, analysis of TEM grids in cryogenic conditions inside the electron microscope (Cryo-TEM imaging) revealed the absence of the suspended

vitrified ice layer, where the tomographic acquisition of the structure could be performed. Instead, only micelles lying on top of the carbon layer was found (Figure 6.9). The larger thickness of the support layer in this condition prevented the acquisition of a tomographic series and therefore, the determination of the interparticle distance.

The interparticle distance is defined as the distance between the edges of a pair of nanoparticles. This distance was determined through the observation of different slices through the 3D reconstructed volume along different orientation for a given pair. The smallest distance found between the different slices corresponded to the interparticle distance. A similar pattern for the interparticle distance of gold and silver nanoparticles was observed. Experimental results over several 3D reconstructed volumes revealed that a great number of nanoparticles were still connected. Unfortunately, it is still unknown if the nanoparticles were originally overlapping after synthesis. However, for those that were separated, a mean distance of 3 ± 1 nm was measured for 20 different pairs of nanoparticles from 7 different clusters. Our findings for the observed interparticle distances are in agreement with the observed plasmonic coupling and the formation of plasmonic hot spots at the gaps between encapsulated nanoparticles, obtained from ultraviolet/visible (UV/VIS) spectroscopy and dynamic light scattering[268].

6.6 Conclusions

Because of the beam sensitivity of supramolecular micelles, conventional techniques for electron tomography were not capable to provide a reliable 3D characterisation. More precisely, the interparticle distance could not be retrieved because of two reasons: beam sensitivity of the organic encapsulation and the structural changes during the sample preparation for electron microscopy analysis. In order to overcome these limitations, TEM imaging at lower doses ($Dose_{rate} \sim 850 \pm 425\ electrons/(nm^2 \cdot s)$) was used to minimize the structural modifications due to beam damage. To avoid structural modifications during the sample preparation, cryogenic techniques were applied. Here, the freeze-drying approach on cryo-fixated grids enabled the investigation of the supramolecular micelles maintaining the structure of the polystyrene shell as close as possible from the pristine structure. The combination of an advanced methodology for the sample preparation with TEM imaging at lower doses enabled a thorough 3D characterisation of the interparticle distance between neighbouring nanoparticles. This parameter is essential if one desires to establish a connection with the observed optical properties of the supramolecular micelles. Such knowledge is essential for the optimization and the design of synthesis protocols that aim the use of plasmonic structures for biomedical purposes.

6.7 Experimental methods

In this section, a summary of the different approaches for the characterization of nanomaterials based on advanced techniques for electron microscopy is provided. Conventional electron tomography technique based on HAADF-STEM imaging was employed for the determination of the number of metallic nanoparticles per micelle. To prevent radiation damage caused by the electron beam in STEM mode, TEM imaging was adopted. Electron tomography in TEM mode in low dose conditions allowed the structural characterization in 3D of micelles, with radiation damage effects minimized. The use of alternative approaches for sample preparation was required due to the complexity of the material, aiming the prevention of structural modifications caused by wet drying processes. Therefore, cryogenic approaches were used for the sample preparation. TEM investigation under cryogenic conditions were not successful due to the geometry of the nanostructure. Instead, freeze-drying approach was employed. Combined with TEM tomography in low dose conditions, the determination of the interparticle distance became possible, enabling a better comprehension of the optical properties, which is in turn essential for the design of new applications and the optimization of synthesis protocols.

6.8 Author contribution

HAADF-STEM series acquisition and tomographic reconstructions were performed by Thaís Milagres de Oliveira and Roy Janssens. Reconstruction segmentation and quantification of number of particles per cluster were performed by Thaís Milagres de Oliveira. Dr. Eva Bladt performed the acquisition of fast tomographic series. TEM image acquisition and reconstruction were performed by Thaís Milagres de Oliveira. Cryo-fixation, cryo- transfer, and freeze-drying procedure were performed by Dr. Nathalie Claes and Thaís Milagres de Oliveira. Quantification of the interparticle distance was performed by Thaís Milagres de Oliveira. Synthesis, optical measurements and investigations of the biostability of the clusters of nanoparticles were performed by our collaborators from Prof. Dr. Luis Liz-Marzán.

The author of the present thesis contributed to this study by providing an analysis of the number of nanoparticles per micelle, by applying different approaches for reducing the radiation damage caused to the structure (low dose TEM tomography), by applying different approaches for sample preparation and by performing the analysis of the interparticle distance between neighbouring particles.

Appendix B. Sample preparation under cryogenic conditions: cryo-fixation

Cryo-fixation aims the fast cooling of the specimen to preserve its native "frozen-hydrated" state[305]. If the specimen is gradually frozen, water expands and crystallizes, which can, in turn, disturb the morphological structure of the specimen[306]. Dubochet and co-workers[307] have shown that pure water deposited on a carbon layer could be frozen in a noncrystalline state (vitreous) if the process would be sufficiently fast (~ 10^5 K/s), preventing molecular arrangements and, consequently, the formation of ice crystals[306,307]. First of all, the TEM grids need to be treated to guarantee their hydrophilic property, so the solution containing nanoparticles in suspension will spread evenly over the entire carbon film. Recently prepared carbon films are naturally hydrophilic, however, they may become hydrophobic over time. Therefore, techniques like plasma treatment are often applied to TEM grids before cryo-fixation. In the present study, the grid was submitted to a plasma of Argon at radio frequency (RF) power of 80% for 2 minutes. Nevertheless, the parameters for the plasma treatment can vary for grid type and are obtained on the base of trial and error experiments. Typically, TEM grids containing a carbon support layer with holes is used, allowing the investigation of nanostructures suspended in the vitreous ice. Next, the grid is attached to a tweezer of an equipment for cryo-fixation, the Vitrobot from ThermoFischer/FEI. To prevent the desiccation of the specimens, the environment surrounding the grid is kept at high humidity conditions (relative humidity of 100%). This is easily achieved and controlled in the Vitrobot equipment. With this environmental conditions, 3-5 μL of solution containing the nanostructures in suspension can be transferred to the grid. Note that the grid is hold vertically inside the Vitrobot and the cryo-fixation procedure needs to be completed within a few minutes, to avoid that the solution will accumulate at the bottom of the grid. To remove the excess, the liquid droplet is blotted with filter paper. Because the solution containing the nanoparticles in suspension is evenly distributed on the carbon film, a very thin layer will be formed after blotting with filter paper. The formation of a thin layer of solution is crucial for optimal heat transfer. However, if a thick layer of fluid is formed, the ice may not vitrify[306]. The thickness of the solution is defined by the blotting time and pressure, which need to be adjusted for each experiment with the ideal parameters are obtained based on trial and error. The last step of cryo-fixation consists in the plunge freeze of the TEM grid into a liquid cryogen, producing a glass-like solid. Typically liquid ethane or propane or a combination of both are used for the plunge freezing, since their thermal conductivity is around 13-15 kK/s[306]. To liquefy ethane or propane gases, liquid nitrogen is commonly used. However, liquid nitrogen is not used for freeze plunging the TEM grid as it thermal conductivity is much lower

(400 K/s[306]), promoting the formation of crystallized ice. Finally, the main steps for cryo-fixation are summarized in Figure B.1.

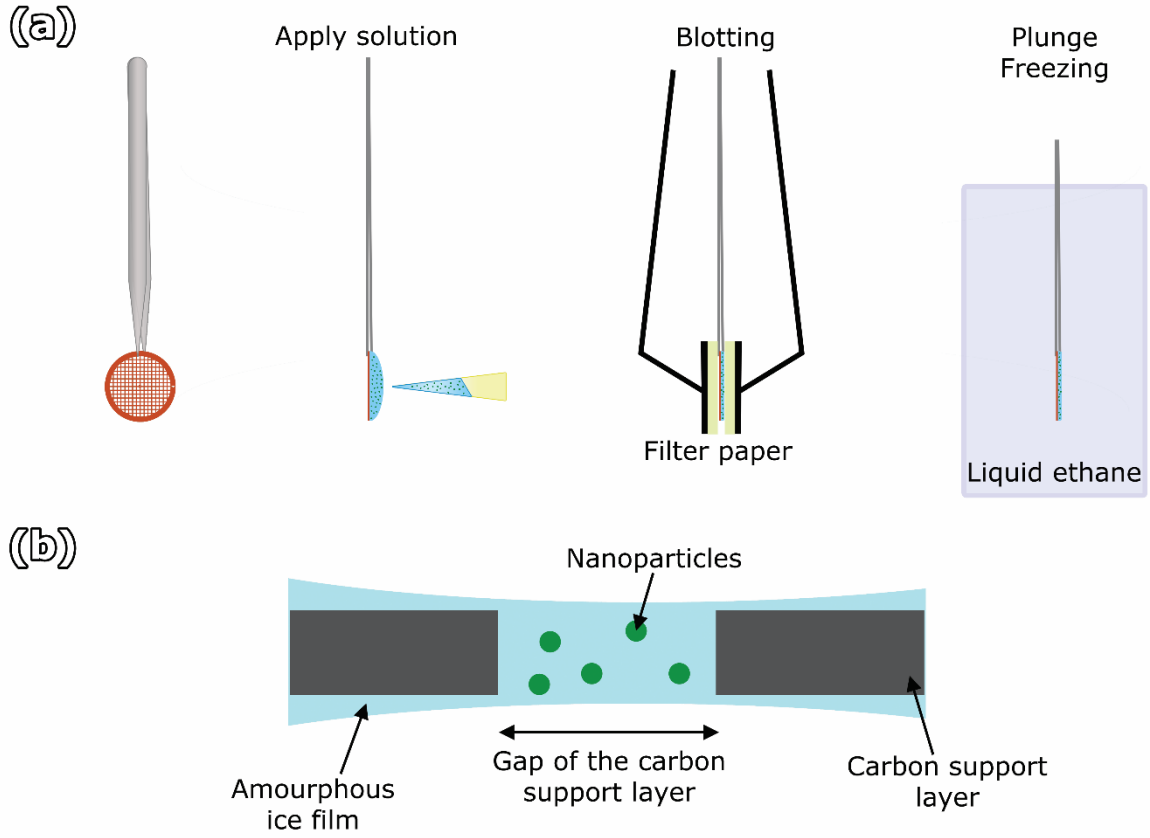

Figure B.1 – (a) Representation of the main steps of the cryo-fixation procedure. (b) Cross section view of the TEM grid with emphasis on the formed vitreous ice layer with suspended nanostructures in the gaps of the carbon support layer.

Chapter 7. Towards 3D characterisation of beam sensitive nanomaterials at the atomic level

7.1 Obstacles of the characterisation of beam sensitive nanomaterials in 3D

One of the main challenges for the 3D characterisation of nanomaterials at the atomic level using advanced techniques for electron microscopy is the modification of their crystal lattice due to radiation damage processes[220]. For instance, studies have shown that the use of high electron dose induces structural modifications in cesium lead halide perovskites[284,308]. Through the processes of knock-on damage and radiolysis, the structure of perovskite nanoparticles are irreversibly altered[309]. Very often, structure degradation and lead cluster formation are observed in metal halide perovskites during electron microscopy investigations[310,311]. Therefore, for a thorough 3D characterisation of nanomaterials that are sensitive to the electron beam, imaging techniques at low dose conditions are essential.

Due to the very small probe sizes in STEM mode (for high-resolution imaging, the probe size is around a few hundreds of picometers[312–314]), the electron dose density is concentrated in a narrow region in comparison to TEM mode. In TEM mode, the electron beam is parallel and not focused into a spot and, therefore, the illumination area can be as large as a few tens or hundreds of nanometres. Consequently, the delivered dose achieved in TEM mode can be a few orders of magnitude lower than what is achieved in STEM mode, as discussed in Chapter 6 (section 6.2). Studies on the radiation damage processes[115,282–284,315–318] have suggested that another parameter for the modification of the crystal structure by the electron beam is the dose rate. It has been shown that the usage of lower dose rates in TEM mode is beneficial for characterisation of beam sensitive nanomaterials at the atomic level, as it preserves the pristine crystal lattice of nanomaterials[282,284,319–323]. Such investigations of the atomic structure of perovskites are of great importance for the further development of synthesis protocols and the design of new/existing applications. More specifically, atomic resolution electron tomography of metal halide perovskites could provide valuable information regarding the density of defects, how the defects are distributed at the surface and in the bulk and, eventually, the atomic displacements caused by the presence of defects. This knowledge combined with optical, thermal and electronic characterization methodologies would enable a better comprehension on the parameters that determine, for instance, the defect tolerance on the physical performance of metal halide perovskites.

More interestingly, the use of low dose TEM imaging for the characterisation of beam sensitive nanomaterials has increased in the past years due to the development of direct electron

detection cameras. This type of camera consists of a complementary metal-oxide-semiconductor (CMOS) detector. Differently from conventional CCD (charged-couple devices) detectors, direct electron detection cameras do not require a scintillator layer prior to the detector to avoid radiation damage and saturation of the detector. Consequently, the resolution (detective quantum efficiency - DQE), the signal-to-noise ratio and the sensitivity achieved with direct electron detection cameras are superior when compared with standard CCD detectors[324,325]. Moreover, due to the direct detection design of such detectors, the acquisition time required for recording a TEM image is much smaller than conventional detectors. Because of the high sensitive of direct electron detectors, the electron dose required for an image acquisition is orders of magnitude lower than conventional techniques, which enables the 2D characterisation of beam sensitive nanomaterials in TEM mode. For instance, Figure 7.1.a shows the structural modifications in $CsPbBr_3$ perovskites induced in STEM mode (total accumulated dose of $288\ electrons/Å^2$), whereas Figure 7.1.b shows the structure obtained in TEM mode at lower doses when using a direct electron detection camera (total accumulated dose of $4.97\ electrons/Å^2$). Still, the presence of lead clusters could still be found (Figure 7.1.b). The lead clustering upon irradiation with the electron beam is already a well established process[90] and results from radiolysis damage effects[309].Moreover, the clustering is associated with the high diffusion of lead atoms followed by coalescence events for temperature conditions inside the electron microscope that exceed -40^oC[309]. Therefore, the use of higher tension of the electron microscope can improve the structure stability[284,309], while the usage of cryogenic conditions can minimize clustering events[309]. Nevertheless, the degree of structural modifications induced by the electron beam can be drastically reduced by performing low dose TEM imaging, where a smoother surface of the nanocubes were observed, in contrast with conventional STEM methodologies (Figure 7.1.a).

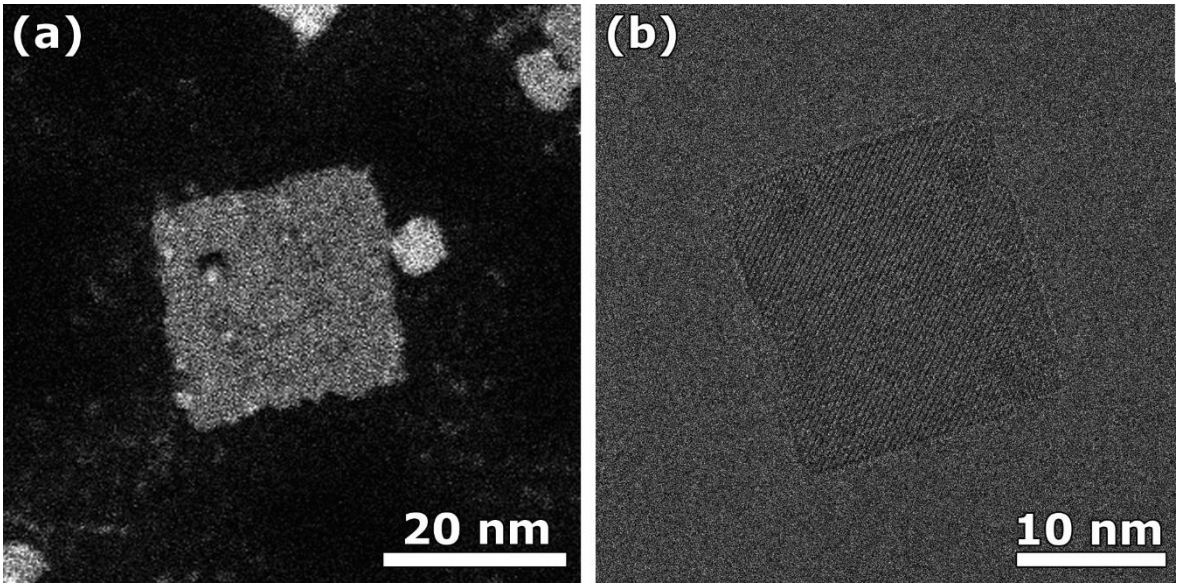

Figure 7.1 – (a) HAADF-STEM image of $CsPbBr_3$ perovskite, where structural modifications are visible (total accumulated dose of $288\ electrons/Å^2$). Image courtesy of Dr. Julien Ramade. Here, surface roughness was observed in the nanocube. (b) Low dose TEM image using a direct electron detection camera of a different nanoparticle from the same batch (total accumulated dose of $4.97\ electrons/Å^2$). In the latter, structural modifications were minimized, where the surface smoothness was preserved. Still, lead clusters can be still be found.

Since the state-of-the-art techniques for the recovery of the atomic structure of nanomaterials in 3D are mainly based in STEM imaging mode, it becomes evident the necessity of the development of alternative techniques for the 3D characterisation of nanomaterials investigated in TEM mode. Such development would open new possibilities for a thorough characterisation of beam sensitive nanomaterials in 3D.

7.2 Limitations of HRTEM imaging: the basis of Exit Wave Reconstruction

Although TEM images provide useful information regarding the size and projected shape, the interpretation and quantification of high-resolution TEM (HRTEM) images are not straightforward, due to strong radiation-matter interaction. Moreover, the transmitted electron wave by the specimen is further modified by the optical components of the electron microscope, where the image contrast observed in HRTEM images represents an interference effect between the information associated with the projected atomic potential of the specimen and the aberrations of the electromagnetic lenses. To circumvent the limitation of image interpretation and quantification, image simulation can be combined with HRTEM imaging, where simulations are carried out for different specimen thicknesses at the same experimental conditions and compared with the experimental images. From

the best match between simulation and experiment, the atomic structure and the correspondent thickness of the material under investigation can be unveiled. However, this process is hampered by the unsolved problem with the Stobbs factor[326–334].

Therefore, alternative techniques for HRTEM image interpretation and quantification are required. A widespread technique is exit wave reconstruction (EWR), which enables the recovery of the exit wave emitted by the sample as well as the deconvolution of the retrieved wave with the contrast transfer function of the microscope (mathematical function that describes the aberrations of the microscope) by inverting the image formation process[335–348]. In this technique, a series of images are acquired over a range of defocus settings of the microscope. The defocus step can be either fixed[335,336,341–348] or variable[349], depending on the type of information to be recovered. By acquiring a series of images with varying defocus, sets of different spatial frequencies are recorded. The information contained in the focal series can be used in an algorithm that will invert the image formation process and delivery the full exit wave function emitted by the specimen. The main advantage of the use of EWR technique is that it enables the recovery of not only the amplitude but also the phase information contained in the emitted wave by the specimen, since the phase is lost during the recording process of the intensities present in the HRTEM images. The phase information is the most relevant for the quantification of the crystal lattice, since it is the result from the interaction of the incoming electron wave with the atomic potential of the specimen[335]. Different algorithms and techniques can be used for the EWR: the Gerchberg-Saxton method[350–352], the parabola (PAM) method[353,354], the maximum likelihood (MAL) method[355], the transport intensity equation (TIE) method[356] and the iterative wave function reconstruction (IWFR method)[357,358]. In this chapter, all the exit wave reconstructions shown were obtained using the Gerchberg-Saxton method implemented in the XWave software[359] (package from MacTempas for Windows operational system). Besides, EWR allows a deconvolution of the emitted wave by the specimen with the aberration parameters of the microscope, further extending the resolution of the high resolution images[337–340].

In summary, the EWR technique is illustrated in Figure 7.2 and consists of: (a) determination of the parameters of the microscope; (b) acquisition of a focal series; (c) image processing of the experimental data (removal of hot spots and image conversion for the correct format of the EWR software); (d) correction of residual shifts between each experimental image; and (e) the image reconstruction.

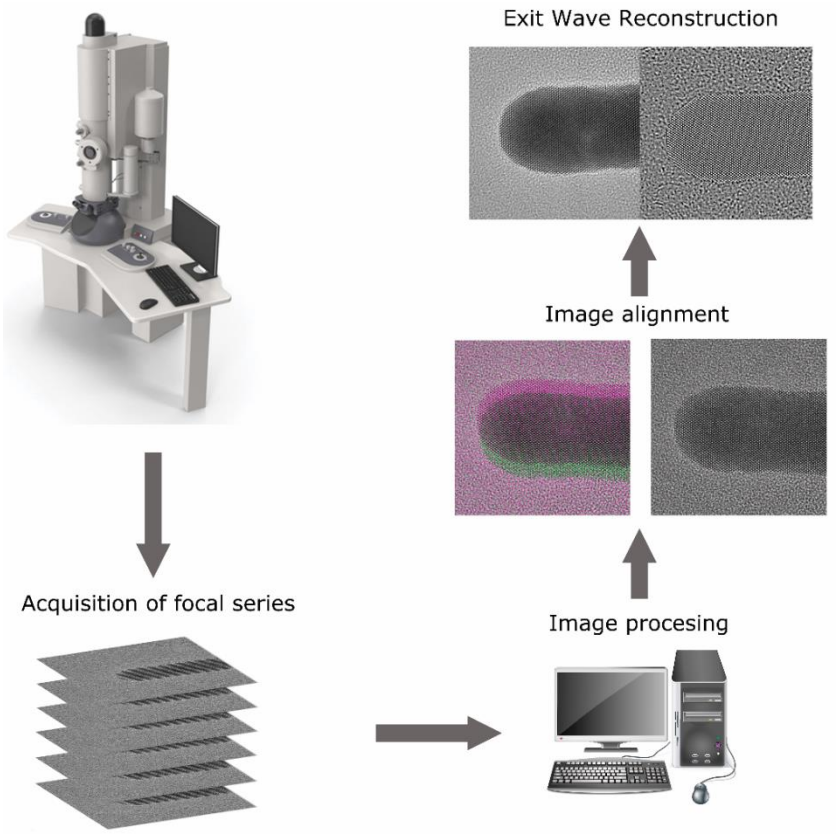

Figure 7.2 – Scheme illustrating the steps to perform exit wave reconstruction.

To illustrate the capabilities of EWR, a focal series of a $CsPbI_3$ was acquired with a ThermoFisher aberration corrected 'cubed' Titan operated at 300kV (Figure 7.3.a) using the parameters mentioned in the previous paragraph. After the exit wave reconstruction, the amplitude and phase were recovered, shown in Figure 7.3.b-c. Here, none structural degradation of the perovskite was observed during or after the image acquisition.

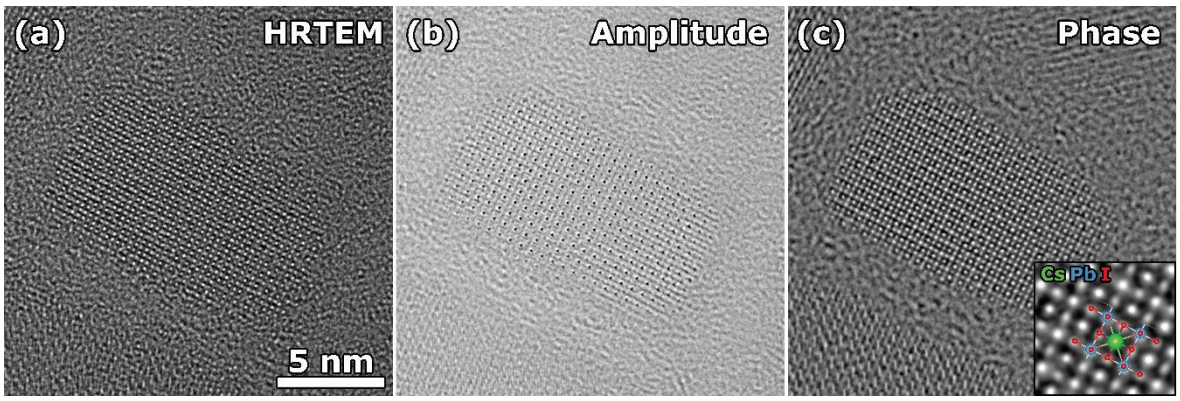

Figure 7.3 – (a) HRTEM image of $CsPbI_3$ at defocus of x nm. Reconstructed (b) amplitude and (c) phase using XWave software. Inset in (c) is a zoom in of the middle region of the image with a superposition of the crystal structure.

7.3 Motivation on the use of the phase images as input for electron tomography

Conventionally, HRTEM images of crystalline objects are acquired when the specimen is aligned along a main zone axis. A correspondence of the HRTEM image with the projected atomic potential of the object has been observed[360]. This phenomenon is the known as the electron channelling[173,342,360–364] and arises from the dynamic interaction of the parallel electron beam with multiple columns of atoms in the crystal structure of the specimen. For this configuration, the atomic columns act as a wave guide for the incident electron beam. The solution of the time independent Schrödinger equation of the electron wave after interaction with a single atomic column is[362,364]

$$\Psi(\boldsymbol{R},z)=1+\sum_{nm}2c_{nm}\sin\left(-\pi\frac{E_{nm}}{E_0}\frac{k_z}{2}z\right)\psi_{nm}(\boldsymbol{R})\times exp\left[-i\pi\left(\frac{E_{nm}}{E_0}\frac{k_z}{2}z-\frac{1}{2}\right)\right] \quad (7.1)$$

where $\boldsymbol{R}$ is the 2D vector parallel to the surface of the specimen, z a 1D vector perpendicular to $\boldsymbol{R}$ and sign opposite to the direction of the electron beam propagation direction, c_{nm} the excitation coefficient, $\psi_{nm}(\boldsymbol{R})$ the eigenfunctions of the Hamiltonian with eigenenergies E_{nm}, E_0 the Kinetic energy of the incident electron beam and $k_z=1/\lambda$ the z-component of the wavevector of the incident electron beam. It has been shown that only the first eigenfunctions is strongly bound for light atoms and sufficiently thin atomic columns[173,360,362–364]. Thus, the corresponding eigenfunction, eigenvalue and excitation coefficient will be called $\psi_{1S}(\boldsymbol{R})$, E_{1S} and c_{1S}, respectively. Within this approximation, equation (7.1) becomes[173,360,362–364]

$$\Psi(\boldsymbol{R},z)\approx 1+2c_{1S}\sin\left(-\pi\frac{E_{1S}}{E_0}\frac{k_z}{2}z\right)\psi_{1S}(\boldsymbol{R})\times exp\left[-i\pi\left(\frac{E_{1S}}{E_0}\frac{k_z}{2}z-\frac{1}{2}\right)\right]. \quad (7.2)$$

This approximation is known as the S-State model. From equation (7.2), the interactive wave function can be obtained, which corresponds to the electron wave after the interaction with the atomic potential subtracted from the transmitted plane wave $\Psi(\boldsymbol{R},z)-1$. The correspondent amplitude and phase of the interactive wave are respectively[173,360,362–364]

$$abs[\Psi(\boldsymbol{R},z)-1]\cong\left|2c_{1S}\sin\left(-\pi\frac{E_{1S}}{E_0}\frac{k_z}{2}z\right)\psi_{1S}(\boldsymbol{R})\right| \quad (7.3)$$

and

$$arg[\Psi(\boldsymbol{R},z)-1]\cong-\pi\left(\frac{E_{1S}}{E_0}\frac{k_z}{2}z-\frac{1}{2}\right). \quad (7.4)$$

Equation (7.3) reveals that the amplitude varies periodically (sinusoidal type) and peaks at the position of the atom columns, whilst equation (7.4) shows a linear dependency with specimen thickness z and chemical composition E_{1S}[173,360,362–364]. For heavier atoms or thicker objects, the second

eigenfunction is also bound, but weakly excited when in comparison with the first[362,364]. Nevertheless, the S-State approximation can still be used. To illustrate the effect of atomic mass in the linearity of the phase, simulations of the exit wave for a wedge object composed by different elements (silicon, copper, silver and gold) were carried out in MULTEM[365,366]. Because silicon is a light element compared with the copper, silver and gold, a linear trend was observed between the thickness increase of the specimen and the phase of the exit wave, as shown in Figure 7.4.a. For increasing atomic mass, disturbances on this linearity was observed (Figure 7.4.b-d). Consequently, the thickness range where the phase of the exit wave shows a perfect linear behaviour decreases with increasing atomic mass.

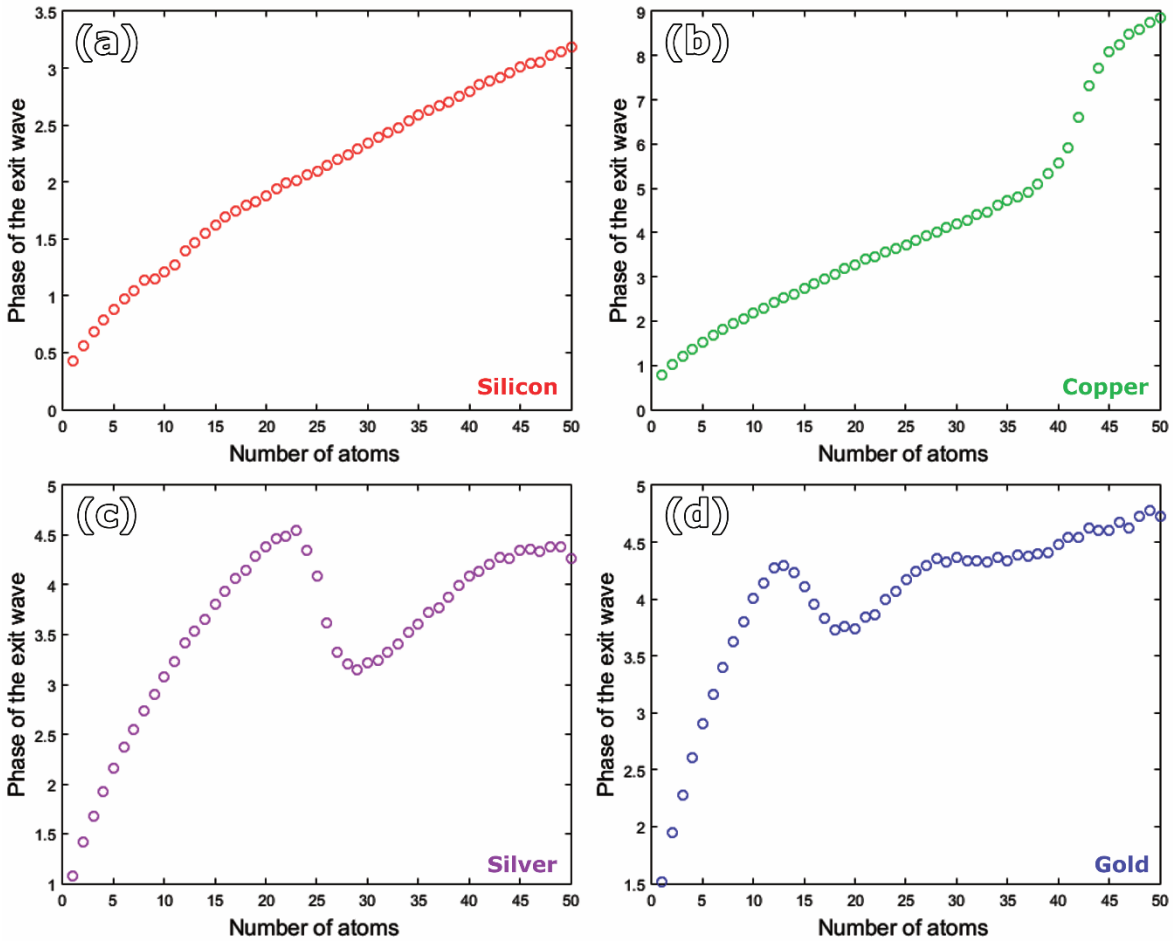

Figure 7.4 – Phase of the exit wave simulated with MULTEM for different chemical elements: (a) silicon, (b) copper, (c) silver and (d) gold. All crystals were oriented along the main zone axis [100]. For increasing the atomic mass, a disturbance of the linearity of the phase is observed.

In principle, HRTEM images cannot be directly used as input for tomographic reconstructions. This limitation stems from the non-directly interpretation of HRTEM images due to the image formation process and the aberration effects present in those images. Besides, as mentioned on section 7.2, only intensities are registered in HRTEM images and therefore the phase information

emitted by the specimen is lost. Therefore, exit wave reconstruction needs to be combined with HRTEM imaging for the development of tomographic approaches based on TEM with atomic resolution.

The theoretically observation of a linear dependency of the phase of the exit wave from the specimen with thickness is the starting point in the development and experimental implementation of electron tomography approaches based on the exit wave reconstruction, since under these conditions the projection requirement of tomography is fulfilled. In principle, this alternative methodology for electron tomography at the atomic level, in combination with the direct electron detection cameras, can be used for the 3D characterization of beam sensitive nanomaterials. In the following two sections, the approach will be theoretically and experimentally verified for gold nanorods as a proof of concept. The choice of nanostructure is based on the stability of the object under the electron beam and its well established atomic structure[112].

7.4 Formulation of the 3D EWR technique: simulated results

The desire of using the phase of the exit wave reconstruction as input for a tomographic reconstruction is not new. In the past, theoretical approaches to retrieve the 3D atomic structure of crystalline[367–370] and amorphous[370,371] objects were employed. Additionally, the 3D atomic structure of nano-objects was experimentally retrieved from a single phase image by different authors[315,328,372–374]. Such methods to retrieve the 3D atomic structure from a single projection are very complex and not always applicable to a wide variety of nanomaterials. Besides, the recovery of the 3D atomic structure based on multiple phase images has not yet been experimentally reported. Therefore, the development of experimental techniques based on multiple projection images that enable the 3D characterisation of beam sensitive nanomaterials is essential.

Inspired by the work of Jinschek and co-workers[367], we propose an experimental methodology for electron tomography based on the phase of the exit wave reconstruction. The methodology consists on the acquisition of a focal series along different tilts of the nanocrystal, followed by the recovery of the amplitude and phase of the complex emitted wave by the specimen through EWR technique. By combining the phase image from different projections, the 3D atomic structure can be retrieved by the use of tomographic algorithms. Moreover, a very limited number of projection images (-45^o, 0^o and +45^o) was chosen as input for a tomographic reconstruction during the development of this experimental methodology. Some nanomaterials are indeed extremely beam sensitive and does not allow a prolonged illumination time, reducing the number of focal series that can be acquired without damaging the material. Similar to studies from Goris et al[112] for STEM mode, only projections images along main zone axis were taken.

Due to very small number of projections, the 3D reconstructed volume is expected to contain artefacts from the missing wedge. To minimize this effect, the prior knowledge of the shape can be incorporate during the tomographic reconstruction. Such information can be obtained through a full tomography series acquisition of the nanomaterial under investigation. The acquisition of a tomographic series for the morphology recovery can be often challenging due to the sensitiveness of the nanomaterial towards the electron beam. To overcome this challenge, alternative approaches can be used, such as the acquisition of a tomographic series in TEM mode at lower magnifications; the acquisition of series using the fast tomography approach (either in TEM or STEM mode); and eventually, the acquisition of TEM series of images at extremely low doses at cryogenic temperatures, to prevent morphological modifications of the structure[309]. For cases where the prior information of the morphology is not available, missing wedge artefacts will be present on the final reconstructed volume with atomic resolution. The degree of artefacts will depend on the number of projections in which a focal series was acquired as well as the tilt interval between the projections, as discussed in Chapter 2 (section 2.4.1).

Once the morphology of the object under investigation is obtained, a mask for the atomic resolution tomography can be created. For this purpose, a segmentation step is applied. To avoid the formation of artefact during the reconstruction, the mask is dilated and the edges are smoothed through a 3D Gaussian filter. The prior information of the shape is incorporated to the tomographic reconstruction in an iterative manner. More specifically, the 3D atomic structure is obtained after 50 iterations of SIRT method and convoluted with the shape mask. The resultant 3D volume is then used as a starting point for another SIRT reconstruction with 50 iterations. This process is repeated 6 times, to ensure the convergence of the reconstruction. Finally, a new SIRT reconstruction with 50 iterations is applied using the previously obtained 3D volume as a starting point, without the use of any prior information. The aim of the last step is to reduce the amount of artefacts that might have been introduced during the convolution of the 3D atomic structure with the mask.

To verify if the use of prior information would introduce extra artefacts in the final tomographic reconstruction, the atomic structure of a simulated gold nanosphere was obtained from a conventional tomographic series (from -72^{o} to +72^{o}, at every 2^{o}) and a limited series (-45^{o}, 0^{o} and +45^{o},) were further reconstructed, as shown in Figure 7.5. For this purpose, gold atoms were assumed as Gaussian spheres and the high resolution images were obtained by projecting the structure along the indicated angles using the Astra Toolbox 1.8[175]. In this manner, the projection requirement is fulfilled. As it can be seen from Figure 7.5.c, the use of a very limited number of projection images in the tilt series resulted in the elongation of the retrieved volume. To minimize this effect, the prior information about the shape (Figure 7.5.d) can be incorporated during the tomographic

reconstruction. By inspecting the volume obtained from the limited tilt series combined with the prior knowledge of the shape (Figure 7.5.e-f), a good agreement was found with the volume obtained from the full tilt series.

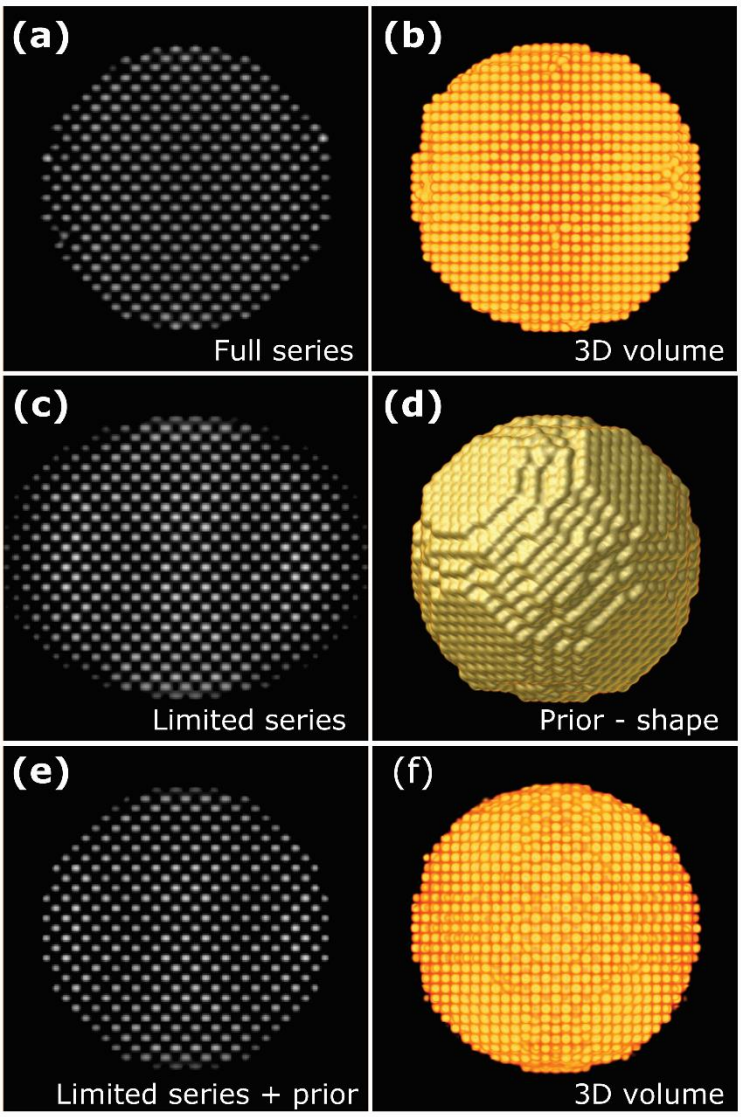

Figure 7.5 – The effect of the use of prior information about the shape in the reconstructed volume. (a) Slice along the yz plane and (b) volume rendering of the reconstructed object from a full tilt series (from -72^{o} to +72^{o}, at every 2^{o}). (c) Slice along the yz plane of the reconstructed object from a limited tilt series (from -45^{o},0^{o} and +45^{o}). In (d) the prior information of the shape is shown. (e) Slice along the yz plane and (f) volume rendering of the reconstructed object from a limited tilt series, using the prior information of the shape. A comparison between (a) and (e) reveals a good resemblance between the two reconstructed volumes.

In summary, the methodology for the recovery of the 3D atomic structure of nanomaterials (3D EWR) consists of:

(a) Determination of the microscope parameters;

(b) Acquisition of a focal series of the specimen along different orientations;

(c) Acquisition of a full tomography series (either in STEM or TEM mode) for the prior information of the shape, if necessary;

(d) Recovery of the amplitude and phase of the complex wave emitted by the specimen through EWR technique;

(e) Alignment of the phase images and the full tomography series;

(f) Reconstruction of the shape of the object based on the full tomography series;

(g) Generation of the shape mask by segmentation, dilatation and edge smoothing;

(h) Reconstruction of the phase images, incorporating the shape mask iteratively during the reconstruction when necessary.

First, the technique is theoretically evaluated based on the simulation of HRTEM images and the complex exit wave for gold nanorods (Figure 7.6), with [100] zone axis parallel to the z-axis. The choice of gold relies on the widespread knowledge of its crystallographic structure, enabling the verification of the performance of the method. A nanorod was chosen due to its shape anisotropy, giving some level of complexity to evaluate the technique in development. The thickness of the nanorod was of 10.2 nm (25 atoms thick along the [100] zone axis). To represent with fidelity the experimental conditions, a carbon support layer with 3 nm thickness was added at the bottom of the nanorod. During the simulation, a configuration with 100 phonons was used.

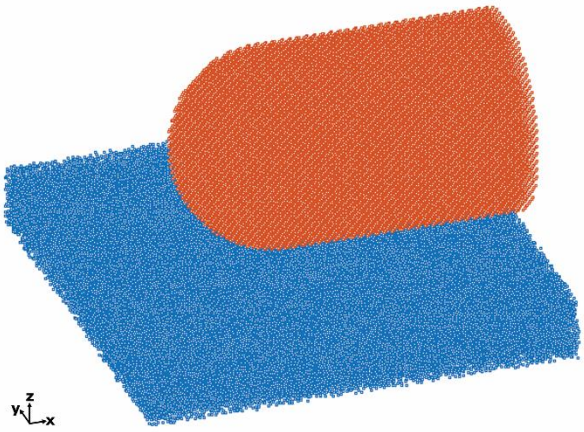

Figure 7.6 – Model of the simulated gold nanorod in red. The carbon support film was also modelled and is shown in blue colour. The crystallographic orientation of the nanorod along the z-direction

corresponds to the [100] zone axis. The structure was obtained with MULTEM[365,366] software for MATLAB.

Here, a focal series of HRTEM images was simulated in MULTEM[365,366] for the system shown in Figure 7.6. To obtain a focal series along [-110] and [110] zone axes, the system was rotate by an angle of -45^{o} and +45^{o} along the long axis of the nanorod, respectively. The microscope parameters were chosen to resemble the experimental setup of the ThermoFisher aberration corrected 'cubed' Titan 60-300 operated at 300kV and are summarized in Table 7-1.

Parameter	Value
Acceleration voltage	300 kV
Spherical aberration	-0.007 μm
Defocus spread	3.2 nm
Information limit	0.084 nm
Starting defocus	+30 nm
Defocus step	-2 nm
Number of images per focal series	30

Table 7-1 – Summary of parameters used during the simulation of the focal series of HRTEM images and the complex exit wave.

A HRTEM image for each case is shown in Figure 7.7, at defocus of 8nm. The exit wave reconstruction of the simulated HRTEM images was carried out using the XWave[359] software. To evaluate the influence of residual errors from the exit wave reconstruction on the tomographic reconstruction, the complex exit wave was also simulated for the same conditions and crystallographic orientations of the different focal series.

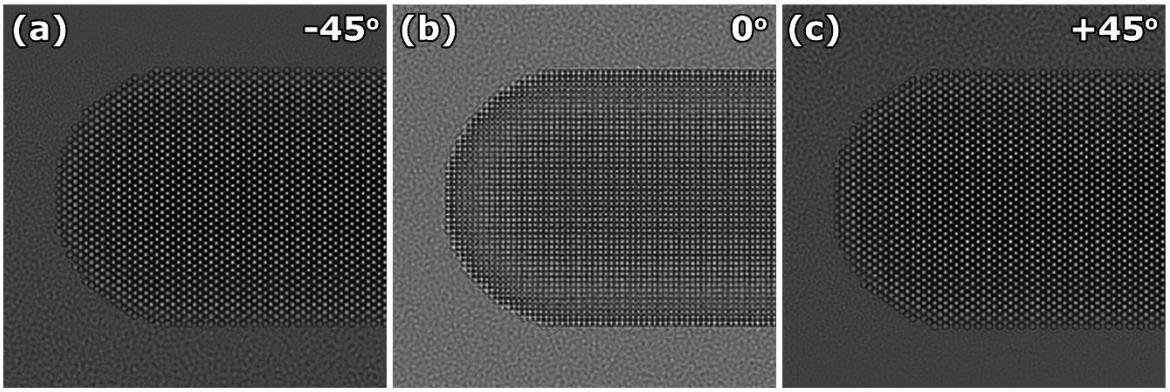

Figure 7.7 – Simulated HRTEM image of the created model (nanorod + carbon support film) for different tilts: (a) -45°, (a) 0° and (a) +45°, with zone axis orientation of [-110], [100] and [110] respectively. The defocus for all images was equal to 8 nm. The pixel size was equal to 0.01044 nm.

Analysis of the simulated complex exit wave (Figure 7.8) revealed the obtained phases were wrapped in the interval $[-\pi, \pi]$. The wrapping effect is a result on how the phases are calculated from a complex function ($z = a + ib$): $\arg z = \tan^{-1}(b/a)$. For this reason, when the phase reaches the limit value of π, a sign inversion takes place, giving rise to the observed contrast reversal in the second column in Figure 7.8. To unwrap the phase, different methods are available[375]. Here, the 2D Goldstein branch cut phase unwrapping method[376,377] was applied to the phase of the simulated exit wave along different zone axis. The resultant phase can be seen in the third column of Figure 7.8, where no contrast reversal is observed at certain atomic columns.

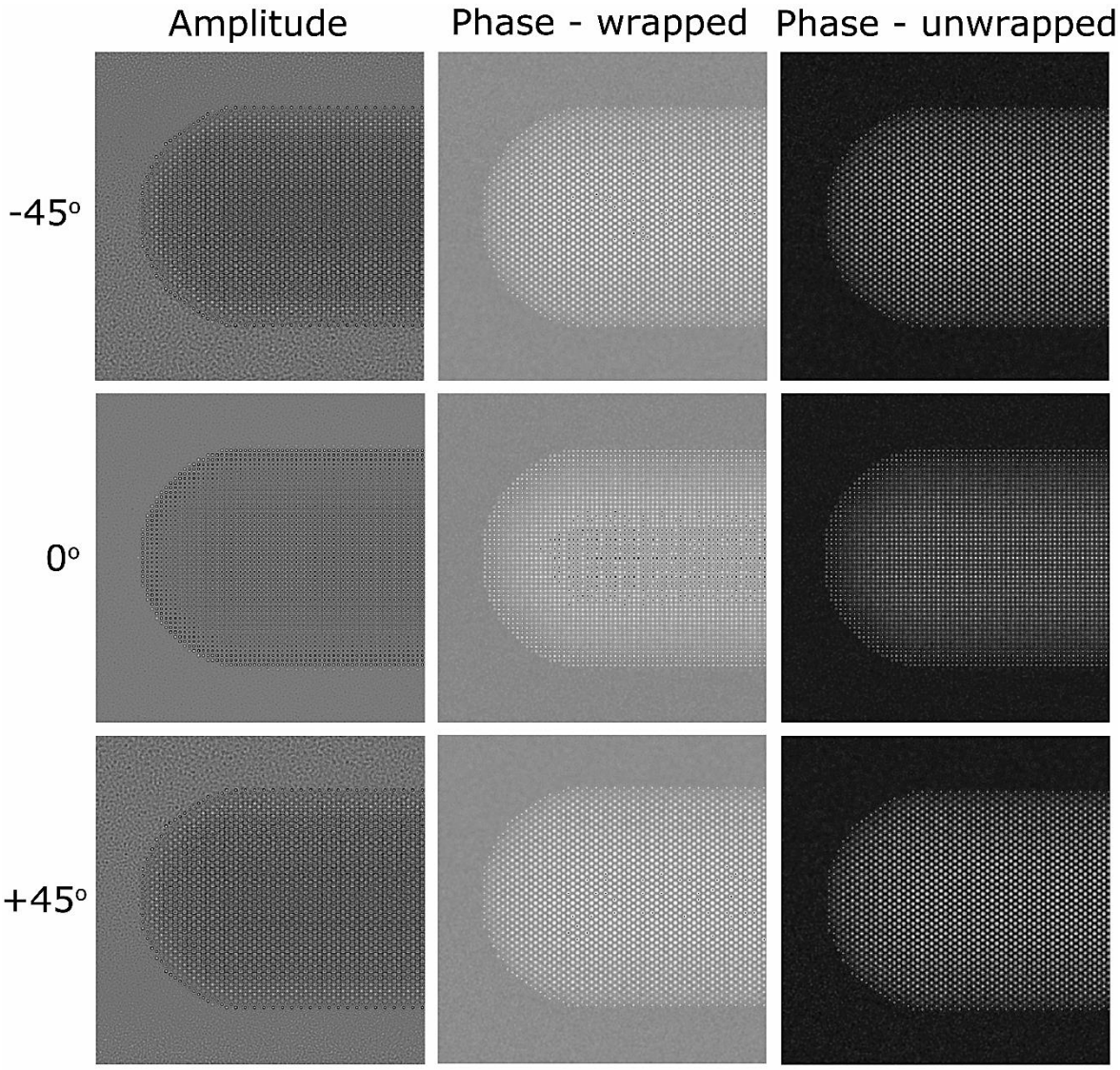

Figure 7.8 – Simulated amplitude and phase of the complex wave function of the nanorod supported by a carbon layer along different orientations. A wrapping effect of the phase was observed in the second column. By applying the 2D Goldstein branch cut phase unwrapping method, the full unwrapped phase could be recovered (third column).

However, analysis of the reconstructed complex waves using XWave sofware[359] revealed the absence of the wrapping effect of the phase, as illustrated in Figure 7.9. For the XWave sofware[359], the phase values recovered during the reconstruction will be lower than the actual phase values obtained through simulations, justifying the absence of the wrapping effect of the phase. Therefore, the phase unwrapping step is not required for complex waves reconstructed using the XWave sofware[359].

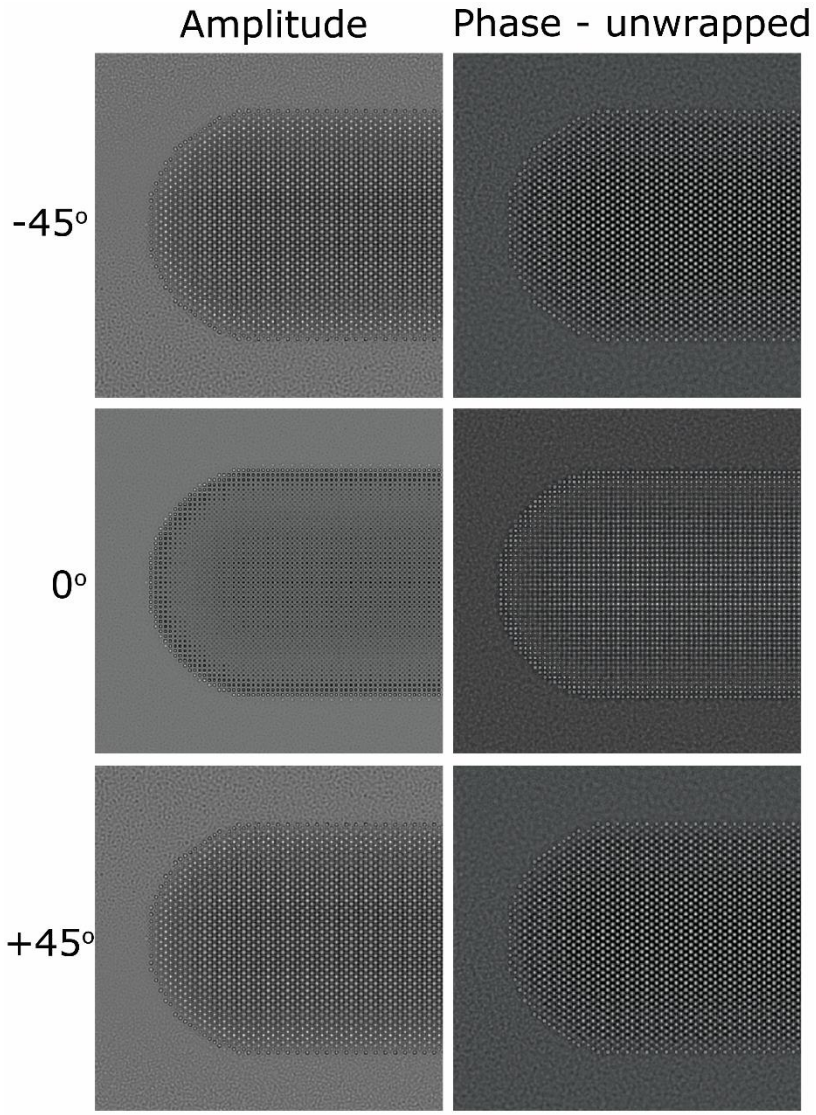

Figure 7.9 – Reconstructed amplitude and phase obtained from the simulation of the focal series of HRTEM images.

Since the channelling effect depends on the crystallographic orientation, a variation on the amplitude and phase of the exit wave for different crystallographic zone axis orientation is expected. This effect stems for the variation of the extinction distance ζ (period of the channelled electron beam by the crystalline object) with varying atomic distances[173,342,360–364]. Thus, the maximum phase value will differ for each crystallographic orientation. Consequently, a series of phase images of an object oriented along different crystallographic zone axes will not meet the projection requirement for tomography, since the scaling of the phase values will not be the same for all images in the tomographic series. To circumvent such limitation, the exit wave of a gold nano-layer was simulated for a crystal oriented along [110] and [100] zone axes, for different thickness ranging from 0.4078 nm to 10 nm, with steps of 0.4078 nm (Figure 7.10.a). To determine the factor that would equalize the

maximum phase value for both crystallographic zone axes, known as the channelling factor, points for different crystal thickness would be plot for the phase values of [100] zone axis *versus* [110] zone axis(Figure 7.10.b). The channelling factor would be derived from the linear regression of the relationship between phase [100] *versus* phase [110] and equals to $A = 1.1729$.

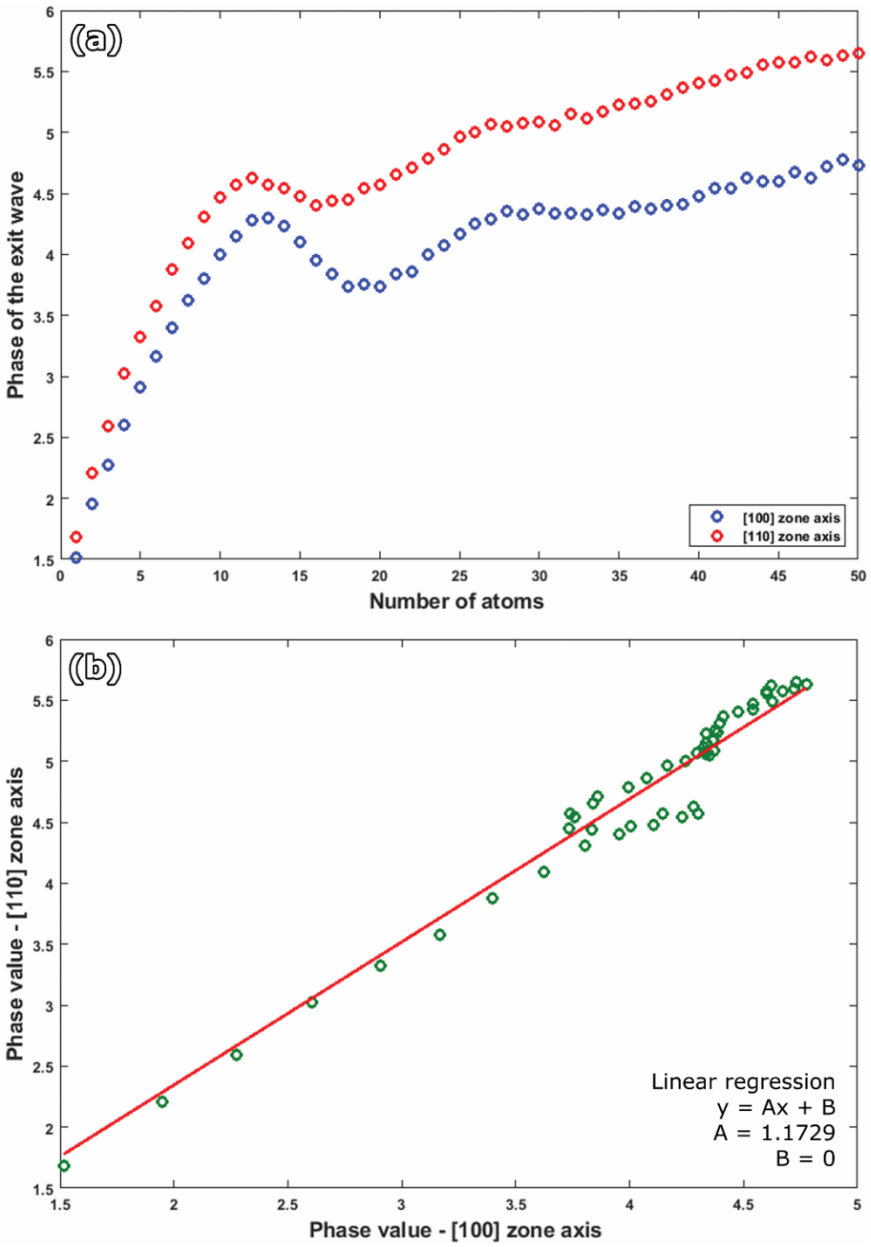

Figure 7.10 – (a) Plot of the phase values for varying thickness (0.4078 to 10 nm) of a gold nanocrystal oriented along the [100] zone axis (blue) and [110] zone axis (red). (b) Plot of the phase value of the [100] zone axis *versus* [110] zone axis in green circles. The red line corresponds to the linear regression of the plotted points, with values given at the bottom right of the graph.

Finally, the obtained unwrapped phases in Figure 7.8 and Figure 7.9 can be used as an input for a tomographic algorithm. For this purpose, it is important that the channelling factor has been

applied correctly to the phase images along different crystallographic zone axes orientation and that all images are well aligned in respect to each other. Since the results presented so far were originated from simulations, no shift between consecutive images was present. Next, the prior knowledge of the shape of the nanorod was incorporated during the tomographic reconstruction to minimize the presence of missing wedge artefacts.

The obtained 3D atomic structure of the gold nanorod model is shown in Figure 7.11.a-c for the simulated complex wave function and in Figure 7.11.d-f for the reconstructed complex wave function from simulated HRTEM images. Due to the very limited number of projections, the prior information of the morphology was incorporated to the final tomographic reconstruction, where the morphology of the object was directly retrieved from the simulated shape of the nanorod. A comparison between the reconstructed 3D volume from the simulated complex wave function and the reconstructed wave function from simulated HRTEM images reveals a variation on the contrast of the atoms on the grid for the latter case. The same pattern was also observed in the simulated HRTEM images at tilt angle of 0^{o}, as it can be seen from Figure 7.11.b. Nevertheless, both retrieved structures are in good agreement with the simulated model for the gold nanorod. The carbon support layer is not visible in the reconstructed slices and volume rendering, due to the smaller image contrast in comparison to the atomic features.

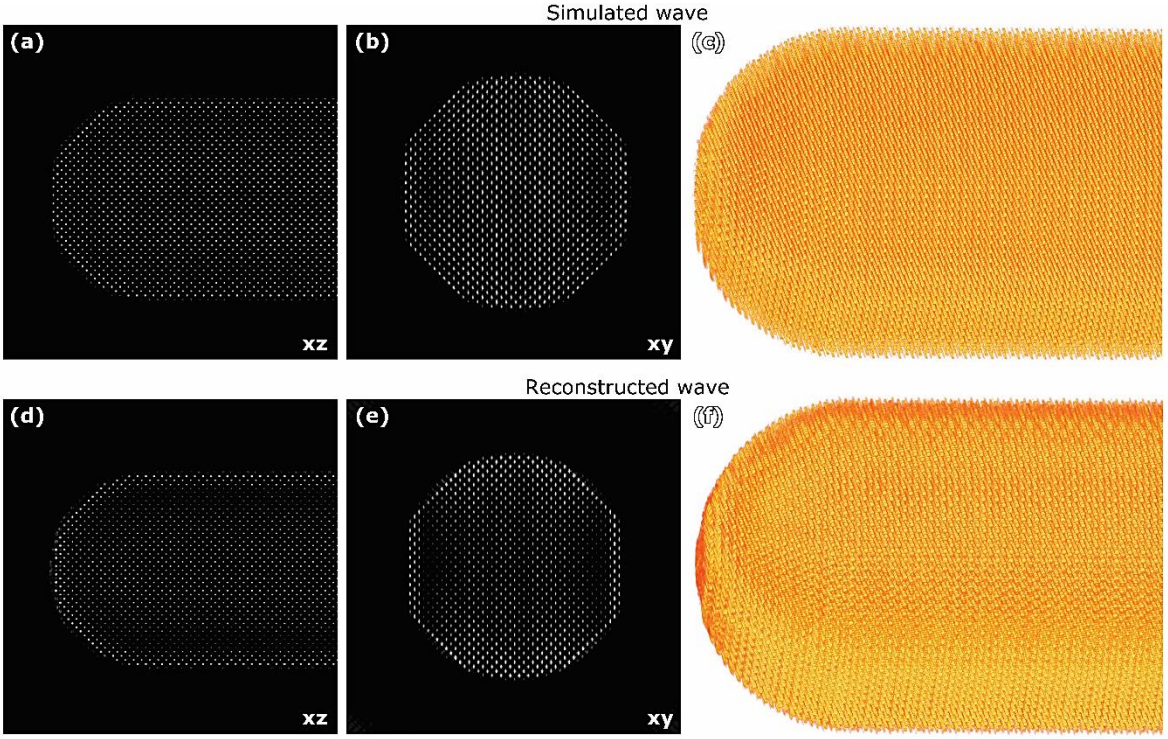

Figure 7.11 – (a)-(b) Slices through the 3D reconstructed atomic structure of the gold nanorod obtained from the simulation of the complex wave function along different orientations using the

prior information of the morphology and (c) its 3D volume rendering. (d)-(e) Slices through the 3D reconstructed atomic structure of the gold nanorod obtained from the reconstruction of the simulated HRTEM images along different orientations and (f) its 3D volume rendering.

7.5 The 3D atomic structure of gold nanorods recovery based on experimental results

To verify the experimentally reproducibility of the methodology for the 3D characterisation of the atomic structure of beam sensitive nanomaterials, gold nanorods were investigated. The choice of gold relies on the widespread knowledge of its crystallographic structure, enabling the verification of the performance of the method. A nanorod was chosen due to its shape anisotropy, giving some level of complexity to evaluate the technique in development. The experimental parameters used for the acquisition of the focal series of HRTEM images were the same as the ones displayed in Table 7-1.

Three focal series were acquired at angles of +54^{o}, +9^{o} and -36^{o}, for crystallographic orientations along the [010], [110] and [100] respectively, using an automatic script for the acquisition of focal series from ThermoFisher. Additionally, a full tomography series was acquired in STEM mode, to provide the prior information of the shape. The exit wave reconstruction was performed in XWave[359] software, with the amplitude and phase images for all projections shown Figure 7.12. A further analysis of the phase images revealed a slight disturbance of the linearity of the phase values for atoms closer to the surface. This effect is attributed to the excess of free ligands in suspension and does not prevent the tomographic reconstruction of the phase images. The alignment of the phase images prior to the tomographic reconstruction was performed manually using Midas[378] module for IMOD[379], since methods based on the cross/phase correlation were not successful. Prior to the reconstruction, the channelling factor $A = 1.1729$ was applied, as discussed in the previous section.

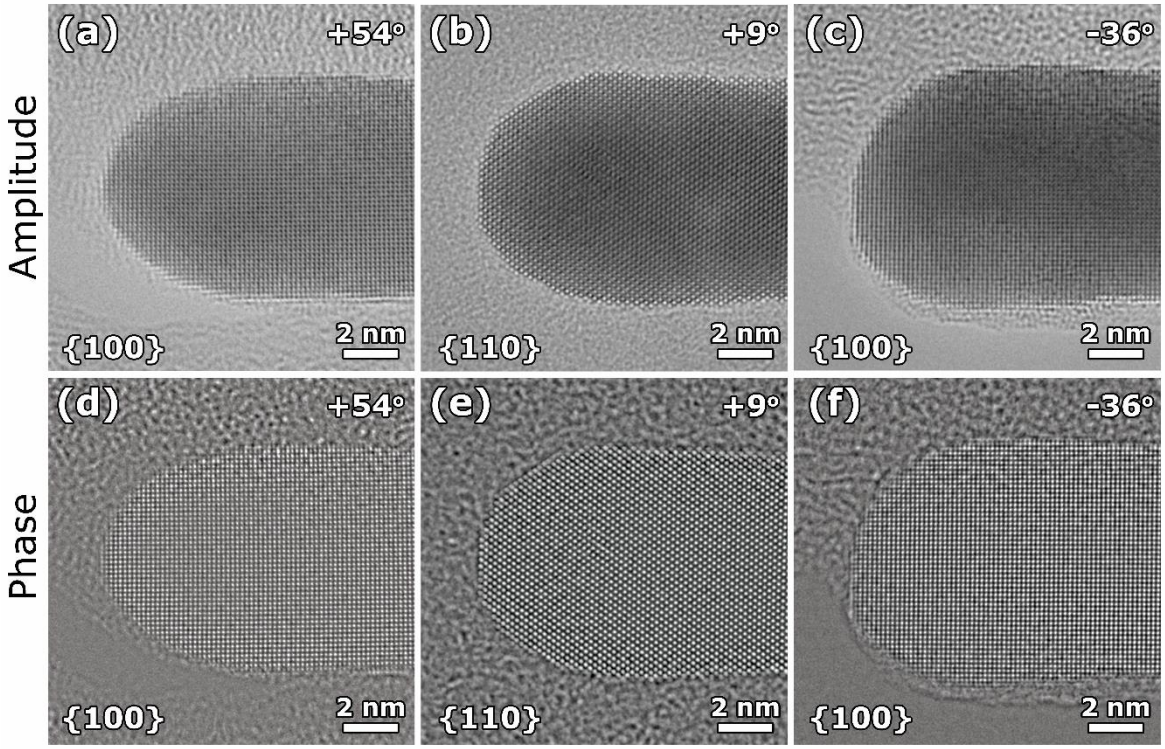

Figure 7.12 – (a)-(c) Recovered amplitude and (d)-(f) phase images obtained with XWave[359] software of a gold nanorod supported by a carbon layer of 3 nm of thickness. The linearity of the phase values are slightly disturbed by the presence of the excess of free ligands.

The tomographic reconstruction was carried out as described in section 7.3, using the prior information of the shape obtained from a conventional HAADF-STEM tomographic series. However, as it can be observed in Figure 7.12, a strong contrast variation of the background was observed on the gold nanorods. Further analysis revealed this contrast was originated from the excess of free ligands present in the solution containing the nanoparticles in suspension. The presence of such strong contrast variation in a tomographic series containing a very limited number of projections gave rise to artefacts in the 3D reconstructed atomic structure, since the presence of amorphous material surrounding the object under investigation is responsible for disturbing the channelling of the electron beam through the gold crystal lattice[380]. Therefore, the excess of amorphous material will be responsible to induce extra variation of the phase values in the reconstructed phase images. To minimize the variation of intensities observed in the 3D reconstructed volume due to the presence of the excess of free ligands, a post-filtering was applied to the 3D object retrieved from electron tomography, after the reconstruction was finalized. This filter consists in the identification and selection of all reflections present in the 3D Fourier transform of the reconstructed object. Gaussian spheres with smoothed edges are generated for each position correspondent to a reflection and multiplied with the 3D Fourier transform (Figure 7.13). The new 3D atomic structure of the

investigated nanomaterial is obtained by applying an inverse Fourier transformation to the filtered 3D Fourier transform and is displayed Figure 7.14. A different gold nanorod was investigated using the 3D EWR methodology and similar results were obtained.

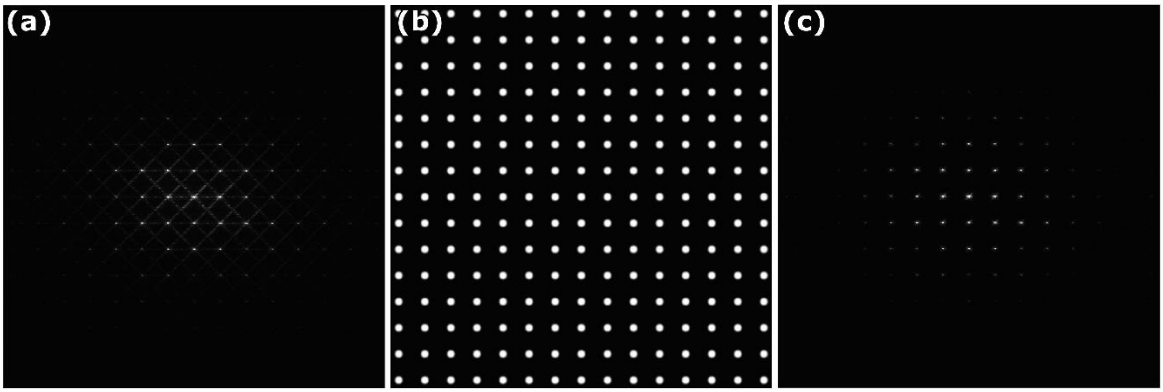

Figure 7.13 – (a) Single slice of the Fourier transform of the 3D reconstructed structure. (b) Mask created on base of the position of the reflections, after Gaussian smoothing. (c) Resultant Fourier transform obtained after applying the generated mask in (b).

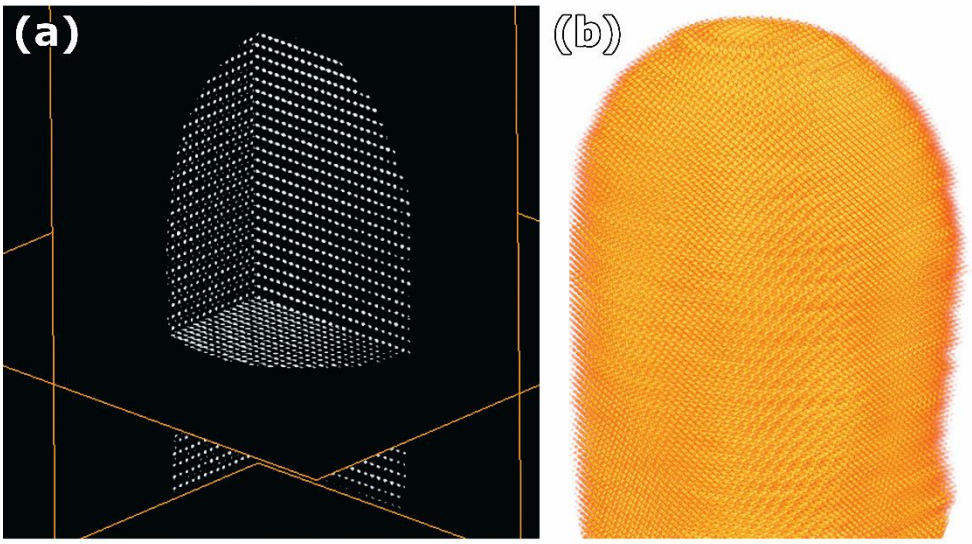

Figure 7.14 – (a) Slices through the 3D reconstructed volume using the 3D EWR methodology along different orientations and (b) respective volume rendering in 3D. Here, the prior information of the morphology obtained from a conventional HAADF-STEM tomographic series was incorporated to the final tomographic reconstruction with atomic resolution.

The results for the 3D atomic structure of gold nanorods are in good agreement with the results obtained through simulations. One interesting aspect was the absence of the phase values variations in the experimental data as it was observed for simulated HRTEM images, as shown in Figure

7.7.b and Figure 7.11.d-e. This effect could be associated with the used models for the dynamical scattering and the quantity of phonon configurations used during the simulation of HRTEM images. In principle, a large number of phonons that resemble the experimental conditions could be used. However, by increasing the number of phonons in the calculations, the computational time/complexity considerably increases. Therefore, a balance between the number of phonons and the computational requirements was established for the present calculations.

The comparison between our experimental results with simulations and the good agreement found validate the 3D EWR methodology. This technique has great potential for the 3D characterisation of beam sensitive nanomaterials through the combination of very low dose imaging conditions with the use of direct electron detectors. Besides, this methodology can also be employed in non-aberration corrected TEMs, enabling a vast range of laboratories around the world to retrieve the 3D atomic structure of a diversity of nanomaterials.

7.6 Towards the recovery of the 3D atomic structure of beam sensitive nanostructures

Finally, the methodology of 3D EWR was evaluated for the 3D characterisation at the atomic level of beam sensitive nanomaterials. Therefore, a ThermoFisher aberration corrected 'cubed' Titan 60-300 microscope operated at 300 kV and equipped with a direct electron detector from Gatan, the K2 summit Direct Detection Camera, was used. In this detector, each pixel has an individual photo-detector and an active amplifier. In this manner, the signal of each pixel can be recorded and processed individually. Moreover, this detector has a special image mode named counting mode, where the analogue signal from each incident electron is replaced by a discrete count. The advantage of this mode is the noise reduction and the increase of the DQE. To ensure the maximum efficiency and the smallest illumination time of beam sensitive nanomaterials, it is essential to develop a new routine for an automatic acquisition of focal series of HRTEM images using the count mode. Therefore, I developed a script for Digital Micrograph software from Gatan for such automatic acquisition, in collaboration with Dr. Armand Béché.

As a test case, an exit wave reconstruction was performed for a metal halide perovskite using the new script for the automatic acquisition. Here each pixel registered $8\ electrons/pixel/s$ and 40 frames were acquired in time interval of 1 s for each defocus. The signal-to-noise ratio of each individual frame is very low and it does not enable direct qualitative interpretation. Due to the specimen drift, a blurring effect was observed after summing all frames (Figure 7.15.a). For a proper alignment of the stack of HRTEM images, cross-correlation with sub-pixel precision was applied

between consecutive images. As a result, the atomic features could be retrieved for the sum of all frames for a given defocus (Figure 7.15.b). The resultant reconstructed amplitude and phase of the complex wave emitted by the specimen are shown in Figure 7.15.c-d. Although the electron dose of each individual frame was low ($128\ electrons/\text{Å}^2$), the signal-to-noise ratio of the final reconstruction is comparable with the results obtained with conventional CCD's.

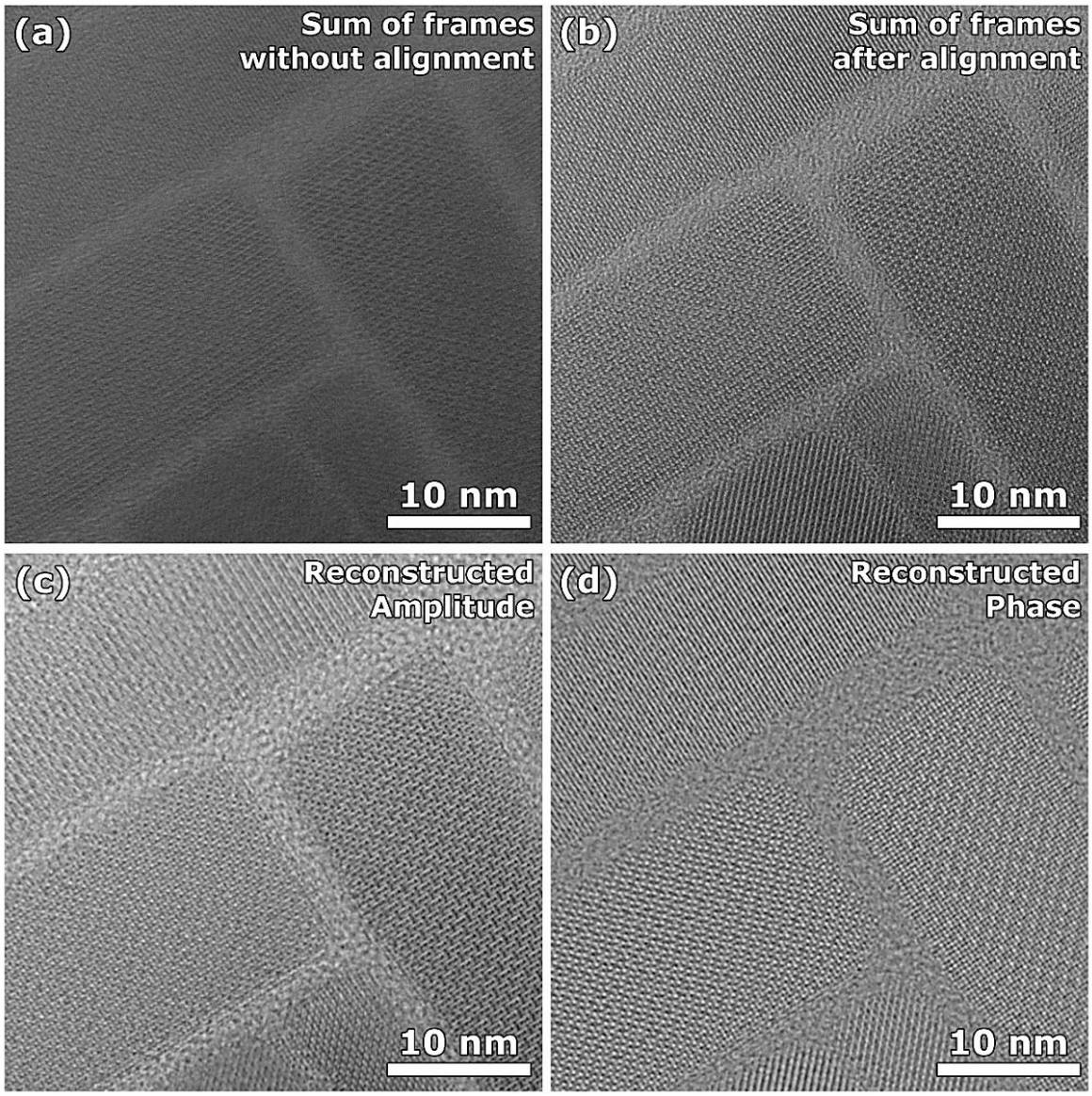

Figure 7.15 – (a) Sum of 40 frames of HRTEM images obtained with the K2 summit Direct Detection Camera of a $CsPbBr_3$ perovskite at defocus of 30 nm. None of the nanocrystals were oriented along a main crystallographic zone axis. The blurring effect of the atomic features is attributed to the drift of the specimen during the acquisition. (b) Sum of the same frames shown in (a) after alignment with sub-pixel precision using cross-correlation. Reconstructed (c) amplitude and (d) phase using XWave software[359].

To further minimize the effect of the variation of contrast in the phase images, TEM grids with a graphene as a support layer were used. The TEM grids with a graphene support layer were prepared in-house by EMAT researchers, following the protocols of Pedrazo-Tardajos et al.[381]. To properly remove the polymeric residues resultant from the film transfer, a protocol with activated carbon was applied[382]: the grid was submerged in a glass container containing the activated carbon at room temperature and heated to 300^{o}C for 15h, with heating step of 5^{o}C/min.

The new methodology was finally applied to small nanocubes of $CsPbBr_3$, which is extremely beam sensitive (Figure 7.1). The microscope parameters are the same as presented in Table 7-1, with exception of the spherical aberration, which corresponded to -0.005 mm. To prevent any structural modification, an electron dose of $4.974\ electrons/Å^2$ was used ($0.5\ electrons/pixel/s$) for the acquisition of the focal series. Here, we acquired a stack of 20 frames per defocus. Due to the extremely low doses, the signal-to-noise ratio was very low for a single frame (Figure 7.16.a). A slight increase on the signal-to-noise ratio was observed after alignment by cross-correlation and summarization of all frames in the same stack (Figure 7.16.b). Because the electron dose of the incident beam was extremely low, the process of orientating of the crystal along main zone axes was not possible. Therefore, a focal series was acquired from a tilt angle of -70^{o} to +70^{o}, with steps of 10^{o}. Examples of reconstructed amplitude and phase images are shown in Figure 7.16.c-f. In principle, any prior information about the shape is required, as a series of phase images along a wide range of angles were obtained. However, in some cases the contrast of the shape in the phase image at given projections were very subtle (Figure 7.16.d), resulting in the presence artefacts from the missing wedge in the reconstructed 3D atomic structure. To minimize the presence of such artefacts, the prior information about the shape of the object was retrieved from the tomographic reconstruction of the amplitude images and incorporated in the reconstruction similarly as described in section 7.3. To remove the presence of atomic features from the amplitude images, a Gaussian filter was applied to blur such features. The volume rendering of the obtained 3D volume (Figure 7.16.g) reveals the presence of atomic resolution features. Still, many artefacts are present in the 3D reconstructed volume, mainly due to the low signal-to-noise ratio. Moreover, an excess of free ligands in the solution containing the nanoparticles in suspension was observed. The effect of the free ligands can be directly seen from Figure 7.16.c-f, where the features corresponding to the graphene support layer are not visible due to the free ligands. Moreover, the future development of automatic methods for the alignment of the tomographic series of phase images could drastically improve the quality of the reconstruction[113].

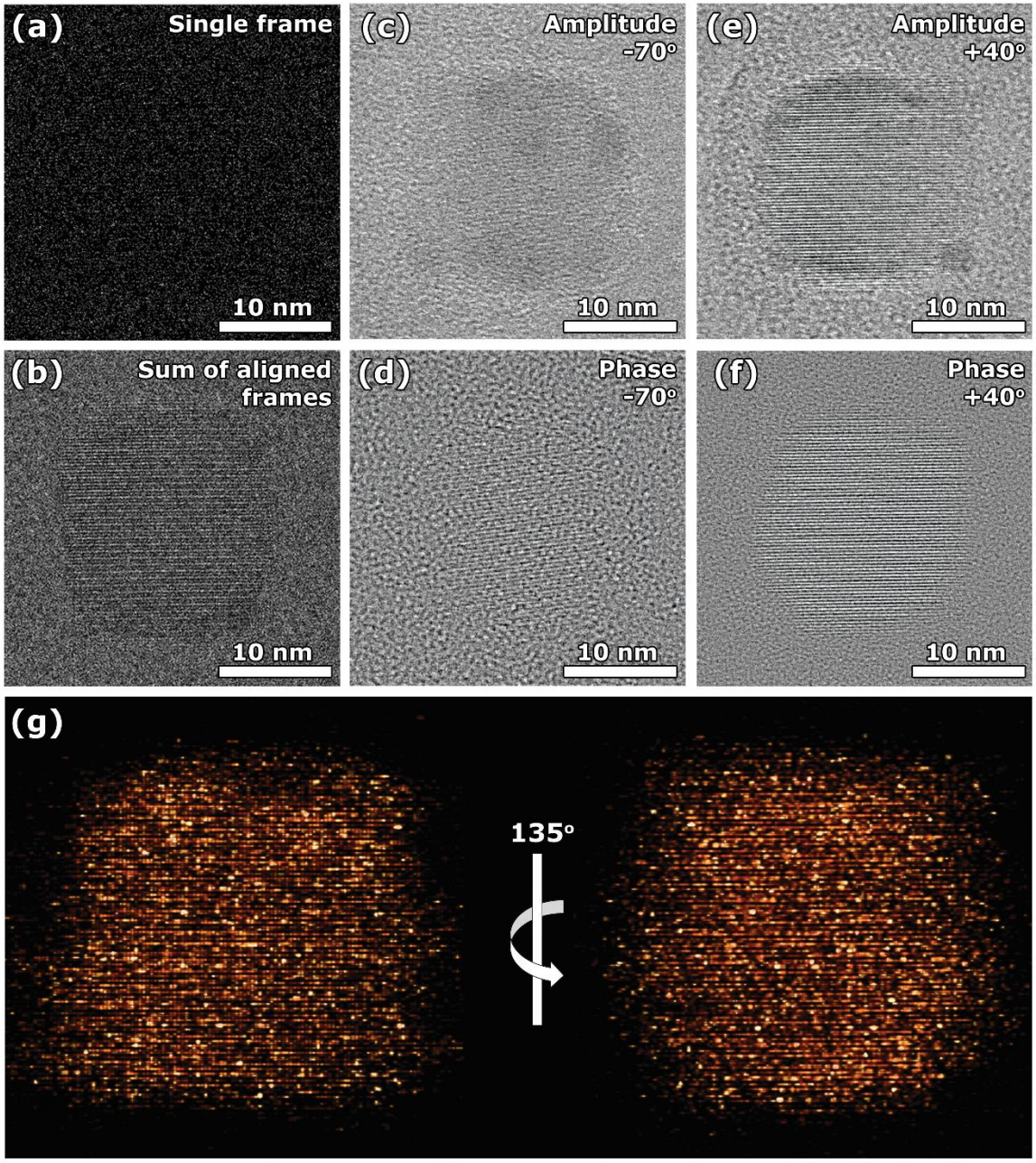

Figure 7.16 – (a) Single frame of a stack of HRTEM images obtained with the K2 summit Direct Detection Camera of $CsPbBr_3$ nanocube, at tilt angle of 0°. (b) Sum of the same frames shown in (a) after alignment with sub-pixel precision using cross-correlation. Reconstructed (c), (e) amplitude and (d), (f) phase using XWave software[359] at different tilt angles. (g) Volume rendering of the retrieved 3D volume, where atomic features can be observed along different orientations. The 3D volume was obtained through the use of prior information of the morphology, using the amplitude images retrieved from the EWR for each projection as input for a tomographic reconstruction.

Although the methodology was experimentally validated for gold nanorods, improvement are still required for the metal halide perovskites investigated in this section. The lower quality observed

in the present reconstruction is mainly attributed to the lower signal-to-noise ratio. To improve this ratio, a modified image restoration based on the convolution neural networks (Appendix A) can be developed for phase images. In this way, the training of the neural network would enable the identification of the presence and the levels of noise in the image as well as their further compensation. Alternatively, the increase of the signal-to-noise ratio can be improved by reducing the camera's photosensor noise[383]. To this aim, Evtikhiev and co-workers[383] proposed a modification of flat-field correction technique to increase the signal-to-noise ratio by spatial noise suppression using the knowledge of the light spatial noise portrait (LSNP) of the detector. As a result, Evtikhiev and co-workers were able to improve the signal-to-noise ratio by a factor of 5.

7.7 Conclusions

In this chapter, we showed the need of novel techniques for the 3D characterisation of nanomaterials that are sensitive to the electron beam. HRTEM imaging is promising technique for the study of beam sensitive nanomaterials, due to the development of direct electron detection cameras. An experimental methodology for the recovery of the 3D atomic structure of nanocrystals was proposed, experimentally tested in model like structures (gold nanorods) and applied to realistic nanomaterials. Still, the quality of the obtained 3D reconstructed volume of realistic cases can be enhanced by improving the sample preparation techniques as well as by using post-processing technique to increase the observed low signal-to-noise ratio. Moreover, further development of an automatic method for the alignment of the phase images is still required. Nevertheless, this methodology can also be employed for the recovery of the 3D atomic structure of a vast range of nanomaterials using non-aberration corrected electron microscopes.

7.8 Experimental methods

In this section, a summary of the different approaches for the characterization of nanomaterials based on advanced techniques for electron microscopy is provided. Low dose TEM imaging combined with advanced single electron detection cameras allowed the visualization of metal halide perovskites with reduced structural modifications by the electron beam. The projected atomic structure of metal halide perovskites were obtained from the phase images retrieved with EWR method. In order to obtain the atomic structure of such materials in 3D, an advanced approach for atomic resolution electron tomography based on the phase images obtained from the EWR were experimentally implemented. Gold nanorods were initially used as proof of concept for the verification and experimental implementation of the approach, based on the simulated and experimental results

respectively. The approach was also employed for beam sensitive metal halide perovskites in combination with single electron detection cameras, where improvements are still required.

7.9 Author contribution

Thaís Milagres de Oliveira acquired all the experimental data of gold nanorods and performed all the exit wave reconstructions shown in this chapter. The focal series of perovskites were acquired in collaboration with Dr. Nathalie Claes, Dr. Eva Bladt and Dr. Julien Ramade. The script for the automatic acquisition of focal series using the K2 summit Direct Detection Camera was developed in collaboration with Dr. Armand Béché. The perovskite samples were synthesized in the laboratory of Prof. Dr. Johan Hofkens from Catholic University of Leuven and the gold nanorods in the laboratory of Prof. Dr. Luis M. Liz-Marzán.

The author of the present thesis contributed to this study by verifying the approach for electron tomography based on exit wave reconstruction through simulated results, by implementing the approach experimentally, by developing techniques for the focal series acquisition using single electron detection cameras and by investigating beam sensitive nanomaterials (perovskites) at the atomic level, in 2D and 3D, where the 3D EWR approach is applied.

Chapter 8. General conclusions and outlook

The 3D characterisation of complex materials is not always straightforward. In this thesis, the limitations for a thorough investigation of realistic nanostructures that go beyond model-like structures were addressed. To visualize the 3D distribution of the structural defects in gold nanoparticles, multimode tomography was employed (Chapters 3 and 5). However, this technique only provides information at the nanoscale. Since the functional properties of nanomaterials are connected with the position of the atoms, the bonding between them and their chemical nature, it is essential to also retrieve the 3D atomic structure of such defects. To achieve this goal, a recently developed technique for atomic resolution tomography was applied. With this approach, the use of prior information about the material under investigation is not required, which makes this technique ideal for the characterisation of nanomaterials containing structural defects. Therefore, we were able to investigate the presence of cavities in hollow nanoparticles and the 3D distribution of different types of defects, such as dislocations, grain and twin boundaries, in different systems of gold nanoparticles, as shown in Chapters 4 and 5.

Although multimode and atomic resolution tomography methodologies provide very unique information, the complexity of such methods prevents their use for the characterisation of a relevant statistical distribution of structural defects in nanoparticles. The knowledge of the defect yield present in nanoparticles is essential for applications and even the optimization process of synthesis of nanomaterials, as shown in Chapters 3 and 4. To this aim, a tilt series of ADF-STEM images were acquired for hundreds of nanoparticles, enabling the identification of multi-crystalline nanoparticles and a statistical classification of defects present in different systems.

More interesting, the dynamical behaviour of defects, such as cavities in hollow nanoparticles, were investigated under *in-situ* heating conditions in 3D, as shown in Chapter 4. As a result, it was observed that the cavities migrated towards the closest external surface of the nanoparticle, albeit for some cases. Furthermore, spectroscopic techniques (EELS-STEM) enabled the determination of the contents of the observed cavities. Therefore, our studies revealed that upon heating of hollow nanoparticles, the contents of the cavities are released in the surrounding environment, as confirmed by molecular dynamics simulations. Such knowledge is of extreme importance in the design of new applications for hollow nanoparticles, such as gas/liquid storage.

Because conventional electron tomography only provides information at the nanoscale, the evolution of the atomic lattice of hollow nanoparticles for increasing temperature conditions is still unclear. Thus, it becomes essential to combine the current *in-situ* heating investigation with advanced

techniques for electron tomography at the atomic level. Such knowledge would enable the characterisation of the facets in the inner surface of hollow nanoparticles at increasing temperature conditions. To this aim, the approach described at Appendix A was applied to hollow nanoparticles and the obtained 3D structures at different temperatures can be seen in Figure 8.1. Here, instead of a migration of the cavity towards the closest external surface of the nanoparticle, the nanoparticle was clearly affected by electron beam damage. To prevent these effects in the future, new approaches for atomic resolution tomography based on the simultaneous acquisition of a stack of frames while tilting the holder are required; similar to what is currently done at the nanoscale level. To enable such acquisition scheme, improvements in the hardware of the microscope are required to maintain the specimen always in the field of view while tilting the holder, since at higher magnifications, variations of only a few nanometres in the position of the object under investigation is sufficient to prevent high-resolution imaging of the same.

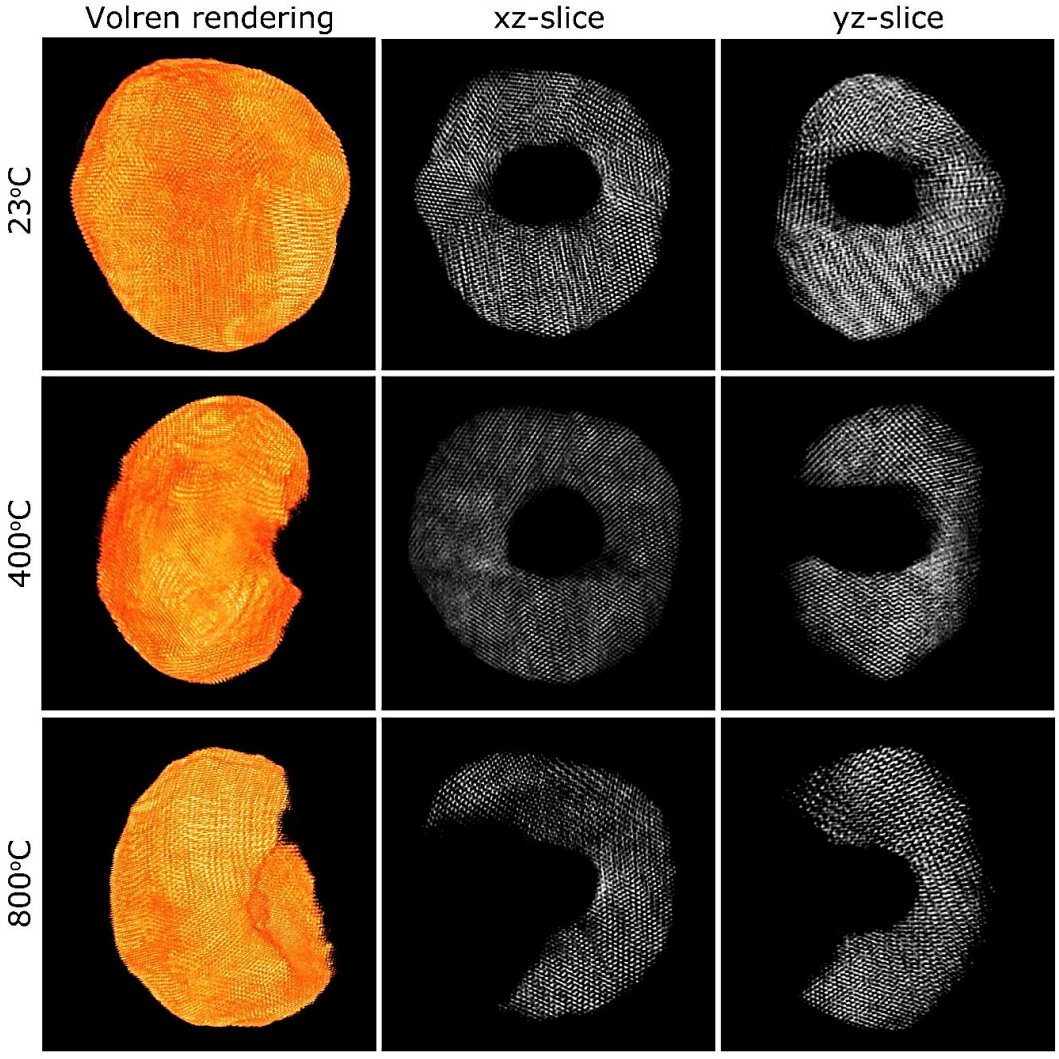

Figure 8.1 – Volume rendering and slices across of the 3D reconstructed with atomic resolution features of a hollow nanoparticle upon increasing temperature conditions.

Moreover, defects can also be correlated with functional properties of nanomaterials. In Chapter 5, we have shown a link between the type of defect observed in welded gold nanorods and the plasmonic properties of such systems. Since the defect type is directly associated with the welding geometry, the engineering of the welding process will result in the production of nano-systems with tunable optical properties.

However, the investigation of other types of nanomaterials are even more complex than metallic nanoparticles, since they might be more sensitive to the electron beam, as it is the case with soft-hard composites and halide perovskites, shown in Chapters 6 and 7. To retrieve the 3D structure of self-assemblies of metallic nanoparticles encapsulated with a polystyrene shell, advanced techniques for sample preparation under cryogenic conditions were combined with low dose TEM imaging. In this manner, the liquid phase was avoided during the sample preparation, minimizing the effects of drying processes, whilst lower electron doses prevented the structural modifications during illumination, as discussed in Chapter 6.

Finally, to retrieve the 3D atomic structure of beam sensitive nanomaterials, a methodology that has been theoretical proposed was applied to experimental data (Chapter 7). This approach combines extremely low electron doses with the use of direct electron detection cameras. Because the quantification and interpretation of HRTEM images are very complex and not straightforward, exit wave reconstruction was used to deliver an image that contains the information about the projected atomic potential of the object under investigation. During the development of the experimental methodology, phase images of gold nanorods along different orientations were obtained. A 3D atomic structure was retrieved from a tomographic reconstruction based on the phase images and the prior knowledge of the morphology of the investigated nanomaterial. Moreover, a 3D reconstruction of a halide perovskite was obtained, containing atomic features. Further experiments are still required to improve the quality of the reconstructed atomic structure of beam sensitive nanomaterials and the focus should be in the increase of the signal-to-noise ratio of phase images and the quality of the solutions containing the nanoparticles in suspension. For instance, the presence of excess of ligands in solution hampers the quality of the obtained HRTEM and phase images, as well as it contributes for an increased growth of organic compounds under electron beam irradiation. Additionally, the development of new methodologies for automatic alignment of the tomographic series of phase images with high signal-to-noise ratio is required, which could drastically improve the quality of the reconstruction.

In summary, it has been demonstrated in the present thesis how the use of advanced techniques of transmission electron microscopy enabled the characterization of more complex

nanostructures. Consequently, a better understanding about the morphology and the physical properties of different nanomaterials was achieved in the course of the present thesis. More specifically, a relationship of the crystallinity of seeds with the final products in the seed-mediated growth approach was established. This finding is of great relevance for the optimization of synthesis protocols and eventually enhance the dispersity yield of the final products. Additionally, the formation of a new type of nanostructure has been observed upon nanosecond laser pulses at specific conditions: hollow nanoparticles. The use of advanced techniques of electron microscopy enabled the comprehension of how cavities are formed upon interaction with ultrashort laser pulses and will contribute in the design of new applications using this type of material. Besides, the influence of the presence of structural defects on the optical properties of welded nanostructures has been established in the present thesis, which will in turn affect the performance of nanostructures in different types of applications in the optical field. Still, some nanomaterials are very sensitive towards the electron beam and the used approaches can no longer be applied. By applying advanced methodologies for sample preparation and electron microscopy techniques, the characterization of sensitive nanostructures in 3D at the nanoscale and even at the atomic level becomes possible. This opens new possibilities to investigate a vast range of complex nanostructures, enabling the optimization of the synthesis protocols, a deeper comprehension of the physical properties and eventually the design and optimization of the applications.

In order to achieve s further evolution of the 3D characterization techniques, new advances in the hardware of the electron microscopes and in the software for the data processing are required for the. In this manner, the investigation of more complex nanostructures can become more and more routinely.

8.1 Experimental methods

In this section, a summary of the different approaches for the characterization of nanomaterials based on advanced techniques for electron microscopy is provided. Atomic resolution electron tomography of hollow nanoparticles was performed under *in-situ* heating conditions for the investigation of the dynamical behaviour of the cavity at the atomic level.

8.2 Author contribution

Thaís Milagres de Oliveira performed the acquisition of the tomographic series for different temperatures with atomic resolution and the reconstruction tomographic series for each temperature Synthesis of gold nanospheres and the nanosecond laser pulses treatment were carried out by the research team of Prof. Dr. Luis M. Liz-Marzán.

The author of the present thesis contributed to this study by providing the dynamical evolution of the cavity at increasing temperature conditions at the atomic level, regarded the influence of the electron beam on the final result.

8.3 List of strategies used in the present thesis

In the present thesis, different methodologies for electron microscopy were used during the characterization of nanomaterials. Here, a list with all different approaches used in the results chapters is presented, with the respective advantages and disadvantages of each method.

Method	Aim	Chapters that used the method	Advantages	Disadvantages
ADF tilt series	For analysis of the distribution of particles with defects.	Chapter 3 and Chapter 4.	Permits an statistical distribution analysis, since it is performed at lower magnifications.	Does not allow a direct determination of the defect type.
Electron tomography (STEM)	Characterization of the structure of nanomaterials in 3D.	Chapter 3, Chapter 4, Chapter 5 and Chapter 6.	Provides the morphology and internal structure of different nanomaterials. Can be combined with spectroscopic techniques and *in-situ* conditions.	Does not provide information regarding the crystal structure of the object under investigation. Can cause radiation damage to beam sensitive nanostructures.
Multimode tomography	Characterization of structural defects in 3D.	Chapter 3 and Chapter 5.	Allows the simultaneous investigation of the structure of the object as well as the 3D distribution of defects.	Does not provide information regarding the nature of the structural defect.

Atomic resolution electron tomography	Characterization of the crystal structure of nanomaterials in 3D.	Chapter 4, Chapter 5 and Chapter 8.	Provides the 3D atomic structure of nanomaterials. Enables further characterization of the lattice, such as the presence of lattice strain. Can be combined with spectroscopic techniques and *in-situ* conditions.	Computational complexity of the post processing of the images, prior to the tomographic reconstruction. The specimen receives more radiation than electron tomography at the nanoscale and are not ideal for beam sensitive nanostructures.
***In-situ* heating**	Characterization of the dynamical behaviour of nanomaterials upon varying temperature conditions.	Chapter 4 and Chapter 8.	Can be combined with electron tomography experiments (nano and atomic scale) and spectroscopic techniques.	Requires specialized TEM holder and apparatus.
Electron tomography (TEM)	Characterization of the structure of nanomaterials in 3D.	Chapter 6.	Provides the 3D structure of nanomaterials. Ideal for soft-hard structures (carbon based shells).	Reconstructions contains more noise when compared with STEM techniques. Artefacts might be present due to the presence of diffraction contrast and the strong contrast from the support layer (carbon). Requires the use of grids with

				ultrathin carbon support or graphene.
3D EWR	Characterization of the crystal structure of nanomaterials in 3D, based on the phase obtained from the EWR.	Chapter 7.	Provides the 3D structure of the object under investigation at the atomic scale.	For low dose conditions, improvements on the signal-to-noise ratio and image alignment are still required.

Table 8-1 – Summary of the strategies used in the present thesis, with respective advantages and disadvantages.

Summary

Nanomaterials have shown increased interest over the past decades, due to their unique physical properties that enabled a new range of applications. Moreover, the use of advanced techniques for the characterization of such nanostructure was vital in the determination of the structure-property relationship that has been observed in nanomaterials. Transmission electron microscopy (TEM) has become the routinely technique for the characterization of nanostructures. However, the obtained images from TEM only corresponds to a two dimensional (2D) projection of a three-dimensional (3D) object. To circumvent such limitation, electron tomography is generally used to retrieve the 3D structure of nanomaterials.

However, electron tomography is commonly applied in the investigation of simple structures (e.g., model-like materials like monocrystalline nanospheres and nanorods). For nanomaterials with increasing complexity (e.g., presence of structural defects and beam sensitive structures), the use of standard techniques becomes limited, which can result in the presence of additional artefacts in the reconstructed 3D structure and/or even some type information loss.

Moreover, very often the investigation of nanomaterials are performed under specific environmental conditions, such as high-vacuum and room temperature. In this manner, only the static behaviour of the nanomaterials are captured. Thus, the characterization of chemical reactions at the surface of nanoparticles, phase transformations at high or varying pressure/temperature and nucleation/growth events cannot be achieved with the standard techniques for 2D/3D electron microscopy. To investigate nanomaterials under realistic conditions, *in-situ* techniques combined with electron tomography are of great importance.

In this thesis, more advanced 3D (S)TEM characterization techniques were employed for a thorough characterization of more complex nanomaterials, at specific and realistic environmental conditions. In the following paragraphs, an overview of each chapter is given.

Chapter 1 presents a basic introduction to nanotechnology and the recent advances in this field. In this thesis, two classes of nanomaterials are investigated: metallic nanoparticles and metal halide perovskite nanostructures. Therefore, a brief description of the relevant physical properties for each system and their respective applications is given. Finally, the need of advanced techniques for the characterization of complex nanomaterials is addressed.

Chapter 2 is devoted to electron tomography. Firstly, electron microscopy is briefly introduced. Next, the theoretical description of the principles behind electron tomography is

discussed. The image modes where a tomographic series can be acquired is addressed and followed by the description of each step to retrieve the 3D structure of the object under investigation: acquisition of a tomographic series, image alignments, alignment of the tilt axis, reconstruction and visualization.

The remaining of this thesis is devoted to the application of advanced techniques for electron tomography for a thorough characterization of complex nanostructures. The thesis is dived in two parts: “Electron tomography of metallic nanoparticles containing structural defects” (chapter 3 to chapter 5) and “Electron tomography of beam sensitive nanomaterials” (chapter 6 and chapter 7).

Chapter 3 demonstrates that an oxidative etching procedure of nanotriangles and nanorods results in spherical nanoparticles that may contain structural defects. High-resolution scanning transmission electron microscopy (STEM) revealed the type of defect found for each system. Moreover, a statistical analysis based on a tilt series of annular dark field (ADF) images demonstrated that the percentage of defects found are dependent on the initial structure prior to the treatment, as well as the conditions used during the oxidative etching treatment. The resulting spherical nanoparticles are further used as seeds in the synthesis process of larger nanostructures through the seed-mediated process. Electron tomography experiments of such systems revealed that the presence of defect in the seeds influence the final shape of the overgrown structures. Moreover, multimode electron tomography revealed that the crystal structure is preserved during the growth process. The use of advanced techniques for the characterization of nanostructures allowed us to stablish a connection between the shape of the overgrown structure and the initial seed during the seed-mediated process.

In Chapter 4, nanosecond laser pulses are used to introduce defects in spherical nanoparticles. The influence of the chemical environment during pulsed laser irradiation on the formation of defects is investigated. High-resolution STEM imaging combined with statistical analysis based on tilt series of ADF images revealed the type and the percentage of defects for each irradiated system. For a given set of conditions during the laser interaction, the formation of hollow nanoparticles is observed. Atomic resolution electron tomography enabled the characterization of the crystal lattice of hollow nanostructures. The use of *in-situ* heating tomography experiments in combination with spectroscopic techniques furthermore revealed the contents inside the cavities of hollow nanoparticles as well as the dynamical behaviour upon increasing temperature conditions. These findings were essential to establish the formation mechanism of cavities in hollow nanoparticles.

In Chapter 5, the welding between the tips of nanorods arranged in a dimer configuration is investigated. Such welding is promoted by the interaction of the dimers of nanorods with

femtosecond laser pulses at relatively high fluences. Electron tomography at the nanoscale in combination with high-resolution STEM imaging enabled us to establish a connection between the welding geometry and the defect type formed at the nanojunction. Additionally, advanced techniques of electron tomography at the atomic level allowed the visualization of the 3D distribution of the different types of defects observed. Next, spectroscopic measurements enabled the characterization of different plasmon modes in conductively connected systems. Moreover, the plasmonic properties is further investigated for welded systems with similar welding geometry and different structural defects at the nanojunction. Our findings revealed that the defect type does not influence the resonant energy of the plasmon modes, but the presence of defects is responsible for a further broadening of the energy spectrum of the resonant mode.

The second part of this thesis focuses on the characterization of beam sensitive nanomaterials. Chapter 6 focuses on the characterization of soft-hard composites. Here, self-assemblies of metallic nanoparticles are coated with a polystyrene shell, for applications in the biomedical field. We address the challenges related to the 3D investigation of soft-hard self-assemblies, such as radiation damage process and the effect of the sample preparation methods. Alternative techniques are used to retrieve the 3D volume, while maintaining the structure as close as possible to its original state. In this chapter, the number of particles per self-assembly and the distance between neighbouring particles are determined. This information is vital for a better comprehension of the plasmonic properties of such systems.

Chapter 7 aims the 3D characterization of beam sensitive nanostructures at the atomic level. Because of the development of direct electron detection cameras, the electron dose can be further reduced, enabling the characterization of sensitive structures. To retrieve the 3D atomic structure of such nanomaterials, an advanced method based on high-resolution TEM images are combined with electron tomography. Experimental tests on gold nanorods validated the methodology, which was further applied to metal halide perovskite nanocubes.

Finally, Chapter 8 presents the general conclusions of this thesis as well as an outlook for the future characterization of complex nanomaterials.

Samenvatting

De interesse voor nanomaterialen is de afgelopen decennia sterk toegenomen omwille van hun unieke fysische eigenschappen. Deze eigenschappen hebben een nieuwe reeks toepassingen mogelijk gemaakt. Om de relatie tussen de structuur en de eigenschappen van nanomaterialen te bepalen, is het gebruik van geavanceerde technieken voor het karakteriseren van dergelijke nanostructuren van cruciaal belang. Transmissie elektronenmicroscopie (TEM) is de routinematige techniek geworden voor het karakteriseren van nanostructuren. De verkregen TEM beelden zijn een tweedimensionale (2D) projectie van een driedimensionaal (3D) object en kunnen erg misleidend zijn. Om een dergelijke beperking te omzeilen, wordt elektronentomografie gebruikt om de 3D structuur van nanomaterialen te bepalen.

Conventionele elektronentomografie wordt over het algemeen toegepast bij het onderzoek van eenvoudige structuren (bijvoorbeeld modelachtige materialen zoals monokristallijne nanosferen en nanostaafjes). Voor nanomaterialen met toenemende complexiteit (bijv. aanwezigheid van structurele defecten en bundelgevoelige structuren), wordt het gebruik van standaardtechnieken onvoldoende. Dit kan resulteren in de aanwezigheid van extra artefacten in de 3D reconstructie en zelfs leiden tot enig type informatieverlies.

Bovendien wordt het onderzoek naar nanomaterialen vaak uitgevoerd onder specifieke omgevingscondities, zoals in hoog vacuüm en op kamertemperatuur. Op deze manier wordt alleen het statische gedrag van de nanomaterialen vastgelegd. Dit wil zeggen dat de karakterisering van chemische reacties aan het oppervlak van nanodeeltjes, fasetransformaties bij hoge of variërende druk/temperatuur en nucleatie/groei niet kunnen worden onderzocht met deze standaardtechnieken voor 2D / 3D-elektronenmicroscopie. Om nanomaterialen onder realistische omstandigheden te onderzoeken zijn in-situ technieken in combinatie met elektronentomografie van groot belang.

In dit proefschrift werden geavanceerde 3D (S)TEM-technieken gebruikt voor een grondige karakterisering van complexere nanomaterialen bij specifieke en realistische omgevingscondities. In de volgende paragrafen wordt een overzicht van elk hoofdstuk gegeven.

In hoofdstuk 1 wordt een inleiding tot nanotechnologie gegeven en worden de recente vorderingen in dit onderzoeksgebied besproken. In dit proefschrift worden twee klassen nanomaterialen onderzocht: metalen nanodeeltjes en metaalhalogenide perovskiet nanostructuren. Er wordt een korte beschrijving van de relevante fysieke eigenschappen voor elk systeem en hun respectievelijke toepassingen gegeven. Ten slotte wordt ingegaan op de behoefte aan geavanceerde technieken voor de karakterisering van complexe nanomaterialen.

Hoofdstuk 2 is gewijd aan elektronentomografie. Eerst wordt elektronenmicroscopie kort geïntroduceerd. Vervolgens wordt de theoretische beschrijving van de principes achter elektronentomografie besproken. De beeldvormingstechnieken waarin een tomografische serie kan worden opgenomen, worden toegelicht. Ten slotte wordt een beschrijving gegeven van elke stap om de 3D-structuur van het onderzochte object te bekomen: opname van een tomografische serie, uitlijning, reconstructie en visualisatie.

De rest van dit proefschrift is gewijd aan de toepassing van geavanceerde technieken voor elektronentomografie voor een grondige karakterisering van complexe nanostructuren. Het proefschrift bestaat uit twee delen: "Elektronentomografie van metalen nanodeeltjes met structurele defecten" (hoofdstuk 3 tot hoofdstuk 5) en "Elektronentomografie van bundelgevoelige nanomaterialen" (hoofdstuk 6 en hoofdstuk 7).

Hoofdstuk 3 toont dat een oxidatieve etsprocedure van nanodriehoeken en nanostaafjes resulteert in bolvormige nanodeeltjes die structurele defecten kunnen bevatten. Hoge resolutie scanning transmissie elektronenmicroscopie (STEM) onthulde het type defect dat voor elk systeem werd gevonden. Bovendien toonde een statistische analyse op basis van een tilt serie van ringvormige donkerveld (ADF) beelden aan dat het percentage van de gevonden defecten afhankelijk is van de initiële structuur voorafgaand aan de behandeling, evenals de experimentele parameters tijdens de oxidatieve etsbehandeling. De resulterende sferische nanodeeltjes worden verder gebruikt als zaden in het syntheseproces van grotere nanostructuren door het zaadgemedieerde proces. Elektronentomografie experimenten van dergelijke systemen toonden dat de aanwezigheid van defecten in de zaden de uiteindelijke vorm van de structuren beïnvloedt. Bovendien onthulde multimode elektronentomografie dat de kristalstructuur behouden blijft tijdens het groeiproces. Het gebruik van geavanceerde technieken voor de karakterisering van nanostructuren stelde ons in staat om een verband te leggen tussen de vorm van de structuur en de initiële zaad tijdens het zaadgemedieerde proces.

In hoofdstuk 4 worden nanoseconde laserpulsen gebruikt om defecten in bolvormige nanodeeltjes te introduceren. De invloed van de chemische omgeving tijdens gepulseerde laserbestraling op de vorming van defecten wordt onderzocht. Met behulp van hoge resolutie STEM-beeldvorming in combinatie met statistische analyse op basis van een reeks ADF beelden kon het type en het percentage defecten voor elk bestraald systeem worden bepaald. Onder bepaalde omstandigheden tijdens de laserinteractie wordt de vorming van holle nanodeeltjes waargenomen. Elektronentomografie met atomaire resolutie maakte de karakterisering mogelijk van het kristalrooster van deze holle nanostructuren. Het gebruik van in-situ opwarming tijdens tomografie-

experimenten in combinatie met spectroscopische technieken onthulde bovendien de inhoud in de holtes van deze holle nanodeeltjes, evenals het dynamische gedrag bij toenemende temperatuuromstandigheden. Deze bevindingen waren essentieel om het vormingsmechanisme van holten in holle nanodeeltjes vast te stellen.

In Hoofdstuk 5 wordt de junctie tussen de uiteinden van nanostaafjes in een dimeer configuratie onderzocht. De junctie wordt bevorderd door de interactie van de dimeren van nanostaafjes met femtoseconde laserpulsen. Elektronentomografie op nanoschaal in combinatie met hoge resolutie STEM-beeldvorming stelde ons in staat om een verband te vinden tussen de geometrie van de connectie en het defecttype dat bij de nanojunctie werd gevormd. Bovendien maakten geavanceerde technieken van elektronentomografie op atomair niveau de visualisatie van de verschillende soorten defecten mogelijk. Door elektronentomografie experimenten te combineren met spectroscopische metingen wordt vervolgens een relatie bepaald tussen de junctie geometrie en de plasmonische eigenschappen. Bovendien worden de plasmonische eigenschappen verder onderzocht voor systemen met een vergelijkbare junctie geometrie en verschillende structurele defecten aan de nanojunctie. Onze bevindingen lieten zien dat het defecttype de resonantie energie van de plasmon-modi niet beïnvloedt, maar de aanwezigheid van defecten is verantwoordelijk voor een verdere verbreding van het energiespectrum van de resonantie-modus.

Het tweede deel van dit proefschrift richt zich op de karakterisering van bundelgevoelige nanomaterialen. In hoofdstuk 6 wordt de karakterisering van zacht-harde composieten besproken. Hier worden zelfassemblages van metalen nanodeeltjes bekleed met een polystyreen schil voor toepassingen in het biomedische veld. Het 3D-onderzoek van zacht-harde zelfassemblages is uitdagend door de elektronenbundel gevoeligheid en het effect van de monster voorbereidingsmethoden. Er worden alternatieve technieken gebruikt om deze zacht-harde composieten te bestuderen. In dit hoofdstuk wordt het aantal deeltjes per zelfassemblage en de afstand tussen naburige deeltjes bepaald. Deze informatie is essentieel voor een beter begrip van de plasmonische eigenschappen van dergelijke systemen.

Hoofdstuk 7 richt zich op de 3D-karakterisering van bundelgevoelige nanostructuren op atomair niveau. Door de ontwikkeling van camera's voor directe elektronendetectie kan de elektronen dosis verder worden verlaagd, wat de karakterisering van gevoelige structuren mogelijk maakt. Om de 3D-atomaire structuur van dergelijke nanomaterialen terug te visualiseren, wordt een geavanceerde methode op basis van hoge resolutie TEM-afbeeldingen gecombineerd met elektronentomografie. Experimentele tests op gouden nanostaafjes valideerden de methodologie, die verder werd toegepast op metaalhalogenide perovskiet nanokubussen.

Tenslotte, in Hoofdstuk 8 worden de algemene conclusies van dit proefschrift gepresenteerd, evenals een vooruitblik voor de toekomstige karakterisering van complexe nanomaterialen.

References

1. Schaefer, H.-E. *Nanoscience: The Science of the Small in Physics, Engineering, Chemistry, Biology and Medicine*. (Springer, 2010).

2. Wolf, E. L. *Nanophysics and Nanotechnology: An Introduction to Modern Concepts in Nanoscience*. (Wiley-VCH, 2004).

3. Lindsay, S. M. *Introduction to Nanoscience*. (Oxford University Press, 2010).

4. Pitkethly, M. J. Nanomaterials – the driving force. *Mater. Today* **7**, 20–29 (2004).

5. Guo, Z. & Tan, L. *Fundamentals and Applications of Nanomaterials*. (Artech House, 2009).

6. Warrier, P. & Teja, A. Effect of particle size on the thermal conductivity of nanofluids containing metallic nanoparticles. *Nanoscale Resarch Lett.* **6**, 247 (2011).

7. Tang, Y. & Ouyang, M. Tailoring properties and functionalities of metal nanoparticles through crystallinity engineering. *Nat. Mater.* **6**, 754–759 (2007).

8. Link, S. & El-Sayed, M. A. Shape and size dependence of radiative, non-radiative and photothermal properties of gold nanocrystals. *Int. Rev. Phys. Chem.* **19**, 409–453 (2000).

9. Lee, K.-S. & El-Sayed, M. A. Gold and Silver Nanoparticles in Sensing and Imaging Sensitivity of Plasmon Response to Size, Shape, and Metal Composition. *J. Phys. Chem. B* **110**, 19220–19225 (2006).

10. Aliofkhazraei, M. *Anti-Abrasive Nanocoatings: Current and future applications*. (Woodhead Publishing in Materials, 2015).

11. Wang, J. U. E. *et al.* Scratch-Resistant Improvement of Sol-Gel Derived Nano-Porous Silica Films. *J. Sol-Gel Sci. Technol.* **18**, 219–224 (2000).

12. Bauer, F. *et al.* Nano / Micro Particle Hybrid Composites for Scratch and Abrasion Resistant Polyacrylate Coatings. *Macromol. Mater. Eng.* **91**, 493–498 (2006).

13. Beck, R., Guterres, S. & Pohlmann, A. *Nanocosmetics and Nanomedicines: New Approaches for Skin Care*. (Springer-Verlag Berlin Heidelberg GmbH, 2011).

14. Kim, H., Seo, M., Park, M.-H. & Cho, J. A Critical Size of Silicon Nano-Anodes for Lithium Rechargeable Batteries. *Angew. Chemie Int. Ed.* **49**, 2146-21–49 (2010).

15. Poizot, P., Laruelle, S., Grugeon, S., Dupont, L. & Tarascon, J. Nano-sizedtransition-

metaloxidesas negative-electrode materials for lithium-ion batteries. *Nature* **407**, 496–499 (2000).

16. Zijlstra, P., Chon, J. W. M. & Gu, M. Five-dimensional optical recording mediated by surface plasmons in gold nanorods. *Nature* **459**, 410–413 (2009).

17. Zhang, Q., Xia, Z., Cheng, Y. & Gu, M. High-capacity optical long data memory based on enhanced Young's modulus in nanoplasmonic hybrid glass composites. *Nat. Commun.* **9**, 1183 (2018).

18. Huang, X., El-sayed, I. H., Qian, W. & El-sayed, M. A. Cancer Cell Imaging and Photothermal Therapy in the Near-Infrared Region by Using Gold Nanorods. *J. Am. Chem. Soc.* **128**, 2115–2120 (2006).

19. Zhang, J., Tang, H., Liu, Z. & Chen, B. Effects of major parameters of nanoparticles on their physical and chemical properties and recent application of nanodrug delivery system in targeted chemotherapy. *Int. J. Nanomedicine* **12**, 8483–8493 (2017).

20. Dreaden, E. C., Alkilany, A. M., Huang, X., Murphy, C. J. & El-Sayed, M. A. The golden age: gold nanoparticles for biomedicine. *Chem. Soc. Rev.* **41**, 2740–2779 (2012).

21. Versiani, A. F. *et al.* Gold nanoparticles and their applications in biomedicine. *Future Virol.* **11**, 293–309 (2016).

22. Cui, Y., Wei, Q., Park, H. & Lieber, C. M. Nanowire Nanosensors for Highly Sensitive and Selective Detection of Biological and Chemical Species. *Science.* **293**, 1289–1293 (2001).

23. Anker, J. N. *et al.* Biosensing with plasmonic nanosensors. *Nat. M* **7**, 442–453 (2008).

24. Barber, D. J. & Freestone, I. C. An investigation of the origin of the colour of the lycurgus cup by analytical transmission electron microscopy. *Archaemotry* **32**, 33–45 (1990).

25. Hornyak, G. L. *et al.* Effective medium theory characterization of Au/Ag nanoalloy-porous alumina composites. *NanoStructured Mater.* **9**, 571–574 (1997).

26. Freestone, I., Meeks, N., Sax, M. & Higgitt, C. The Lycurgus Cup - A Roman nanotechnology. *Gold Bull.* **40**, 270–277 (2007).

27. The Lycurgus Cup. Available at: https://www.britishmuseum.org/research/collection_online/collection_object_details.aspx?objectId=61219&partId=1&searchText=lycurgus+cup&page=1. (Accessed: 23rd July 2019)

28. Hubenthal, F. Noble Metal Nanoparticles: Synthesis and Optical Properties. in *Comprehensive Nanoscience and Nanotechnology* (eds. Andrews, D. L., Lipson, R. H. & Nann, T.) 375–495 (Academic Press, 2011). doi:10.1016/B978-0-12-803581-8.00585-3

29. Xia, Y., Gilroy, K. D., Peng, H. & Xia, X. Seed-Mediated Growth of Colloidal Metal Nanocrystals. *Angew. Chemie Int. Ed.* **55**, 2–38 (2016).

30. Niu, W., Zhang, L. & Xu, G. Seed-Mediated Growth of Noble Metal Nanocrystals: Crystal Growth and Shape Control. *Nanoscale* **5**, 3172–3181 (2013).

31. Murphy, C. J. *et al.* Anisotropic Metal Nanoparticles Synthesis, Assembly, and Optical Applications. *J. Phys. Chem. B* **109**, 13857–13870 (2005).

32. González-Rubio, G. *et al.* Disentangling the effect of seed size and crystal habit on gold nanoparticle seeded growth. *Chem. Commun.* **53**, 11360–11363 (2017).

33. Grzelczak, M., Pérez-Juste, J., Mulvaney, P. & Iz-Marzán, L. M. Shape control in gold nanoparticle synthesis. *Chem. Soc. Rev.* **37**, 1783–1791 (2008).

34. Gole, A. & Murphy, C. J. Seed-Mediated Synthesis of Gold Nanorods Role of the Size and Nature of the Seed. *Chem. Mater.* **16**, 3633–3640 (2004).

35. Liu, M. & Guyot-Sionnest, P. Mechanism of Silver (I) -Assisted Growth of Gold Nanorods and Bipyramids. *J. Phys. Chem. B* **109**, 22192–22200 (2005).

36. Louis, C. & Pluchery, O. *Gold Nanoparticles for Physics, Chemistry and Biology*. (Imperial College Press, 2012). doi:10.1142

37. Miller, J. T. *et al.* The effect of gold particle size on Au – Au bond length and reactivity toward oxygen in supported catalysts. *J. Catal.* **240**, 222–234 (2006).

38. Griffiths, D. *Introduction to Electrodynamics*. (Prentice Hall, 1999).

39. Jackson, J. D. *Classical Electrodynamics*. (John Wiley & Sons, Inc., 1999).

40. Born, M. & Wolf, E. *Principles of Optics: Electromagnetic theory of propagation, interference and diffraction of light*. (Cambridge University Press, 2002).

41. Kosuda, K. M., Bingham, J. M., Wustholz, K. L. & Van Duyne, R. P. Nanostructures and Surface-Enhanced Raman Spectroscopy. in *Comprehensive Nanoscience and Nanotechnology* 1–35 (Elsevier Ltd., 2015). doi:10.1016/B978-0-12-803581-8.00611-1

42. Dressel, M. & Gruner, G. *Electrodynamics of Solids: Optical Properties of Electrons in Matter*.

(Cambridge University Press, 2003).

43. Fox, M. *Optical properties of solids*. (Oxford University Press, 2001).

44. Hartland, G. V. Optical Studies of Dynamics in Noble Metal Nanostructures. *Chem. Rev.* **111**, 3858–3887 (2011).

45. Besteiro, L. V., Kong, X. T., Wang, Z., Hartland, G. & Govorov, A. O. Understanding Hot-Electron Generation and Plasmon Relaxation in Metal Nanocrystals: Quantum and Classical Mechanisms. *ACS Photonics* **4**, 2759–2781 (2017).

46. Chen, K. P., Drachev, V. P., Borneman, J. D., Kildishev, A. V. & Shalaev, V. M. Drude relaxation rate in grained gold nanoantennas. *Nano Lett.* **10**, 916–922 (2010).

47. Bosman, M. *et al.* Encapsulated annealing: Enhancing the plasmon quality factor in lithographically-defined nanostructures. *Sci. Rep.* **4**, 1–6 (2014).

48. He, Y. Q., Liu, S. P., Kong, L. & Liu, Z. F. A study on the sizes and concentrations of gold nanoparticles by spectra of absorption, resonance Rayleigh scattering and resonance non-linear scattering. *Spectrochim. Acta - Part A Mol. Biomol. Spectrosc.* **61**, 2861–2866 (2005).

49. Willets, K. A. & Van Duyne, R. P. Localized Surface Plasmon Resonance Spectroscopy and Sensing. *Annu. Rev. Phys. Chem.* **58**, 267–297 (2007).

50. Cottancin, E. *et al.* Optical properties of noble metal clusters as a function of the size: comparison between experiments and a semi-quantal theory. *Theor. Chem. Acc.* **116**, 514–523 (2006).

51. González, A. L. & Noguez, C. Influence of Morphology on the Optical Properties of Metal Nanoparticles. *J. Comput. Theor. Nanosci.* **4**, 231–238 (2007).

52. Pérez-Juste, J., Pastoriza-Santos, I., Liz-Marzán, L. M. & Mulvaney, P. Gold nanorods: Synthesis, characterization and applications. *Coord. Chem. Rev.* **249**, 1870–1901 (2005).

53. Chen, H., Shao, L., Li, Q. & Wang, J. Gold nanorods and their plasmonic properties. *Chem. Soc. Rev.* **42**, 2679–2724 (2013).

54. Payne, E. K., Shuford, K. L., Park, S., Schatz, G. C. & Mirkin, C. A. Multipole Plasmon Resonances in Gold Nanorods. *J. Phys. Chem. B* **110**, 2150–2154 (2006).

55. Vigderman, L., Khanal, B. P. & Zubarev, E. R. Functional Gold Nanorods : Synthesis , Self-Assembly , and Sensing Applications. *Adv. Mater.* **24**, 4811–4841 (2012).

56. Amendola, V., Pilot, R., Frasconi, M., Maragò, O. M. & Iatì, M. A. Surface plasmon resonance in gold nanoparticles: A review. *J. Phys. Condens. Matter* **29**, 1–49 (2017).

57. Kleinman, S. L., Frontiera, R. R., Henry, A.-I., Dieringer, J. A. & Duyne, R. P. Van. Creating, characterizing, and controlling chemistry with SERS hot spots. *Phys. Chem. Chem. Phys.* **15**, 21–36 (2013).

58. Alvarez-Puebla, R., Liz-Marzán, L. M. & Abajo, F. J. G. de. Light Concentration at the Nanometer Scale. *J. Phys. Chem. Lett.* **1**, 2428–2434 (2010).

59. Lassiter, J. B. *et al.* Close Encounters between Two Nanoshells. *Nano Lett.* **8**, 1212–1218 (2008).

60. Pavaskar, P., Theiss, J. & Cronin, S. B. Plasmonic hot spots : nanogap enhancement vs . focusing effects from surrounding nanoparticles. *Opt. Express* **20**, 14656–14662 (2012).

61. Karabel, S. *et al.* Plasmonic assemblies of gold nanorods on nanoscale patterns of poly (ethylene glycol): Application in surface-enhanced Raman spectroscopy. *J. Colloid Interface Sci.* **532**, 449–455 (2018).

62. Liu, Y., Liu, Y. & Shen, Y. Nano‐assembly and welding of gold nanorods based on DNA origami and plasmon‐induced laser irradiation. *Int. J. Intell. Robot. Appl.* **2**, 445–453 (2018).

63. Baffou, G. & Quidant, R. Thermo-plasmonics: Using metallic nanostructures as nano-sources of heat. *Laser Photonics Rev.* **7**, 171–187 (2013).

64. Sönnichsen, C., Franzl, T., Wilk, T., Plessen, G. Von & Feldmann, J. Drastic Reduction of Plasmon Damping in Gold Nanorods. *Phys. Rev. Lett.* **88**, 077402 (2002).

65. Ziegler, T., Hendrich, C., Hubenthal, F., Vartanyan, T. & Trager, F. Dephasing times of surface plasmon excitation in Au nanoparticles determined by persistent spectral hole burning. *Chem. Phys. Lett.* **386**, 319–324 (2004).

66. Lamprecht, B., Leitner, A. & Aussenegg, F. R. Rapid communication Femtosecond decay-time measurement of electron-plasma oscillation in nanolithographically designed silver particles. *Appl. Phys. B* **64**, 269–272 (1997).

67. Furube, A. & Hashimoto, S. Insight into plasmonic hot-electron transfer and plasmon molecular drive: new dimensions in energy conversion and nanofabrication. *NPG Asia Mater.* **9**, e454 (2017).

68. Chang, S.-S., Shih, C.-W., Chen, C.-D., Lai, W.-C. & Wang, C. R. C. The Shape Transition of Gold Nanorods. *Langmuir* **15**, 701–709 (1999).

69. Fales, A. M., Vogt, W. C., Pfefer, J. & Ilev, I. K. Quantitative Evaluation of Nanosecond Pulsed Laser-Induced Photomodification of Plasmonic Gold Nanoparticles. *Sci. Rep.* **7**, 1–11 (2017).

70. Link, S., Burda, C., Nikoobakht, B. & El-Sayed, M. A. Laser-Induced Shape Changes of Colloidal Gold Nanorods Using Femtosecond and Nanosecond Laser Pulses. *J. Phys. Chem. B* **104**, 6152–6163 (2000).

71. Albrecht, W. *et al.* Single Particle Deformation and Analysis of Silica-Coated Gold Nanorods before and after Femtosecond Laser Pulse Excitation. *Nano Lett.* **16**, 1818–1825 (2016).

72. Kurita, H., Takami, A. & Koda, S. Size reduction of gold particles in aqueous solution by pulsed laser irradiation. *Appl. Phys. Lett.* **72**, 789–791 (1998).

73. Yamada, K., Miyajima, K. & Mafuné, F. Thermionic emission of electrons from gold nanoparticles by nanosecond pulse-laser excitation of interband. *J. Phys. Chem. C* **111**, 11246–11251 (2007).

74. Takami, A., Kurita, H. & Koda, S. Laser-Induced Size Reduction of Noble Metal Particles. *J. Phys. Chem. B* **103**, 1226–1232 (1999).

75. González-Rubio, G. *et al.* Femtosecond laser reshaping yields gold nanorods with ultranarrow surface plasmon resonances. *Science.* **358**, 640–644 (2017).

76. Link, S., Burda, C., Mohamed, M. B., Nikoobakht, B. & El-Sayed, M. A. Laser Photothermal Melting and Fragmentation of Gold Nanorods: Energy and Laser Pulse-Width Dependence. *J. Phys. Chem. A* **103**, 1165–1170 (1999).

77. Liu, D. *et al.* Rapid Synthesis of Monodisperse Au Nanospheres through a Laser Irradiation-Induced Shape Conversion, Self-Assembly and Their Electromagnetic Coupling SERS Enhancement. *Sci. Rep.* **5**, 1–9 (2015).

78. González-Rubio, G. *et al.* Femtosecond Laser-Controlled Tip-to-Tip Assembly and Welding of Gold Nanorods. *Nano Lett.* **15**, 8282–8288 (2015).

79. González-Rubio, G., Guerrero-Martínez, A. & Liz-Marzán, L. M. Reshaping, Fragmentation, and Assembly of Gold Nanoparticles Assisted by Pulse Lasers. *Acc. Chem. Res.* **49**, 678–686 (2016).

80. Jeon, J.-W. *et al.* The Effect of Laser Pulse Widths on Laser — Ag Nanoparticle Interaction : Femto- to Nanosecond Lasers. *Appl. Sci.* **8**, 112 (2018).

81. Behzadi, S. *et al.* Cellular uptake of nanoparticles: journey inside the cell. *Chem. Soc. Rev.* **46**, 4218–4244 (2017).

82. Alkilany, A. M. & Murphy, C. J. Toxicity and cellular uptake of gold nanoparticles: what we have learned so far? *J. Nanoparticle Res.* **12**, 2313–2333 (2010).

83. Khlebtsov, N. & Dykman, L. Biodistribution and toxicity of engineered gold nanoparticles: a review of in vitro and in vivo studies. *Chem. Soc. Rev.* **40**, 1647–1671 (2011).

84. Elahi, N., Kamali, M. & Baghersad, M. H. Recent biomedical applications of gold nanoparticles: A review. *Talanta* **184**, 537–556 (2018).

85. Jia, H., Zeng, J., Song, W., An, J. & Zhao, B. Preparation of silver nanoparticles by photo-reduction for surface-enhanced Raman scattering. *Thin Solid Films* **496**, 281–287 (2006).

86. Haidar, I. *et al.* Highly stable silica-coated gold nanorods dimers for solution-based SERS. *Phys. Chem. Chem. Phys.* **18**, 32272–32280 (2016).

87. Alexander, K. D., Skinner, K., Zhang, S., Wei, H. & Lopez, R. Tunable SERS in Gold Nanorod Dimers through Strain Control on an Elastomeric Substrate. *Nano Lett.* **10**, 4488–4493 (2010).

88. Scarabelli, L., Coronado-Puchau, M., Giner-Casares, J. J., Langer, J. & Liz-Marzán, L. M. Monodisperse Gold Nanotriangles: Size Control, Large-Scale Self-Assembly, and Performance in Surface-Enhanced Raman Scattering. *ACS Nano* **8**, 5833–5842 (2014).

89. Tinguely, J. C. *et al.* Gold Nanoparticles for Plasmonic Biosensing: The Role of Metal Crystallinity and Nanoscale Roughness. *Bionanoscience* **1**, 128–135 (2011).

90. Shamsi, J., Urban, A. S., Imran, M., De Trizio, L. & Manna, L. Metal Halide Perovskite Nanocrystals: Synthesis, Post-Synthesis Modifications, and Their Optical Properties. *Chem. Rev.* **119**, 3296–3348 (2019).

91. Lu, P. *et al.* Metal halide perovskite nanocrystals and their applications in optoelectronic devices. *InfoMat* **1**, 430–459 (2019).

92. Frei, H. & Berkeley, L. *Unconventional Thin Film Photovoltaics*. (Royal Society of Chemistry, 2016). doi:10.1039/9781782624066-fp001

93. Akkerman, Q. A., Rainò, G., Kovalenko, M. V. & Manna, L. Genesis, challenges and opportunities for colloidal lead halide perovskite nanocrystals. *Nat. Mater.* **17**, 394–405 (2018).

94. Li, S. *et al.* Metal Halide Perovskite Single Crystals: From Growth Process to Application. *Crystal* **8**, 220 (2018).

95. Wei, Y., Cheng, Z. & Lin, J. An overview on enhancing the stability of lead halide perovskite

quantum dots and their applications in phosphor-converted LEDs. *Chem. Soc. Rev.* **48**, 310–350 (2019).

96. Klein-Kedem, N., Cahen, D. & Hodes, G. Effects of Light and Electron Beam Irradiation on Halide Perovskites and Their Solar Cells. *Acc. Chem. Res.* **49**, 347–354 (2016).

97. Meggiolaro, D. *et al.* Iodine chemistry determines the defect tolerance of lead-halide perovskites. *Energy Environ. Sci.* **11**, 702–713 (2018).

98. Yavari, M. *et al.* How far does the defect tolerance of lead-halide perovskites range? The example of Bi impurities introducing efficient recombination centers. *J. Mater. Chem. A* **7**, 23838–23853 (2019).

99. Protesescu, L. *et al.* Nanocrystals of Cesium Lead Halide Perovskites (CsPbX3, X = Cl, Br, and I): Novel Optoelectronic Materials Showing Bright Emission with Wide Color Gamut. *Nano Lett.* **15**, 3692–3696 (2015).

100. Pan, G. *et al.* Doping Lanthanide into Perovskite Nanocrystals: Highly Improved and Expanded Optical Properties. *Nano Lett.* **17**, 8005–8011 (2017).

101. Ansari, M. I. H., Qurashi, A. & Nazeeruddin, M. K. Frontiers, opportunities, and challenges in perovskite solar cells: A critical review. *J. Photochem. Photobiol. C Photochem. Rev.* **35**, 1–24 (2018).

102. Ramasamy, P. *et al.* All-inorganic cesium lead halide perovskite nanocrystals for photodetector applications. *Chem. Commun.* **52**, 2067–2070 (2016).

103. Midgley, P. A. & Bals, S. Electron Tomography. in *Handbook of Nanoscopy* (eds. Van Tendeloo, G., Van Dyck, D. & Pennycook, S. J.) 253–279 (Wiley-VCH, 2012).

104. Hao, F., Nehl, C. L., Hafner, J. H. & Nordlander, P. Plasmon resonances of a gold nanostar. *Nano Lett.* **7**, 729–732 (2007).

105. Weyland, M. & Midgley, P. A. Electron tomography. *Mater. Today* **7**, 32–40 (2004).

106. Midgley, P. A. & Dunin-borkowski, R. E. Electron tomography and holography in materials science. *Nat. Mater.* **8**, 271–280 (2009).

107. Zanaga, D. *et al.* A New Method for Quantitative XEDS Tomography of Complex Heteronanostructures. *Part. Paricle Syst. Charact.* **33**, 396–403 (2016).

108. Goris, B. *et al.* Three dimensional mapping of Fe dopants in ceria nanocrystals using direct

spectroscopic electron tomography. *Ultramicroscopy* **171**, 55–62 (2016).

109. Liakakos, N. *et al.* Co − Fe Nanodumbbells: Synthesis, Structure, and Magnetic Properties. *Nano Lett.* **14**, 2747–2754 (2014).

110. Winckelmans, N. *et al.* Multimode Electron Tomography as a Tool to Characterize the Internal Structure and Morphology of Gold Nanoparticles. *J. Phys. Chem. C* **122**, 13522–13528 (2018).

111. Aert, S. Van, Batenburg, K. J., Rossell, M. D., Erni, R. & Tendeloo, G. Van. Three-dimensional atomic imaging of crystalline nanoparticles. *Nature* **470**, 374–377 (2011).

112. Goris, B. *et al.* Atomic-scale determination of surface facets in gold nanorods. *Nat. Mater.* **11**, 930–935 (2012).

113. Goris, B. *et al.* Measuring Lattice Strain in Three Dimensions through Electron Microscopy. *Nano Lett.* **15**, 6996–7001 (2015).

114. Website. Available at: https://www.jvmuntean.com/. (Accessed: 9th February 2020)

115. Kisielowski, C. Observing Atoms at Work by Controlling Beam-Sample Interactions. *Adv. Mater.* **27**, 5838–5844 (2015).

116. Lee, J. D. *et al.* Tuning the Electrocatalytic Oxygen Reduction Reaction Activity of PtCo Nanocrystals by Cobalt Concentration with Atomic-Scale Understanding. *ACS Appl. Mater. Interfaces* **11**, 26789–26797 (2019).

117. Gustafsson, M. G. L. Surpassing the lateral resolution limit by a factor of two using structured illumination microscopy. *J. Microsc.* **198**, 82–87 (2000).

118. Egerton, R. F. *Physical Principles of Electron Microscopy: An Introduction to TEM, SEM and AEM*. (Springer Internation Publishing, 2016).

119. Ruska, E. The development of the eletron microscope and of electron microscopy (Nobel Lecture). *Angew. Chemie Int. Ed.* **26**, 595–605 (1987).

120. Brooks, S. *Aberration-Corrected Analytical Transmission Electron Microscopy*. (John Wiley & Sons, Inc., 2011).

121. Crewe, A. V., Wall, J. & Langmore, J. Visibility of Single Atoms. *Science* **12**, 1338–1340 (1970).

122. Haider, M. *et al.* Towards 0.1 nm resolution with the first spherically corrected transmission electron microscope. *J. Electron Microsc. (Tokyo).* **47**, 395–405 (1998).

123. Haider, M., Hartel, P., Muller, H., Uhlemann, S. & Zach, J. Current and future aberration

correctors for the improvement of resolution in electron microscopy. *Philos. Trans. R. Soc. A Math. Phys. Eng. Sci.* **367**, 3665–3682 (2009).

124. Radon, J. On the determination of functions from their integral values along certain manifolds. *IEEE Trans. Med. Imaging* **MI–5**, 170–176 (1986).

125. Kirkland, A. I. & Haigh, S. J. *Nanocharacterisation*. (Royal Society of Chemistry, 2015).

126. Shepp, L. A. & Logan, B. F. The Fourier Reconstruction of a Head Section. *IEEE Trans. Nucl. Sci.* **NS21**, 21–43 (1974).

127. Sentosun, K. 2D and 3D Characterization of Plasmonic and Porous Nanoparticles using Transmission Electron Microscopy. (University of Antwerp, 2018). doi:10.1021/ac60261a003

128. Van den Broek, W. *et al.* Correction of non-linear thickness effects in HAADF STEM electron tomography. *Ultramicroscopy* **116**, 8–12 (2012).

129. Goris, B., Polavarapu, L., Bals, S., Van Tendeloo, G. & Liz-Marzán, L. M. Monitoring galvanic replacement through three-dimensional morphological and chemical mapping. *Nano Lett.* **14**, 3220–3226 (2014).

130. FEI. *ChemiSTEM Technology: A revolution in EDX analytics*. (2013).

131. Williams, D. B. & Carter, C. B. *Transmission Electron Microscopy: A Textbook for Materials Science*. (Springer, 2009).

132. Thomas, J. & Gemming, T. *Analytical Transmission Electron Microscopy: An introduction for Operators*. (Springer, 2014).

133. Watanabe, M. & Williams, D. B. The quantitative analysis of thin specimens: a review of progress from the Cliff-Lorimer to the new ζ -factor methods. *J. Microsc.* **221**, 89–109 (2006).

134. Zanaga, D., Altantzis, T., Sanctorum, J., Freitag, B. & Bals, S. An alternative approach for ζ-factor measurement using pure element nanoparticles. *Ultramicroscopy* **164**, 11–16 (2016).

135. Zhong, Z., Goris, B., Schoenmakers, R., Bals, S. & Batenburg, K. J. A bimodal tomographic reconstruction technique combining EDS-STEM and HAADF-STEM. *Ultramicroscopy* **174**, 35–45 (2017).

136. Fultz, B. & Howe, J. *Transmission Electron Microscopy and Diffractometry of Materials*. (Springer, 2013).

137. Website. Available at: https://en.wikipedia.org/wiki/Electron_energy_loss_spectroscopy.

(Accessed: 11th October 2019)

138. Goris, B., Turner, S., Bals, S. & Van Tendeloo, G. Three-dimensional valency mapping in ceria nanocrystals. *ACS Nano* **8**, 10878–10884 (2014).

139. Archanjo, B. S. *et al.* Plasmon 3D Electron Tomography and Local Electric-Field Enhancement of Engineered Plasmonic Nanoantennas. *ACS Photonics* **5**, 2834–2842 (2018).

140. Horl, A. *et al.* Tomographic imaging of the photonic environment of plasmonic nanoparticles. *Nat. Commun.* **8**, 1–6 (2017).

141. Nicoletti, O. *et al.* Three-dimensional imaging of localized surface plasmon resonances of metal nanoparticles. *Nature* **502**, 80–84 (2013).

142. Arslan, I., Tong, J. R. & Midgley, P. A. Reducing the missing wedge: High-resolution dual axis tomography of inorganic materials. *Ultramicroscopy* **106**, 994–1000 (2006).

143. Tong, J., Arslan, I. & Midgley, P. A novel dual-axis iterative algorithm for electron tomography. *J. Struct. Biol.* **153**, 55–63 (2006).

144. Goris, B., Van den Broek, W., Batenburg, K. J., Heidari Mezerji, H. & Bals, S. Electron tomography based on a total variation minimization reconstruction technique. *Ultramicroscopy* **113**, 120–130 (2012).

145. Chen, D. *et al.* The properties of SIRT, TVM, and DART for 3D imaging of tubular domains in nanocomposite thin-films and sections. *Ultramicroscopy* **147**, 137–148 (2014).

146. Erni, R. *Aberration-Corrected Imaging in Transmission Electron Microscopy: An Introduction*. (World Scientific Publishing Company, 2010).

147. Vanrompay, H. *et al.* 3D characterization of heat-induced morphological changes of Au nanostars by fast in situ electron tomography. *Nanoscale* **10**, 22792–22801 (2018).

148. Goris, B. *et al.* Atomic scale determination of surface facets in gold nanorods. *Nat. Mater.* **11**, 930–935 (2012).

149. Claes, N. *et al.* Characterization of silver-polymer core–shell nanoparticles using electron microscopy. *Nanoscale* **10**, 9186–9191 (2018).

150. Altantzis, T. *et al.* Three-Dimensional Quantification of the Facet Evolution of Pt Nanoparticles in a Variable Gaseous Environment. *Nano Lett.* **19**, 477–481 (2019).

151. McDowell, M. T., Jungjohann, K. L. & Celano, U. Dynamic Nanomaterials Phenomena

Investigated with in Situ Transmission Electron Microscopy: A Nano Letters Virtual Issue. *Nano Lett.* **18**, 657–659 (2018).

152. Kumar, C. S. S. R. *In-situ Characterization Techniques for Nanomaterials*. (Springer, 2018).

153. Vanrompay, H. *et al.* 3D characterization of heat-induced morphological changes of Au nanostars by fast: In situ electron tomography. *Nanoscale* **10**, 22792–22801 (2018).

154. Albrecht, W. *et al.* Thermal Stability of Gold/Palladium Octopods Studied in Situ in 3D: Understanding Design Rules for Thermally Stable Metal Nanoparticles. *ACS Nano* **13**, 6522–6530 (2019).

155. Skorikov, A. *et al.* Quantitative 3D Characterization of Elemental Diffusion Dynamics in Individual Ag@Au Nanoparticles with Different Shapes. *ACS Nano* **13**, 13421–13429 (2019).

156. Website. Available at: https://denssolutions.com/.

157. Siddardha, K. In situ and 3D environmental transmission electron microscopy of Pd-Al2O3 nano catalysts: Fast tomography with applications to other catalytic systems in operando conditions and to electron beam sensitive nanomaterials. (Univesité de Lyon, 2017).

158. Zhong, H., Mirkovic, T. & Scholes, G. D. Nanocrystal Synthesis. in *Comprehensive Nanoscience and Nanotechnology* (ed. Elsevier Ltd.) 153–201 (2011).

159. Noue, Y. I. *et al.* Stepwise Preparation of Spherical Gold Nanoparticles Passivated with Cationic Amphiphiles. *Anal. Sci.* **32**, 875–880 (2016).

160. Nikoobakht, B. & El-sayed, M. A. Preparation and Growth Mechanism of Gold Nanorods (NRs) Using Seed-Mediated Growth Method. *Chem. Mater.* **15**, 1957–1962 (2003).

161. Yuan, X. *et al.* Understanding seed-mediated growth of gold nanoclusters at molecular level. *Nat. Commun.* **8**, 927 (2017).

162. Nucleation, S. H. Nucleation. in *Encyclopedia of Materials: Science and Technology* 6388–6392 (Elsevier, 2001).

163. Sugimoto, Lt. Chapter 1 - Nucleation. in *Monodispersed Particles* 1–85 (Elsevier, 2001).

164. Meseguer, J., Pérez-Grande, I. & Sanz-Andrés, A. Phase change capacitors. in *Spacecraft Thermal Control* 209–223 (Elsevier, 2012). doi:10.1533/9780857096081.209

165. Xia, Y., Xiong, Y., Lim, B. & Skrabalak, S. E. Shape-Controlled Synthesis of Metal Nanocrystals: Simple Chemistry Meets Complex Physics? *Angew. Chemie Int. Ed.* **48**, 60–103 (2009).

166. Long, R., Zhou, S., Wiley, B. J. & Xiong, Y. Oxidative etching for controlled synthesis of metal nanocrystals: atomic addition and subtraction. *Chem. Soc. Rev.* **43**, 6288–6310 (2014).

167. Liz-Marzán, L. M. & Grzelczak, M. Growing anisotropic crystals at the nanoscale. *Science (80-.).* **356**, 1120–1121 (2017).

168. Yu, Y., Zhang, Q., Liu, B. & Lee, J. Y. Synthesis of Nanocrystals with Variable High-Index Pd Facets through the Controlled Heteroepitaxial Growth of Trisoctahedral Au Templates. *J. Am. Chem. Soc.* **132**, 18258–18265 (2010).

169. Wiley, B., Sun, Y., Mayers, B. & Xia, Y. Shape-Controlled Synthesis of Metal Nanostructures The Case of Silver. *Chem. A Eur. J.* **11**, 454–463 (2005).

170. Xiong, Y. & Xia, Y. Shape-Controlled Synthesis of Metal Nanostructures The Case of Palladium. *Adv. Mater.* **19**, 3385–3391 (2007).

171. Wiley, B., Herricks, T., Sun, Y. & Xia, Y. Polyol Synthesis of Silver Nanoparticles: Use of Chloride and Oxygen to Promote the Formation of Single-Crystal, Truncated Cubes and Tetrahedrons. *Nano Lett.* **4**, 1733–1739 (4AD).

172. Scarabelli, L., Sánchez-Iglesias, A., Pérez-Juste, J. & Liz-Marzán, L. M. A 'Tips and Tricks' Practical Guide to the Synthesis of Gold Nanorods. *J. Phys. Chem. Lett.* **6**, 4270–4279 (2015).

173. Van Dyck, D. & Op de Beeck, M. A simple intuitive theory for electron diffraction. *Ultramicroscopy* **64**, 99–107 (1996).

174. Bladt, E., Pelt, D. M., Bals, S. & Batenburg, K. J. Electron tomography based on highly limited data using a neural network reconstruction technique. *Ultramicroscopy* **158**, 81–88 (2015).

175. Aarle, W. Van *et al.* The ASTRA Toolbox : A platform for advanced algorithm development in electron tomography. *Ultramicroscopy* **157**, 35–47 (2015).

176. Sentosun, K., Sanz Ortiz, M. N., Batenburg, K. J., Liz-Marzán, L. M. & Bals, S. Combination of HAADF-STEM and ADF-STEM Tomography for Core-Shell Hybrid Materials. *Part. Part. Syst. Charact.* **32**, 1063–1067 (2015).

177. Yang, F., Zhang, D., Zhang, H. & Huang, K. Cupping artifacts correction for polychromatic X-ray cone-beam computed tomography based on projection compensation and hardening behavior. *Biomed. Signal Process. Control* **57**, 101823 (2020).

178. Byrne, A. *et al.* Mechanisms of Iodide – Triiodide Exchange Reactions in Ionic Liquids : A Reactive Molecular-Dynamics Exploration. *Internaltional J. Mol. Sci.* **20**, 1123 (2019).

179. Liu, X. *et al.* Facile Synthesis of Pd Nanocubes with Assistant of Iodide and Investigation of Their Electrocatalytic Performances Towards Formic Acid Oxidation. *Nanomaterials* **9**, 375 (2019).

180. Huang, X. *et al.* Synthesis of PtPd Bimetal Nanocrystals with Controllable Shape, Composition and Their Tunable Catalytic Properties. *Nano Lett.* **12**, 4265–4270 (2012).

181. Smith, D. K., Miller, N. R. & Korgel, B. A. Iodide in CTAB Prevents Gold Nanorod Formation. *Langmuir* **25**, 9518–9524 (2009).

182. King, M. E. & Personick, M. L. Iodide-Induced Differential Control of Metal Ion Reduction Rates: Synthesis of Terraced Palladium-Copper Nanoparticles with Dilute Bimetallic Surfaces. *J. Mater. Chem. A* **6**, 22179–22188 (2018).

183. Langille, M. R., Personick, M. L., Zhang, J. & Mirkin, C. A. Defining Rules for the Shape Evolution of Gold Nanoparticles. *J. Am. Chem. Soc.* **134**, 14542–14554 (2012).

184. Zhang, Y., Schwartzberg, A. M., Xu, K., Gu, C. & Zhang, J. Z. Electrical and Thermal Conductivities of Gold and Silver Nanoparticles in Solutions and Films and Electrical Field Enhanced Surface-Enhanced Raman Scattering (SERS). *Proc. SPIE - Phys. Chem. Interfaces Nanomater. IV* **5929**, 592912 (2015).

185. González-Rubio, G. *et al.* Formation of Hollow Gold Nanocrystals by Nanosecond Laser Irradiation. *J. Phys. Chem. Lett.* **11**, 670–677 (2020).

186. Gordon, J. P., Zeiger, H. J. & Townes, C. H. The Maser-New Type of Microwave Amplifier, Frequency Standard, and Spectrometer. *Phys. Rev.* **99**, 1264–1274 (1955).

187. Maiman, T. H. Optical and Microwave-optical Experiments in Ruby. *Phys. Rev. Lett.* **4**, 564–566 (1960).

188. Shank, C. V. & Ippen, E. P. Subpicosecond kilowatt pulses from a mode-locked cw dye laser. *Appl. Phys. Lett.* **24**, 373 (1974).

189. Zewail, A. H. Femtochemistry: Atomic-Scale Dynamics of the Chemical Bond. *J. Phys. Chem. A* **104** 5660–5694 (2000). doi:10.1021/jp001460h

190. Demtröder, W. *Laser Spectroscopy: Basic concepts and instrumentation*. (Springer, 2003).

191. Plech, A., Kotaidis, V., Grésillon, S., Dahmen, C. & Plessen, G. von. Laser-induced heating and melting of gold nanoparticles studied by time-resolved x-ray scattering. *Phys. Rev. B* **70**, 195423 (2004).

192. Nguyen, S. C. *et al.* Study of Heat Transfer Dynamics from Gold Nanorods to the Environment via Time-Resolved Infrared Spectroscopy. *ACS Nano* **10**, 2144–2151 (2016).

193. Werner, D., Furube, A., Okamoto, T. & Hashimoto, S. Femtosecond Laser-Induced Size Reduction of Aqueous Gold Nanoparticles In Situ and Pump−Probe Spectroscopy Investigations Revealing Coulomb Explosion.pdf. *J. Phys. Chem. C* **115**, 8503–8512 (2011).

194. Pyatenko, A., Yamaguchi, M. & Suzuki, M. Mechanisms of Size Reduction of Colloidal Silver and Gold Nanoparticles Irradiated by Nd:YAG Laser. *J. Phys. Chem. C* **113**, 9078–9085 (2009).

195. Falamas, A., Tosa, N. & Tosa, V. Dynamics of laser excited colloidal gold nanoparticles functionalized with cysteine derivatives. *J. Quant. Spectrosc. Radiat. Transf.* **162**, 207–212 (2015).

196. Pyatenko, A., Wang, H., Koshizaki, N. & Tsuji, T. Mechanism of pulse laser interaction with colloidal nanoparticles. *Laser Photonics Rev.* **7**, 596–604 (2013).

197. Giammanco, F., Giorgetti, E., Marsili, P. & Giusti, A. Experimental and Theoretical Analysis of Photofragmentation of Au Nanoparticles by Picosecond Laser Radiation. *J. Phys. Chem. C* **114**, 3354–3363 (2010).

198. Lescoute, E. *et al.* Experimental observations and modeling of nanoparticle formation in laser-produced expanding plasma. *Phys. Plasmas* **15**, 063507 (2008).

199. Ahmadi, T. S., Logunov, S. L. & El-Sayed, M. A. Picosecond Dynamics of Colloidal Gold Nanoparticles. *J. Phys. Chem.* **100**, 8053–8056 (1996).

200. Logunov, S. L., Ahmadi, T. S., El-Sayed, M. A., Khoury, J. T. & Whetten, R. L. Electron Dynamics of Passivated Gold Nanocrystals Probed by Subpicosecond Transient Absorption Spectroscopy. *J. Phys. Chem. B* **101**, 3713–3719 (1997).

201. Link, S., Burda, C., Mohamed, M. B., Nikoobakht, B. & El-Sayed, M. A. Femtosecond transient-absorption dynamics of colloidal gold nanorods: Shape independence of the electron-phonon relaxation time. *Phys. Rev. B - Condens. Matter Mater. Phys.* **61**, 6086–6090 (2000).

202. Baffou, G. & Rigneault, H. Femtosecond-pulsed optical heating of gold nanoparticles. *Phys. Rev. B* **84**, 035415 (2011).

203. Link, S., Wang, Z. L. & El-Sayed, M. A. How Does a Gold Nanorod Melt? [#]. *J. Phys. Chem. B* **104**, 7867–7870 (2000).

204. Yamada, K., Tokumoto, Y., Nagata, T. & Mafune, F. Mechanism of Laser-induced Size-reduction

of Gold Nanoparticles as Studied by Nanosecond Transient Absorption Spectroscopy. *J. Phys. Chem. B* **110**, 11751–11756 (2006).

205. Ziefuß, A. R. *et al.* Laser fragmentation of colloidal gold nanoparticles with high- intensity nanosecond pulses driven by a single-step fragmentation mechanism with a defined educt particle-size threshold. *J. Phys. Chem. C* **122**, 22125–22136 (2018).

206. Tsuji, T., Okazaki, Y. & Tsuji, M. Photo-induced morphological conversions of silver nanoparticles prepared using laser ablation in water-Enhanced morphological conversions using halogen etching. *J. Photochem. Photobiol. A Chem.* **194**, 247–253 (2008).

207. Zaarour, M. *et al.* Photochemical preparation of silver nanoparticles supported on zeolite crystals. *Langmuir* **30**, 6250–6256 (2014).

208. Kshirsagar, P. *et al.* Synthesis of highly stable silver nanoparticles by photoreduction and their size fractionation by phase transfer method. *Colloids Surfaces A Physicochem. Eng. Asp.* **392**, 264–270 (2011).

209. Moustaoui, H. *et al.* Shape and Size Effect on Photothermal Heat Elevation of Gold Nanoparticles: Absorption Coefficient Experimental Measurement of Spherical and Urchin-Shaped Gold Nanoparticles. *J. Phys. Chem. C* **123**, 17548–17554 (2019).

210. Hu, J. *et al.* Colloidal porous gold nanoparticles. *Nanoscale* **10**, 18473–18481 (2018).

211. Perner, M. *et al.* Optically induced damping of the surface plasmon resonance in gold colloids. *Phys. Rev. Lett.* **78**, 2192–2195 (1997).

212. Taylor, A. B., Siddiquee, A. M. & Chon, J. W. M. Below Melting Point Photothermal Reshaping of Single Gold Nanorods Driven by Surface Diffusion. *ACS Nano* **8**, 12071–12079 (2014).

213. Zijlstra, P., Chon, J. W. M. & Gu, M. White light scattering spectroscopy and electron microscopy of laser induced melting in single gold nanorods. *Phys. Chem. Chem. Phys.* **11**, 5915 (2009).

214. Singh, S. & Khare, N. Effect of intrinsic strain on the optical bandgap and magnetic properties of single domain - CoFe2O4 nanoparticles. *Appl. Phys. A* **124**, 107 (2018).

215. Yang, L. *et al.* Lattice strain effects on the optical properties of MoS2 nanosheets. *Sci. Rep.* **4**, 5949 (2014).

216. Dhara, S., Imakita, K., Giri, P. K. & Fujii, M. Strain dependence of the nonlinear optical properties of strained Si nanoparticles. *Opt. Lett.* **39**, 3833–3836 (2014).

217. Hytch, M. J., Snoeck, E. & Kilaas, R. Quantitative measurement of displacement and strain fields from HREM micrographs. *Ultramicroscopy* **74**, 131–146 (1998).

218. Buurlage, J.-W., Kohr, H., Palenstijn, W. J. & Batenburg, K. J. Real-time quasi-3D tomographic reconstruction. *Meas. Sci. Technol.* **29**, 064005 (2018).

219. Buurlage, J. W. *et al.* Real-time reconstruction and visualisation towards dynamic feedback control during time-resolved tomography experiments at TOMCAT. *Sci. Rep.* **9**, 18379 (2019).

220. Reimer, L. & Kohl, H. *Transmission Electron Microscopy: Physics of Image Formation*. (Springer, 2008).

221. Spence, J. C. H. *High-Resolution Electron Microscopy*. (Oxford University Press, 2013). doi:10.1017/CBO9781107415324.004

222. Albrecht, W. *et al.* Thermal Stability of Gold/Palladium Octopods Studied in Situ in 3D: Understanding Design Rules for Thermally Stable Metal Nanoparticles. *ACS Nano* **13**, 6522–6530 (2019).

223. Skorikov, A. *et al.* Quantitative 3D Characterization of Elemental Diffusion Dynamics in Individual Ag @ Au Nanoparticles with Different Shapes. *ACS Nano* **Just accepted** (2019).

224. Stukowski, A. Visualization and analysis of atomistic simulation data with OVITO-the Open Visualization Tool. *Model. Simul. Mater. Sci. Eng.* **18**, 015012 (2010).

225. Palenstijn, W. J., Batenburg, K. J. & Sijbers, J. Performance improvements for iterative electron tomography reconstruction using graphics processing units (GPUs). *J. Struct. Biol.* **176**, 250–253 (2011).

226. Jo, J. G., Cho, S. J., Park, M. C., Jhon, Y. M. & Ju, B. K. Modified hybrid input-output algorithm for phase retrieval. *Tech. Dig. - 25th Int. Vac. Nanoelectron. Conf. IVNC 2012* P2-63 (2012). doi:10.1109/IVNC.2012.6316827

227. Huang, T. S., Rinaldi, K. A. & Lee, H. Comparison of Phase Retrieval Algorithms. *ICASSP, IEEE Int. Conf. Acoust. Speech Signal Process. - Proc.* **21**, 1199–1200 (1987).

228. Ekici, O. *et al.* Thermal analysis of gold nanorods heated with femtosecond laser pulses. *J. Phys. D. Appl. Phys.* **41**, 185501 (2008).

229. Zhang, H. *et al.* Experimental study on the transition of plasmonic resonance modes in double-ring dimers by conductive junctions in the terahertz regime. *Opt. Express* **24**, 27415–27422 (2016).

230. Koya, A. N. & Lin, J. Bonding and charge transfer plasmons of conductively bridged nanoparticles: The effects of junction conductance and nanoparticle morphology. *J. Appl. Phys.* **120**, 093105 (2016).

231. Koya, A. N. & Lin, J. Charge transfer plasmons: Recent theoretical and experimental developments. *Appl. Phys. Rev.* **4**, 021104 (2017).

232. Zhang, M. *et al.* Screened bonding , antibonding and charge transfer plasmon modes in conductively connected nanorod heterodimer. *J. Opt.* **20**, 025001 (2018).

233. Perez-Gonzalez, O., Zabala, N. & Aizpurua, J. Optical characterization of charge transfer and bonding dimer plasmons in linked interparticle gaps. *New J. Phys.* **13**, 083013 (2011).

234. Fontana, J. & Ratna, B. R. Highly tunable gold nanorod dimer resonances mediated through conductive junctions. *Appl. Phys. Lett.* **105**, 011107 (2014).

235. Fontana, J. *et al.* Rise of the charge transfer plasmon : programmable concatenation of conductively linked gold nanorod dimers. *ACS Photonics* **5**, 904–911 (2016).

236. Wen, F. *et al.* Charge Transfer Plasmons: Optical Frequency Conductances and Tunable Infrared Resonances. *ACS Nano* **9**, 6428–6435 (2015).

237. Haidar, I. *et al.* Design of Stable Plasmonic Dimers in Solution: Importance of Nanorods Aging and Acidic Medium. *J. Phys. Chem. C* **119**, 23149–23158 (2015).

238. Osberg, K. D. *et al.* Dispersible Gold Nanorod Dimers with Sub-5 nm Gaps as Local.pdf. *Nano Lett.* **12**, 3828–3832 (2012).

239. Funston, A. M., Novo, C., Davis, T. J. & Mulvaney, P. Plasmon coupling of gold nanorods at short distances and in different geometries. *Nano Lett.* **9**, 1651–1658 (2009).

240. Lormand, G. Electrical Properties of Grain Boundaries. *J. Phys. Coloques* **43**, C6-283-C6-292 (1982).

241. Huang, W., Qian, W. & El-Sayed, M. A. Effect of the Lattice Crystallinity on the Electron−Phonon Relaxation Rates in Gold Nanoparticles. *J. Phys. Chem. C* **111**, 10751–10757 (2007).

242. Jain, P. K., Eustis, S. & El-sayed, M. A. Plasmon Coupling in Nanorod Assemblies : Optical Absorption , Discrete Dipole Approximation Simulation , and Exciton-Coupling Model. *J. Phys. Chem. B* **110**, 18243–18253 (2006).

243. Chu, M. W. *et al.* Probing bright and dark surface-plasmon modes in Individual and coupled

noble metal nanoparticles using an electron beam. *Nano Lett.* **9**, 399–404 (2009).

244. Lerch, S. & Reinhard, B. M. Effect of interstitial palladium on plasmon-driven charge transfer in nanoparticle dimers. *Nat. Commun.* **9**, 1608 (2018).

245. Miller, M. M. & Lazarides, A. A. Sensitivity of metal nanoparticle plasmon resonance band position to the dielectric environment as observed in scattering. *J. Opt. A Pure Appl. Opt.* **8**, S239–S242 (2006).

246. Oliveira, T. M. De *et al.* 3D characterization of gold nanorods after welding under femtosecond laser irradiation. *Submitted* (2020).

247. Slaughter, L. S., Wu, Y., Willingham, B. A., Nordlander, P. & Link, S. Effects of symmetry breaking and conductive contact on the plasmon coupling in gold nanorod dimers. *ACS Nano* **4**, 4657–4666 (2010).

248. Hoggard, A. *et al.* Using the plasmon linewidth to calculate the time and efficiency of electron transfer between gold nanorods and graphene. *ACS Nano* **7**, 11209–11217 (2013).

249. Hohenester, U. Simulating electron energy loss spectroscopy with the MNPBEM toolbox. *Comput. Phys. Commun.* **185**, 1177–1187 (2014).

250. Waxenegger, J., Trügler, A. & Hohenester, U. Plasmonics simulations with the MNPBEM toolbox: Consideration of substrates and layer structures. *Comput. Phys. Commun.* **193**, 138–150 (2015).

251. Hohenester, U. & Trügler, A. MNPBEM - A Matlab toolbox for the simulation of plasmonic nanoparticles. *Comput. Phys. Commun.* **183**, 370–381 (2012).

252. Tauzin, L. J. *et al.* Exploring the Relationship between Plasmon Damping and Luminescence in Lithographically Prepared Gold Nanorods. *ACS Photonics* **5**, 3541–3549 (2018).

253. Foerster, B. *et al.* Chemical Interface Damping Depends on Electrons Reaching the Surface. *ACS Nano* **11**, 2886–2893 (2017).

254. Novo, C. *et al.* Contributions from radiation damping and surface scattering to the linewidth of the longitudinal plasmon band of gold nanorods: A single particle study. *Phys. Chem. Chem. Phys.* **8**, 3540–3546 (2006).

255. Kittel, C. *Introduction to Solid State Physics*. (John Wiley & Sons, Inc., 2005). doi:10.1088/0031-9112/8/9/012

256. Ni, G. *et al.* Fundamental limits to graphene plasmonics. *Nature* **557**, 530–533 (2018).

257. Kolwas, K. Decay Dynamics of Localized Surface Plasmons: Damping of Coherences and Populations of the Oscillatory Plasmon Modes. *Plasmonics* **14**, 1629–1637 (2019).

258. Grigorchuk, N. I. Radiative damping of surface plasmon resonance in spheroidal metallic nanoparticle embedded in a dielectric medium. *J. Opt. Soc. Am. B* **29**, 3404 (2012).

259. Melikyan, A. & Minassian, H. On surface plasmon damping in metallic nanoparticles. *Appl. Phys. B Lasers Opt.* **78**, 453–455 (2004).

260. Shao, L., Tao, Y., Ruan, Q., Wang, J. & Lin, H.-Q. Comparison of the plasmonic performances between lithographically fabricated and chemically grown gold nanorods. *Phys. Chem. Chem. Phys.* **17**, 10861--10870 (2015).

261. Landau, L. D. & Lifshitz, E. M. *Electrodynamics of Continuous Media*. (Pergamon Press, 1984).

262. Maier, S. A. *Plasmonics: Fundamentals and appliations*. (Springer, 2007).

263. Kennedy, L. C. *et al.* A new era for cancer treatment: Gold-nanoparticle-mediated thermal therapies. *Small* **7**, 169–183 (2011).

264. Li, J. L. & Gu, M. Gold-nanoparticle-enhanced cancer photothermal therapy. *IEEE J. Sel. Top. Quantum Electron.* **16**, 989–996 (2010).

265. Huang, X. & El-Sayed, M. A. Gold nanoparticles : Optical properties and implementations in cancer diagnosis and photothermal therapy. *J. Adv. Res.* **1**, 13–28 (2010).

266. Nune, S. K. *et al.* Nanoparticles for biomedical imaging. *Expert Opin. Drug Deliv.* **6**, 1175–1194 (2009).

267. Park, K., Tuttle, G., Sinche, F. & Harper, S. L. Stability of citrate-capped silver nanoparticles in exposure media and their effects on the development of embryonic zebrafish (Danio rerio). *Arch. Pharm. Res.* 125–133 (2013). doi:10.1007/s12272-013-0005-x

268. Scarabelli, L. *et al.* Encapsulation of Noble Metal Nanoparticles through Seeded Emulsion Polymerization as Highly Stable Plasmonic Systems. *Adv. Funct. Mater.* **29**, 1809071 (2019).

269. Asapu, R. *et al.* Silver-polymer nanoparticles for ultrastable plasmon-enhanced photocatalysis. *Appl. Catal. B Environ.* **200**, 31–38 (2017).

270. Sanz-ortiz, M. N., Sentosun, K., Bals, S. & Liz-marza, L. M. Templated Growth of Surface Enhanced Raman Scattering-Active Branched Gold Nanoparticles within Radial Mesoporous

Silica Shells. *ACS Nano* **9**, 10489–10497 (2015).

271. Pellegrino, T. *et al.* Hydrophobic Nanocrystals Coated with an Amphiphilic Polymer Shell: A General Route to Water Soluble Nanocrystals. *Nano Lett.* **4**, 703–707 (2004).

272. Li, B. *et al.* Bypassing multidrug resistance in human breast cancer cells with lipid/polymer particle assemblies. *Int. J. Nanomedicine* **7**, 187–197 (2012).

273. Maria, D. M. *et al.* Biocompatibility, uptake and endocytosis pathways of polystyrene nanoparticles in primary human renal epithelial cells. *J. Biotechnol.* **193**, 3–10 (2015).

274. Johnston, H. J. *et al.* Evaluating the uptake and intracellular fate of polystyrene nanoparticles by primary and hepatocyte cell lines in vitro. *Toxicol. Appl. Pharmacol.* **242**, 66–78 (2010).

275. Wong, H. L. *et al.* A Mechanistic Study of Enhanced Doxorubicin Uptake and Retention in Multidrug Resistant Breast Cancer Cells Using a Polymer-Lipid Hybrid Nanoparticle System. *J. Pharmacol. Exp. Ther.* **317**, 1372–1381 (2006).

276. Taglietti, A. *et al.* Antibacterial Activity of Glutathione-Coated Silver Nanoparticles against Gram Positive and Gram Negative Bacteria. *Langmuir* **28**, 8140–8148 (2012).

277. Ivask, A. *et al.* Toxicity Mechanisms in Escherichia coli Vary for Silver Nanoparticles and Di ff er from Ionic Silver. *ACS Nano* **8**, 374–386 (2014).

278. Zanaga, D. *et al.* Quantitative 3D analysis of huge nanoparticle assemblies. *Nanoscale* **8**, 292–299 (2016).

279. Schmidtke, C. *et al.* Polymer-Assisted Self-Assembly of Superparamagnetic Iron Oxide Nanoparticles into Well-Defined Clusters: Controlling the Collective- Magnetic Properties. *Langmuir* **23**, 11190–11196 (2014).

280. Steinigeweg, D., Schütz, M., Salehi, M. & Schlücker, S. Gold Nanoparticles: Fast and Cost-Effective Purification of Gold Nanoparticles in the 20–250 nm Size Range by Continuous Density Gradient Centrifugation. *Small* **7**, 2443–2448 (2011).

281. Vanrompay, H. *et al.* 3D characterization of heat-induced morphological changes of Au nanostars by fast in situ electron tomography. *Nanoscale* **10**, 22792–22801 (2018).

282. Kisielowski, C. *et al.* Real-time sub-Angstrom imaging of reversible and irreversible conformations in rhodium catalysts and graphene. *Phys. Rev. B* **88**, 024305 (2013).

283. Barton, B. *et al.* Atomic Resolution Phase Contrast Imaging and In-Line Holography Using

Variable Voltage and Dose Rate. *Microsc. Microanal.* **18**, 982–994 (2012).

284. Yu, Y. *et al.* Atomic Resolution Imaging of Halide Perovskites. *Nano Lett.* **16**, 7530–7535 (2016).

285. Michen, B. *et al.* Avoiding drying-artifacts in transmission electron microscopy: Characterizing the size and colloidal state of nanoparticles. *Sci. Rep.* **5**, 09793 (2015).

286. Bladt, E. Optimization of electron tomography for the three dimensional study of nanoparticle assemblies. *Master Dissertation* (University of Antwerp, 2013).

287. Toor, A., Feng, T. & Russell, T. P. Self-assembly of nanomaterials at fluid interfaces. *Eur. Phys. J. E* **39**, 57 (2016).

288. Liao, H. & Zheng, H. Liquid Cell Transmission Electron Microscopy. *2Annual Rev. Phys. Chem.* **67**, 719–747 (2016).

289. Milne1, J. L. S. *et al.* Cryo-electron microscopy : A primer for the non-microscopist. *FEEBS J.* **280**, 28–45 (2013).

290. Dimaio, F. & Chiu, W. *Tools for Model Building and Optimization into Near-Atomic Resolution Electron Cryo- Microscopy Density Maps*. *Methods in Enzymology* **579**, (Elsevier Inc., 2016).

291. Ladinsky, M. S. *Micromanipulator-Assisted Vitreous Cryosectioning and Sample Preparation by High-Pressure Freezing*. *Methods in Enzymology* **481**, (Elsevier Inc., 2010).

292. Kuntsche, J., Horst, J. C. & Bunjes, H. Cryogenic transmission electron microscopy (cryo-TEM) for studying the morphology of colloidal drug delivery systems. *Int. J. Pharm.* **417**, 120–137 (2011).

293. Website. Available at: https://www.nobelprize.org/prizes/lists/all-nobel-prizes-in-chemistry. (Accessed: 11th December 2019)

294. Wang, Y. Cryo-electron microscopy finds place in materials science. *Sci. China Mater.* **61**, 129–130 (2018).

295. Patterson, J. P., Xu, Y., Moradi, M., Sommerdijk, N. A. J. M. & Friedrich, H. CryoTEM as an Advanced Analytical Tool for Materials Chemists. *Acc. Chem. Res.* **50**, 1495–1501 (2017).

296. Mckenzie, B. E. *et al.* The evolution of bicontinuous polymeric nanospheres in aqueous solution. *Soft Matter* **12**, 4113–4122 (2016).

297. Baumgartner, J. *et al.* Nucleation and growth of magnetite from solution. *Nat. Mater.* **12**, 310–314 (2013).

298. Nudelman, F. *et al.* The role of collagen in bone apatite formation in the presence of hydroxyapatite nucleation inhibitors. *Nat. Mater.* **9**, 9–14 (2010).

299. Li, Y. *et al.* Atomic structure of sensitive battery materials and interfaces revealed by cryo – electron microscopy. *Science (80-.).* **510**, 506–510 (2017).

300. Website. Available at: https://www.fischione.com/products/holders/model-2550-cryo-transfer-tomography-holder.

301. Wyckoff, R. W. G. Electron micrographs from concentrated solutions of the tobacco mosaic virus protein. *Biochim. Biophys. Acta* **1**, 143–146 (1947).

302. Williams, R. C. A method of freeze-drying for electron microscopy. *Experumental Cell Res.* **4**, 188–201 (1952).

303. Wang, D. *et al.* Interplay between spherical confinemen and particle shape on the self-assembly of rounded cubes. *Nat. Commun.* **9**, 2228 (2018).

304. Wang, D. *et al.* Binary icosahedral quasicrystals of hard spheres in spherical confinement. *Soft Condens. Matter* **Submitted**, (2019).

305. Adrian, M., Dubochet, J., Lepault, J. & McDowall, A. W. Cryo-electron microscopy of viruses. *Nature* **308**, 32–36 (1984).

306. Dobro, M. J., Melanson, L. A., Jensen, G. J. & McDowall, A. W. *Plunge Freezing for Electron Cryomicroscopy*. *Methods in Enzymology* **481**, (Elsevier Inc., 2010).

307. Dubochet, J. & McDowall, A. W. Vitrification of pure water for electron microscopy. *J. Microsc.* **124**, RP3–RP4 (1981).

308. Dang, Z. *et al.* Low-Temperature Electron Beam-Induced Transformations of Cesium Lead Halide Perovskite Nanocrystals. *ACS Omega* **2**, 5660–5665 (2017).

309. Dang, Z. *et al.* In Situ Transmission Electron Microscopy Study of Electron Beam-Induced Transformations in Colloidal Cesium Lead Halide Perovskite Nanocrystals. *ACS Nano* **11**, 2124–2132 (2017).

310. Tong, Y. *et al.* Highly Luminescent Cesium Lead Halide Perovskite Nanocrystals with Tunable Composition and Thickness by Ultrasonication. *Angew. Chemie Int. Ed.* **55**, 13887–13892 (2016).

311. Alberti, A. *et al.* Pb clustering and PbI2 nanofragmentation during methylammonium lead

iodide perovskite degradation. *Nat. Commun.* **10**, 2196 (2019).

312. Weyland, M. & Muller, D. A. Tuning the convergence angle for optimum STEM performance. *FEI NanoSolutions* **1**, 24–35 (2005).

313. Sasaki, T. *et al.* Evaluation of probe size in STEM imaging at 30 and 60kV. *Micron* **43**, 551–556 (2012).

314. James, E. M. & Browning, N. D. Practical aspects of atomic resolution imaging and analysis in STEM. *Ultramicroscopy* **78**, 125–139 (1999).

315. Chen, F., Van Dyck, D. & Kisielowski, C. In-line three-dimensional holography of nanocrystalline objects at atomic resolution. *Nat. Commun.* **7**, 10603 (2016).

316. Kisielowski, C., Helveg, S., Hansen, L. & Specht, P. Controlling Beam-Sample Interaction in Low Dimensional Materials by Low Dose Rate Electron Microscopy. *Microsc. Microanal.* **21**, 1321–1322 (2015).

317. Jiang, N. & Spence, J. C. H. On the dose-rate threshold of beam damage in TEM. *Ultramicroscopy* **113**, 77–82 (2012).

318. Kisielowski, C. On the pressing need to address beam–sample interactions in atomic resolution electron microscopy. *J. Mater. Sci.* **51**, 635–639 (2016).

319. Meyer, J. C., Kotakoski, J. & Mangler, C. Atomic structure from large-area, low-dose exposures of materials: A new route to circumvent radiation damage. *Ultramicroscopy* **145**, 13–21 (2014).

320. Zhang, D. *et al.* Atomic-resolution transmission electron microscopy of electron beam-sensitive crystalline materials. *Science (80-.).* **359**, 675–679 (2018).

321. Calderon, H. A. *et al.* Maintaining the genuine structure of 2D materials and catalytic nanoparticles at atomic resolution. *Micron* **68**, 164–175 (2015).

322. Haber, J. A., Anzenburg, E., Yano, J., Kisielowski, C. & Gregoire, J. M. Multiphase nanostructure of a quinary metal oxide electrocatalyst reveals a new direction for OER electrocatalyst design. *Adv. Energy Mater.* **5**, 1–11 (2015).

323. Zhu, Y. *et al.* Unravelling surface and interfacial structures of a metal-organic framework by transmission electron microscopy. *Nat. Mater.* **16**, 532–536 (2017).

324. *User's Guide - K2 Summit and K2 Base Direct Detection Camera*. (Gatan, Inc).

325. Faruqi, A. R. & Mcmullan, G. Direct imaging detectors for electron microscopy. *Nucl.*

Instruments Methods Phys. Res. A **878**, 180–190 (2018).

326. Hÿtch, M. J. & Stobbs, W. M. Quantitative comparison of high resolution TEM images with image simulations. *Ultramicroscopy* **53**, 191–203 (1994).

327. Hÿtch, M. J. & Stobbs, W. M. The use of non-linear characteristics of a lattice fringe image for the characterisation of imaging parameters. *Ultramicroscopy* **53**, 63–72 (1994).

328. Van Dyck, D., Lobato, I., Chen, F. R. & Kisielowski, C. Do you believe that atoms stay in place when you observe them in HREM? *Micron* **68**, 158–163 (2015).

329. Krause, F. F. *et al.* Comparison of intensity and absolute contrast of simulated and experimental high-resolution transmission electron microscopy images for different multislice simulation methods. *Ultramicroscopy* **134**, 94–101 (2013).

330. Boothroyd, C. B. Why don't high-resolution simulations and images match? *J. Microsc.* **190**, 99–108 (1998).

331. Thust, A. The Stobbs factor in HRTEM: Hunt for a phantom? *EMC 2008 14th Eur. Microsc. Congr. 1–5 Sept. 2008, Aachen, Ger.* **1**, 163–164 (2008).

332. Boothroyd, C. B. & Dunin-Borkowski, R. E. The contribution of phonon scattering to high-resolution images measured by off-axis electron holography. *Ultramicroscopy* **98**, 115–133 (2004).

333. Howie, A. Hunting the Stobbs factor. *Ultramicroscopy* **98**, 73–79 (2004).

334. Thust, A. High-resolution transmission electron microscopy on an absolute contrast scale. *Phys. Rev. Lett.* **102**, 5–8 (2009).

335. O'Keefe, M. A., Buseck, P. R. & Iijima, S. Computed crystal structure images for high resolutioin electron microscopy. *Nature* **247**, 322–324 (1978).

336. Coene, W., Janssen, G., Op de Beeck, M. & Van Dyck, D. Phase Retrieval through Focus Variation for Ultra-Resolution in Field-Emission Transmission Electron Microscopy. *Phys. Rev. Lett.* **69**, 3743–3746 (1992).

337. Thust, A., Overwijk, M. H. F., Coene, W. M. J. & Lentzen, M. Numerical correction of lens aberrations in phase-retrieval HRTEM. *Ultramicroscopy* **64**, 249–264 (1996).

338. Tang, D., Zandbergen, H. W., Jansen, J., Op De Beeck, M. & Van Dyck, D. Fine-tuning of the focal residue in exit-wave reconstruction. *Ultramicroscopy* **64**, 265–276 (1996).

339. Hsieh, W. K., Chen, F. R., Kai, J. J. & Kirkland, A. I. Resolution extension and exit wave reconstruction in complex HREM. *Ultramicroscopy* **98**, 99–114 (2004).

340. Erni, R., Rossell, M. D. & Nakashima, P. N. H. Optimization of exit-plane waves restored from HRTEM through-focal series. *Ultramicroscopy* **110**, 151–161 (2010).

341. Keefe, M. A. O. *et al.* Sub-Angstrom high-resolution transmission electron microscopy at 300 keV. *Ultramicroscopy* **89**, 215–241 (2001).

342. Op De Beeck, M. & Van Dyck, D. Direct structure reconstruction in HRTEM. *Ultramicroscopy* **64**, 153–165 (1996).

343. Zandbergen, H. W., Tang, D., Jansen, J. & Cava, R. J. The use of through focus exit wave reconstruction in the structure determination of several intermetallic superconductors. *Ultramicroscopy* **64**, 231–247 (1996).

344. Steinecker, A. & Mader, W. Exit wave reconstruction using a conventional transmission electron microscope. *J. Microsc.* **190**, 281–290 (1998).

345. Thust, A., Coene, W. M. J., Op de Beeck, M. & Van Dyck, D. Focal-series reconstruction in HRTEM: simulation studies on non-periodic objects. *Ultramicroscopy* **64**, 211–230 (1996).

346. Coene, W. M. J., Janssen, A. J. E. M., Denteneer, T. J. J., Op de Beeck, M. & Van Dyck, D. Focus Variation Image Reconstruction in Field Emission TEM. *MSA Bull.* **24**, 472–486 (1994).

347. Van Dyck, D. & Zandbergen, H. W. Exit Wave Reconstructions Using Through Focus Series of HREM Images. *Microsc. Res. Tech.* **49**, 301–323 (2000).

348. Kirkland, A. I. & Haigh, S. J. Exit Wavefunction Reconstruction. *Jeol news* **44**, 6–11 (2009).

349. Haigh, S. J., Jiang, B., Alloyeau, D., Kisielowski, C. & Kirkland, A. I. Recording low and high spatial frequencies in exit wave reconstructions. *Ultramicroscopy* **133**, 26–34 (2013).

350. Ophus, C. & Ewalds, T. Guidelines for quantitative reconstruction of complex exit waves in HRTEM. *Ultramicroscopy* **113**, 88–95 (2012).

351. Yang, G., Dong, B., Gu, B., Zhuang, J. & Ersoy, O. K. Gerchberg–Saxton and Yang–Gu algorithms for phase retrieval in a nonunitary transform system: a comparison. *Appl. Opt.* **33**, 209 (1994).

352. Gerchberg, R. W. & Saxton, W. O. Gerchberg—Saxton algorithm: experimental realisation and modification for the problem of formation of multimode laser beams. *Optik (Stuttg).* **35**, 237–246 (1972).

353. Van Dyck, D., Op De Beek, M. & Coene, W. A new approach to object wavefunction reconstruction in electron microscopy. *Opt.* **93**, 103–107 (1993).

354. Op De Beeck, M., Van Dyck, D. & Coene, W. Wave function reconstruction in HRTEM: The parabola method. *Ultramicroscopy* **64**, 167–183 (1996).

355. Coene, W. M. J., Thust, A., Op De Beeck, M. & Van Dyck, D. Maximum-likelihood method for focus-variation image reconstruction in high resolution transmission electron microscopy. *Ultramicroscopy* **64**, 109–135 (1996).

356. Allen, L. J. & Oxley, M. P. Phase retrieval from series of images obtained by defocus variation. *Opt. Commun.* **199**, 65–75 (2001).

357. Allen, L. J., McBride, W., O'Leary, N. L. & Oxley, M. P. Exit wave reconstruction at atomic resolution. *Ultramicroscopy* **100**, 91–104 (2004).

358. Ishizuka, K. Phase retrieval from image intensities: Why does exit wave restoration using IWFR work so well? *J. Electron Microsc. (Tokyo).* **62**, 109–118 (2013).

359. Website. Available at: https://www.totalresolution.com/reconstruction.htm. (Accessed: 4th February 2020)

360. Aert, S. Van, Geuens, P., Dyck, D. Van, Kisielowski, C. & Jinschek, J. R. Electron channelling based crystallography. *Ultramicroscopy* **107**, 551–558 (2007).

361. De Beeck, M. O. & Van Dyck, D. An analytical approach for the fast calculation of dynamical scattering in HRTEM. *Phys. Status Solidi* **150**, 587–602 (1995).

362. Geuens, P. & Van Dyck, D. The S-state model: A work horse for HRTEM. *Ultramicroscopy* **93**, 179–198 (2002).

363. Van Dyck, D. & Chen, J. H. A simple theory for dynamical electron diffraction in crystals. *Solid State Commun.* **109**, 501–505 (1999).

364. Geuens, P. & Dyck, D. V. A. N. The S-State Model for Electron Channeling in High-Resolution Electron Microscopy. *Adv. Imaging Electron Phys.* **136**, 111–226 (2005).

365. Lobato, I. & Van Dyck, D. MULTEM: A new multislice program to perform accurate and fast electron diffraction and imaging simulations using Graphics Processing Units with CUDA. *Ultramicroscopy* **156**, 9–17 (2015).

366. Lobato, I., van Aert, S. & Verbeeck, J. Progress and new advances in simulating electron

microscopy datasets using MULTEM. *Ultramicroscopy* **168**, 17–27 (2016).

367. Jinschek, J. R. *et al.* 3-D reconstruction of the atomic positions in a simulated gold nanocrystal based on discrete tomography: Prospects of atomic resolution electron tomography. *Ultramicroscopy* **108**, 589–604 (2008).

368. Borisenko, K. B. *et al.* Toward 3D structural information from quantitative electron exit wave analysis. *J. Phys. Conf. Ser.* **371**, 3–7 (2012).

369. Saghi, Z., Xu, X. & Möbus, G. Model based atomic resolution tomography. *J. Appl. Phys.* **106**, 024304 (2009).

370. Ren, D., Ophus, C., Chen, M. & Waller, L. A multiple scattering algorithm for three dimensional phase contrast atomic electron tomography. *Ultramicroscopy* **208**, 112860 (2020).

371. Borisenko, K. B. *et al.* Toward electron exit wave tomography of amorphous materials at atomic resolution. *J. Alloys Compd.* **536**, S94–S98 (2012).

372. Jia, C. L. *et al.* Determination of the 3D shape of a nanoscale crystal with atomic resolution from a single image. *Nat. Mater.* **13**, 1044–1049 (2014).

373. Dyck, D. Van, Jinschek, J. R. & Chen, F. 'Big Bang' tomography as a new route to atomic-resolution electron tomography. *Nature* **486**, 243–246 (2012).

374. Chen, F. R., Kisielowski, C. & Van Dyck, D. Prospects for atomic resolution in-line holography for a 3D determination of atomic structures from single projections. *Adv. Struct. Chem. Imaging* **3**, 8 (2017).

375. Ghiglia, D. C. & Pritt, M. D. *Two-Dimensional Phase Unwrapping: Theory, Algorithms, and Software*. (Wiley-Interscience, 1998).

376. Goldstein, R. M., Zebker, H. A. & Werner, C. L. Satellite radar interferometry: Two-dimensional phase unwrapping. *Radio Sci.* **23**, 713–720 (1988).

377. Spottiswoode, B. 2D phase unwrapping algorithms, MATLAB Central File Exchange. Available at: https://www.mathworks.com/matlabcentral/fileexchange/22504-2d-phase-unwrapping-algorithms. (Accessed: 28th November 2017)

378. Website. Available at: http://bio3d.colorado.edu/imod/doc/man/midas.html#TOP. (Accessed: 7th February 2020)

379. Website. Available at: http://bio3d.colorado.edu/imod/. (Accessed: 7th February 2020)

380. Aert, S. Van, Chang, L. Y., Bals, S., Kirkland, A. I. & Tendeloo, G. Van. Effect of amorphous layers on the interpretation of restored exit waves. *Ultramicroscopy* **109**, 237–246 (2009).

381. Pedrazo-Tardajos, A., Claes, N., Mosquera, J., Liz-Marzán, L. M. & Bals, S. Towards direct visualization of surface ligands by transmission electron microscopy. *In progress.*

382. Algara-Siller, G., Lehtinen, O., Turchanin, A. & Kaiser, U. Dry-cleaning of graphene. *Appl. Phys. Lett.* **104**, 153115 (2014).

383. Evtikhiev, N. N., Cheremkhin, P. A., Krasnov, V. V., Rodin, V. G. & Starikov, S. N. Increasing signal-to-noise ratio of registered images by using light spatial noise portrait of camera's photosensor. *Intell. Robot. Comput. Vis. XXXI Algorithms Tech.* **9025**, 90250X (2014).

List of scientific contributions

Publications

1 G. Gonzalez-Rubio, *T. Milagres de Oliveira*, T. Altantzis, A. La Porta, A. Guerrero-Martinez, S. Bals, L. Scarabelli, L.M. Liz-Marzan. **Disentangling the effect of seed size and crystal habit on gold nanoparticles seeded growth** Chem. Commun., 53, 11360 (2017). DOI 10.1039/c7cc06854a

2 V. Cremers, R. Rampelgerg, A. Barhoum, P. Walters, N. Claes, *T. Milagres de Oliveira*, G. Van Assche, S. Bals, J. Dendooven, C. Detavernier. **Oxidation barrier of Cu and Fe powder by Atomic Layer Deposition** – Surface & Coatings Technology, 349, 1032 (2018). DOI 10.1016/j.surfcoat.2018.06.048

3 L. Scarabelli, M. Schumacher, D. Jimenez de Aberasturi, J.P. Merkl, M. Henriksen-Lacey, *T. Milagres de Oliveira*, M. Janschel, C. Schmidtke, S. Bals, H. Weller, L.M. Liz-Marzán. **Encapsulation of Noble Metal Nanoparticles through Seeded Emulsion Polymerization as Highly Stable Plasmonic Systems**. Advanced Functional Materials. 1809071 (2019) DOI 10.1002/adfm.201809071

4 V. Cremers, G. Rampelberg, K. Baert, S. Abrahami, N. Claes, *T. Milagres de Oliveira*, H. Terryn, S. Bals, J. Dendooven, and C. Detavernier. **Corrosion protection of Cu by Atomic Layer Deposition.** Journal of Vacuum Science Technology A, 37 (2019) DOI 10.1116/1.5116136.

5 G. González-Rubio, *T. Milagres de Oliveira*, W. Albrecht, P. Díaz-Núñez, J. C. Castro-Palacio, L. Scarabelli, L. Bañares, A. Rivera, O. Peña-Rodríguez, S. Bals, L. M. Liz-Marzán, A. Guerrero-Martínez. **Hollow Gold Nanocrystals by Nanosecond Laser Irradiation.** J. Phys. Chem. Lett., 11, 670 (2020). DOI 10.1021/acs.jpclett.9b03574.

6 *T. Milagres de Oliveira*, W. Albrecht, I. Lobato, T. Altantzis, G. González-Rubio, A. Guerrero-Martínez, S. Van Aert, L.M. Liz-Marzán, S. Bals. **3D characterization of gold nanorods after welding under femtosecond laser irradiation**. *Submitted.*

Oral presentations

1. Three-dimensional characterisation of nanomaterials: from model-like systems to real nanostructures. Online EMAT Friday Lecture, University of Antwerp, Campus Groenenborger, Antwerp, 03/04/2020
2. Atomic resolution investigation of Gold nanoparticles irradiated with laser pulses. NANODAY 2018, NOVA University of Lisbon, Caparica Campus, Portugal 09/10/2018
3. Novel Approaches for Three-Dimensional Characterization of Nanomaterials at the Atomic Level. ACIN 2018, University of Namur, Namur 16/07/2018/-20/07/2018
4. Novel Approaches for Three-Dimensional Characterization of Nanomaterials at the Atomic Level. EMAT Friday Lecture, University of Antwerp, Campus Groenenborger, Antwerp, 02/03/2018
5. Alternative Techniques for Atomic Resolution Electron Tomography. 12th ATOM meeting, Antwerp, 21/09/2017 – 22/09/2017
6. Alternative Techniques for Electron Tomography at the Atomic Scale. EMAT Friday Lecture, University of Antwerp, Campus Groenenborger, Antwerp, 27/01/2017

Poster presentations

1. 3D Characterization of Gold Nanoparticles Irradiated with Pulsed Lasers. 3rd Faculty of Science Research Day, University of Antwerp, Campus Groenenborger, Antwerp, 23/01/2019
2. Alternative Techniques for Atomic Resolution Electron Tomography. 2nd Faculty of Science Research Day, University of Antwerp, Campus Groenenborger, Antwerp, 17/01/2018
3. Investigation of particles coated with ALD by means of Electron Microscopy. SIM User Forum 2017, Antwerp, 06/06/2017

Acknowledgments

First, I would like to thank and express my gratitude to my supervisor Prof. Dr. Sara Bals for her guidance during my PhD. I am very grateful for the chance to learn a lot from you Sara, professionally and personally. Also, thank you for giving me the opportunity to complete my PhD thesis at EMAT under your supervision.

I would like to thank my jury members Prof. Dr. Milorad Milosevic, Prof. Dr. Paul Scheunders, Prof. Dr. Johan Hofkens, Prof. Dr. Kees Joost Batenburg and Dr. Wiebke Albrecht for reading my thesis and the valuable input received which helped me improving my thesis. I also would like to thank Prof. Dr. Milorad Milosevic for your support and assistance at the beginning and at the end of my PhD.

I would like to thank our collaborators Prof. Dr. Luis M. Liz-Marzán and his team as well as Prof. Dr. Johan Hofkens and his team for providing the wonderful samples that made this thesis possible.

I also would like to express my gratitude to Adrián Pedrazo-Tarjados, Alexander Skorikov, Dr. Annick De Backer, Dr. Armand Béché, Prof. Dr. Dirk Van Dyck, Dr. Eva Bladt, Hans Vanrompay, Dr. Ivan Pedro Lobato Hoyos, Dr. Julien Ramade, Mikail Mychinko, Dr. Nathalie Claes, Prof. Dr. Sandra Van Aert, Prof. Dr. Thomas Altantzis and Dr. Wiebke Albrecht for all valuable discussions, assistance in the experiments/reconstruction and all the collaboration in the past four years. You greatly contributed in the shaping of my thesis. I also would like to thank Dr. Nathalie Claes for providing the Dutch translation of the Summary of the thesis.

Many thanks to all staff members of the university, specially Dr. Armand Béché and Dr. Ursula Ludacka for all the help at the microscopes and the training received, Dr. Tine Derez for your assistance in sample preparation lab and for providing great TEM grids, Liesbet Laurens for assisting me with graphical art, for the knowledge you shared and the cover design, Lydia Cassiers and Miek Van Loock for all the bureaucratic assistance and Koen De Cauwsemaecker for the IT assistance in the past four years.

Many thanks to all EMAT members and specially Bárbara Malheiros, Carolien Callaert, Gunnar Lumbeeck, Nathalie Claes, Olesia Karakulina, Saeid Pourbabak and Tine Derez for your friendship, the memorable lunch breaks, walks in the park and the external activities. I also would like to thank all colleagues who shared an office with me for the memorable moments.

I also wold like to express my gratitude to all my professors from UFMG, in special to Prof. Dr. Karla Balzuweit, for guiding me through the microscopy field and for sharing your knowledge with me.

Karla, I am very grateful for all the opportunities you gave me. Thank you for being my role model, professionally and personally.

A special thanks to my friends in Brazil that are together with me since I started my studies in Physics, in special, Ana Clara Sampaio Pimenta, Danielle Cristina Teles Ferreira, Lucas Schuab and Pamêlla Miranda for all the support in the past 10 years.

Finally, I would like to express my gratitude to my family for the love and support. Specially to my dear husband, Solon Duarte Pinho, for all the moments together, for your unconditional love, for your comprehension and support in the past 11 years. Without you, I would not be able to complete this thesis.